

NORTHWESTERN UNIVERSITY

Insights on the Intracellular Mechanism of Action of the Anticancer and
Antiangiogenic Copper Chelator Drug: Ammonium Tetrathiomolybdate (TM)

A DISSERTATION

SUBMITTED TO THE GRADUATE SCHOOL
IN PARTIAL FULFILLMENT OF THE REQUIREMENTS

For the degree

DOCTOR OF PHILOSOPHY

Field of Chemistry

By

HAMSELL M. ALVAREZ

EVANSTON, ILLINOIS

June, 2008

© Copyright by Hamsell M. Alvarez 2008

All Rights Reserved

ABSTRACT

Insights on the molecular mechanism of action of the anticancer and antiangiogenic copper chelator drug: Ammonium Tetrathiomolybdate (TM)

Hamsell M. Alvarez

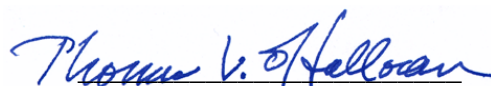
The biological antagonism between copper and molybdenum, first observed when cattle developed copper deficiencies after ingesting high levels of plant-born molybdenum, is currently being used in humans to treat two conditions: Wilson's Disease as well as several forms of metastatic cancer. There is surprisingly little known about the interaction of the biologically active tetrathiomolybdate ion (TM) with copper-proteins. TM has been proposed to alter copper metabolism and induce copper deficiency due to its powerful ability of chelating copper ions.

While the mechanism of how TM and copper interact in a physiological environment has not been clarified, preliminary results provide the molecular and structural characterization of the interaction of TM with the yeast intracellular copper chaperone, Atx1 and with the bovine superoxide dismutase, beSOD1. TM reacts quickly with Atx1 forming a robust purple trimer $[\text{TM}][(\text{Cu})(\text{Cu-Atx1})_3]$ complex, which represent the first detailed-structure of a $[\text{TM}][\text{Cu-protein}]$ interaction. This complex was isolated by analytical gel filtration, and characterized by ICP-OES, Bradford assay, UV-Visible spectroscopy, Fluorescence spectroscopy, X-ray absorption spectroscopy (XAS), and X-ray protein crystallography. Moreover, we proposed a detailed in-vitro molecular characterization of the interaction of TM with beSOD1, confirming the inhibition of this protein by partial copper removal, and formation of a $[\text{CuTM}]_x$ polymeric complex, which was confirmed by XAS.

The cellular uptake of TM using human hepatocellular cancer cells was explored by ICP-MS and X-ray fluorescence microscopy. We find that incubation of cancer cells with TM lead to the uploading and intracellular distribution of the drug. Analysis of whole cells shows a higher concentration of TM near the nucleus. Micro-XANES measurements at various cellular locations show a characteristic Mo^(VI) near-edge feature with tetrahedral coordination environment. Moreover, the ability of TM to inhibit cell proliferation and SOD1 activity was determined by a modified MTT and UV-VIS spectroscopy assay with a IC₅₀ = 7.3 μM (t_{incub} = 60 h) and 0.309 μM (t_{incub} = 60 h), respectively.

The disruption of the intracellular copper metabolism by formation of a suggested [(TM)(Cu)(Atx1)(Ccc2a)] complex as a result of the interaction between [TM][(Cu)(Cu-Atx1)₃] with apo-Ccc2a, was suggested by electrophoresis in native agarose gels, followed by a combination of ESI-MS, ICP-MS and LA-ICP-MS.

Given that the exact molecular target of the chelation therapy with TM is still a mystery, the cellular uptake and distribution of this copper chelator drug (TM), and its different reactivity and behavior with copper proteins (Atx1 and beSOD1), help us to start the elucidation on an intracellular mechanism of action of this drug. We suggest that copper proteins may have different Cu-dependent physiological pathways to react with TM, producing copper deficiency in the Cu-Mo antagonism, and in the treatment of the chronic copper poisoning, Wilson's disease and cancer.



Thomas V. O'Halloran
Dissertation Advisor

ACKNOWLEDGEMENTS

When I came to Chicago, IL from Charlotte, NC, almost five years and a half ago it was a very big transition in life for me, leaving the country side with its corn bread, sweet tea, and NASCAR races, to come to the big and windy Chicago, with its deep-dish pizza, snowy winters, and baseball.

I would like to express my appreciation to my thesis advisor Dr. Thomas O'Halloran for all his help and support during my PhD graduate studies, teaching me important lessons about perseverance and pursuit of perfection in science. Also, I would like to acknowledge to my graduate committee: Dr. Amy Rosenzweig, Dr. Hilary Godwin, Dr. Thomas Meade and Dr. Alfonso Mondragón for accepting the invitation to be part of my thesis committee and for their invaluable advices during my qualifying examination and research proposal.

I would like to thank in a very special way to my family in Lima, Perú; to my mom and dad, for all their help when I moved to Chicago, for being supportive always, specially in difficult times, and for encouraging me in my peculiar and difficult hope to become a scientist; to my sister for always support me with a smile and never ceased to believe that I could complete my doctorate even when I was not so certain, and finally to my cousin Alejandro, who helped me a lot when I left Charlotte to move to Chicago.

I must thank my girlfriend, Ann, who supported me for almost two years and a half to finish the last part of my PhD. She has given me the strength and confidence especially during some very difficult times at the end, which are part to be a PhD graduate student.

I would also like to thank my friends and colleagues from the Chemistry Department, which are like a second family here in the US. First, past and current members of the TVO

group; Lydia for mentoring during my first year, teaching me the basics of protein purification; Eric for being a good friend and roommate, and teach me a lot about synthetic chemistry; Janet and Haimei for her invaluable help with the human cells, microscopy and ICP-OES; Chandler and Yi for his friendship and help crystallizing and resolving the structure of our favorite purple complex, Monica for always being a good friend, visit me at my desk several times during the day and talk in ‘español’ forever, even that nobody understand us, and for her invaluable help to complete the decisive Chapter 6 of this thesis; and finally to Anja (protein preparations and purifications), Becky (ICP-MS & LA-ICP-MS), Meera (good partner as a super TA), Ben S. (DNA), Ryan, Rich (Fluorescence spectroscopy), Ryosuke (SOD1), Ben G., Nina (Western Blot) and Anna (preparation of Ccc2a). Also, I would also like to thank my friends from outside of my lab, Federico (Poepelmeir’s Lab), and all the past members from the Graduate Student Association for Latino and Spanish Activities, ‘G-SALSA’ (Monica, Perla, Simon, Fernando, Luis, Miguel, Beto, Juan, Genya, Dario, Luciano, Cesar, Jimena, Passant, etc) for all the memorably fun moments that I will never forget with the latin community from Northwestern University.

I would like to thank the faculty and staff from the Chemistry and Department at Northwestern University for all their help, in particular I would like to acknowledge Dr. Saman Shafaie (ASL) for his help with the ICP-OES. Finally I would like to extend my gratefulness to Dr. Stefan Vogt and Dr. Barry Lai from the APS at the Argonne National Lab for their help and advice with the X-ray fluorescence microscopy experiments; to Dr. James Penner-Hahn, Dr. Maria Clausen and Rebekah Kelly from the University of Michigan for his help with the Cu and Mo X-ray absorption spectroscopy experiments; to Dr. Alfonso Mondragón from the Department of Biochemistry, Molecular Biology and Cell Biology from Northwestern University for his

invaluable guidance for solving the X-ray structure of the purple complex; to Dr. Pamela Focia from the Department of Molecular Pharmacology and Biological Chemistry at the Feinberg School of Medicine for her help in the X-ray data collection at the APS; to the Malkin Fellowship from the Robert H. Lurie Comprehensive Cancer Center; to Dr. Yan Wang from the Chicago Biomedical Consortium at the University of Illinois at Chicago for his help with the ESI-MS; to Dr. Heather Relyea for proofreading my papers before submission, to Dr. Alberto Giesecke from the Academia Nacional de Ciencias del Perú, for his help and nomination for the 56th Meeting of Nobel Laureates in Lindau, Germany; and finally Dr. Daniel Rabinovich from the Department of Chemistry at the University of North Carolina at Charlotte for his invaluable scientific support and friendship.

TABLE OF CONTENTS

COPYRIGHT	2
ABSTRACT	3
ACKNOWLEDGMENTS	5
TABLE OF CONTENTS	8
LIST OF TABLES	15
LIST OF FIGURES	16
LIST OF SCHEMES	23
CHAPTER 1: INTRODUCTION AND SCOPE OF THE THESIS	25
1.1 Teart and Swayback	25
1.2 Chemistry of copper thiomolybdates	27
1.3 Chronic copper poisoning (CCP)	29
1.4 Wilson's disease	29
1.5 Angiogenesis and cancer	31
1.7 Scope of thesis	34
CHAPTER 2: SOLUTION COORDINATION CHEMISTRY OF THE INTERACTION OF THE YEAST CU-METALLOCHAPERONE (Cu-Atx1) WITH TM	38
Abstract	38
2.1 Introduction	39
2.2 Experimental Procedures	40
2.2.1 Synthesis and characterization of ammonium tetrathiomolybdate	40
2.2.2 Preparation and purification of protein samples	41

2.2.3 Preparation of Cu-Atx1	41
2.2.4 Ultrafiltration	41
2.2.5 Analytical gel filtration	42
2.2.6 UV-Visible spectroscopy	43
2.2.7 UV-Visible titration spectroscopy	43
2.2.8 Fluorescence spectroscopy	43
2.2.9 Preparation of XAS samples	43
2.2.10 X-ray absorption data collection and analysis	44
2.3 Results	47
2.3.1 Ultrafiltration	47
2.3.2 Analytical gel filtration	47
2.3.3 UV-visible spectroscopy	52
2.3.4 Fluorescence spectroscopy	58
2.3.5 X-ray absorption spectroscopy	58
2.4 Discussion and Conclusion	61
CHAPTER 3: STRUCTURAL COORDINATION CHEMISTRY OF THE INTERACTION OF THE YEAST CU-METALLOCHAPERONE (Cu-Atx11) WITH TM: '[TM]((Cu)(Cu- Atx1) ₃]'	
Abstract	69
3.1 Introduction	70
3.2 Experimental Procedure	71

	10
3.2.1 Preparation and purification of wild-type Atx1	71
3.2.2 Preparation and purification of Se-Met-Atx1	71
3.2.3 Matrix-assisted laser desorption/ionization time-of-flight mass spectrometry (MALDI/TOF MS)	72
3.2.4 Preparation of Cu-Atx1 and Se-Met-Cu-Atx1	74
3.2.5 Preparation of crystallization sample	74
3.2.6 Crystallization and data collection	75
3.2.7 Structure determination and refinement	75
3.3 Results	75
3.3.1 Crystallization	75
3.3.2 Protomer structure	84
3.3.3 [CuSMo] cluster and multiple anomalous dispersion (MAD)	84
3.4 Discussion and Conclusion	88
CHAPTER 4: SOLUBLE COORDINATION CHEMISTRY AND INHIBITION OF THE BOVINE SUPEROXIDE DISMUTASE (Cu₂Zn-beSOD1) WITH TM	96
Abstract	96
4.1 Introduction	97
4.2 Experimental Procedure	98
4.2.1 Synthesis and characterization of ammonium tetrathiomolybdate	98
4.2.2 Preparation and purification of protein samples	98
4.2.3 Ultrafiltration	99
4.2.4 UV-Visible spectroscopy	99

	11
4.2.5 UV-Visible titration spectroscopy	99
4.2.6 Protein gel extraction	100
4.2.7 Copper depletion studies	100
4.2.8 Electrophoresis: SDS-PAGE	100
4.2.9 Electrophoresis: SOD1 activity assay	101
4.2.10 UV-Visible spectroscopy SOD1 activity assay	101
4.2.11 Preparation of XAS samples	102
4.2.12 X-ray absorption data collection and analysis	104
4.3 Results	106
4.3.1 Ultrafiltration	106
4.3.2 UV-Visible spectroscopy	107
4.3.3 Protein gel extraction	110
4.3.4 Copper depletion	110
4.3.5 Electrophoresis: SDS-PAGE	112
4.3.6 SOD1 activity assay: Electrophoresis and UV-Visible spectroscopy	114
4.3.7 X-ray absorption spectroscopy	119
4.4 Discussion and Conclusion	121
CHAPTER 5: CELLULAR UPTAKE, DISTRIBUTION AND CYTOTOXICITY OF TM IN HUMAN HEPATOCELLULAR CARCINOMA CELLS (HEPG2)	128
Abstract	128
5.1 Introduction	129
5.2 Experimental Procedure	130

5.2.1 Synthesis and characterization of ammonium tetrathiomolybdate	130
5.2.2 Culture methods	130
5.2.3 Cytotoxicity studies	130
5.2.4 Cell uptake studies (ICP-MS)	133
5.2.5 Preparation of whole cell samples for X-ray fluorescence analysis	134
5.2.6 Preparation of thin-section cell samples for X-ray fluorescence analysis	135
5.2.7 Collection of XRF data	135
5.2.8 Micro X-ray absorption near-edge structure (micro-XANES)	138
5.2.9 Preparation of cytosolic extract from HEPG2 cells	138
5.2.10 UV-Visible spectroscopy SOD1 activity assay	139
5.3 Results	139
5.3.1 Light microscopy studies of TM-HEPG2 cells	139
5.3.2 Cytotoxicity studies of HEPG2 cells with TM	140
5.3.3 HEPG2-TM cell uptake studies	140
5.3.4 X-ray fluorescence microscopy (XRF) of HEPG2 cells	142
5.3.5 XRF of control HEPG2 cells	147
5.3.6 XRF of TM-treated HEPG2 cells	147
5.3.7 XRF of thin-section of TM-treated HEPG2 cells	147
5.3.8 Micro-XANES of TM-treated HEPG2 cells	153
5.3.9 TM-intracellular inhibition of SOD1 activity in HEPG2 cells	153
5.4 Discussion and Conclusion	158

	13
CHAPTER 6: TM INHIBITION OF COPPER TRANSFER ACTIVITY OF	
ATX1	161
Abstract	161
6.1 Introduction	162
6.2 Experimental Procedure	164
6.2.1 Preparation and purification of protein samples	164
6.2.2 UV-Vis Titration spectroscopy	164
6.2.3 Native agarose gel electrophoresis	164
6.2.4 Isolation of proteins and components of protein-protein complexes by gel extraction	164
6.2.5 Identification of proteins and components of protein-protein complexes by ESI- MS, ICP-MS and LA-ICP-MS	165
6.3 Results	166
6.3.1 UV-Vis Titration spectroscopy	166
6.3.2 Native gel electrophoresis	168
6.3.3 Identification of proteins and components of protein-protein complexes by ESI-MS	169
6.3.4 ICP-MS/LA-ICP-MS metal content determination in proteins and protein-protein complexes isolated from agarose gel	180
6.4 Discussion and Conclusion	185
REFERENCES	189
Chapter 1	189
Chapter 2	193

	14
Chapter 3	196
Chapter 4	198
Chapter 5	200
Chapter 6	201
CURRICULUM VITA	203

LIST OF TABLES

CHAPTER 2:

Table 2.1: Mass balance of protein, Cu and Mo during ultrafiltration studies.	47
Table 2.2: Metal and protein [] (μM) of chromatographic fraction in Figure 2.1A.	49
Table 2.3: Metal and protein [] (μM) of chromatographic fraction in Figure 2.1B.	50
Table 2.4: Metal and protein [] (μM) of chromatographic fraction in Figure 2.2.	52
Table 2.5: Metal and protein [] (μM) of chromatographic fraction in Figure 2.3.B.	54
Table 2.6: Results of Cu and Mo EXAFS curve fitting for [TM][Cu-Atx1].	64
Table 2.7: Fluorescence spectroscopy for copper metallothioneins.	66

CHAPTER 3:

Table 3.1: Data collection and refinement statistics.	76
---	----

CHAPTER 4:

Table 4.1: Mass balance of protein, Cu, and Mo during ultrafiltration experiment.	107
Table 4.2: Metal and protein concentration table of gel extract (μM).	111
Table 4.3: % of SOD1 activity remaining after incubation with TM and $[\text{MoO}_2\text{S}_2]^{2-}$.	114
Table 4.4: Results of the Cu and Mo EXAFS curve fitting for (Cu, Zn-beSOD1 + TM).	121

CHAPTER 5:

Table 5.1: X-ray fluorescence energies of S, Cl and Mo.	144
---	-----

CHAPTER 6:

Table 6.1: Stoichiometry of Cu and Mo from protein gel extracts (μmol).	182
--	-----

LIST OF FIGURES

CHAPTER 1:

- Figure 1.1: X-ray structures of some Cu tetrathiomolybdate anions 28
- Figure 1.2: Sequential steps for angiogenesis. 32
- Figure 1.3: Copper trafficking pathways within a eukaryotic cell. 35

CHAPTER 2:

- Figure 2.1: A. Analytical gel filtration chromatograms of apo-Atx1, apo-Atx1 + TM (1:1.4), Cu-Atx1 and Cu-Atx1 + TM (1:1.4); and B. apo-Hah1, apo-Hah1 + TM (1:1.4), Cu-Hah1 and Cu-Hah1 + TM (1:1.4). 48
- Figure 2.2: A. Analytical gel filtration chromatograms of 0.5 mM Cu-Atx1 + TM (1:0.4, 1:1.4); B. 2.0 mM Cu-Atx1 + TM (1:0.4, 1:1.4). 51
- Figure 2.3: A. Analytical gel filtration chromatograms of 2.0 mM Cu-Atx1 + TM (1:0.4) ($t_{\text{incub}} = 30 \text{ min, 1 h, 1.5 h, 2 h}$); B. Analytical gel filtration chromatograms of 3.0 mM X-Atx1 (X = Cu, Ag, Au) + TM (1:0.4). 53
- Figure 2.4: UV-visible absorbance of 0.2 mM apo-Atx1 + TM (1:0.4), 0.2 mM Cu-Atx1 + TM (1:0.4), 0.08 mM TM and $[\text{Cu}(\text{CH}_3\text{CN})_4][\text{PF}_6] + \text{TM}$ (1:1). 54
- Figure 2.5: A. UV-visible absorbance of TM as a function of apo-Atx1 concentration; B. Absorbance as a function of added apo-Atx1 monitored at 317 and 468 nm (molar ratio plot). 56
- Figure 2.6: UV-visible absorbance of TM as a function of Cu-Atx1 concentration. 57

Figure 2.7: A. UV-visible absorbance of TM and purified [TM][X-Atx1] (X = Cu, Ag, Au); B. Plot of the extinction coefficient (ϵ_{obs}) against λ of [TM][X-Atx1].	17 59
Figure 2.8: Fluorescence of [TM][Cu-Atx1], A. Emission spectrum with excitation at 280 nm; B. Excitation spectrum detected at 410 nm.	60
Figure 2.9: A. Cu-XANES of [TM][Cu-Atx1]; B. Mo-XANES of [TM][Cu-Atx1].	62
Figure 2.10: A, B. Cu-EXAFS spectrum and Cu K-edge Fourier transform of [TM][Cu-Atx1]; C, D. Mo-EXAFS spectrum and Mo K-edge Fourier transform of [TM][Cu-Atx1].	63
 CHAPTER 3:	
Figure 3.1: MALDI/TOF mass spectrum of Se-Met-Atx1.	73
Figure 3.2: Analytical gel filtration chromatogram of 3.0 mM Cu-Atx1 + TM (1:0.4).	78
Figure 3.3: Single crystals (#1) of [TM][(Cu)(Cu-Atx1) ₃] using 2.0 M (NH ₄) ₂ SO ₄ plus 5% 2-propanol.	79
Figure 3.4: Single crystals (#2) of [TM][(Cu)(Cu-Atx1) ₃] using 0.2 M sodium formate plus 20% PEG 3350.	79
Figure 3.5: Rod cluster and isolated single crystals (#3) of [TM][(Cu)(Cu-Atx1) ₃] using 0.2 M sodium formate plus 20% PEG 3350.	80
Figure 3.6: A, B: Plate crystals (#4) of [TM][(Cu)(Cu-Atx1) ₃] using 0.15 M DL-Malic acid pH 7.0 plus 20% PEG 3350; C, D: Diffraction pattern of [TM][(Cu)(Cu-Atx1) ₃] at 1.8 Å.	82
Figure 3.7: Rod cluster (#5) and single crystals (#6) of [TM][(Cu)(Se-Met-Cu-Atx1) ₃] using 0.15 M DL-Malic acid plus 20% PEG3350.	83

Figure 3.8: A. Single crystals of (#7) [TM]((Cu)(Cu-Atx1) ₃) 0.15 M DL-Malic pH 7.0 plus 20% PEG3350; B. Diffraction pattern of [TM]((Cu)(Cu-Atx1) ₃) at 2.3 Å.	18 85
Figure 3.9: Overall structure of {[TM]((Cu)(Cu-Atx1) ₃) ₄ .	86
Figure 3.10: Inter-chain H-bonds (purple dashed line) of a [TM]((Cu)(Cu-Atx1) ₃) trimer.	87
Figure 3.11: Structure of a [TM]((Cu)(Cu-Atx1) ₃) trimer.	89
Figure 3.12: Structure of the ‘nest-shaped’ [S ₆ Cu ₄ MoS ₄] cluster in the [TM]((Cu)(Cu-Atx1) ₃) trimer complex.	90
Figure 3.13: H-bond network (with Lys65, Thr14 and Gly17) and positive α helix 2 dipole.	91
Figure 3.14: A. Superposition of Hg-Atx1 with monomer B (Cu-Atx1) from [TM]((Cu)(Cu-Atx1) ₃); B. Superposition of Cu-Hah1 with monomer B (Cu-Atx1) from [TM]((Cu)(Cu-Atx1) ₃).	94
CHAPTER 4:	
Figure 4.1: beSOD1 inhibition calibration curve using WST-1 UV-Visible spectroscopy SOD1 activity assay.	103
Figure 4.2: UV-visible absorbance of 0.08 mM Cu,Zn-beSOD1, 0.08 mM Cu,Zn-beSOD1 + TM (1:1), 0.08 mM TM, 0.08 mM CuSO ₄ •5H ₂ O + TM (1:1).	108
Figure 4.3: UV-visible absorbance of TM as a function of Cu,Zn-beSOD1 concentration.	109
Figure 4.4: SOD1 gel extraction, A. 4-15% NATIVE PAGE of SOD1; B. NATIVE PAGE of SOD1 + TM (1:25); C. UV-visible spectra of gel extracts.	111

	19
Figure 4.5: 1. Changes in Mo, Zn and Cu concentration in SOD1 incubated with Different amounts of TM after PD-10 gel filtration chromatography; 2. 4-15% NATIVE-PAGE SOD1 activity assay and UV-visible spectroscopy activity assay	113
Figure 4.6: 12% SDS-PAGE of SOD1 with different amounts of TM.	115
Figure 4.7: 4-15% NATIVE-PAGE SOD1 activity assay.	116
Figure 4.8: 4-15% NATIVE-PAGE SOD1 activity assay and densitometric analysis.	117
Figure 4.9: UV-visible spectroscopy beSOD1 activity assay.	118
Figure 4.10: A. Cu-XANES of (Cu, Zn-beSOD1 + TM); B. Mo-XANES of (Cu, Zn-beSOD1 + TM).	120
Figure 4.11: A, B. Cu EXAFS spectrum and Cu K-edge fourier transform of (Cu, Zn-beSOD1 + TM); C, D. Mo EXAFS spectrum and Mo K-edge fourier transform of (Cu, Zn-beSOD1 + TM).	122
 CHAPTER 5:	
Figure 5.1: Graphical determination of optimal HEPG2 cell count.	132
Figure 5.2: Light microscope images of HEPG2 cells after 1h of incubation with different concentrations of TM.	141
Figure 5.3: MTT cytotoxicity assay control experiment, A. HEPG2 cell prolifera- tion vs. time; B. Interference TM-MTT.	143
Figure 5.4: MTT cytotoxicity assay.	144
Figure 5.5: Comparison of the intracellular Mo concentrations in HEPG2 cells (mM/cell) by ICP-MS.	145
Figure 5.6: Light microscope image and XRF elemental distribution maps of Mo	

	20
and Cl for TM-treated HEPG2 whole cell collected at 11.0 keV (A), 20.1 (B);	
C. Fluorescence spectrum integrated over TM-treated HEPG2 cell collected at 11.0 keV and 20.1 keV.	146
Figure 5.7: XRF elemental distribution maps of Cl, K, Zn, Cu and Mo for a TM-untreated HEPG2 whole cell.	148
Figure 5.8: Light microscope image and XRF elemental distribution maps of P, K, Ca, Zn, Cu and Mo for a TM-treated HEPG2 whole cell (1 mM, 24 h) at 20.1 keV.	149
Figure 5.9: Light microscope image and XRF elemental distribution maps of P, K, Ca, Zn, Cu and Mo for TM-treated HEPG2 whole cells (1 mM, 24 h) at 20.1 keV.	150
Figure 5.10: Light microscope image and XRF elemental distribution maps of P, K, Ca, Zn, Cu and Mo for TM-treated HEPG2 whole cells (1 mM, 24 h) at 20.1 keV.	151
Figure 5.11: 1. XRF elemental distribution maps of Mo for TM-treated HEPG2 whole cells (1 mM, 24 h) at 20.1 keV; 2. HEPG2 total intracellular Mo concentration in mM/cell (pc/cell).	152
Figure 5.12: Light microscope image and XRF elemental distribution maps of Cl, K, Zn, Cu and Mo for a TM-treated thin-section of HEPG2 cell (1 mM, 24 h) At 20.1 keV.	154
Figure 5.13: XANES of reference compounds.	155
Figure 5.14: 1. XRF elemental distribution maps of Mo for a TM-treated HEPG2 cell (1 mM, 24 h) at 20.1 keV; 2. XANES spectra acquired at various locations.	155
Figure 5.15: 1. XRF elemental distribution maps of Mo for a TM-treated HEPG2 cell (1 mM, 24 h) at 20.1 keV; 2. XANES spectra acquired at various locations.	156
Figure 5.16; 1. XRF elemental distribution maps of Mo for a TM-treated HEPG2 cell	

(1 mM, 24 h) at 20.1 keV; 2. XANES spectra acquired at various locations. 156

Figure 5.17: UV-visible spectroscopy HEPG2-SOD1 activity assay. 157

CHAPTER 6:

Figure 6.1: A. UV-visible absorbance of [TM][(Cu)(Cu-Se-Met-Atx1)₃] as a function of apo-Ccc2a concentration, B. Absorbance as a function of added apo-Ccc2a monitored at 332 and 495 nm (molar ratio plot). 167

Figure 6.2: Native agarose gel electrophoresis with analysis of protein-protein complex formation. 170

Figure 6.3: ESI-MS spectrum of protein band # 1. 171

Figure 6.4: ESI-MS spectrum of protein band # 2. 171

Figure 6.5: ESI-MS spectrum of protein band # 3. 173

Figure 6.6: ESI-MS spectrum of protein band # 4. 173

Figure 6.7: ESI-MS spectrum of protein band # 5. 175

Figure 6.8: ESI-MS spectrum of protein band # 6. 175

Figure 6.9: ESI-MS spectrum of protein band # 7. 176

Figure 6.10: ESI-MS spectrum of protein band # 8 (RT: 11.38 min). 176

Figure 6.11: ESI-MS spectrum of protein band # 8 (RT: 12.48 min). 177

Figure 6.12: ESI-MS spectrum of protein band # 9. 177

Figure 6.13: ESI-MS spectrum of protein band # 10. 178

Figure 6.14: ESI-MS spectrum of protein band # 11 (RT: 11.08 min). 178

Figure 6.15: ESI-MS spectrum of protein band # 11 (RT: 11.98 min). 179

Figure 6.16: ESI-MS spectrum of protein band # 12. 179

Figure 6.17: ESI-MS spectrum of protein band # 13.	181
Figure 6.18: Control native gel lanes with corresponding LA-ICP-MS scans for Cu.	183
Figure 6.19: Native gel lanes with corresponding LA-ICP-MS scans for Cu & Mo.	184

LIST OF SCHEMES

CHAPTER 1:

Scheme 1.1 Timeline of Ammonium Tetrathiomolybdate	26
Scheme 1.2 Hypothetical mechanism of copper depletion in ‘teart’ disorder.	28
Scheme 1.3 Structures of copper chelators drugs and copper competitive drugs used for the treatment of Wilson’s disease.	30
Scheme 1.4 TM’s extracellular mechanism of Cu depletion in the treatment of Wilson’s disease.	31
Scheme 1.5: Crystal structure of Cu-Atx1 (A) and Cu, Zn-beSOD1 (B).	36

CHAPTER 2:

Scheme 2.1: Possible binding modes for the core center of the [TM][Cu-Atx1].	67
Scheme 2.2: Model structures for $[(\text{HSCu})_3\text{S}_4\text{Mo}]^{2-}$ and $[\text{S}_2\text{MoS}_2\text{CuS}_2\text{MoS}_2]^{3-}$.	68
Scheme 2.3 Hypothetical formation of [TM][Cu-Atx1].	68

CHAPTER 3:

Scheme 3.1: Structure of the anion $[\text{Cu}_{12}\text{Mo}_8\text{S}_{32}]^{4-}$.	92
Scheme 3.2: Summary of TM reaction with Cu-Atx1.	95

CHAPTER 4:

Scheme 4.1: Principle of the WST-1 UV-Visible spectroscopy SOD1 activity assay.	103
Scheme 4.2: Stiefel’s internal electron transfer reaction model.	125
Scheme 4.3: Model for the polymeric $[\text{CuTM}]_x$ cluster.	126
Scheme 4.5: Diagram for inhibition mechanism of beSOD1 by TM.	127

CHAPTER 5:

	24
Scheme 5.1: Principle of the MTT cell cytotoxicity spectroscopy assay.	132
Scheme 5.2: Typical layout of a X-ray fluorescence microprobe.	137
Scheme 5.3: Intracellular uptake mechanism of TM by HEPG2 cells.	160
CHAPTER 6:	
Scheme 6.1: Proposed path for the intracellular transfer of Cu ^(II) from Atx1 to Ccc2a.	163
Scheme 6.2: Schematic representation of migration of negatively and positively charged proteins.	169
Scheme 6.3: Products of the reaction of Cu-Se-Met-Atx1 + apo-Ccc2a (1:1).	186
Scheme 6.4: Products of the reaction of [TM][Cu(Cu-Se-Met-Atx1) ₃] + apo-Ccc2a (1:1).	186
Scheme 6.5: A. Normal copper Atx1-chaperone pathway in yeast, B. TM affected copper Atx1-chaperone pathway in yeast.	188

Chapter 1

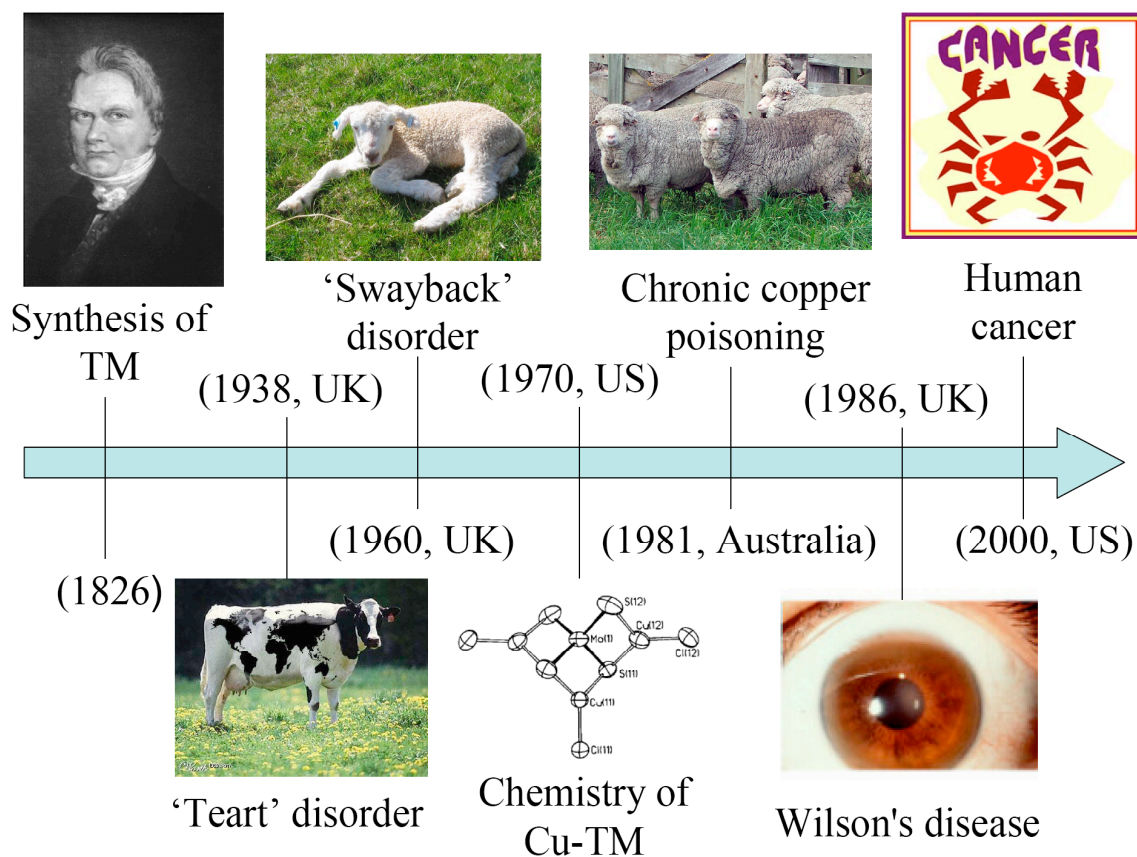
Introduction and Scope of the Thesis

The chemistry of ammonium tetrathiomolybdate (TM) was first described over 180 years ago. TM was first synthesized by J. J. Berzelius in 1826 by passing H_2S through a solution of ammonium molybdate.¹ Later in 1938, Mo has been associated to a disease called ‘Teart’ (or ‘Peat scours’) which was connected to the well-known ‘Cu-Mo antagonism’.² In 1960, Mills discovered that high dietary intakes of Mo and inorganic sulfates took by ewes during gestation result in the birth of copper-deficient lambs (‘Swayback’).³ TM’s first use was the treatment of sheep with chronic copper poisoning (CCP) by S. Gooneratne in 1981.⁴ Five years later, in 1986, J. Walshe applied this approach as the first clinical trial of this drug for the treatment of Wilson’s disease, a genetic disorder of copper metabolism.⁵ Recently, G. Brewer began using TM as an antiangiogenic low toxicity copper chelator drug for the treatment of several metastatic cancers.⁶ This chapter will explain some hallmarks in the history of the ammonium tetrathiomolybdate, detailing the chemical lineage from its relationship with the ‘teart’ disorder to its antiangiogenic effects in cancer (Scheme 1.1).

1.1 Teart and Swayback

Copper and molybdenum metal centers have been identified in a great variety of metalloproteins. Biological interactions between the two metals have been found initially in the ‘Teart’ and ‘Swayback’ diseases.^{2,3} The teart disorder is characterized by a molybdenum-induced copper deficiency.⁷ This disorder is thought to begin with formation of Cu-thiomolybdate

Scheme 1.1 Timeline of Ammonium Tetrathiomolybdate.

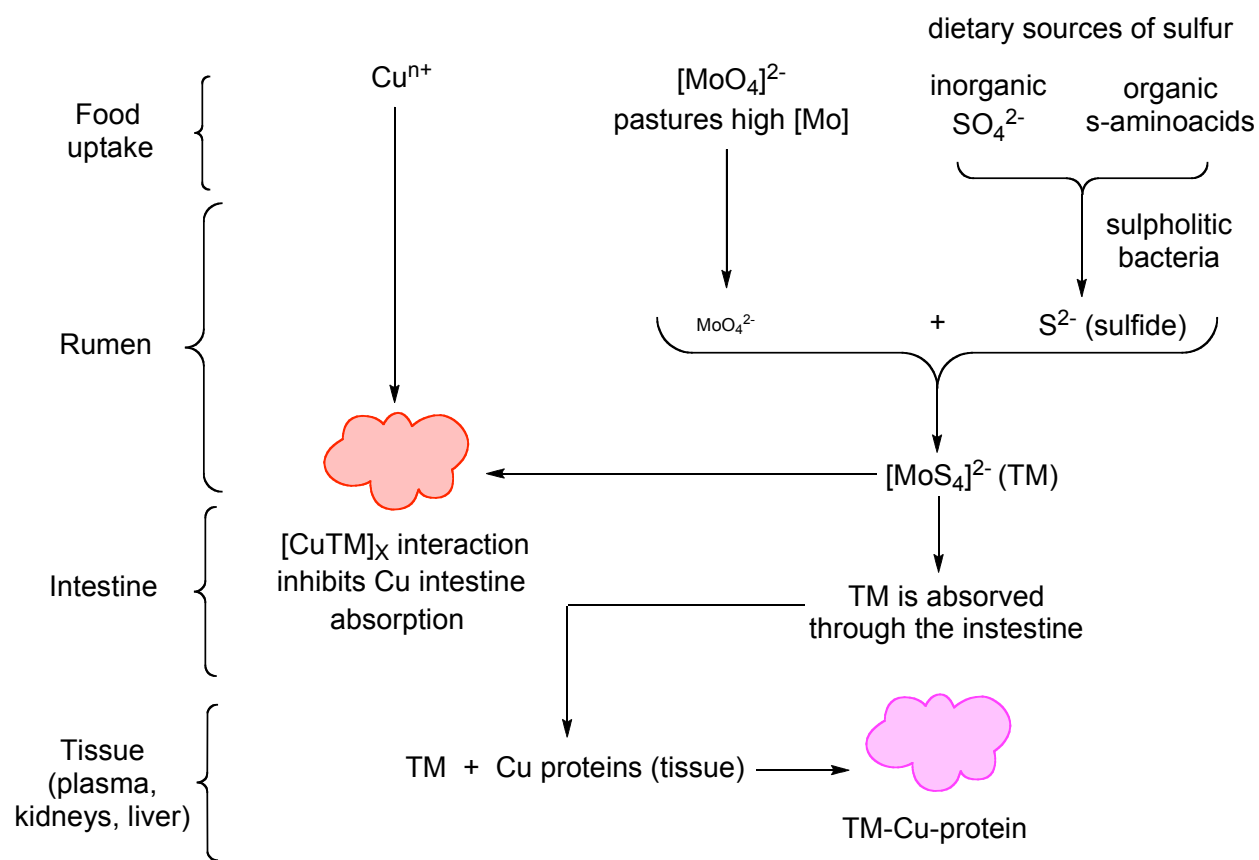


compounds. [CuTM] complexes form in the digestive track of cattle and sheep after ingestion of plants with high concentrations of molybdenum. Two kinds of [CuTM] complexes were described: a [CuTM]_x polymer which prevents intestinal copper absorption, and an inactive TM-Cu-protein interaction which causes a bloodstream's copper depletion (Scheme 1.2).⁷ The 'Teart' syndrome was characterized by anemia, diarrhea, growth retardation, skeletal abnormalities, achromotrichia, etc. Several experimental trials using copper oral boluses and injections have demonstrated the efficacy of a copper supplementation treatment.⁸

Another Cu-Mo antagonism disorder that has long been recognized is the Neonatal Ataxia or 'Swayback'. This neurological disorder observed in lambs is caused by a low copper diet or a molybdenum-induced copper deficiency.^{9,3} It is characterized by producing high

mortality of newborns, and incoordination movements due to lesions in the cerebrum and spinal cord. The occurrence of ‘Swayback’ can be prevented by copper supplementation of the ewe during pregnancy.

Scheme 1.2 Hypothetical mechanism of copper depletion in ‘Teart’ disorder.⁷



1.2 Chemistry of copper thiomolybdates

The chemistry of the $[\text{CuTM}]$ complexes laid the groundwork for understanding how $[\text{CuTM}]$ complexes were formed during the ‘teart’ and ‘swayback’ disease.

The coordination chemistry of thiomolybdates has been long studied due to the unique bridging ligand properties of the sulfide ions.¹⁰ Reaction of thiomolybdates with different metals

lead to formation of simple linear compounds as well as multi-metal clusters complexes with atypical structural attributes. Among all thiomolybdates, tetrathiomolybdate plays a key role in the inorganic biochemistry of copper, which will be discussed later in this Chapter.

Although no structural studies of TM-Cu-protein complexes have been described until now, there are several inorganic complexes that model the hypothetical TM-Cu-protein interaction. In 1970 P. Binnie identified the synthesis and structural characterization of the polymeric cuprous ammonium thiomolybdate ($\text{CuNH}_4\text{MoS}_4$).¹¹ Later, in 1998, T. Ecclestone and S. Laurie described the synthesis and XAS characterization of a $[\text{Cu}_{1.6}\text{MoS}_4\text{X}_y]$ complex (where X: Cl^- , Br^- & y : 1; or X: SO_4^{2-} & y : 0.5).^{12,13} In addition, several $[\text{CuTM}]$ complexes with additional stabilizing ligands have also been synthesized, from simple small compounds as $[\text{MoS}_4(\text{CuCl})_3]^{2-}$, to large inorganic clusters as $[\text{Mo}_2\text{S}_8\text{Cu}_8\text{Cl}_8]^{4-}$ (Figure 1.1).^{14,15}

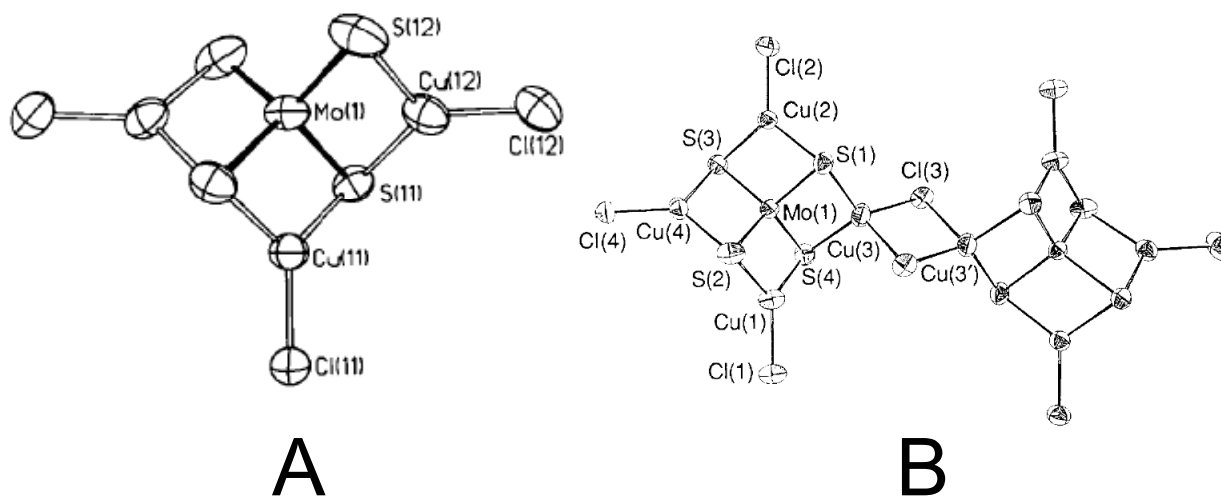


Figure 1.1 X-ray structures of some Cu tetrathiomolybdate anions (A: $[\text{MoS}_4(\text{CuL})_3]^{2-}$ and B $[\text{Mo}_2\text{S}_8\text{Cu}_8\text{Cl}_8]^{4-}$).^{14,15}

1.3 Chronic copper poisoning (CCP)

As discussed earlier, the Mo-induced copper deficiency observed in the ‘Teart’ and ‘Swayback’ disorders led to the utilization of Mo dietary supplements as an antidote for the treatment of acute copper intoxication known as the chronic copper poisoning (CCP). This copper metabolism disorder was found in numerous sheep with symptoms of anemia, jaundice, hemoglobinemia, icterus, methemoglobinemia, etc.¹⁶ These symptoms appeared after the liver accumulates copper; its subsequent release raises the copper concentration in blood twenty times the normal level.¹⁷ The increase of copper in circulation can produce not only significant damage to red blood cells but also to kidney tubule cells (‘black kidney’).¹⁸ The prevention and treatment of CCP with intravenous injection of TM was discovered in 1981 by S Gooneratne.⁴

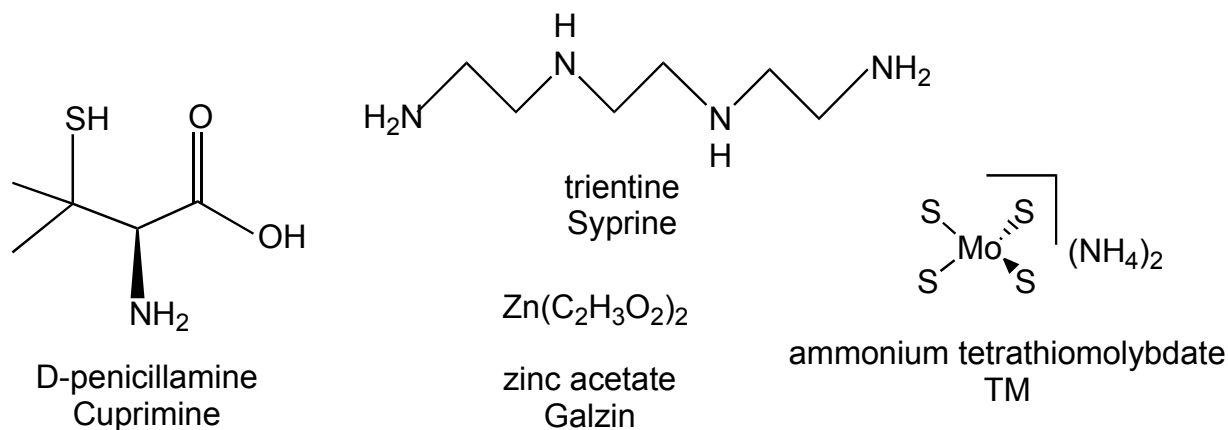
1.4 Wilson’s disease

The development of TM to combat CCP in sheep provided the initial motivation for using TM as a copper chelator drug. Specifically using TM in the treatment of the rare genetic disorder, Wilson’s disease (first described in 1912).¹⁹ Patients affected by this hereditary syndrome display multiple symptoms such as liver and spleen’s swelling, yellowing of the eyes (including the Kayser-Fleischer ring), anemia, kidney damage, rigid muscles, softening of the bones, speech problems, etc.^{20,21} This disease has been identified as a copper transport disorder, in which copper accumulation is caused by malfunction of the Wilson’s disease protein (WND).²²

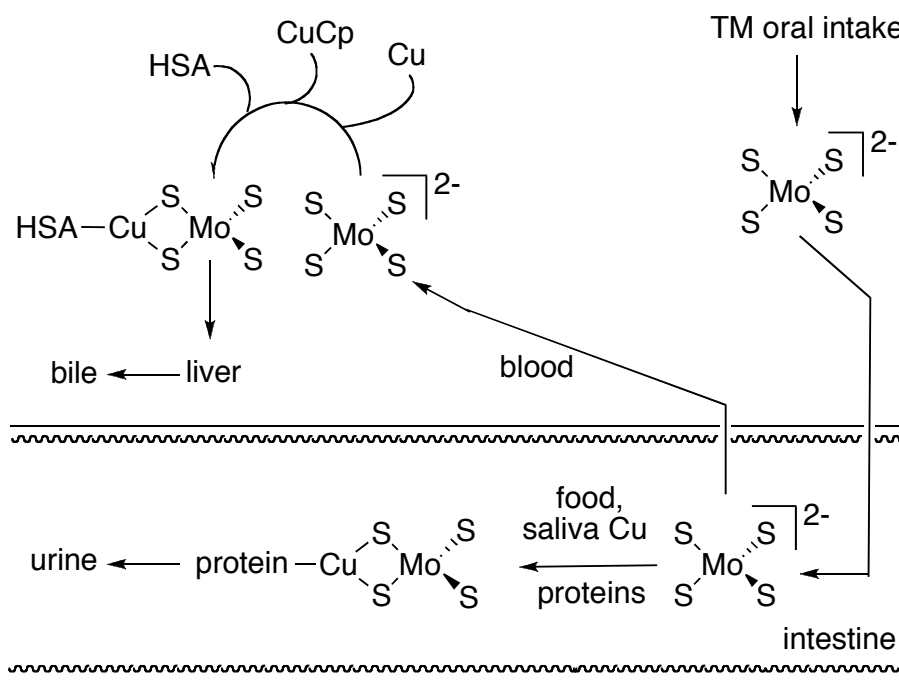
Early on, this copper metabolism disorder was treated using several copper chelators drugs, before TM was identified as one of the most effective alternatives. J. Walshe introduced the used of D-Penicillamine (1956) and Trientine (1982) (Scheme 1.3), which induce copper deficiency through urine excretion.^{23,24} These compounds lower the affinity of copper-binding

proteins for copper. Due to the high toxicity and numerous side effects caused by these agents, in 1961 G. Schouwink proposed an alternative less toxic therapy with zinc acetate (Scheme 1.3).²⁵ This new drug causes the reduction of copper levels in blood, through the synthesis and excretion of intestinal copper metallothioneins. After clinical trials revealed that Zn acetate was mostly a maintenance drug, J. Walshe in 1986 proposed the novel application of a TM treatment (Scheme 1.3) for patients with Wilson's disease.⁵ Ten years later, clinical trials confirmed the high efficacy and low toxicity of this drug with minor side effects (such as reversible mild anemia).^{26,27} In 1991 G. Brewer suggested an extracellular mechanism to detail how this metallodrug was causing a copper deficiency.²⁸ In Brewer's mechanism TM can interrupt the intestinal absorption of copper or can be absorbed into the bloodstream, producing the urine or bile excretion of TM-Cu-protein complexes, respectively (Scheme 1.4)

Scheme 1.3 Structures of copper chelators and copper competitive drugs used for the treatment of Wilson's disease.



Scheme 1.4 TM's extracellular mechanism of Cu depletion in the treatment of Wilson's disease.



1.5 Angiogenesis and cancer

The substantial recovery of Wilson's disease patients under a TM Cu-lowering therapy, and the high efficacy of TM in several preclinical animal cancer models, made TM a promising metallodrug against cancer and inflammatory diseases. Since 2000, TM has been under evaluation as an antiangiogenic drug for the treatment of cancer, and the next section will detail how TM targets the angiogenesis dependence on copper.⁶

1.5.1 Angiogenesis. In 1971, J. Folkmann introduced the concept of angiogenesis. In this process cancer cells replicate larger than 2 mm upon a neovascularization.²⁹ Normal levels of angiogenesis are mostly detected during fetal development and childhood, while in adults represents a highly metastatic malignancy.³⁰ The onset of tumor angiogenesis has been hypothesized to occur due to the imbalance between tumor angiogenic factors (TAF) (*i.e.* VEGF,

FGF, TGF- β , etc) and inhibitors (*i.e.* thrombospondin, angiostatin, endostatin, etc).³¹ It has been suggested that this neovascularization process consists of several sequential steps.³² These steps include TAF secretion and recognition by endothelial cell receptors, activation of endothelial cells for proliferation, dissolution of the extracellular matrix by action of the matrix metalloproteinases (MMP's), and formation of a mature network of blood vessels to support tumor's metastasis and development (Figure 1.2).

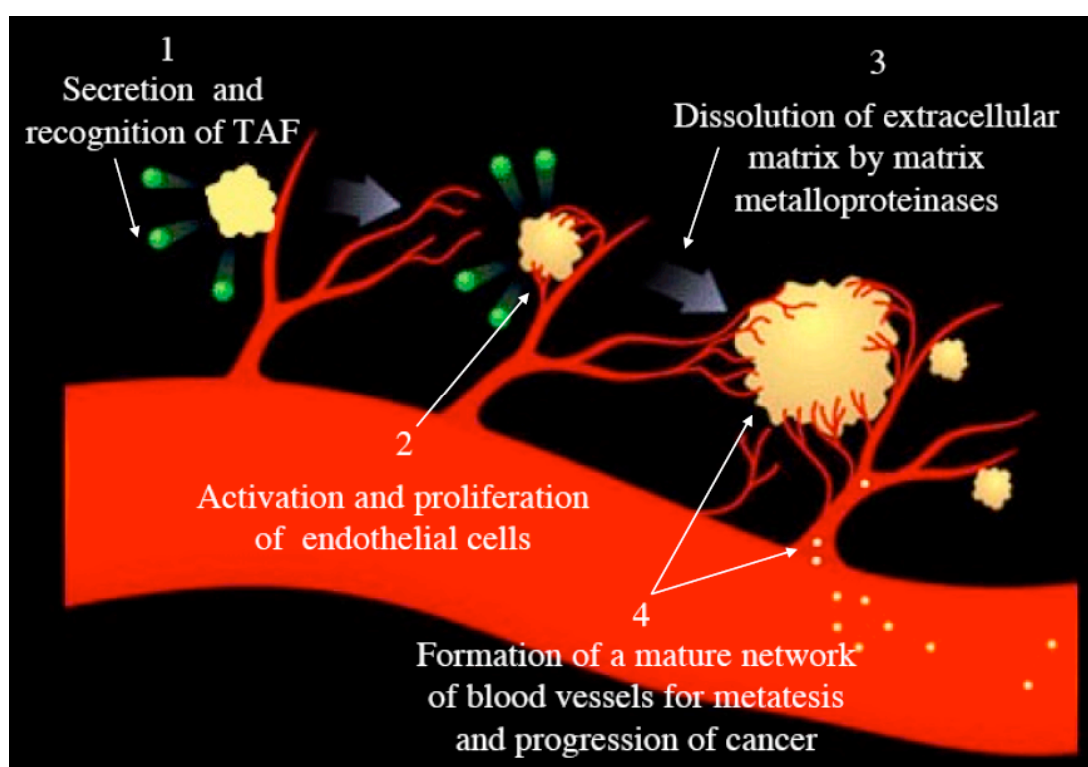


Figure 1.2 Sequential steps of angiogenesis.³³

There has been a rigorous search to characterize TAF inhibitors to block the angiogenesis' signaling cascade. In 2004, the FDA approved Bevacizumab (Avastin®, Genentech/Roche) as the first antiangiogenic antibody/drug for the treatment of colon cancer.³⁴

This drug targets one of the most important TAF, Vascular endothelial growth factor (VEGF), know as the key mediator of pathologic angiogenesis.³⁵ Since then, several other angiogenesis inhibitors have been under cancer clinical trials (i.e. Endotastin, Neovastat, Combretastatin A4, TNP-470, Squalamine, Thalidomide, Semaxanib, etc).

1.5.2 Copper and angiogenesis. Several lines of evidence support the idea that copper is critically important for angiogenesis. In 1988, A. Parke initially suggested that copper sulfate and copper ceruloplasmin induce angiogenesis levels in a rabbit cornea model, while T. Matsubara proposed that copper chelator drugs such as D-penicillamine produced the reverse effect.^{36,37} Two years later, S. Brem found the reduction of angiogenesis in the brain tumors of copper deficient rabbits by penicillamine and a low copper diet.³⁸ In 1998, G. Hu discovered that copper induces proliferation of human umbilical artery and vein endothelial cells.³⁹ Between 2002 and 2003, L. Mandinov and Q. Pan demonstrated that a combination of a low-copper diet and TM produced the inhibition of some tumor angiogenic factors (IL-1, FGF1, and NF- κ B).^{40,41} Much more recently, L. Finney et al. showed that endothelial cells undergoing angiogenesis exhibit a relocation of 80–90% of intracellular copper to the tips of cytoplasmatic projections.⁴²

It has also been suggested that copper can be used as a diagnostic marker of cancer. Atomic absorption spectrophotometry studies revealed high concentrations of copper in a variety of tumor extracts.^{43,44} Even that elevated serum copper levels can be linked with tumor incidence, tumor burden, malignant progression and recurrence; it is important to note that this fact may only be the consequence of inflammatory or cardiovascular diseases.^{45,46}

Copper has been related to tumor angiogenesis but the exact connection and mechanism for copper activation of TAF and induction of malignant tumor cells to metastasize has yet to be elucidated.

1.5.3 Copper as a target for angiogenesis. G. Brewer proposed targeting copper using TM to slow or stabilize tumor growth in cancer based on several successful animal trials.^{41,47} TM clinical trials (Phase I & II) tested patients with a variety of advanced cancers (breast, colon, lung, prostate and kidney).^{6,48} Ceruloplasmin was used as a surrogate marker for Cu deficiency, and TM doses of 150 – 180 mg/day were applied. These studies demonstrated a rate of disease stabilization with minor side effects as mild fatigue and sulfurous eructation.⁴⁹ The University of Michigan Cancer Center, is currently performing 3 phase II clinical trials in esophageal carcinoma, prostate cancer and colorectal carcinoma with TM⁵⁰⁻⁵²; while Attenuon, a pharmaceutical company in San Diego, CA, is executing two phase II clinical trials in advanced cutaneous melanoma and prostate cancer using ATN-224^{53,54}. In ATN-224, choline cations replace the ammoniums of TM, appearing to increase the stability of the drug. The increasing number of clinical trials indicates the importance of the new copper chelation therapy with TM.

1.6 Scope of the thesis.

Although a specific TM molecular target of action has not yet been proposed, it is likely that this TM copper chelation therapy is working through several extracellular and intracellular pathways with a variety of copper-dependent protein targets. For example, the different proteins involved in the copper trafficking pathway in eukaryotes (Figure 1.3)⁵⁵ and yeast such as Ctr1, Atox1 (Atx1), Wilson's disease protein (Ccc2), Ceruloplasmin (Fet3), hCcs (yCcs), hSOD1 (ySOD1), Cox17, Sco1, Sco2, Cyt_{ox}, and metallothioneins. Cellular uptake studies of TM open an additional intracellular component of the already proposed extracellular mechanism of action.

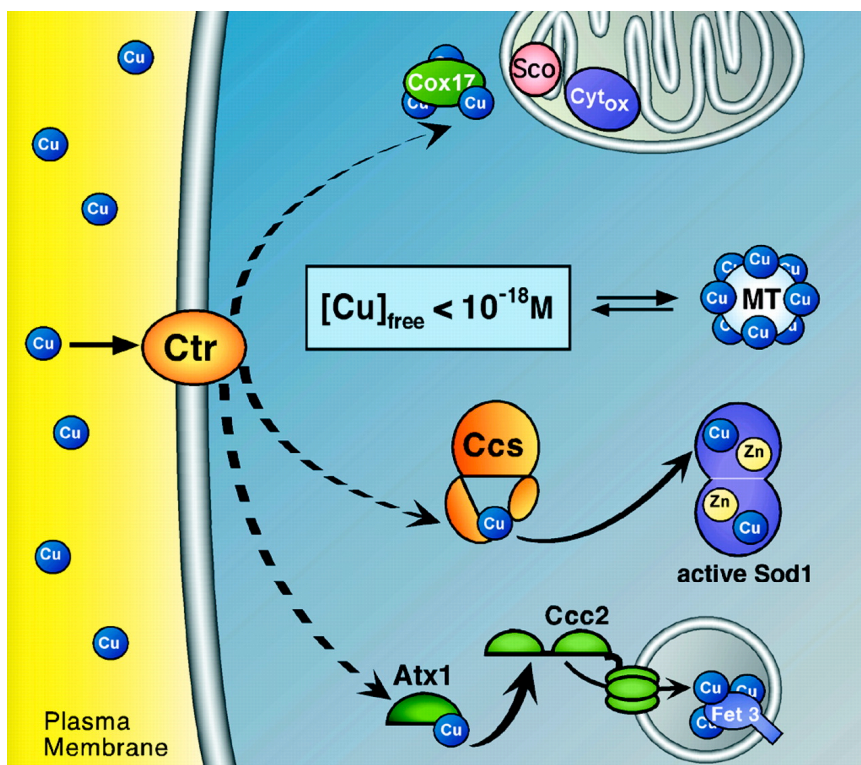


Figure 1.3 Copper trafficking pathways within a eukaryotic cell.⁵⁵

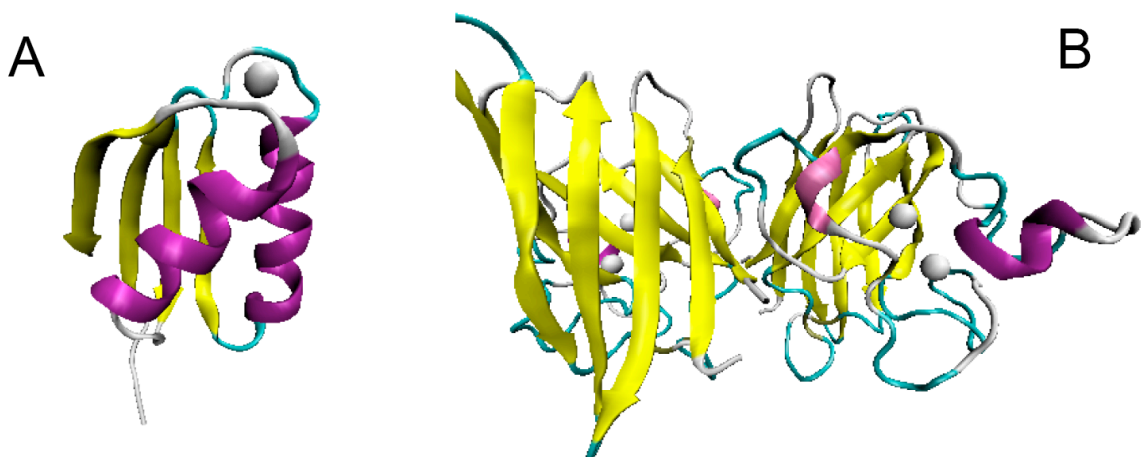
The main research objective of this thesis is to understand how TM reacts with cytoplasmatic copper proteins, in order to help elucidate the complex intracellular mechanism of action for TM.

In chapter 2 and 3 of the thesis, a novel synthesis, characterization and structure of a TM-Cu-protein adduct is described for the first time. A robust purple compound results from the reaction of the intracellular copper chaperone (Atx1) with TM. This complex was isolated by analytical gel filtration, and characterized by ICP-OES, Bradford assay, UV-Visible spectroscopy, Fluorescence spectroscopy, and X-ray absorption spectroscopy (XAS). Additionally, single X-ray protein crystallography reveals the structure of the [TM]((Cu)(Cu-Atx1)₃) complex. TM-Cu-protein complexes were hypothesized to be responsible for the copper

depletion during the ‘Teart’ and ‘Swayback’ disorders, or be involved in the TM treatment of the chronic copper poisoning, Wilson’s disease and cancer.

Chapter 4 details the characterization of a partial copper removal and inhibition of the bovine form of the copper, zinc superoxide dismutase (beSOD1) through the formation of a $[\text{CuTM}]_x$ polymeric complex, which was confirmed by X-ray absorption spectroscopy. In the same chapter, it is concluded that the different reactivity and behavior of SOD1 and Atx1 against TM, is due to structural and binding strength differences of the protein’s copper active sites (Scheme 1.5). For Atx1, the copper ion is tightly bound ($k_D \sim 10^{-19} \text{ M}$)⁵⁶ and located at the surface-exposed loop of the protein⁵⁷; while for SOD1, the low affinity coppers ($k_{D1} \sim 10^{-8.95} \text{ M}$, $k_{D2} \sim 10^{-4.95} \text{ M}$)⁵⁸ are deeply buried inside the protein.⁵⁹ The strong affinity and accessible copper in the Atx1 explains the formation of the $[\text{TM}][(\text{Cu})(\text{Cu-Atx1})_3]$ complex instead of a copper removal from the protein. The active site of the Cu, Zn-beSOD1 is located at the bottom of a highly positive deep conical channel with a narrow width of $< 4 \text{ \AA}$, which can be hypothetically used by the negatively charged TM to reach the active site and cause the partial copper removal.^{60,61}

Scheme 1.5 Crystal structure of the Cu-Atx1 (A) and Cu, Zn-beSOD1 (B).



Chapter 5 explores the cellular uptake, distribution and coordination environment of TM in human hepatocellular cancer cells (HEPG2), using a combination of ICP-MS and X-ray fluorescence microscopy techniques. Additionally, the ability of TM to inhibit cell proliferation, and intracellular SOD1 activity is identified by a combination of modified MTT and UV-VIS spectroscopy assay. The cellular uptake of TM validates the new hypothesis of the interaction of TM with copper proteins. This uptake adds an intracellular approach to the previously suggested extracellular mechanism of action of this copper chelation therapy with TM.

Lately, Chapter 6 proposes the inhibition of the copper transfer activity of the Atx1 metallochaperone to the domain A of the ATPase Ccc2, due to the formation of a [(TM)(Cu)(Atx1)(Ccc2a)] complex after the reaction of Ccc2a with [TM][(Cu)(Cu-Atx1)₃]. The proposed TM-induced disruption of the intracellular copper metabolism represents one of the possible pathways for the action of this metallodrug.

Chapter 2

Solution Coordination Chemistry of the Interaction of the Yeast Cu-Metallochaperone (Cu-Atx1) with TM

Abstract

Ammonium Tetrathiomolydate (TM) is a very low toxicity antiangiogenic drug undergoing several clinical trials for the treatment of cancer. TM is thought to act as an extracellular copper chelator; however an intracellular mechanism of action can also be envisioned in which TM disrupts the cell's tightly controlled Cu trafficking. As part of this hypothetical mechanism of action, we suggest that TM reacts quickly with the yeast copper chaperone Atx1. Intriguingly, we find that extended reaction of TM at millimolar concentration with Cu-Atx1 forms a stable [TM][Cu-Atx1] complex, which was robust to purification by analytical gel filtration. The [TM][Cu-Atx1] was characterized using UV-visible spectroscopy by the shifting of the TM (S—Mo) LMCT bands (317, 467 nm) due to its coordination with copper (375, 532 nm). Room temperature fluorescence spectroscopy is characterized by high- and low-energy emission lines at 410 nm and 650 nm respectively, suggesting the existence of a [CuS] cluster. Cu and Mo K-edge EXAFS of the [TM][Cu-Atx1] suggest that both metals have only sulfur ligands, and that each molybdenum has approximately two to three copper neighbors, while every copper has approximately one molybdenum neighbor, suggesting the existence of a dimer or trimer [TM][Cu-Atx1]. These results have implications in elucidating an intracellular mechanism of action for this drug.

2.1 Introduction

Copper is the third most abundant inorganic element in the human body and plays a critical catalytic role in cell physiology. It is an essential redox cofactor in different cellular enzymes, including the respiratory oxidases.¹ Several disorders in man are directly linked to the disruption of the physiological trafficking of copper.² There have been organized and enthusiastic efforts to understand the different roles of copper deficiency and overload in medicine. The interaction and synergistic or antagonistic effects of copper with molybdenum have been studied in detail across the literature, with higher attention on a complex anion called ammonium tetrathiomolybdate.

The synthesis of the thiomolybdate family of complexes have been studied since the nineteenth century when Berzelius³ introduced its formation by passing H₂S through an aqueous solution of [MoO₄]²⁻. Recently, the chemistry and biology of these compounds have gained more attention due to their emerging relevance in medicine. Of these compounds, ammonium tetrathiomolybdate is the most well-known for its easy preparation and high stability at higher temperatures.^{4,6} This compound is easily characterized by UV-visible and IR absorption bands.⁷ The deep red color of TM was caused by the appearance of S–Mo LMCT bands in the visible region ($\lambda_1 = 241 \text{ nm}$, $\epsilon_1 = 23200 \text{ M}^{-1}\text{cm}^{-1}$; $\lambda_2 = 317 \text{ nm}$, $\epsilon_2 = 17600 \text{ M}^{-1}\text{cm}^{-1}$; and $\lambda_3 = 467 \text{ nm}$, $\epsilon_3 = 12400 \text{ M}^{-1}\text{cm}^{-1}$), which can be characterized as $t_1 \rightarrow 4t_2$, $3t_2 \rightarrow 2e$, and $t_1 \rightarrow 2e$ electronic transitions, respectively.⁸ ⁹⁵Mo NMR spectroscopy has also been used to characterize the TM anion, due to the high sensitivity of the ⁹⁵Mo chemical shift to the coordination-environment variations in Mo^{VI} complexes.⁹⁻¹¹

Tetrathiomolybdate is used in the treatment of different disorders involving copper overload due to its strong ability to chelate copper. As mentioned in Chapter 1, TM has been

found to be a central and causative agent of the physiological ‘copper-molybdenum antagonism’¹²⁻¹⁴, and used as a non-toxic oral chelation drug to treat three diseases: Copper chronic poisoning, Wilson’s disease¹⁵⁻¹⁷ and metastatic cancer.¹⁸⁻¹⁹

The mechanism of action for TM is generally thought to involve an *extracellular* mechanism of action (see Chapter 1)²⁰. Some recent preliminary studies claim that TM can be taken up and accumulated by human umbilical vein endothelial cells (HUVEC) and multiple myeloma cells (MM1S)²¹. In conjunction with the results presented in Chapter 5, cellular uptake studies showed that TM may also has a complementary intracellular mechanism of action which has several possible cytoplasmatic protein targets.^{22,23}

This Chapter provides the initial molecular characterization of the interaction of TM with one of these possible cytoplasmatic targets: the yeast intracellular copper chaperone, Atx1 (the human homologue is known as Hah1 or Atox1). TM reacts quickly with Atx1 forming a robust purple complex, which was isolated by analytical gel filtration, and characterized by ICP-OES, Bradford assay, UV-Visible, fluorescence (in collaboration with Richard Ahn), and X-ray absorption spectroscopy (XAS) (data collection and analysis were performed by the laboratory of Professor J. Penner-Hahn, Univ. of Michigan). A deeper understanding of the reactivity and behavior of TM with copper proteins will help to elucidate the intracellular mechanism of action of this drug and suggest this copper protein as a possible target of this new copper chelation therapy.

2.2 Experimental Procedures

2.2.1 Synthesis and characterization of ammonium tetrathiomolybdate. As described by Mellor⁵ and Laurie⁶, ammonium tetrathiomolybdate was synthesized and characterized by

^{95}Mo NMR data (in D_2O): δ (in ppm) 2259, IR data (cm^{-1}): 3125 (sh), 2360 (w), 2336 (w), 1384 (m), 835 (w) and UV/Vis [H_2O , λ_{max} (nm), $\epsilon \times 10^{-3}$ ($\text{M}^{-1} \text{cm}^{-1}$)]: 241 (23.3), 317 (16.1), 468 (11.1).⁴⁻⁶

2.2.2 Preparation and purification of protein samples. The wild-type Atx1 and Hah1 protein were expressed, prepared and purified as previously described.^{24,25}

2.2.3 Preparation of Cu-Atx1. Cu-Atx1 was typically prepared by incubation of apoprotein with a Cu^{I} salt at 4°C under an inert atmosphere. $[\text{Cu}(\text{CH}_3\text{CN})_4][\text{PF}_6]$ (1 equivalent) was added, with stirring, to a solution of apo-Atx1, and DTT (20-fold molar excess relative to protein) in 50 mM Tris, pH 8.0. Any excess of the metal was washed out by an ultrafiltration protocol and the protein was exchanged to a solution of 20 mM MES, pH 6.0. The protein concentration was measured by an IgG calibrated Bradford assay with a previously determined correction factor of 0.54 based on amino acid hydrolysis²⁴ (Protein Chemistry Laboratory, Texas A & M University, College Station). Copper concentration ($[\text{Cu}]:[\text{Atx1}] \sim 1.0$) was determined by inductively coupled plasma optical emission spectrometry (ICP-OES) using a Varian Vista-MPX CCD Simultaneous ICP-OES. Solutions of Cu^{I} -Atx1 were kept at a -70°C freezer in a glovebox with no observable formation of Cu^{II} . Electrospray mass spectrometry (ESI-MS) of Cu-Atx1 (previous desalting) in MilliQ water revealed a single peak of $m/z^{\text{obs}} = 8150.5$ ($m/z^{\text{calc}} = 8151.0$), which corresponds to full-length Cu-Atx1 lacking its N-terminal methionine. A similar metallation protocol was performed to prepare Cu-Atox1 (using $[\text{Cu}(\text{CH}_3\text{CN})_4][\text{PF}_6]$), Ag-Atx1 (using AgNO_3) and Au-Atx1 (using sodium aurothiomalate).

2.2.4 Ultrafiltration. Ultrafiltration studies were performed using a centrifugal filter device (MICROCON) with a MW cut-off membrane of 3 kDa (Millipore, Bedford, MA). 200 μL of a mixture of 0.17 mM apo-Atx1 or $\text{Cu}(\text{I})$ -Atx1 plus TM (1:1) was loaded into the Microcon-3

at 4°C and placed in a Fisher Scientific Marathon 16 Km centrifuge at 10,000 rpm for 30 min.

Unreacted TM was washed away using 3 ultrafiltration cycles of 250 µL of 20 mM MES, 150 mM NaCl, pH 6.0. Protein concentration was determined by Bradford Assay for Atx1, while Cu and Mo concentrations were determined by ICP-OES (Table 2.1).

2.2.5 Analytical gel filtration. Analytical gel filtration was performed on a Superdex 75 HR 10/30 column (Amersham Biosciences, GE Healthcare) at 4°C using an ÄKTA chromatography system. After equilibration in a solution of 20 mM MES, 150 mM NaCl, pH 6.0, approximately 250 µl of 0.5 mM apo-Atx1, 0.5 mM Cu-Atx1, 0.5 mM Apo-Atx1 plus 3.84 mM TM (1:1.4) ($t_{\text{rxn}} = 30$ min), or 0.5 mM Cu-Atx1 plus 3.84 mM TM (1:1.4) ($t_{\text{rxn}} = 30$ min) were injected onto the column. The samples were then eluted in 20 mM MES, 150 mM NaCl, pH 6.0, at a flow rate of 0.3 mL/min. The chromatograms were obtained by monitoring the absorbance at 280 nm. The retention volume (V_r) of each peak was recorded and then compared to a calibration curve of vitamin B12, ribonuclease A, myoglobin, chymotripsinogen A and bovine serum albumin. Where $(V_e - V_o)/(V_r - V_o)$ was plotted against the log of the molecular weight, V_o being the void volume of the column and V_r the bed volume of the column. A similar experiment was performed with apo-Hah1 and Cu-Hah1. Similar conditions were used for concentration-dependent studies using protein concentrations of 0.5 and 2.0 mM, at different [TM]:[Cu-Atx1] ratios of 0.4 and 1.4. For time-dependent studies 2.0 mM Cu-Atx1 incubated with TM for 30 min, 1 h, 1.5 h and 2 h were used. Moreover, for UV-visible studies (explained below), mixtures (500 µl) of 3.0 mM X-Atx1 (X = Cu, Ag and Au) + TM (1:0.4) were injected into the FPCL under the conditions described before. Cu and Mo concentrations of the fractions collected after analytical gel filtration were determined using ICP-OES and protein concentrations using the Bradford assay.

2.2.6 UV-visible spectroscopy. Absorption spectra (λ : 200 – 700 nm) were recorded at 25°C using a Cary 300 Bio UV-Visible spectrophotometer using quartz cuvettes (teflon stoppers) with a 1 cm path length and 1 ml cell volume. UV-visible spectra of 0.2 mM apo-Atx1 plus TM (1:0.4), 0.2 mM Cu-Atx1 plus TM (1:0.4), 0.08 mM TM, and 0.2 mM $[\text{Cu}(\text{CH}_3\text{CN})_4][\text{PF}_6]$ plus TM (1:1) were recorded after 30 min of reaction.

2.2.7 UV-Vis Titration spectroscopy. To a 38.4 μM solution of TM (20 mM MES, pH 6.0, 0.15 M NaCl) were added 3.84 μl aliquots of a 0.5 mM apo-Atx1, and Cu-Atx1 solution at 25°C. Upon each addition, the sample solution was stirred for 10 min with a magnetic stirring device and the UV-visible spectrum was subsequently monitored and corrected for dilution. The UV-visible trace for apo-Atx1 was analyzed by a molar ratio plot for determining the dilution effect. UV-visible spectra of 0.2 mM $[\text{TM}][\text{X-Atx1}]$ complexes (X = Cu, Ag, Au) were recorded after purification by analytical gel filtration and concentration by ultrafiltration (see gel filtration above) (note: for Ag and Au complexes, repetitive gel filtration runs were performed to obtain a reasonable amount of sample for characterization). Extinction coefficients were calculated by a plot of UV-visible absorbance against Mo concentration (ICP-OES) of different dilutions of $[\text{TM}][\text{X-Atx1}]$.

2.2.8 Fluorescence Spectroscopy. Preliminary fluorescence spectra studies of a 22 μM $[\text{TM}][\text{Cu-Atx1}]$ complex (based on Cu) were recorded on a LS-50B Luminescence Spectrometer (Perkin Elmer, Norwalk, CN) at 25 °C using a 15 nm excitation and emission slit width, a scan rate of 100 nm/min and a WG ($\lambda = 335$ nm) cut on filter. The path length was 1.0 cm with a cell volume of 120 μl .

2.2.9 Preparation of XAS sample. Duplicate samples were prepared for XAS analysis. The $[\text{TM}][\text{Cu-Atx1}]$ sample was prepared using a mixture of approximately 500 μl of a 3.0 mM

Cu-Atx1 plus TM (1:0.4) ($t_{\text{rxn}} = 30$ min, aerobic conditions, $T = 4^{\circ}\text{C}$) (20 mM MES, 150 mM NaCl, pH = 6.0). The mixture solution was purified by FPLC analytical gel filtration (Superdex 75 HR10/30) forming three different peaks in the chromatogram. These fractions were collected (2 mL each) and concentrated to approximately 100 μL using a centrifugal filter device with a MW cut-off membrane of 3 kDa (MICROCON). The first peak corresponds to an approximate molecular weight of 10.0 kDa ($[\text{Atx1}] = 0.32$ mM, $[\text{Cu}] = 0.11$ mM and no $[\text{Mo}]$; $[\text{Cu}]:[\text{Atx1}] = 0.35$), to the second peak, 26.7 kDa (color purple, $[\text{Atx1}] = 2.9$ mM, $[\text{Cu}] = 2.5$ mM and $[\text{Mo}] = 0.8$ mM; $[\text{Cu}]:[\text{Mo}] = 3.1$, $[\text{Cu}]:[\text{Atx1}] = 0.9$, $[\text{Atx1}]:[\text{Mo}] = 3.6$), and to the third peak, 55.5 kDa ($[\text{Atx1}] = 2.0$ mM, $[\text{Cu}] = 1.6$ mM, $[\text{Mo}] = 0.43$ mM; $[\text{Cu}]:[\text{Mo}] = 3.7$, $[\text{Cu}]:[\text{Atx1}] = 0.80$, $[\text{Atx1}]:[\text{Mo}] = 4.6$). The concentrated deep purple solution corresponding to 26.7 kDa, represents the $[\text{TM}][\text{Cu-Atx1}]$ complex, which was used further for XAS analysis. Glycerol was added to a final concentration of 30%. Samples were transferred to XAS cuvettes (Lucite body with Kapton windows), frozen in $\text{N}_2(\text{l})$ at -20°C and stored at -80°C until XAS measurements were made. The protein concentration was measured by the Bradford assay and Cu, Mo by ICP-OES.

2.2.10 X-ray absorption data collection and analysis. Frozen samples were sent to our collaborators. Data collection and analysis for this experiment was performed and analyzed by Dr. Rebekah Kelly and Prof. James Penner-Hahn. A brief account of their conclusions follows here. The Cu K-edge data were collected at SSRL on beamline 9-3 (3 GeV, ~ 90 mA), using a Si(220) double-crystal monochromator with a Rh-coated mirror upstream for harmonic rejection. Incident intensity was measured using an N_2 -filled ion chamber. Fluorescence data was collected using a 30-element Ge solid-state detector array. The sample temperature was held at 12 K in an Oxford liquid helium flow cryostat during the measurements. The total integrated count rate was held below 90 kHz to avoid saturating the detector, and the average windowed

fluorescence count rate was ~ 7 -12 KHz per channel in the EXAFS region. Each scan had 10 eV increments prior to the edge (8780 - 8970 eV), 0.5 eV increments for the pre-edge and edge region (8970 - 9020 eV), 0.05 \AA^{-1} increments for two EXAFS regions (2.29 – 13.1 \AA^{-1}) with integration times of 1 s in the pre-edge and edge regions and 1-10 s (k^3 weighted) in the EXAFS for a total scan time of ~ 35 minutes. Energy calibration was done using a Cu(s) foil as an internal standard, with the first inflection point of the foil defined as 8980 eV. For all samples each detector channel was checked for glitches and all good channels (~ 20 -24) were averaged and were calculated using 4 and 3 scans for Cu-Atx1. XANES data were normalized by fitting the data to the McMaster absorption coefficients below and above the edge using a single background polynomial and scale factor.²⁶⁻²⁷ The EXAFS background correction was performed by fitting a three-region quartic spline for all the copper samples. Fourier transforms were calculated using k^3 weighted data over a range of 1.13 – 13 \AA^{-1} for both the copper samples. The data were then converted to k -space using

$$k = \sqrt{\frac{2m_e(E - E_0)}{\hbar^2}} \quad \text{where } E_0 = 9000 \text{ eV.}$$

EXAFS data can be described by following equation, where $c(k)$ is the fractional modulation, in the absorption coefficient above the edge, N_s is the number of scatterers at

$$\chi(k) = \sum_s \frac{N_s S_s(k) A_s(k)}{k R_{as}^2} \exp(-2k^2 \sigma_{as}^2) \exp\left(\frac{-2R_{as}}{\lambda}\right) \sin(2k R_{as} + \phi_{as}(k))$$

a distance R_{as} , $A_s(k)$ is the backscattering amplitude, σ_{as}^2 is the root-mean-square variation in R_{as} , $\phi_{as}(k)$ is the phase shift experienced by the photoelectron wave in passing through the potentials

of the absorbing, l is the mean free path of the photoelectron and backscattering atoms, and $S_s(k)$ is a scale factor specific to the absorber-scattering pair and the sum is taken over all scattering interactions.²⁸ The program FEFF v7.02²⁹ was used to calculate amplitude and phase functions, $A_s(k)\exp(-2R_{as}/l)$ and $f_{as}(k)$ for a copper-sulfur interaction at 2.26 Å, a copper-molybdenum interaction at 2.70 Å and a copper-copper interaction at 5.40 Å. E_0 was initially set at 9000 eV and S_s , was fixed at 0.89.

Mo K-edge data was collected as described above with the following exceptions. The total integrated count rate was held below 90 kHz to avoid saturating the detector, and the average windowed fluorescence count rate was ~ 2 -7 KHz per channel in the EXAFS region. Each scan had 10 eV increments prior to the edge (19788 - 19988 eV), 0.3 eV increments edge region (19989 - 20030 eV), 0.05 Å⁻¹ increments for two EXAFS regions (1.62 – 16.1 Å⁻¹) with integration times of 1 s in the pre-edge and edge regions and 1-20 s (k^3 weighted) in the EXAFS region for a total scan time of ~ 26 minutes. Energy calibration was done using a Mo(s) foil as an internal standard, with the first inflection point of the foil defined as 20003 eV. For all samples each detector channel was checked for glitches and all good channels (25) were averaged and were calculated using 6 and 4 scans for Atx1. XANES data were normalized by fitting the data to the McMaster absorption coefficients below and above the edge using a single background polynomial and scale factor²⁶⁻²⁷ The EXAFS background correction was performed by fitting a three-region quartic spline for all the cobalt samples. Fourier transforms were calculated using k^3 weighted data over a range of 1-15.5 Å⁻¹ for all the molybdenum samples. EXAFS fits were performed as described above with the following exceptions. The program FEFF v7.02²⁹ was used to calculate amplitude and phase functions, $A_s(k)\exp(-2R_{as}/l)$ and $f_{as}(k)$ for a molybdenum-sulfur interaction at 2.21 Å, a molybdenum-copper interaction at 2.70 Å.

2.3 Results

2.3.1 Ultrafiltration. Ultrafiltration studies of apo-Atx1 plus TM (1:1) showed that all TM went through the membrane to the eluate fraction. Similar studies of Cu-Atx1 plus TM (1:1) showed that copper, molybdenum and protein were retained in the supernatant fraction after centrifugation, revealing the importance of copper for the interaction between the protein and TM and suggesting the hypothetical formation of a [TM][Cu-Atx1] interaction (Table 2.1).

Table 2.1. Mass balance of protein, Cu, and Mo during ultrafiltration studies^a.

		Reaction Mixture mmols ^a	Supernatant Fraction mmols ^a	Eluate Fraction mmols ^a
Apo-Atx1 reaction	Atx1 ^b	3.40 x 10 ⁻⁵	3.24 x 10 ⁻⁵	----
	Mo ^b	3.20 x 10 ⁻⁵	---	3.14 x 10 ⁻⁵
Cu-Atx1 reaction	Atx1 ^c	3.40 x 10 ⁻⁵	3.29 x 10 ⁻⁵	----
	Cu ^c	3.20 x 10 ⁻⁵	3.08 x 10 ⁻⁵	0.08 x 10 ⁻⁵
	Mo ^c	3.20 x 10 ⁻⁵	2.71 x 10 ⁻⁵	0.40 x 10 ⁻⁵

^anumber of mmols (Cu, Mo and protein) calculated before and after ultrafiltration in supernatant and eluate fractions. ^bFrom apo-Atx1 + TM reaction. ^cFrom Cu-Atx1 + TM reaction.

2.3.2 Analytical Gel Filtration. Analytical gel filtration experiments were carried out with either apo-Atx1, Cu-Atx1, alone or combined with TM. The chromatograms for apo-Atx1 alone, Cu-Atx1 alone and the apo-Atx1 plus TM mixture (1:1.4) ($t_{\text{rxn}} = 30$ min) each displayed one peak (#1) near 10 kDa (apo-Atx1: 9.7, Cu-Atx1: 10.6 and Apo-Atx1 + TM: 10.2), which corresponds to the Atx1 protein monomer within the uncertainty of the measurement (Figure 2.1A). Metal and protein concentrations of the chromatographic fractions are shown in Table

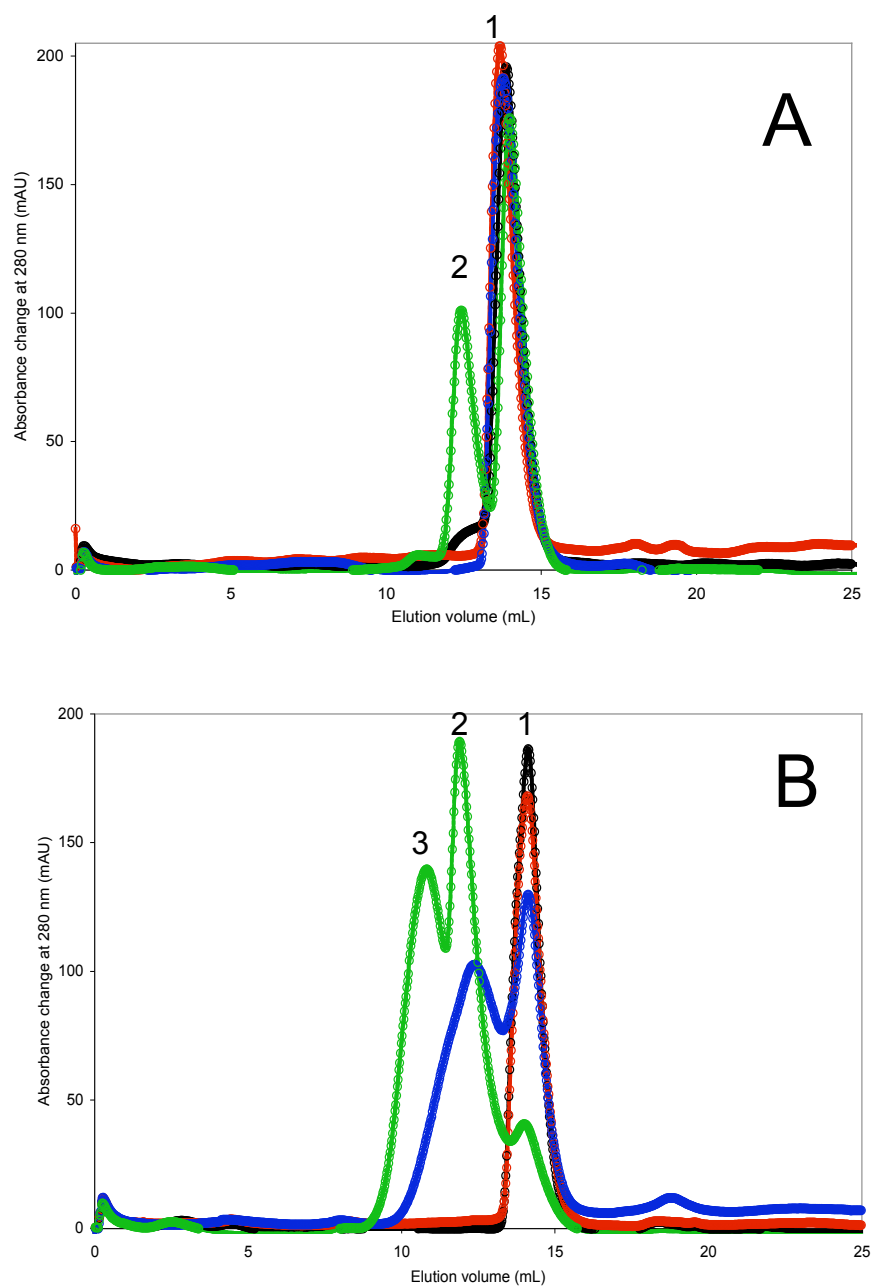


Figure 2.1 A. Analytical gel filtration chromatograms of 0.5 mM apo-Atx1 (○), apo-Atx1 + TM (1:1.4) (○), Cu-Atx1 (○) and Cu-Atx1 + TM (1:1.4) (○); B. Analytical gel filtration chromatograms of 0.5 mM apo-Hah1 (○), apo-Hah1 + TM (1:1.4) (○), Cu-Hah1 (○) and Cu-Hah1 + TM (1:1.4) (○).

2.2. The Cu-Atx1 plus TM mixture (1:1.4) ($t_{\text{rxn}} = 30$ min), however showed two peaks, one at approximately 9.9 kDa (#1), and a second (#2) at approximately 26.0 kDa ([Cu]:[Mo] = 3.6, [Cu]:[Atx1] = 1.0, [Atx1]:[Mo] = 3.4) suggesting the formation of a [TM][Cu-Atx1] complex (Figure 2.1A, Table 2.2), which can be identified as a dimer or trimer interaction.

Table 2.2 Metal and protein concentrations (μM) of chromatographic fractions in Figure 2.1A.

	Apo-Atx1	Apo-Atx1 + TM	Cu-Atx1	Cu-Atx1 + TM # 1	Cu-Atx1 + TM # 2
[Atx1]	5.3	5.2	5.2	3.1	2.3
[Cu]	-	-	5.0	2.1	2.4
[Mo]	-	-	-	-	0.67

Similar results were observed for Atox1; apo-Atox1 and apo-Atox1 plus TM (1:1.4) ($t_{\text{rxn}} = 30$ min) showed one similar peak (#1) approximately at 10.5 and 10.6 kDa respectively. In contrast with Cu-Atx1, Cu-Atox1 showed two peaks, the first one (#1) at 10.3 kDa and a second one (#2) at 22.7 kDa, which represents a $\text{Cu}(\text{Atox1})_2$ dimer.²⁵ Additionally, Cu-Atox1 + TM (1:1.4) ($t_{\text{rxn}} = 30$ min) showed 3 peaks; the first one (#1) at 10.5 kDa, a second one (#2) at 32.9 kDa, and a third peak (#3) at 57.4 kDa (Figure 2.1B). Metal and protein concentrations of the chromatographic fractions are shown in Table 2.3. The reaction between Cu-Atox1 and TM may indicate the formation of a [TM][Cu-Atox1] dimer or trimer complex as with the Atx1, ([Cu]:[Mo] = 3.2, [Cu]:[Atox1] = 1.1, [Atox1]:[Mo] = 3.0) and of other oligomeric complexes (Figure 2.1B, Table 2.3).

Analytical gel filtration studies also suggested that lower concentrations of Cu-Atx1

Table 2.3. Metal and protein concentrations (μM) of chromatographic fraction in Figure 2.1B.

	Apo-Atox1	Apo-Atox1 + TM	Cu-Atox1 # 1	Cu-Atxo1 # 2
[Atox1]	5.2	5.1	3.2	2.3
[Cu]	-	-	3.1	1.3
[Mo]	-	-	-	-
	Cu-Atox1 + TM #1	Cu-Atox1 + TM # 2	Cu-Atox1 + TM # 3	
[Atox1]	0.18	4.1	1.1	
[Cu]	0.1	4.5	1.5	
[Mo]	-	1.4	0.72	

result in a smaller proportion of the putative [TM][Cu-Atx1] complex, while higher concentrations favor its formation. At a low concentration of Cu-Atx1 (0.5 mM), the formation of the [TM][Cu-Atx1] complex increased as the [TM]:[Atox1] ratio was increase from 0.4 (25.7 kDa) to 1.4 (26.0 kDa) (Figure 2.2A, Table 2.4). Using a higher concentration of Cu-Atx1 (2 mM), we observed higher proportion of the [TM][Cu-Atx1] complex at a [TM]:[Atox1] ratio of 0.4 (28.3 kDa) instead of 1.4 (27.6 kDa) where the formation of this complex was minimal (Figure 2.2B, Table 2.4).

Higher-order oligomers have been shown to form over time. These oligomers appear to be tetramer or pentamer complexes based on metal and protein analysis, and approximate molecular weight. After 2 hours, we observed unreacted Cu-Atx1 (10.6 kDa, [Atox1] = 9.4 μM , [Cu] = 7.8 μM and no [Mo]), the [TM][Cu-Atx1] complex (28.2 kDa, [Atox1] = 71.2 μM , [Cu] = 70 μM and [Mo] = 22.6 μM), and the tetramer/pentamer complex (53.8 kDa, [Atox1] = 5.3 μM ,

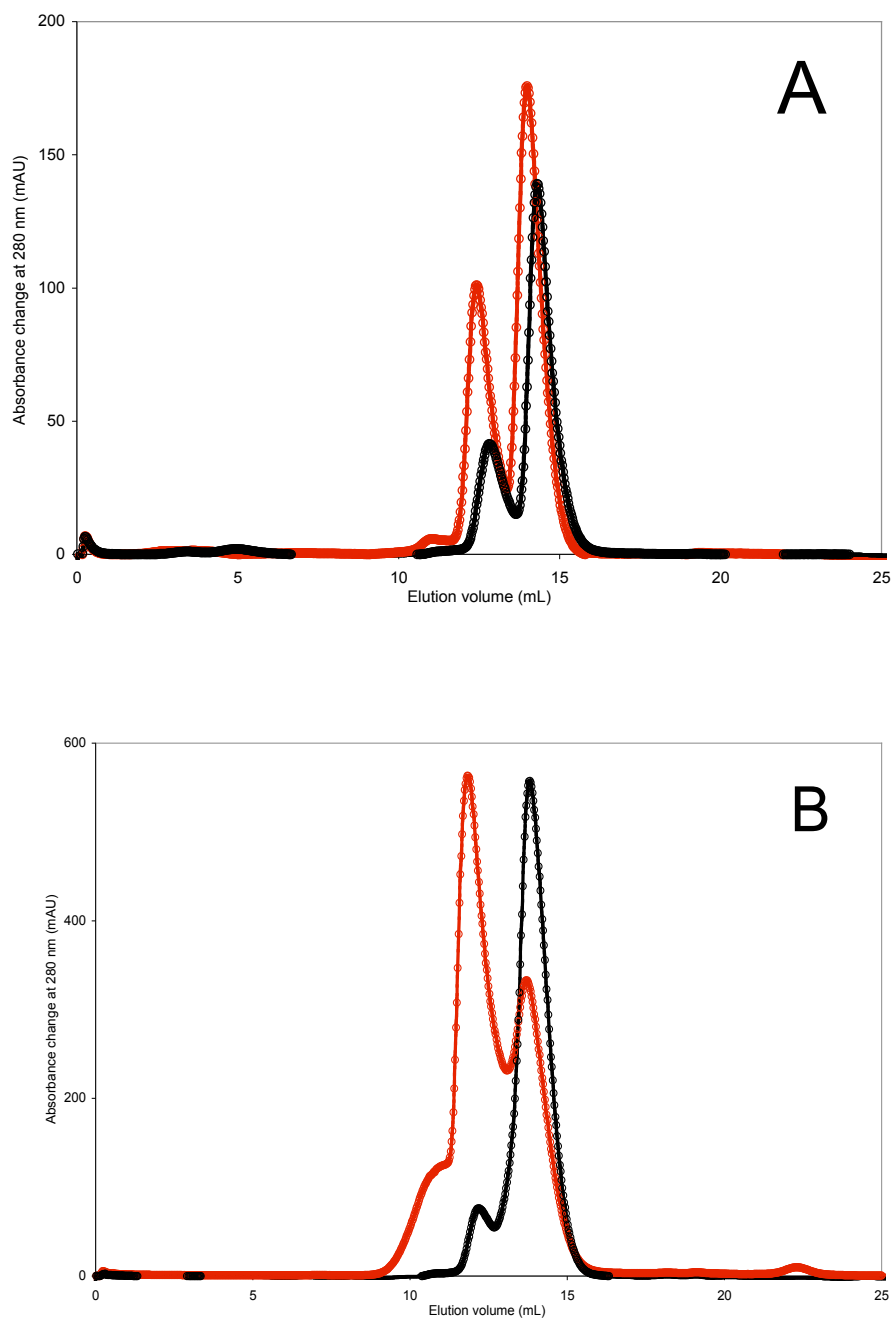


Figure 2.2 A. Analytical gel filtration chromatograms of 0.5 mM Cu-Atx1 + TM (1:0.4) (○), Cu-Axt1 + TM (1:1.4) (○); B. Analytical gel filtration chromatograms of 2.0 mM Cu-Atx1 + TM (1:1.4) (○), Cu-Axt1 + TM (1:0.4) (○).

[Cu] = 4.2 μ M and [Mo] = 1.1 μ M) (Figure 2.3A).

Table 2.4. Metal and protein concentrations (μ M) of chromatographic fractions in Figure 2.2.

	Cu-Atx1 (0.5 mM) + TM (1:0.4)	Cu-Atx1 (0.5 mM) + TM (1:1.4)	Cu-Atx1 (2.0 mM) + TM (1:0.4)	Cu-Atx1 (2.0 mM) + TM (1:1.4)
[Atx1]	2.0	2.8	60.1	2.1
[Cu]	1.9	2.4	63.2	2.3
[Mo]	0.55	0.67	18.9	0.66

Following the conditions used to prepare the [TM][Cu-Atx1] complex with Cu-Atx1 and TM for XAS analysis (see Materials and Methods), we were able to prepare and purify [TM][Atx1] complexes with Ag and Au. In contrast with Cu-Atx1, repetitive analytical gel filtration runs were performed in order to obtain a reasonable amount of the Ag and Au analogues for characterization. Metal and protein concentrations of the chromatographic fractions are shown in Table 2.5. For the red Ag analogue, we observed 2 peaks, the first one (#1) at 10.5 kDa, and the second one (#2) at 25.1 kDa, which represent the [TM][Ag-Atx1] ([Ag]:[Mo] = 3.2, [Ag]:[Atx1] = 1.1, [Atx1]:[Mo] = 3). For the dark orange Au analogue, the first peak (#1) was observed at 10.2 kDa, and the second peak (#2) at 24.6 kDa, which represented the [TM][Au-Atx1] ([Au]:[Mo] = 3.4, [Au]:[Atx1] = 0.9, [Atx1]:[Mo] = 3.8) (Figure 2.3B, Table 2.5).

2.3.3 UV-Visible Spectroscopy. UV-visible spectra of apo-Atx1, Cu-Atx1, and [Cu⁰(CH₃CN)₄][PF₆]₄ with TM, and TM alone, revealed that apo-Atx1 plus TM does not show any major difference in comparison with the TM spectrum, with the exception of the tyrosine

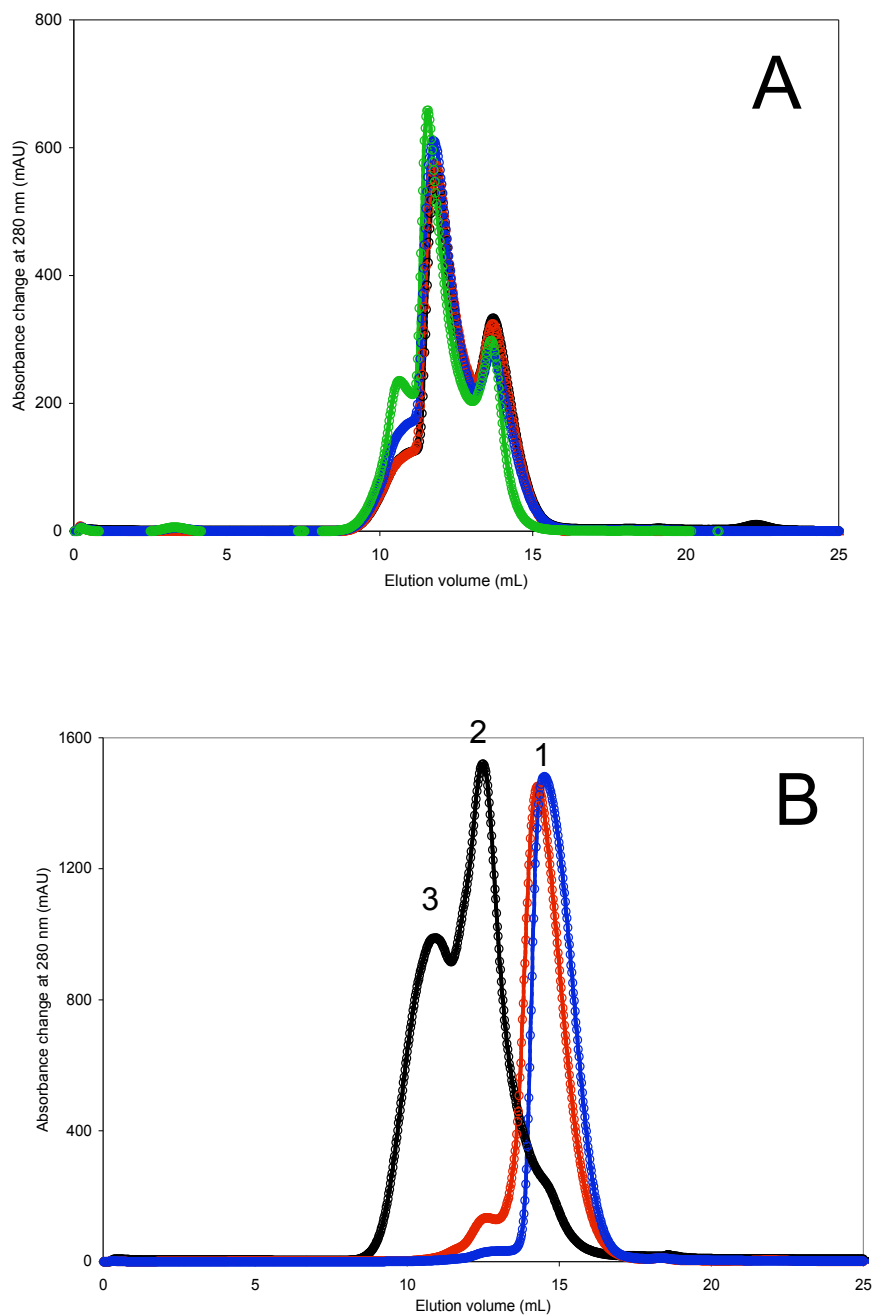


Figure 2.3 A. Analytical gel filtration chromatograms of 3.0 mM Cu-Atx1 + TM (1:0.4) (○: t_{rxn} = 30 min; ○: t_{rxn} = 1 h; ○: t_{rxn} = 1.5 h; ○: t_{rxn} = 2 h); B. Analytical gel filtration chromatograms of 3.0 mM X-Atx1 (X: Cu = ○, Ag = ○, Au = ○) + TM (1:0.4).

Table 2.5. Metal and protein concentrations (mM) of chromatographic fraction in Figure 2.3B.

	Cu-Atx1 + TM #1	Cu-Atx1 + TM #2	Cu-Atx1 + TM #3	Ag-Atx1 + TM #1	Ag-Atx1 + TM #2	Au-Atx1 + TM #1	Au-Atx1 + TM #2
[Atx1]	0.32	2.9	2.0	5.5	0.27	5.9	0.12
[Cu]	0.11	2.5	1.6	0.60	0.29	5.0	0.11
[Mo]	-	0.8	0.43	-	0.09	-	0.032

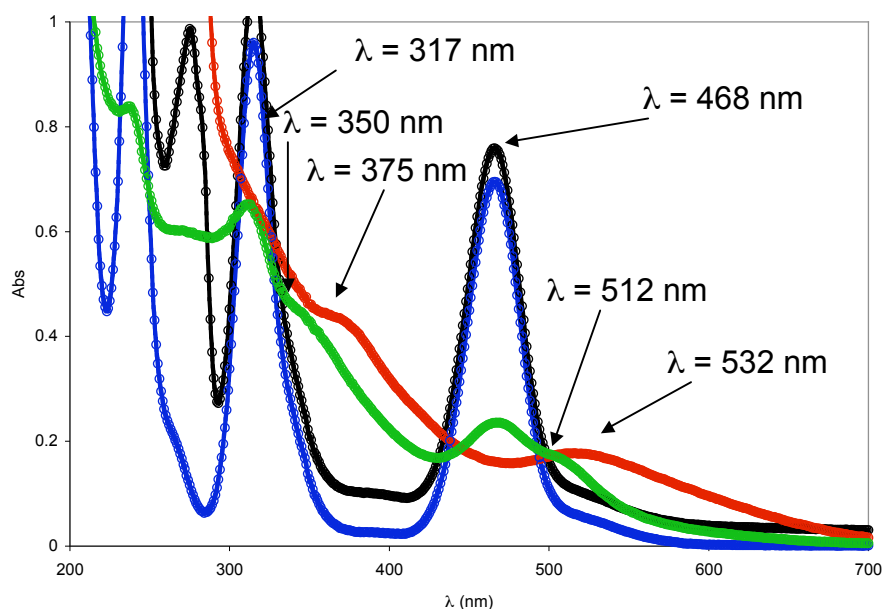


Figure 2.4 UV-visible absorbance of 0.2 mM apo-Atx1 + TM (1:0.4) (O), 0.2 mM Cu-Atx1 + TM (1:0.4) (Δ), 0.08 mM TM (\square) and 0.2 mM $[\text{Cu}(\text{CH}_3\text{CN})_4][\text{PF}_6]$ + TM (1:1) (\diamond), after reaction for 30 min (20 mM MES, pH = 6.0, 0.15 M NaCl, 25°C, aerobic conditions).

absorption around 280 nm due to the protein (Figure 2.4). In contrast, the spectrum of Cu-Atx1 plus TM was similar to the one of the $[\text{Cu}^{\text{I}}(\text{CH}_3\text{CN})_4][\text{PF}_6]$ -TM mixture, suggesting the formation of a similar kind of [Cu-TM] interaction (Figure 2.4).

A titration of TM with apo-Atx1 did not show the disappearance of the S—Mo LMCT bands or the formation of new absorption maxima (aside from the expected increase at 280 nm), which suggests that copper is essential for the interaction between these proteins and TM (Figure 2.5.A). This dilution effect, observed for the apo-Atx1-TM system was confirmed by a molar ratio plot (i. e. when absorbance is corrected for dilution) depicted for wavelengths 317 and 468 nm (Figure 2.5.B). When different proportions of Cu-Atx1 and TM were mixed in buffered solutions during a UV-visible titration, the loss of the characteristic S—Mo ligand to metal charge transfer bands (LMCT) ($t_1 \rightarrow 4t_2$; $\lambda = 241$ nm, $3t_2 \rightarrow 2e$; $\lambda = 317$ nm, $t_1 \rightarrow 2e$; $\lambda = 468$ nm) of TM was observed (Figure 2.6.A). Addition of TM lead to a broadening of the spectrum with the formation of two shoulders with λ_{max} around 375 and 532 nm, which are the result of the shifting of the S—Mo LMCT bands due to the new bond formation with a copper center [Cu—S—Mo]. These changes are consistent with the previously suggested formation of a [TM][Cu-Atx1] interaction. Titration of TM with a Cu^{I} ($[\text{Cu}^{\text{I}}(\text{CH}_3\text{CN})_4][\text{PF}_6]$) salt showed similar results to the ones obtained for the Atx1 system (data not shown).

The UV-visible spectrum of [TM][X-Atx1] analogue interactions with Cu, Ag and Au, after purification by analytical gel filtration and concentration by ultrafiltration, showed a similar spectrum with λ_{max} at 375 and 532 nm for the copper analogue, 336 and 505 nm for the silver analogue, and 483 nm for the gold analogue (Figure 2.7.A). The observation of similar values of λ_{max} for these d^{10} metals is consistent with the shifting of the S—Mo LMCT bands due to the coordination with TM. A plot of the UV-visible absorbance against molybdenum concentration

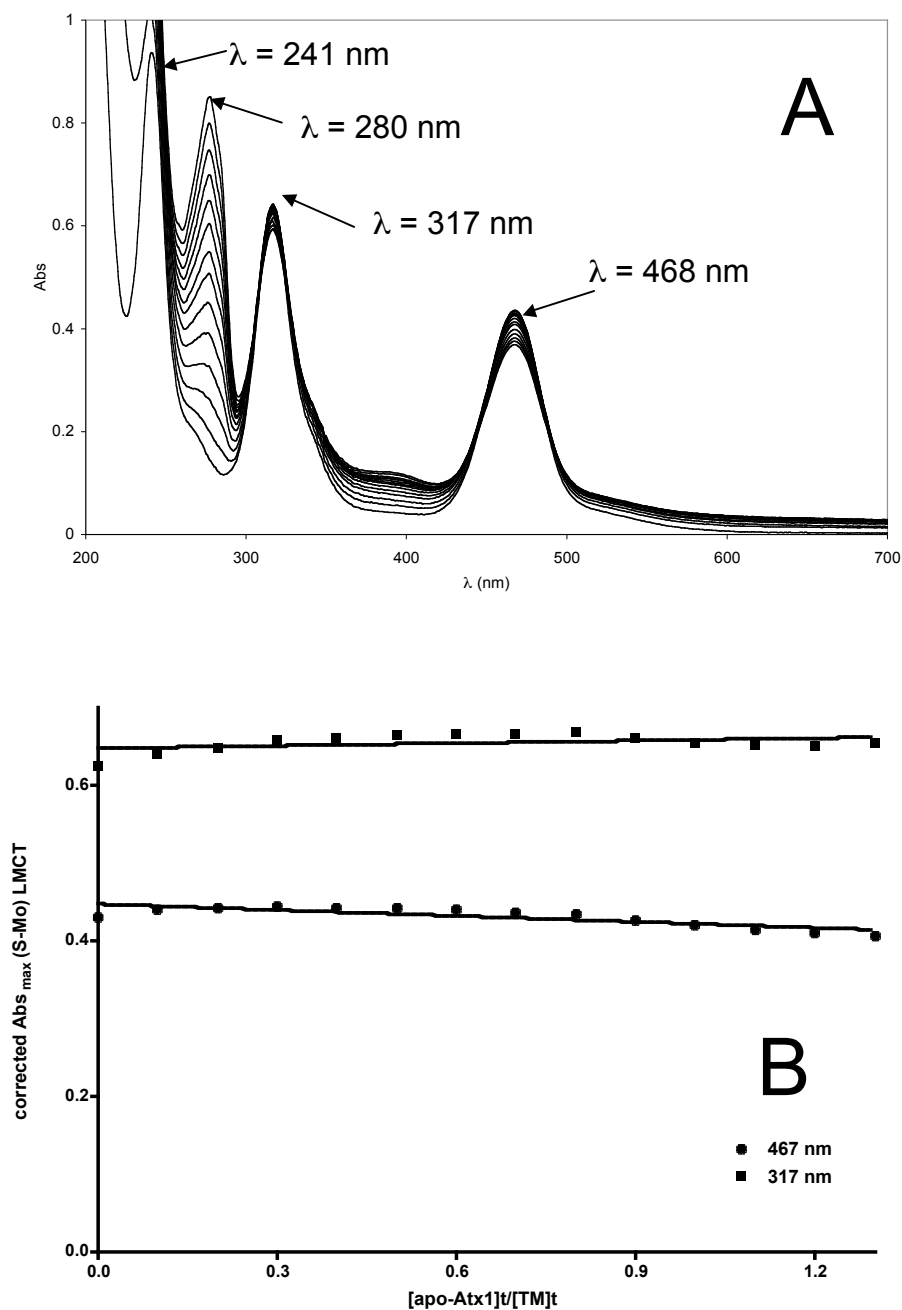


Figure 2.5. A. UV-visible absorbance of TM as a function of apo-Atx1 concentration. 38.4 μ M of TM was titrated with 0 – 1.3 equiv of 0.5 mM apo-Atx1 (20 mM MES, pH = 6.0, 0.15 M NaCl, 25°C, aerobic conditions); B. Absorbance as a function of added apo-Atx1 monitored at 317 and 468 nm (molar ratio plot).

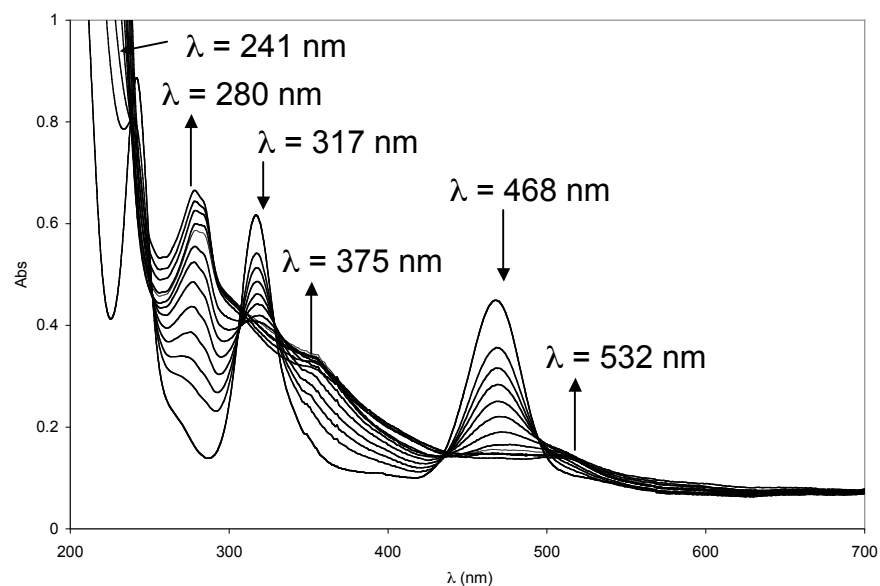


Figure 2.6. UV-visible absorbance of TM as a function of Cu-Atx1 concentration. 38.4 μ M of TM was titrated with 0 – 2.0 equiv of 0.5 mM Cu-Atx1 (20 mM MES, pH = 6.0, 0.15 M NaCl, 25°C, aerobic conditions).

(ICP-OES) of these [TM][X-Atx1] complexes at different dilutions was used to determine the accurate extinction coefficient for these complexes; Cu: $\epsilon_{375} = 8537$ and $\epsilon_{532} = 4004 \text{ M}^{-1}\text{cm}^{-1}$; Ag: $\epsilon_{336} = 8347$ and $\epsilon_{505} = 4390 \text{ M}^{-1}\text{cm}^{-1}$; and Au: $\epsilon_{483} = 4244 \text{ M}^{-1}\text{cm}^{-1}$ (Figure 2.7.B). Shifting of the UV-visible S—Mo LMCT bands due to coordination with Cu reveals that TM interacts with this copper protein forming [TM][Cu-Atx1] interactions, from which a dimer or trimer complex can be isolated and purified by gel filtration.

2.3.4 Fluorescence Spectroscopy. The characteristic fluorescence of tetra-nuclear Cu^I thiolate clusters has been extensively studied in small inorganic molecules³⁰ and more recently in copper metallothioneins (Cu-TM).^{31,32} Representative fluorescence emission and excitation spectra of the [TM][Cu-Atx1] complex are shown in Figure 2.8. The emission spectrum at room temperature is characterized by a weak high-energy and intense low-energy emission bands at 410 and 650 nm, respectively. A maximum in emission intensity was observed with excitation at 280 nm. The excitation spectrum obtained by monitoring the emission intensity at 410 nm shows a peak with a maximum at 300 nm. In contrast, when the 650 nm band is monitored, the excitation spectrum displays a peak at around 280 nm. The large Stokes shift observed is very characteristic for the emission of Cu^I complexes.³⁰ A more detailed description of the fluorescence characteristic of the [TM][Cu-Atx1] complex is included in the discussion of this Chapter.

2.3.5 X-ray Absorption Spectroscopy. The coordination environment of the metal core of the [TM][Cu-Atx1] sample was studied by X-ray absorption spectroscopy to probe the different structural features of the interaction of TM with this copper protein (Atx1). The Cu and Mo K near-edge structure (XANES) spectra of the [TM][Cu-Atx1] is described in detail in Figure 2.9, respectively. The Cu K near-edge spectrum of the [TM][Cu-Atx1] complex

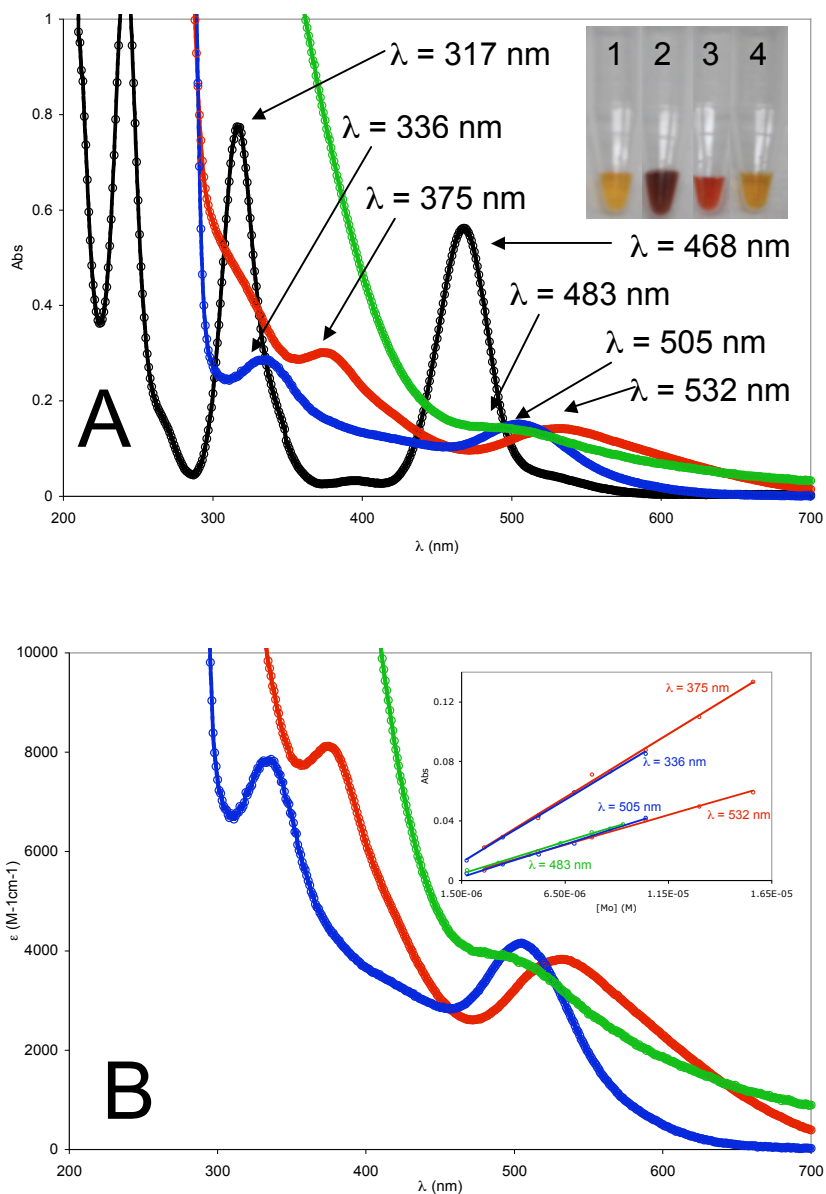


Figure 2.7. A. UV-visible absorbance of TM (○) and purified 0.2 mM [TM][X-Atx1] [X = Cu (●), Ag (●) and Au (●)]. Inset: 1. TM; 2. ([TM][X-Atx1]), X = Cu; 3. Ag; 4. Au; B. Plot of the extinction coefficient (ϵ_{obs}) against λ of 0.2 mM [TM][X-Atx1] [X = Cu (●), Ag (●), Au (●)]. Inset: Plot of UV-vis Abs against Mo concentration of different dilutions of [TM][X-Atx1] [X = Cu (●) (λ_{max} : 375 nm, $\epsilon = 8537 M^{-1}cm^{-1}$; 532 nm, $\epsilon = 4004 M^{-1}cm^{-1}$), Ag (●) (λ_{max} : 336 nm, $\epsilon = 8347 M^{-1}cm^{-1}$; 505 nm, $\epsilon = 4390 M^{-1}cm^{-1}$), and Au (●) (λ_{max} : 483 nm, $\epsilon = 4244 M^{-1}cm^{-1}$)].

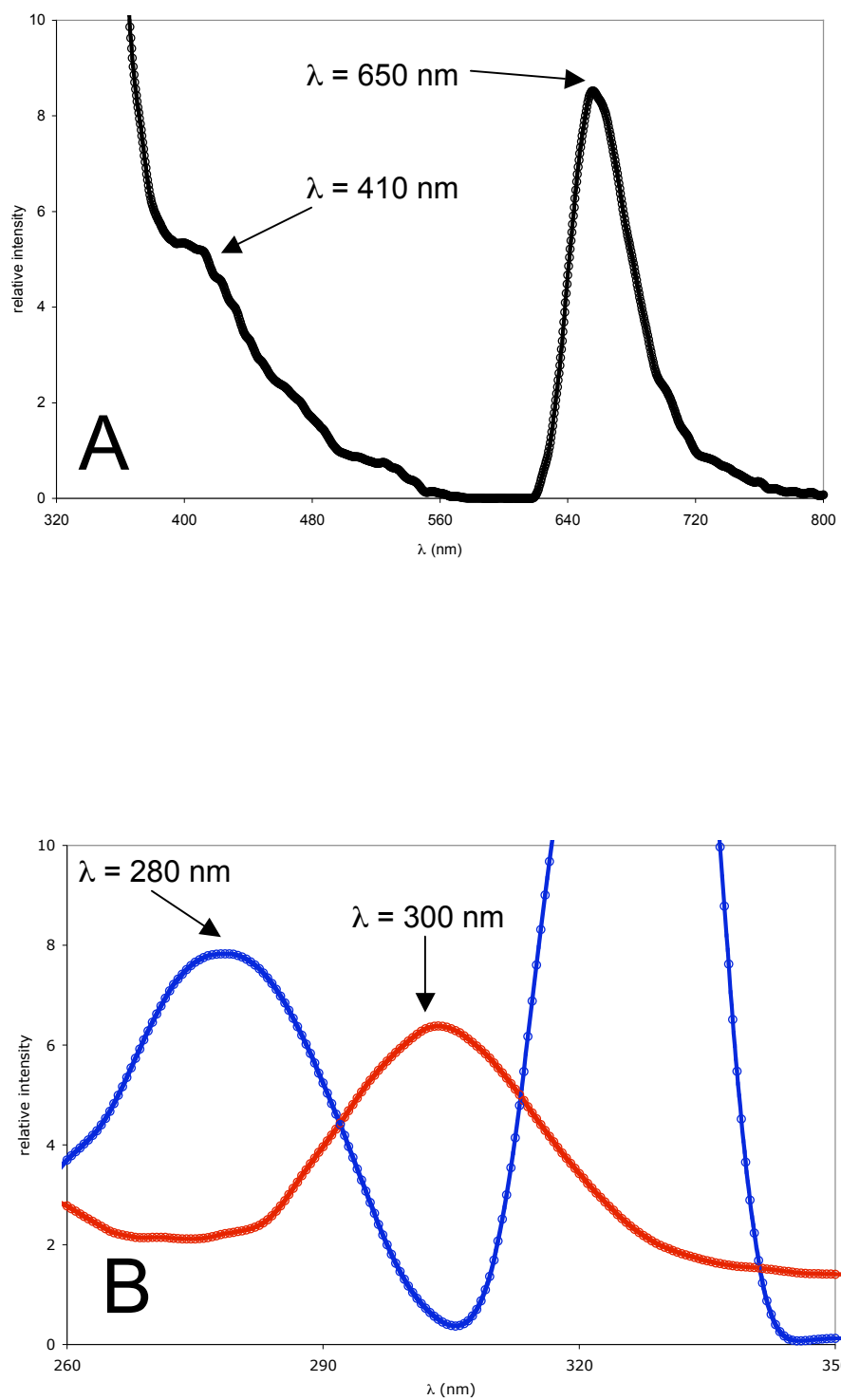


Figure 2.8 Fluorescence of 22 μ M [TM][Cu-Atx1] at 25°C. A. Emission spectrum with excitation at 280 nm (O); B. Excitation spectrum detected at 410 (O) and 650 nm (O).

suggested that copper is either three (T-shape or trigonal planar) or four coordinate (tetrahedral). The absence of the $\text{Cu}^{2+} 1s \rightarrow 3d$ transition at 8979 eV, suggest a Cu^{1+} oxidation state,³³ which is in agreement with the non-EPR signal spectrum performed at 77 K (data not shown) (Figure 2.9.A). The Mo K near-edge spectrum strongly resembled that of tetrathiomolybdate³⁴ with a slightly less intense shoulder at 20006 eV, suggesting a four coordinate Mo (tetrahedral) and an oxidation state of 6^+ . This shoulder has been attributed to formally forbidden $1s \rightarrow 4d$ transition characteristic of a Mo—S in a tetrahedral environment. The Mo XANES suggests that the presence of the Cu-Atx1 does not alter the geometry of TM when bound to the protein (Figure 2.9.B).

Cu and Mo K-edge extended X-ray absorption fine structure (EXAFS) spectra of the [TM][Cu-Atx1] complex (Figure 2.10) clearly showed both, metal-sulfur (Cu—S, Mo—S) and metal-metal (Cu···Mo) backscattering. Quantitative curve-fitting analysis of the copper EXAFS showed two major peaks; a more prominent peak at $R + \alpha = 1.9 \text{ \AA}$ that can be modeled by 3 Cu—S at 2.30 \AA , plus a less intense peak at $R + \alpha = 2.4 \text{ \AA}$ that can be modeled by 1 Cu···Mo at 2.76 \AA (Figure 2.10.A, B); while the Mo showed 2 major peaks also, a prominent peak at $R + \alpha = 1.9 \text{ \AA}$ that can be modeled by 4 Mo—S at 2.24 \AA , plus a less intense peak at $R + \alpha = 2.4 \text{ \AA}$ that can be modeled by 2 or 3 Mo···Cu at 2.76 \AA . The fit results of Cu and Mo K-edge EXAFS data for the [TM][Cu-Atx1] are shown in Table 2.6. Thus the EXAFS analysis indicates that both metals have only sulfur ligands, and that each molybdenum has approximately two to three copper neighbors, while every copper has approximately one molybdenum neighbor.

2.4 Discussion and Conclusion

Here we proposed for the first time a biological [TM][Cu-protein] complex showing a detail study of its solution coordination chemistry using spectroscopy.

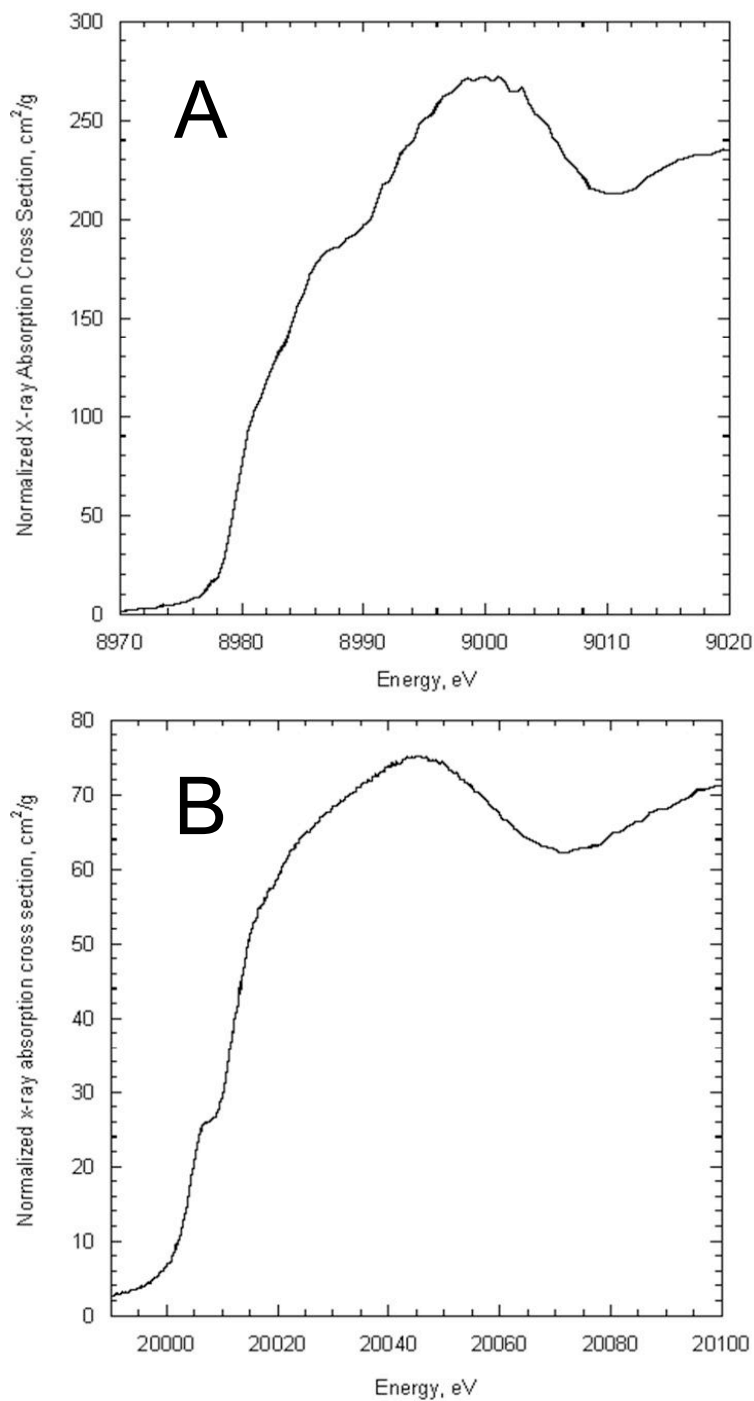


Figure 2.9 A. Cu-XANES of 2.9 mM [TM][Cu-Atx1]: Absence of a Cu²⁺ 1s → 3d transition at 8979 eV suggests a 1⁺ oxidation state; B. Mo-XANES of 2.9 mM [TM][Cu-Atx1]: Similar features in comparison with TM with a slightly less intense shoulder at ~20006 eV, suggesting a Mo⁶⁺.

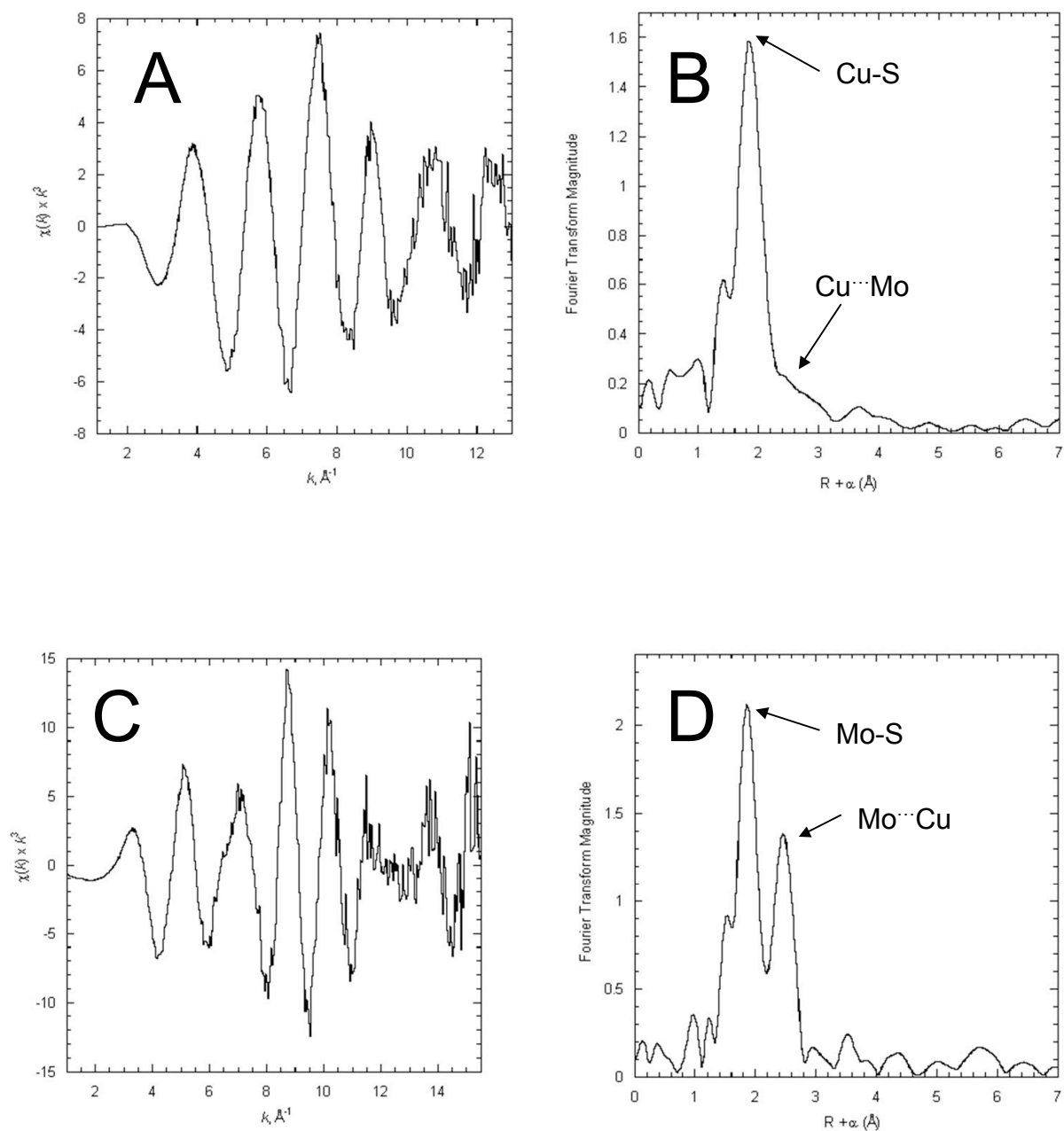


Figure 2.10 A. Cu EXAFS spectrum and B. Cu K-edge Fourier transform of 2.9 mM [TM][Cu-Atx1]: 3 Cu—S at 2.30 Å with $\sigma^2 = 0.0042$ and a 1 Cu—Mo at 2.76 Å with $\sigma^2 = 0.0063$; C. Mo EXAFS spectrum and D. Mo K-edge Fourier transform of 2.9 mM [TM][Cu-Atx1]: 4 Mo—S at 2.24 Å with $\sigma^2 = 0.0033$ and 2/3 Mo—Cu at 2.76 Å with $\sigma^2 = 0.0027$.

Table 2.6 Results of Cu and Mo EXAFS Curve Fitting for [TM][Cu-Atx1].

	CN ^a	R ^b	σ^{2c}	CN ^a	R ^b	σ^{2c}	F ^d
Cu ¹⁺	4S	2.31	6.3				0.338
	3S	2.30	4.3				0.366
	3S	2.30	4.2	1Mo	2.76	6.3	0.268
Mo ⁶⁺	4S	2.24	3.3				
	4S	2.24	3.4	1Cu	2.76	4.7	1.064
	4S	2.24	3.3	2/3 Cu	2.76	2.7	0.839

^aInteger coordination number. ^bBond length in Å. ^cDebye-Waller factor x 10³ in Å². ^dMean-square-deviation between data and fit.

The ultrafiltration and gel filtration studies suggest a robust and time/concentration-dependent TM-Cu-protein complex, which is identified as the [TM][Cu-Atx1] dimer or trimer interaction.

The S–Mo LMCT bands of TM ($\lambda_1 = 241$ nm, $\epsilon_1 = 23200$ M⁻¹cm⁻¹; $\lambda_2 = 317$ nm, $\epsilon_2 = 17600$ M⁻¹cm⁻¹; and $\lambda_3 = 467$ nm, $\epsilon_3 = 12400$ M⁻¹cm⁻¹) due to the MoS- π MO can be characterized as $t_1 \rightarrow 4t_2$, $3t_2 \rightarrow 2e$, and $t_1 \rightarrow 2e$ electronic transitions.^{35,36} The absorbance spectrum of [TM][Cu-Atx1] shows LMCT bands at 375 nm ($\epsilon = 8537$ M⁻¹cm⁻¹) and 532 nm ($\epsilon = 4004$ M⁻¹cm⁻¹), which are the result of the bathochromic shifting of the S–Mo LMCT bands of TM, due to the perturbation of the MoS- π MO cause by the sulfur coordination to a close d-shell copper from Atx1 (Cu¹⁺ by XANES). This bathochromic shifting effect was also observed in the [TM][X-Atx1] (X = Ag and Au) complexes, showing distinct S–Mo LMCT bands at 336 nm ($\epsilon = 8347$ M⁻¹cm⁻¹) and 505 nm ($\epsilon = 4390$ M⁻¹cm⁻¹) for the Ag analogue; and at 483 nm ($\epsilon = 4244$ M⁻¹cm⁻¹)

for the Au analogue. The bathochromic shifting effect follows a serial order, being more intense for the Cu analogue and less intense for the Au analogue (Cu > Ag > Au), due that the internal disturbance of the MoS- π MO will be stronger when the TM-sulfur coordinates to a smaller high-electronegativity atom with electrons with higher ionization energy.

Other biological systems such as the orange protein (ORP) from *D. gigas*, and the hypothetical [Cu²⁺/BSA/TM] complex have also exhibited a similar bathochromic shifting. The UV-visible spectrum shows two distinct S-Mo LMCT bands at 338 nm ($\epsilon = 11000 \text{ M}^{-1}\text{cm}^{-1}$) and 480 nm ($\epsilon = 5500 \text{ M}^{-1}\text{cm}^{-1}$)³⁷ for the ORP and at 338 nm and 482 nm for [Cu²⁺/BSA/TM].³⁸

We can suggest that the high ($\lambda = 410 \text{ nm}$) and low energy bands ($\lambda = 650 \text{ nm}$) observed in the emission spectrum of the [TM][Cu-Atx1] complex can be assigned to 2 different triplet excited states, a triplet cluster-centered (³CC) excited state ($\lambda = 410 \text{ nm}$), and a triplet LMCT (³LMCT) excited state ($\lambda = 650 \text{ nm}$).³⁰ The ³CC is delocalized over the metal core with d-s contributions (Cu-Cu), while the ³LMCT is predominately composed of ligand p orbitals (S-Cu). Due that TM and Cu-TM complexes don't exhibit any fluorescence (data not shown), we can suggest that the fluorescence of this drug-protein adduct is mostly due to the presence of a Cu^I-thiolate cluster localized at the core center of this interaction. Similar fluorescence studies are reported for the characterization of adamantane-like Cu^I₄-thiolate clusters found in the rabbit Cu^I₈-MT, and the human Cu^I₁₂-MT3 copper metallothioneins (Table 2.7).^{31,32}

The Cu-EXAFS of the [TM][Cu-Atx1] complex suggests a Cu^I coordination site with a single Cu-S shell at 2.30 Å, which is in agreement with the bond lengths for other tri-coordinate Cu^{I+} complexes.³⁹ Attempts to fit the data with 4 Cu-S give unreasonably higher Debye-Waller factors. The fits improve when Mo is included and the best fit indicates that Cu is interacting with only one Mo at 2.76 Å.

Table 2.7 Fluorescence spectroscopy for copper metallothioneins.^{31,32}

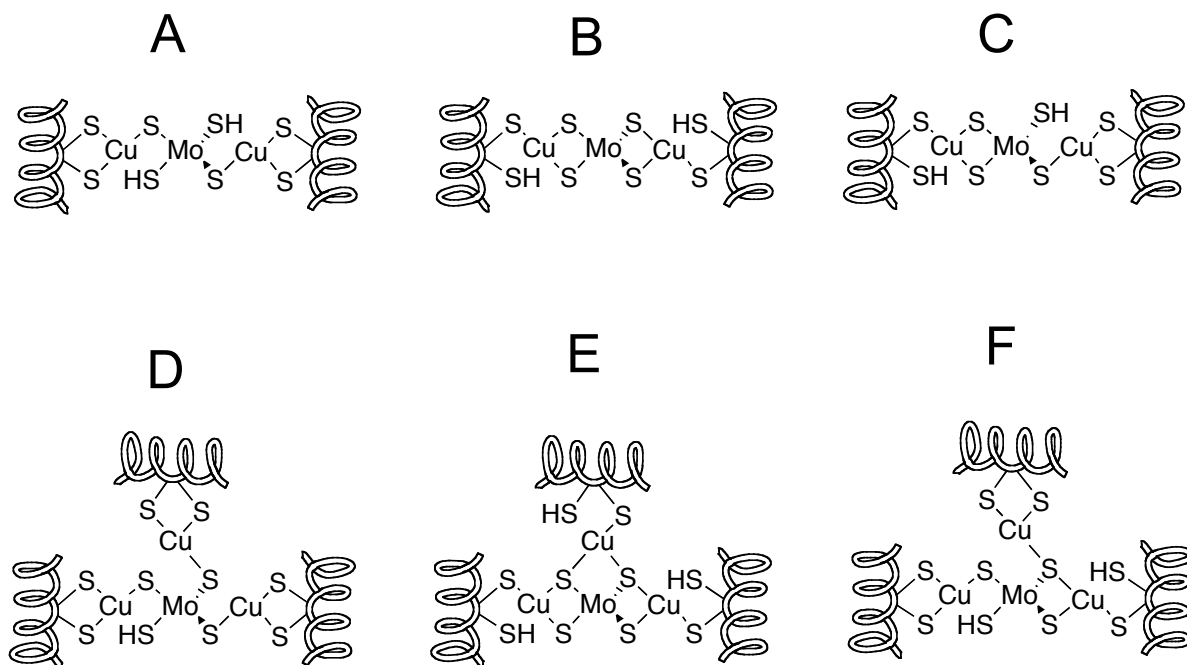
	T, λ_{exc} (nm)	Emission (nm)	T, λ_{emis} (nm)	Excitation (nm)
rabbit Cu ^I ₈ -MT	room, 318	430 ^a , 630, 695 ^b	room, 630	270 ^b , 320 ^b
	77K, 318	425, 610	77 K, 425; 610	260 ^a , 305 ^a ; 300
human Cu ^I ₁₂ -MT3	room, 300	610, 700 ^b	-	-
	77, 300	420 ^a , 600 ^a	-	-

^aweak intensity. ^bsholder.

From the Mo perspective, the EXAFS data fits a MoS₄ (Mo–S = 2.24 Å) with an interaction from two or three Cu scatterers at an interatomic distance of 2.76 Å, which agrees with the distance suggested by Cu-EXAFS. These combined XAS results are consistent with a dimer or trimer [TM][Cu-Atx1] complex supported previously by analytical gel filtration, ICP-OES and Bradford assay. We can suggest 3 different possible binding modes (Scheme 2.1) for the [TM][Cu-Atx1] dimer interaction, one with the copper protein coordinated to two sulfurs (cysteines) from the Atx1 and one sulfur from the TM (causing distortion from a linear arrangement) (Scheme 2.1A); a second one, with the copper protein coordinated with two sulfurs from the TM and one sulfur from the Atx1 (causing also distortion from a linear arrangement) (Scheme 2.1B); and a third one will be any mixture of these two possible models (Scheme 2.1C, one of the possible mixtures). Exactly in the same way, we can expect 3 other possible binding modes for the [TM][Cu-Atx1] trimer interaction (Scheme 2.1D, E, F).

The Mo···Cu interatomic distance, Mo–S and Cu–S bond lengths found for the [TM][Cu-Atx1] dimer or trimer are very close to the ones found in other biological systems that have a

Scheme 2.1 Possible binding modes for the core center of the [TM][Cu-Atx1].

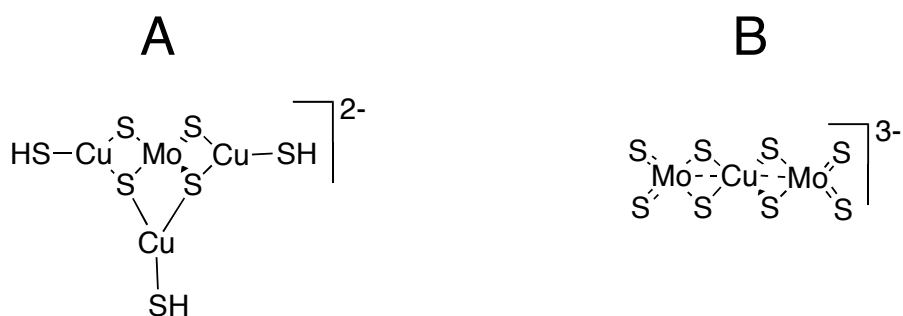


[Mo–S–Cu] core center. The orange protein (ORP) from *D. gigas* with a sulfur bridged Mo₂Cu cluster (Scheme 2.2B) has 1 Mo···Cu at 2.75 Å, 4 Mo–S at 2.21 Å, 4 Cu–S at 2.31 Å and 2 Cu···Mo at 2.74 Å;⁴⁰ and the liver lysosomes from TM-treated Long Evans Cinnamon rats (Wilson’s disease model) (Scheme 2.2A) shows 3 Mo···Cu at 2.70 Å, 4 Mo–S at 2.24 Å, 3–3.5 Cu–S at 2.28 Å and slightly less than 1 Cu···Mo at 2.70 Å.⁴¹

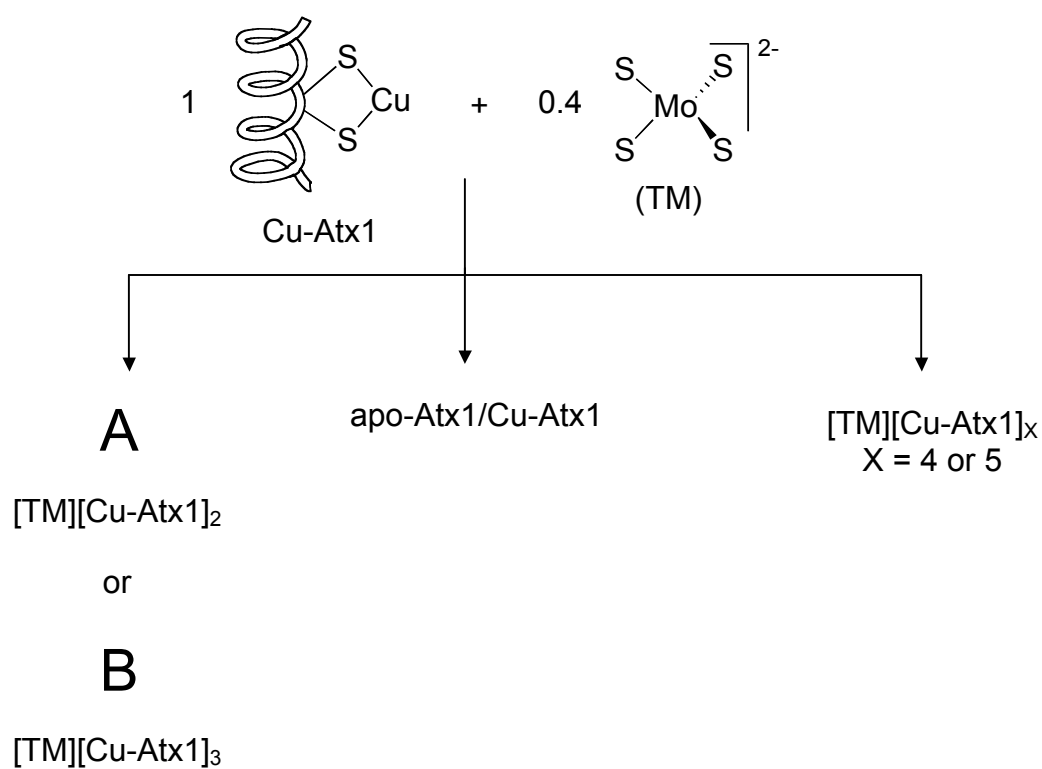
The present work demonstrates that the accessibility of the Cu site at the surface-exposed loop region of the Atx1 facilitates the formation of a [TM][Cu-Atx1] dimer or trimer interaction and an ‘unknown’ [TM][Cu-Atx1]_x (X = 4 or 5) complex, by a hypothetical mechanism (Scheme 2.3). The characterization of the [TM][Cu-Atx1] complex may shed some light on the understanding of the chemical and biological intracellular modus operandi of this drug in this

novel antioangiogenic copper chelation therapy. Further experiments are required to identify the other 'unknown' product of the reaction between Cu-Atx1 and TM.

Scheme 2.2 Model structures for the $[(\text{HSCu})_3\text{S}_4\text{Mo}]^{2-}$ and $[\text{S}_2\text{MoS}_2\text{CuS}_2\text{MoS}_2]^{3-}$ complex ion.^{40,41}



Scheme 2.3 Hypothetical formation of $[\text{TM}][\text{Cu-Atx1}]$.



Chapter 3

Structural Coordination Chemistry of the Interaction of the Yeast Cu-Metallochaperone (Cu-Atx1) with TM: '[TM][(Cu)(Cu-Atx1)₃]

Abstract

Several interactions between copper proteins and ammonium tetrathiomolybdate (TM) have been linked to the production of a copper deficiency in biological systems. The first molecular structure of this kind of interaction is presented for the isolated purple product created by the reaction between the yeast copper chaperone (Atx1) and TM, which was purified by analytical gel filtration ([TM]:[Cu-Atx1] = 0.4). The complex was characterized by ICP-OES and Bradford assay, showing a [Cu]:[Mo] = 3.4, [Cu]:[Atx1] = 1.0, and [Atx1]:[Mo] = 3.3. UV-Visible spectroscopy showed the shifting of the TM (S–Mo) LMCT bands to 375 and 532 nm due to its coordination with copper. A combination of molecular replacement with multiple-wavelength anomalous dispersion for copper (Cu-MAD) was used to elucidate the structure of this complex. This structure reveals a trimer of Atx1 proteins and an unexpected [S₆Cu₄MoS₄] cluster, with a Mo surrounded by three tetra-coordinated Cu atoms in a nest-shaped arrangement, and an additional tri-coordinated copper, which is purely ligated by the Atx1 proteins. The atomic structure of the [TM][(Cu)(Cu-Atx1)₃] drug-protein adduct will provide insights for understanding the mechanism of action of TM as a copper chelator drug.

3.1 Introduction

The molecular mechanism, by which TM can affect a broad set of physiological states, including teart, CCP, Wilson's disease, and cancer, is no yet established. A non-absorbable physiological [TM][Cu-protein] complex has been proposed to form in blood plasma cells and in apical lysosomes of kidney tubule cells as a result of the Cu-Mo antagonism and the TM treatment in copper intoxicated sheep.^{1,2} The TM therapy of the Wilson's disease appears to work by a urine excretion of the previously discussed [TM][Cu-protein] complex, or by a biliar excretion of a more specific [TM][Cu-Albumin] interaction after absorption of TM in blood.³

In comparison, we can find different hypotheses in the literature about possible mechanisms of action that explain how TM is able to inhibit tumor development in cancer. One of them is the cytoplasmatic inhibition of Cu-dependent signaling proteins and growth factors,⁴ by copper depletion or formation of inactive TM complexes. Possible Cu-dependent proteins include the fibroblast growth factor (FGF), superoxide dismutase (SOD1), cytochrome C oxidase (CCO), lysyl oxidase (LOX), ceruloplasmin (Cp), and vascular endothelial growth factor (VEGF) among others.⁵⁻⁷ Hence, the synthesis and characterization of a [TM][Cu-protein] complex may shed some light on the chemical and biological modus operandi of TM in Cu-Mo antagonism and in copper chelation therapy with TM.

Although there are several x-ray studies of small [(CuL)_nTM] inorganic complexes (n = 1-6, L = N and P ligands), a detailed protein structural study that provides an example of a [TM][Cu-protein] biological model complex is still lacking.⁸ In 1984, Chidambaram used EPR spectroscopy to propose that TM inhibits the oxidase activity of ceruloplasmin (Cp) by forming an irreversible [TM]₆[Cu₆Cp] complex.⁹ Later, Bristow (1985) and Quagraine (2001) showed that TM binds to serum albumin forming a [TM][Cu-BSA] complex using Mo⁹⁵ NMR and UV-

Visible spectroscopy, respectively.^{10,11} In 1995, Suzuki suggested that the accumulation of Cu-containing metallothioneins (Cu-MT) in the liver of TM-treated LEC rats (Long-Evans rats with a cinnamon-like color) results in the formation of a $[\text{TM}]_n[\text{Cu}_n\text{-MT}]$ complex.^{12,13}

Given that the specific molecular target and unifying mechanism of the chelation therapy with TM is still an enigma, we proposed here the structural characterization of a $[\text{TM}][(\text{Cu})(\text{Cu-Atx1})_3]$ complex, which represents the first detailed-structure of a $[\text{TM}][\text{Cu-protein}]$ interaction. The X-ray structure, in agreement with previously discussed XAS spectroscopy (Chapter 2), revealed a trimer complex with three Atx1 proteins, suggesting a novel $[\text{S}_6\text{Cu}_4\text{MoS}_4]$ cluster and a fourth copper at the core center of this protein-drug adduct.

This $[\text{TM}][(\text{Cu})(\text{Cu-Atx1})_3]$ complex may provide the initial clues for understanding the mechanism of how TM and copper-proteins interact in a physiological environment to produce copper deficiency in the Cu-Mo antagonism and in the treatment of Wilson's disease and cancer with TM.

All the biochemical sample characterization and crystallization results described in this Chapter were carried out by myself or by Chandler D. Robinson, an undergraduate research associate working under my supervision. Data collection and analysis was principally carried out by Dr. Yi Xue with assistance and advise from Dr. Pamela Focia and Dr. Alfonso Mondragón.

3.2 Experimental Procedures

3.2.1 Preparation and purification of wild-type Atx1. The wild-type Atx1 protein was expressed, prepared and purified as previously described.¹⁴

3.2.2 Preparation and purification of Se-Met-Atx1. A 250 ml starter culture of the transformed *E. coli* strain BL21(DE3) containing the pet11d/Atx1 expression plasmid was grown overnight at 37°C with shaking at 180 rpm using a series 25 incubator shaker from New

Brunswick Scientific (Edison, NJ) in LB medium supplemented with ampicillin. This starter culture was then used to inoculate 15 L of prewarmed Se-Met minimal medium (Se-MetMM). Each liter of Se-MetMM was prepared as follow, a mixture of 1.0 L of MQ H₂O with 1.0 g of (NH₄)₂SO₄, 4.5 g of KH₂PO₄, 10.5 g of K₂HPO₄, 0.5 g of Na citrate, 42 mg of each of the 19 common L-amino acids (excluding Met), and 125 mg of each nucleotide (adenosine, guanosine, thymidine and uridine) was autoclavated using a BIOFLO 4500 fermentor/bioreactor from New Brunswick Scientific (Edison, NJ). Then a mixture of the following components was added per liter of Se-MetMM before inoculation; 12.5 ml of 40% (w/v) glucose, 1.0 ml of 1M MgSO₄, 0.4 ml 10 mg/ml thiamine, 2.0 ml of 2 mg/ml d-biotin, 3.0 ml of 10 mg/ml L-Se-Met, 1.0 ml of 100 mg/ml of ampicillin and 3.0 ml of 10 mg/ml Fe₂(SO₄)₃. Cells in this medium were grown at 37°C to OD₆₀₀ of 0.6 and then induced with 1 ml of 200 mM IPTG (per liter of Se-MetMM) for 6 hours.^{15,16} The Se-Met-Atx1 was isolated by free-thaw extraction and purified following a protocol previously described.¹⁴

3.2.3 Matrix-assisted laser desorption/ionization time-of-flight mass spectrometry (MALDI/TOF MS). The Se-Met-Atx1 was analyzed using a matrix of 10 mg of α -cyano-4-hydroxy-cinnamic acid in 500 μ l solution of acetonitrile, 500 μ l of MQ H₂O and 1 μ l of trifluoroacetic acid. For MALDI/TOF MS, a mixture of 3 μ l of Se-Met-Atx1 plus 1 μ l of 1 mg/ml horse myoglobin (standard) was dissolved with 90 μ l of the previously described matrix. Then, 1 μ l of this solution was spotted onto the MALDI plate and dried at room temperature. Measurements were performed on a Voyager PRO DE MALDI/TOF MS from Applied Biosystems (Framingham, CA), using a pulse N₂ laser with a 2 ns pulse width. Spectra were recorded in the positive ion linear mode. As shown in Figure 3.1, the Atx1 expressed by the *E. coli* BL21(DE3) in Se-MetMM was able to incorporate the Se-Met amino acid with greater than

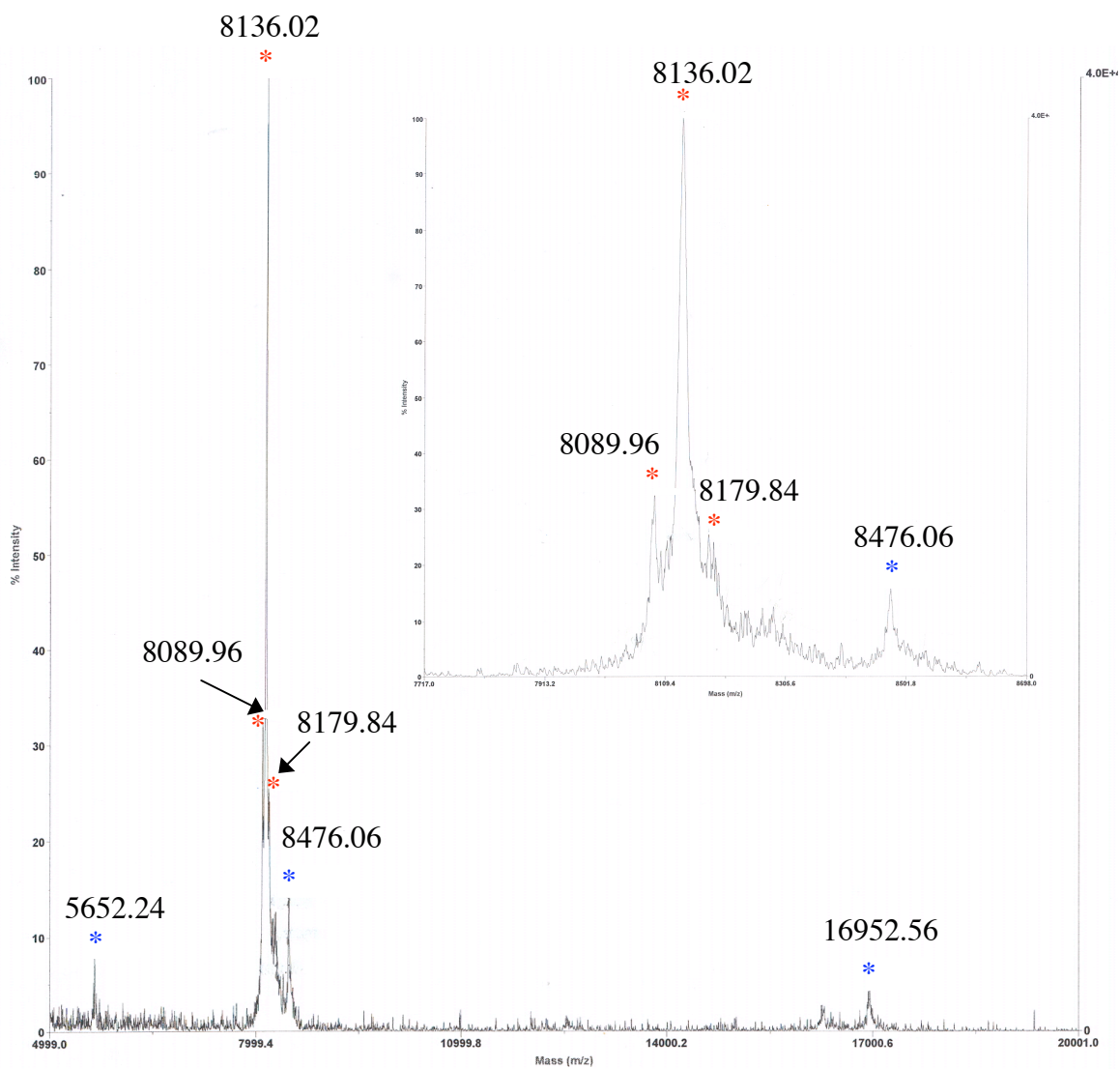


Figure 3.1 MALDI/TOF mass spectrum of the Se-Met-Atx1 is denoted by (*) [Atx1: $m/z^{\text{calc}} = 8089.46$ and $m/z^{\text{obs}} = 8089.96$; Se-Met-Atx1: $m/z^{\text{calc}} = 8136.35$ and $m/z^{\text{obs}} = 8136.02$; (Se-Met)₂-Atx1: $m/z^{\text{calc}} = 8183.25$ and $m/z^{\text{obs}} = 8179.84$]. Peaks denoted by (*) are from +1, 2 and 3-charged states of horse myoglobin standard [$m/z^{\text{obs}} = 16952.56$ (+1), 8476.06 (2+), 5652.24 (3+)].

95% efficiency. Since mostly all the NH₂-terminal Met was removed in vivo, only one Met can be substituted for Se-Met in the purified Atx1. The calculated difference in the molecular mass between the recombinant Atx1 and its Se-Met analogue is 46.89 ($m/z^{\text{calc}} = 8089.46$ for the Atx1 and $m/z^{\text{calc}} = 8136.35$ for the Se-Met-Atx1). The molecular mass determination by MALDI/TOF gave a mass difference of 46.06 ($m/z^{\text{obs}} = 8089.96$ for the Atx1 and $m/z^{\text{obs}} = 8136.02$ for the Se-Met-Atx1), which matches the expected value very well. A very little amount of (Se-Met)₂-Atx1 is also detected by MALDI-TOF: $m/z^{\text{calc}} = 8183.25$ and $m/z^{\text{obs}} = 8179.84$.

3.2.4 Preparation of Cu-Atx1 and Se-Met-Cu-Atx1. Both proteins were prepared following the protocol described in Chapter 2.

3.2.5 Preparation of crystallization sample. The [TM][((Cu)(Cu-Atx1)₃] (and [TM][((Cu)(Se-Met-Cu-Atx1)₃] analogue) sample was prepared using a mixture of approximately 670 μl of a 3.0 mM Cu-Atx1 plus TM (1:0.4) ($t_{\text{rxn}} = 30$ min, aerobic conditions, $T = 4^\circ\text{C}$) (20 mM MES, 150 mM NaCl, pH 6.0). The mixture solution was purified by FPLC analytical gel filtration (Superdex 75 HR10/30) forming three different peaks in the chromatogram. These fractions were collected (2 mL each) and concentrated to approximately 100 μL using a centrifugal filter device with a MW cut-off membrane of 3 kDa (MICROCON). The fractions that correspond to the first peak shows an approximate molecular weight of 10.1 kDa ([Atx1] = 0.65 mM, [Cu] = 0.36 mM and no [Mo]; [Cu]:[Atx1] = 0.55), to the second peak, 29.5 kDa (color: purple, [Atx1] = 3.1 mM, [Cu] = 3.2 mM and [Mo] = 0.95 mM; [Cu]:[Mo] = 3.4, [Cu]:[Atx1] = 1.0, [Atx1]:[Mo] = 3.3), and to the third peak, 52.1 kDa (color: brown, [Atx1] = 1.3 mM, [Cu] = 1.1 mM, [Mo] = 0.29 mM; [Cu]:[Mo] = 3.8, [Cu]:[Atx1] = 0.85, [Atx1]:[Mo] = 4.5). The concentrated deep purple solution corresponding to the 29.5 kDa peak represent the [TM][((Cu)(Cu-Atx1)₃] sample, which was further used for protein crystallizations with the

correspondent characterization (as described in Chapter 2) by Bradford assay (Atx1 concentration), ICP-OES (Cu and Mo), UV-Visible and Fluorescence spectroscopy.

3.2.6 Crystallization and data collection. A detailed description of the different crystallization solutions and conditions used is included in the results section of this chapter. Before data collection, we immersed the deep purple crystals in a cryo-protectant solution of 25% glycerol, 0.15 M DL-malic acid pH 7.0 and 20% polyethylene glycol 3350 for about 3 min and flash-cooled them in liquid nitrogen. Native diffraction (2.3 Å) and multiple-wavelength anomalous dispersion (MAD) (Cu edge) data were collected from frozen crystals (#7) at the SBC-CAT and IMCA-CAT beamlines at the Advanced Photon Source (Argonne National Laboratory), respectively. For the Cu-MAD, the data sets were collected at peak, inflection and low remote wavelengths. We used a 3K X 3K Mar charge-couple device (CCD) detector and processed the data using Denzo and Scalepack.¹⁷ A summary of the data-collection statistics is given in Table 3.1. Crystallization studies were performed by Hamsell M. Alvarez and Chandler D. Robinson.

3.2.7 Structure Determination and Refinement. The determination of the structure of the [TM][(Cu)(Cu-Atx1)₃] was solved by Yi Xue.

3.3 Results

3.3.1 Crystallization. To investigate the molecular interaction between Cu-Atx1 and TM, we crystallized and solved the structure of the [TM][(Cu)(Cu-Atx1)₃] complex after purification by analytical gel filtration (see Experimental Procedure and Figure 3.2) and several trials of crystallization conditions.

The first purple crystals (#1) were obtained by vapor diffusion in hanging drops (1 µl of complex + 1 µl of well solution) equilibrated over 2.0 M (NH₄)₂SO₄ plus 5% 2-propanol well

Table 3.1 Data collection and refinement statistics for crystal (#7).

Data collection	Cu-MAD			
	Native	Peak	Inflection	Low remote
Data set	Native	Peak	Inflection	Low remote
Beamline ^a	19-BM	17-ID-B	17-ID-B	17-ID-B
Wavelength (Å)	0.9787	1.3799	1.3805	1.3850
Resolution limits (Å)	50.0 - 2.30	50.0 - 2.30	50.0 - 2.50	50.0 - 2.72
Completeness (%) ^f	97.0 (84.0)	94.3 (64.0)	99.1 (92.4)	99.7 (98.5)
Data redundancy ^f	5.0 (2.9)	3.3 (1.4)	3.6 (2.0)	3.7 (3.0)
R _{sym} (%) ^{b,f}	8.1 (47.0)	8.3 (34.2)	6.9 (51.6)	6.8 (54.0)
I/<s> ^f	16.7 (2.0)	11.9 (1.7)	15.5 (1.6)	17.1 (2.1)
Space group	P2 ₁ 2 ₁ 2			
Unit-cell parameters (Å °)	109.9 182.2	90.0 90.0		
	52.7	90.0		
Phasing Statistics	Peak	Inflection	Low remote	
Phasing Power (iso) ^c	0.44	1.4	N/A	
Phasing Power (ano) ^c	1.5	0.86	0.17	
Cu sites found	14			
FOM after SHARP	0.19			
FOM after SOLOMON	0.64			
FOM after DM	0.86			
Refinement Statistics				
R _{work} /R _{free} (%) ^d	21.3% / 26.5%			
R.m.s. bond lengths (Å)	0.014			
R.m.s. bond angles (°)	1.393			
Protein atoms	6746			
No. of water molecules	372			
Residues - Ramachandran (%) ^e				
Most favoured	99.0			
Additional allowed	100.0			

^aAll data sets were collected at 100 K at the Advanced Photon Source. ^b $R_{\text{sym}} = \sum |I_{\text{obs}} - I_{\text{avg}}| / \sum I_{\text{obs}}$
^cThe phasing power is defined as the ratio of the rms value of heavy atom structure factor amplitude to the rms value of the lack-of closure error. ^d $R_{\text{values}} = \sum |F_{\text{obs}} - F_{\text{calc}}| / \sum F_{\text{obs}}$. 5% of the reflections were reserved for the calculation of R_{free} . ^eThe validation was performed by program MOLPROBITY.⁴⁹ ^fValues in parentheses are for the highest resolution shell.

solution (750 μ l). Very small and unstable single crystals (#1) appeared after equilibration for 1 day at 18°C and 1 day at 10°C. The crystals (#1) were stable for a maximum of 4 days and they grew to maximum dimensions of 0.04 x 0.04 x 0.04 mm (length x width x height) (Figure 3.3) (#1).

The second attempt to crystallize this compound was also using vapor diffusion (0.5 μ l of complex + 0.5 μ l of well solution) but with a 0.2 M sodium formate plus 20% PEG 3350 well solution (750 μ l). Single purple crystals (#2) appeared after equilibration for 5 days at 18°C, 1 day at 14°C and 1 day at 23°C. The 18-14°C and 14-23°C temperature transitions might be crucial factors that spurred nucleation and crystal formation to occur. The crystals (#2) were much more stable than before, lasting for about 1 month before any decomposition, and they grew to maximum dimensions of 0.10 x 0.04 x 0.05 mm (Figure 3.4) (#2). The crystals (#2) decomposed due to high temperature and inadequate handling conditions at the synchrotron facilities at the APS (Argonne, IL). Further crystallization attempts using the same conditions (0.5 μ l of complex + 0.5 μ l of well solution) and changing the proportion of the hanging drop compositions (1.0/1.5/2.0 μ l of complex + 1.0/1.5/2.0 μ l of well solution) resulted in the formation of rod clusters of purple crystals (#3) (well solution = 750 μ l). Data of the isolated single crystals (#3) (average \sim 0.10 x 0.03 x 0.04 mm) from these clusters were collected (2.3 Å) at the APS (Argonne). Attempts to solve the structure using molecular replacement with Phaser¹⁸ using a monomeric high resolution (1.02 Å) Hg-Atx1 search model (PDB code: 1CC8)¹⁹, failed to resolve the phase as the crystals were twinned (#3), showing a different orientation of the multiple lattices of the various domains within the same crystal. Additionally, an optimization of the crystallization conditions [using modifications of pH (6–8) and % PEG 3350 (18–21)] resulted in precipitation or absence of crystals formation (Figure 3.5.A, B, C & D) (#3).

The third attempt to crystallize this compound was using a 0.15 M DL-Malic acid pH 7.0 plus 20% PEG 3350 (0.5 μ l of complex + 0.5 μ l of well solution) (well solution = 750 μ l). Plate crystals (#4) appeared after equilibration for 2 days at 18°C, 4 days at 14°C and 1 day at 23°C. The crystals (#4) were more unstable, lasting for only about a week before any decomposition, and they grew to maximum dimensions of 0.25 x 0.05 x 0.05 mm (Figure 3.6.A & B) (#4). After cryopreservation with 25% glycerol (in addition to the well solution), data for these crystals (#4) were collected (1.8 Å) revealing a diffraction pattern with single and consistent lines, and individual and round diffraction spots, which are not on top or side of each other, suggesting the presence of a single protein crystal (#4) without any twinning issues

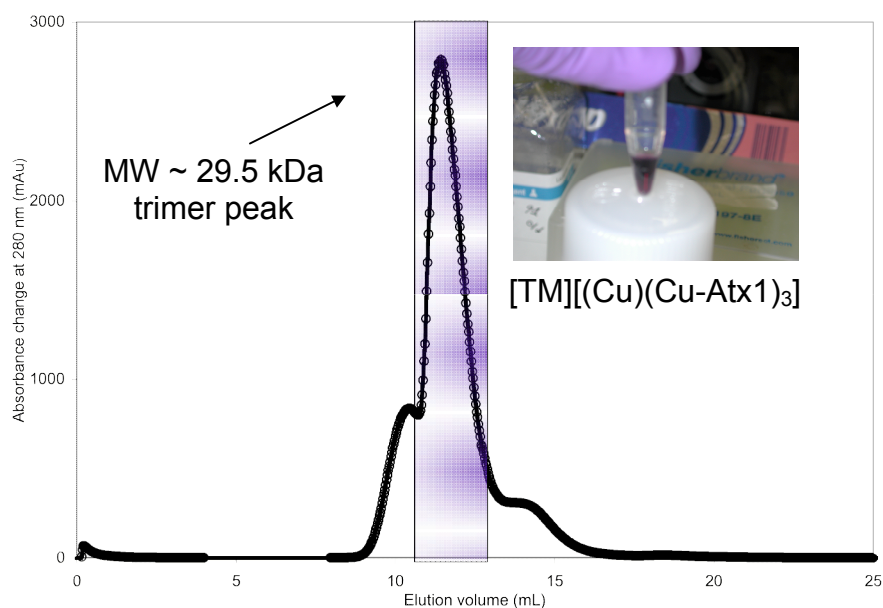


Figure 3.2 Analytical gel filtration chromatogram of 3.0 mM Cu-Atx1 + TM (1:0.4). Inset: Concentrated solution of $[TM][(Cu)(Cu-Atx1)_3]$ after purification by analytical gel filtration and concentration by ultrafiltration.

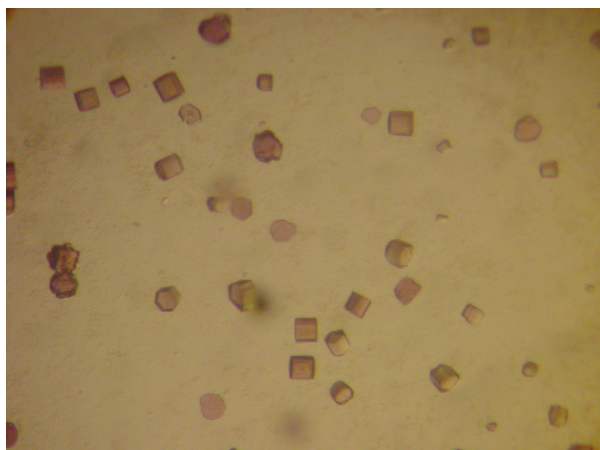


Figure 3.3 Single crystals (#1) of [TM][(Cu)(Cu-Atx1)₃] for structure determination with approximate dimensions of 0.04 mm x 0.04 mm x 0.04 mm, well solution: 2.0 M (NH₄)₂SO₄ plus 5% 2-propanol.

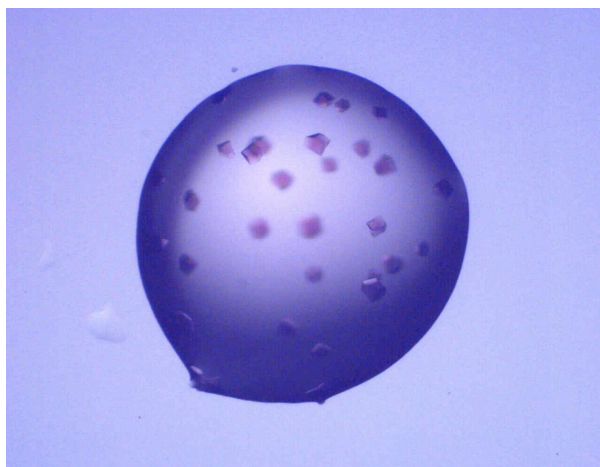


Figure 3.4 Single crystals (#2) of [TM][(Cu)(Cu-Atx1)₃] for structure determination with approximate dimensions of 0.10 mm x 0.04 mm x 0.05 mm, well solution: 0.2 M sodium formate plus 20% PEG 3350.

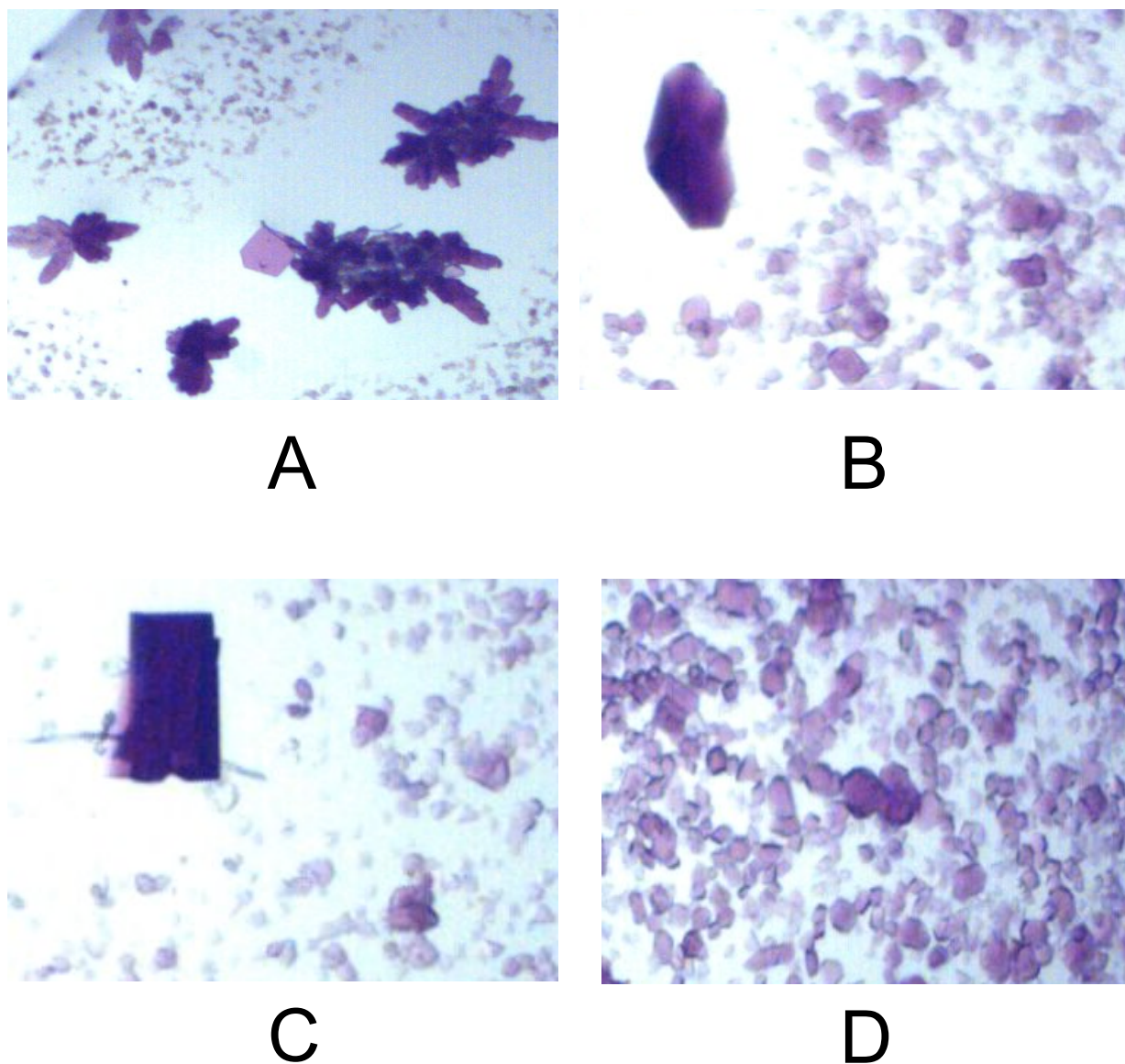
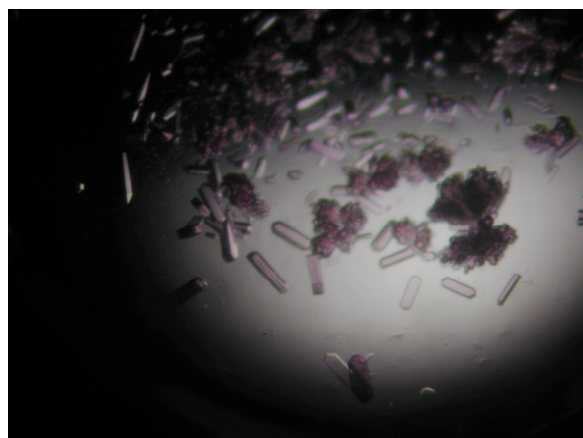


Figure 3.5 Rod cluster and isolated single crystals (#3) of $[\text{TM}][(\text{Cu})(\text{Cu-Atx1})_3]$ for structure determination with approximate average dimensions of $0.10 \text{ mm} \times 0.03 \text{ mm} \times 0.04 \text{ mm}$, well solution: 0.2 M sodium formate plus 20% PEG 3350 [hanging drop composition ($X \text{ }\mu\text{l}$ of complex + $Y \text{ }\mu\text{l}$ of well solution): A = $0.5 + 0.5$, B = $1.0 + 1.0$, C = $1.5 + 1.5$, and D = $2.0 + 2.0$].

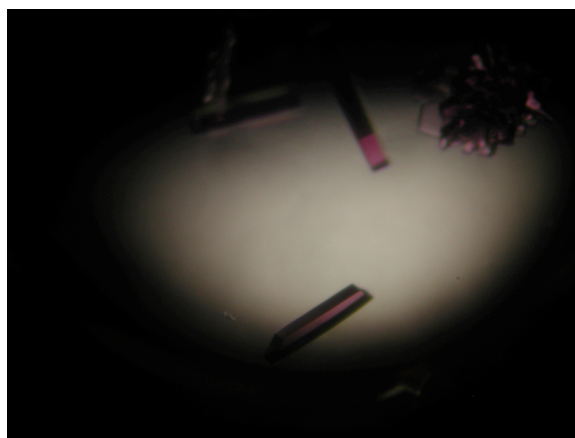
(Figure 3.6.C & D). Unfortunately, collected data was not of the quality expected to resolve the structure, due to a significant amount of lattice distortions ('mosaicity') due that maybe the cryopreservant solution used for flash freezing was not appropriate. Also, only 180 ° of data were collected because the loop containing the frozen crystal was slightly bent and partially obstructed the beam path to the crystal.

The fourth attempt to crystallize the purple complex used the same conditions as before (0.15 M DL-Malic acid pH 7.0 plus 20% PEG 3350) but using the modified Se-Met-Cu-Atx1 to prepare the [TM][(Cu)(Se-Met-Cu-Atx1)₃] (see experimental procedure above). The new Se of this protein and multiple anomalous dispersion (MAD) x-ray crystallography²⁰ can be crucial to solve the phasing problems observed before. We used different amounts of well solution (200 µl) plus extra 50% PEG 3350 (7.5 or 10.0 µl) and a hanging drop composition of 1.0 µl of 1:2 diluted complex plus 1.0 µl of well solution (Figure 3.7.A & B) (#5); or 1:2 diluted well solution (750 µl) and a hanging drop composition of 1.0 µl of original or 1:2 diluted complex plus 1.0 µl of well solution (Figure 3.7.C & D) (#6). Rod cluster and single deep purple crystals (#5 & #6) appeared half a day after equilibration at 14°C and grew to maximum average dimensions of 0.40 x 0.05 x 0.05 mm (Figure 3.7.A & B, rod cluster) (#5) and 0.15 x 0.03 x 0.04 mm (figure 3.7.C & D, single crystal) (#6). These crystals (#5 & #6) were not stable enough for collection of data due that during cryopreservation (25% glycerol plus well solution), the crystals cracked or dissolved after cooling in liquid nitrogen.

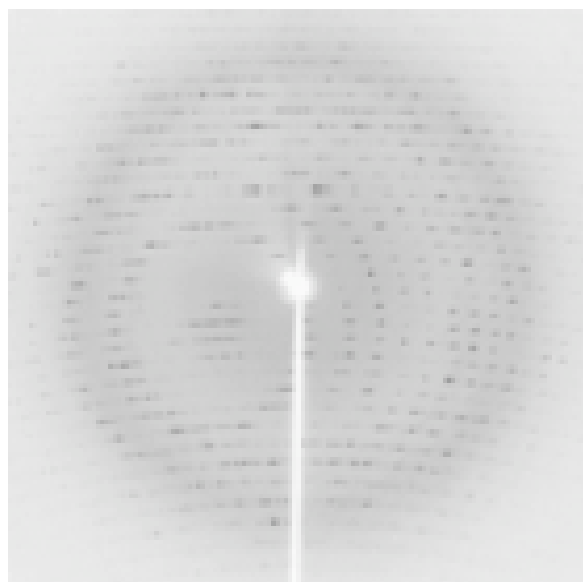
Finally, using the same crystallization solution (0.15 M DL-Malic acid pH 7.0 plus 20% polyethylene glycol 3350) but increasing the hanging drop proportion composition (1.0 µl of



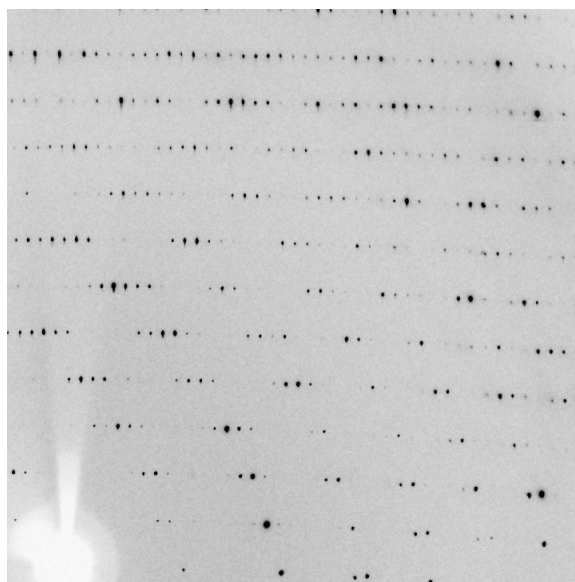
A



B



C



D

Figure 3.6 A & B: Plate crystals (#4) of $[\text{TM}][(\text{Cu})(\text{Cu-Atx1})_3]$ for structure determination with approximate dimensions of 0.25 mm x 0.05 mm x 0.05 mm, well solution: 0.15 M DL-Malic acid pH 7.0 plus 20% PEG 3350. C & D: Diffraction pattern of $[\text{TM}][(\text{Cu})(\text{Cu-Atx1})_3]$ at 1.8 Å.

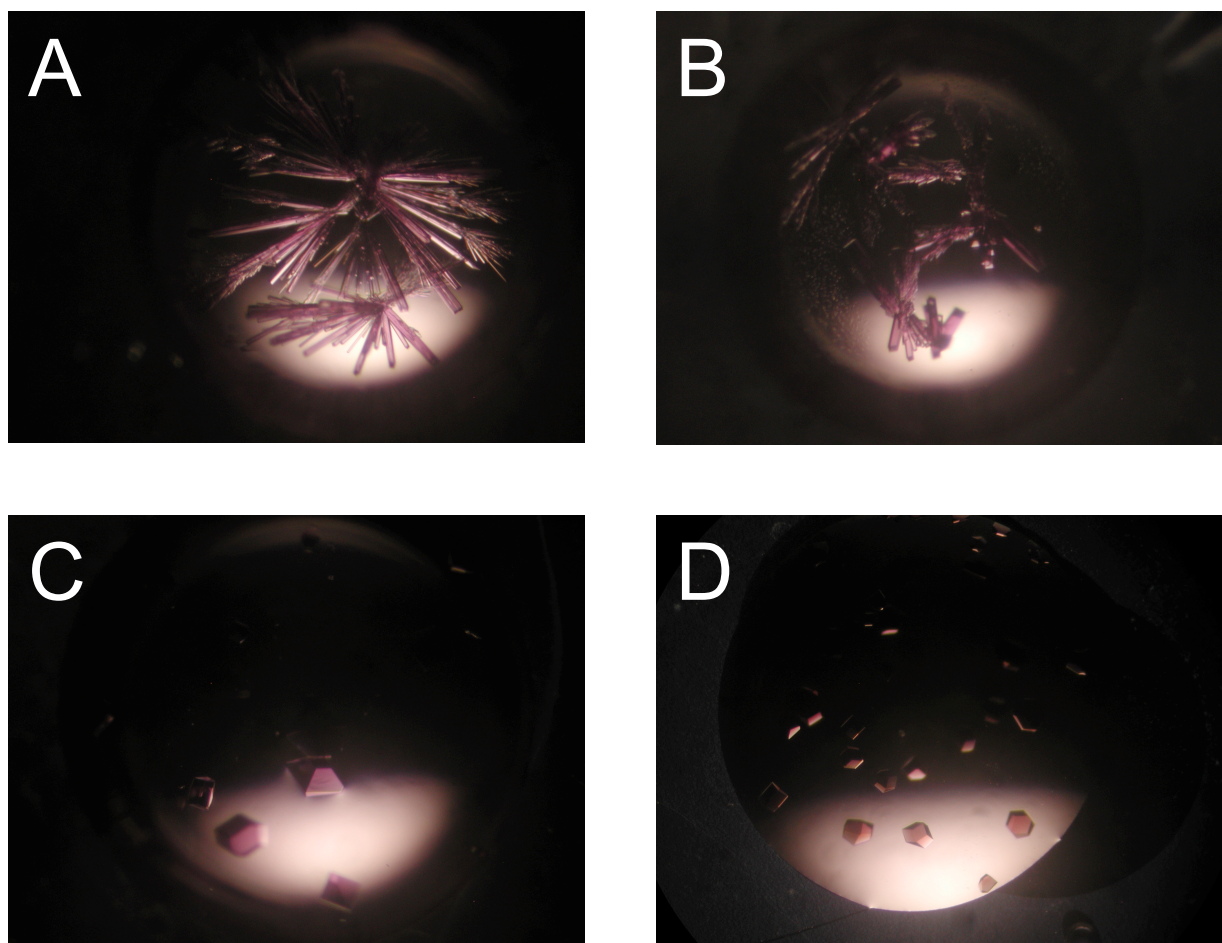


Figure 3.7 Rod cluster (#5) and single crystals (#6) of $[\text{TM}][(\text{Cu})(\text{Se-Met-Cu-Atx1})_3]$ for structure determination with approximate average dimensions of 0.40 mm x 0.05 mm x 0.05 mm (A & B) and 0.15 mm x 0.03 mm x 0.04 mm (C & D) and, well solution: 0.15 M DL-Malic acid plus 20% PEG 3350. [A → hanging drop: 1.0 μl of 1:2 diluted sample complex + 1.0 μl well solution, and well solution: 200 μl + 7.5 μl 50% PEG 3350; B → hanging drop: 1.0 μl of 1:2 diluted sample complex + 1.0 μl well solution, and well solution: 200 μl + 10.0 μl 50% PEG 3350; C → hanging drop: 1.0 μl of original sample complex + 1.0 μl well solution, and well solution: 750 μl of 1:2 diluted well solution; and D → hanging drop: 1.0 μl of 1:2 diluted sample complex + 1.0 μl well solution, and well solution: 750 μl of 1:2 diluted well solution.

complex + 1.0 μ l of well solution) (well solution = 750 μ l), we obtained single deep purple crystals (#7) that appeared 4–5 days after equilibration at 14°C and grew to maximum dimensions of 0.15 x 0.06 x 0.04 mm (figure 3.8.A) (#7). Using these crystals we were able to resolve the structure of the [TM][(Cu)(Cu-Atx1)₃] after the appropriate cryopreservation and data collection (2.3 Å) (Figure 3.8.B & C), as described in the experimental procedure.

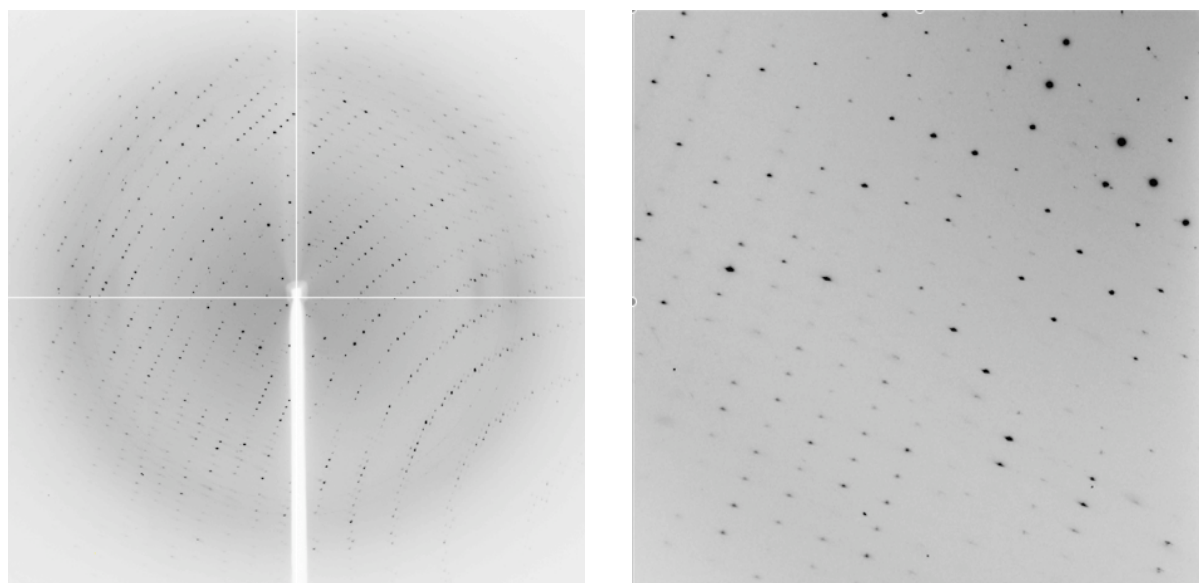
A brief overview of the crystallographic characterization of this complex is included in this chapter. More detailed information can be found in Yi Xue's thesis.

3.3.2 Protomer structure. The [TM][(Cu)(Cu-Atx1)₃] complex showed 12 Atx1 monomers per asymmetric unit ($\{[TM][(Cu)(Cu-Atx1)_3]\}_4$), forming two hexameric groups, which consist of two parallel layers of trimers related by a 3-fold non-crystallographic symmetry (NCS) axis (Figure 3.9). Analysis of this [TM][(Cu)(Cu-Atx1)₃] interaction suggested no detectable protein-protein interactions within the structure, only a few H-bonds and van der Waals contacts between the monomers of Atx1 were detected. For example, [TM][(Cu)(Cu-Atx1)₃] trimers (i.e. ABC) showed only 2 inter-chain H-bonds, between monomers A & C, and B & A, involving the Arg68 and Lys62 residues (Figure 3.10); and van der Waals contacts at the metal binding loop and the loop region between the α helix 2 and β strand 4.

3.3.3 [CuSMo] cluster and Multiple Anomalous Dispersion (MAD). The [TM][(Cu)(Cu-Atx1)₃] trimer (Figure 3.11) shows an innovative multinuclear 'nest-shaped' [CuSMo] cluster, where the [MoS₄] group (TM) is directly coordinated to 3 Cu atoms (the fourth Cu atom is coordinated to the 3 Cys 15 of 3 Atx1's) that are linked to the Atx1 proteins through the metal binding cysteines (Cys15 and Cys18) forming a [S₆Cu₄MoS₄] cluster (Figure 3.12). In this cluster the Mo atom was tetrahedrally coordinated by four S atoms (Mo–S distances range = 2.21~2.27 Å, average = 2.24 Å), and showed weak interactions with



A



B

C

Figure 3.8 A: Single crystals (#7) of [TM]((Cu)(Cu-Atx1)₃) for structure determination with approximate dimensions of 0.15 mm x 0.06 mm x 0.04 mm, well solution: 0.15 M DL-Malic acid pH 7.0 plus 20% PEG 3350. B & C: Diffraction pattern of [TM]((Cu)(Cu-Atx1)₃) at 2.3 Å.

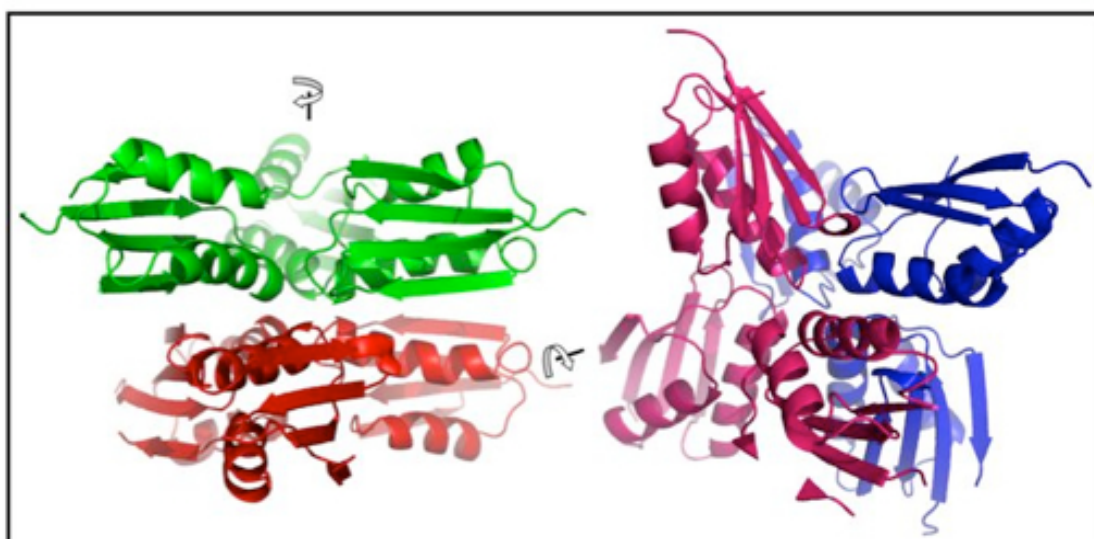


Figure 3.9 Overall structure of $\{[TM][(Cu)(Cu-Atx1)_3]\}_4$ showing two hexameric groups of Atx1, where each hexamer is composed of two parallel layers of $[TM][(Cu)(Cu-Atx1)_3]$ trimers related to each other by a 3-fold non-crystallographic symmetry (NCS) axis (arrows).

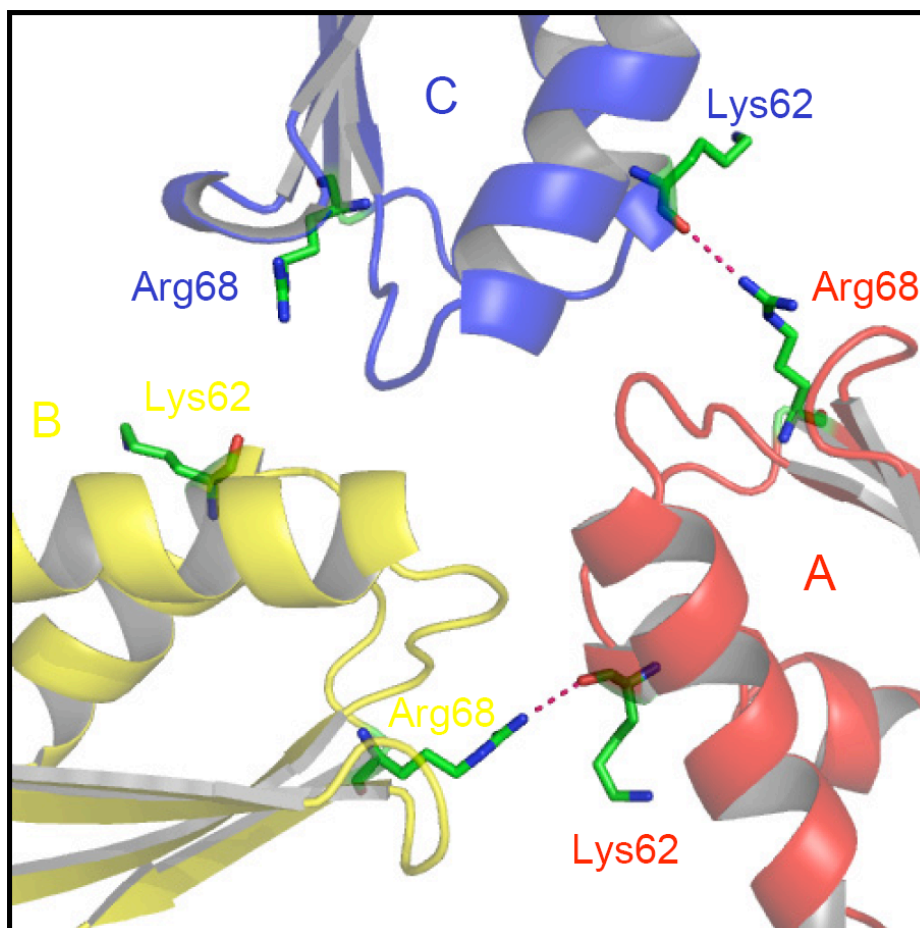


Figure 3.10 Inter-chain H-bonds (purple dashed line) of a $[TM]((Cu)(Cu-Atx1)_3)$ trimer (ABC), involving Arg68 and Lys62 between monomers B/A and A/C.

three Cu atoms (2.76 ~ 2.82 Å, 2.79 Å). Each of these Cu atoms assumed a distorted tetrahedral coordination surrounded by two S atoms from TM (2.28 ~ 2.45 Å, 2.31 Å) and two cysteines S atoms from Atx1 (2.27 ~ 2.48 Å, 2.31 Å). The fourth copper atom was located directly opposite to the TM, showing a trigonal planar coordination, being ligated by three S atoms (Cys15) of Atx1 (2.24 ~ 2.29 Å, 2.27 Å). A H-bond network (Figure 3.13) between 3 positively charged lysines (Lys65) and the sulfides from TM and the thiolates of Cys18 helped to neutralize the negative character of the $[\text{Cu}_4\text{MoS}_4]^{4-}$ cluster ($1 \text{ Mo}^{(6+)} + 4 \text{ S}^{(2-)} + 4 \text{ Cu}^{(1+)} + 6 \text{ Cys-SG}^{(1-)} = 4-$) (Cys18-S-Lys65 = 3.2 Å, TM-S-Lys65 = 3.6 Å, TM- μ_3 -S-Lys65 = 3.8 Å).

3.4 Discussion and Conclusion

In 1979, Mills suggested for the first time that TM forms complexes with copper and proteins.²¹ These TM-Cu-protein complexes were hypothesized to be involved in the ‘Teart’ and in the TM chelation therapy of the chronic copper poisoning (CCP), Wilson’s disease and cancer.

There are several spectroscopy studies of [CuTM] complexes; however our detailed protein x-ray crystallography study of the novel [TM][(Cu)(Cu-Atx1)₃] complex provides the first atomic level insight into any TM-Cu-protein interactions. This X-ray structure finally clarifies the stoichiometry and coordination environment of the previously suggested [TM][Cu-Atx1] XAS-model (Chapter 2), and the observed slightly higher [Cu]/[Mo] ratio ([Cu]/[Mo] = 3.4), revealing an unexpected fourth copper within the structure of the $[\text{S}_6\text{Cu}_4\text{MoS}_4]$ cluster, found at the core of this [TM][(Cu)(Cu-Atx1)₃] model complex. In addition, our model is in complete agreement with the proposed interaction characterized by XAS from the liver lysosomes of TM-treated LEC rats (animal model of Wilson’s disease),²² which suggests that our [TM][(Cu)(Cu-Atx1)₃] model may reflect how this drug will interact with Cu-proteins in vivo.

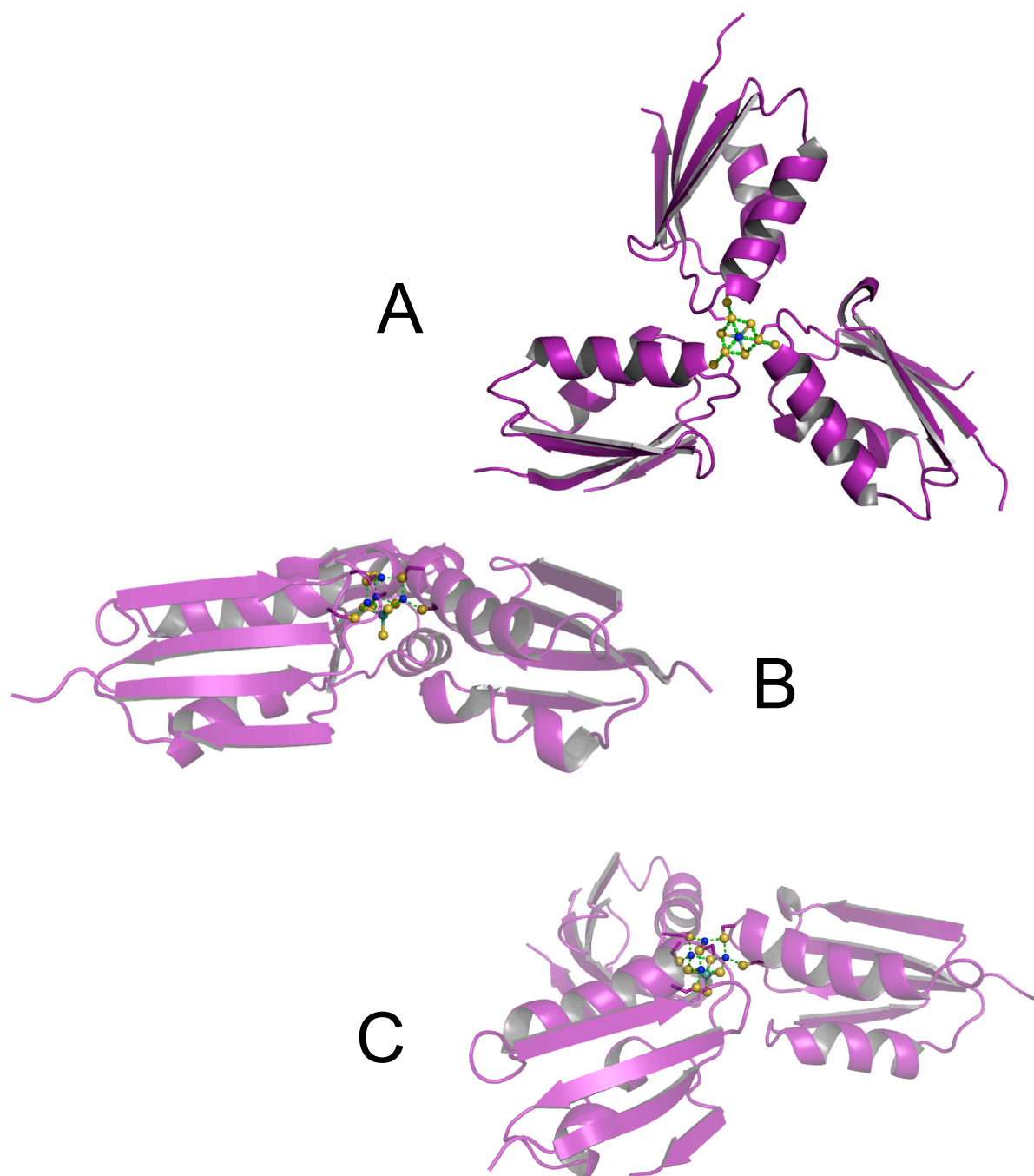


Figure 3.11 Structure of a [TM][(Cu)(Cu-Atx1)₃] trimer [(A) top view, (B) side view, & (C) tilted view] (Atx1 = purple cartoon ribbon diagram, Cu atom = blue sphere, S atom = yellow sphere, Mo atom = cyan sphere, & coordination bond = green dashed line).

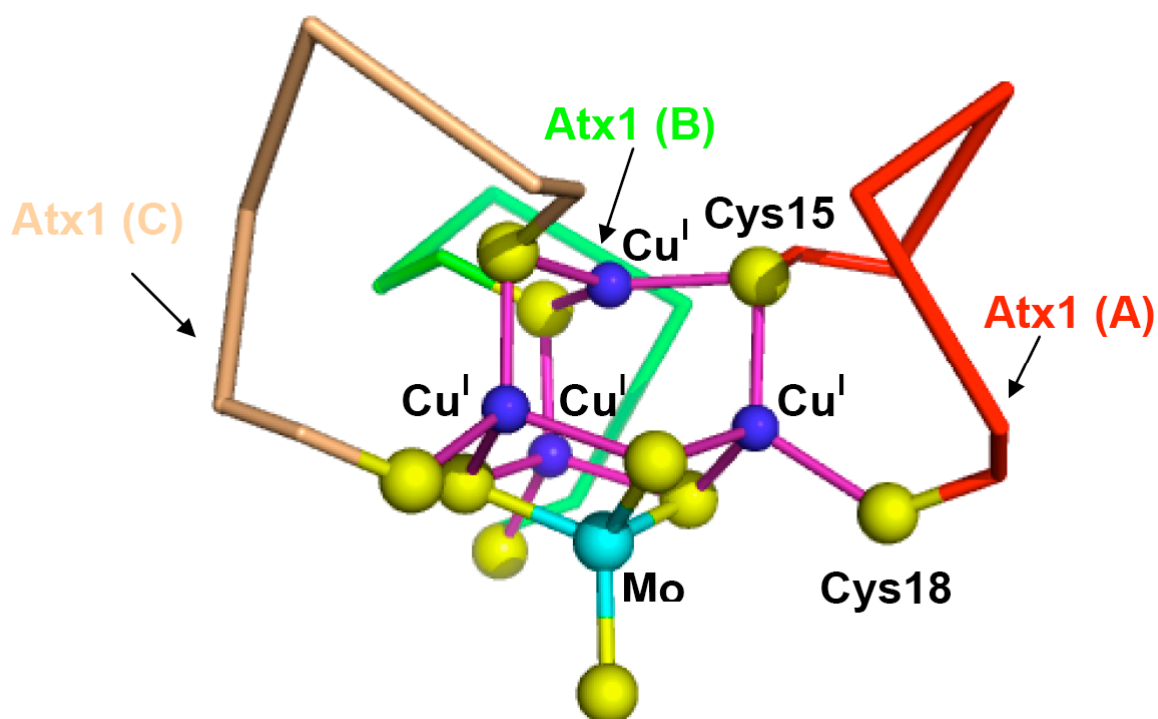


Figure 3.12 Structure of the ‘nest-shaped’ $[S_6Cu_4MoS_4]$ cluster in the $[TM] [(Cu)(Cu-Atx1)_3]$ trimer complex (Cu atom = blue sphere, Mo atom = cyan sphere, S atom from Cys15 (Atx1), Cys18 (Atx1) & TM = yellow sphere, S atoms from Cys15 & Cys18 of each of the 3 Atx1 are connected by a red, green and light pink lines).

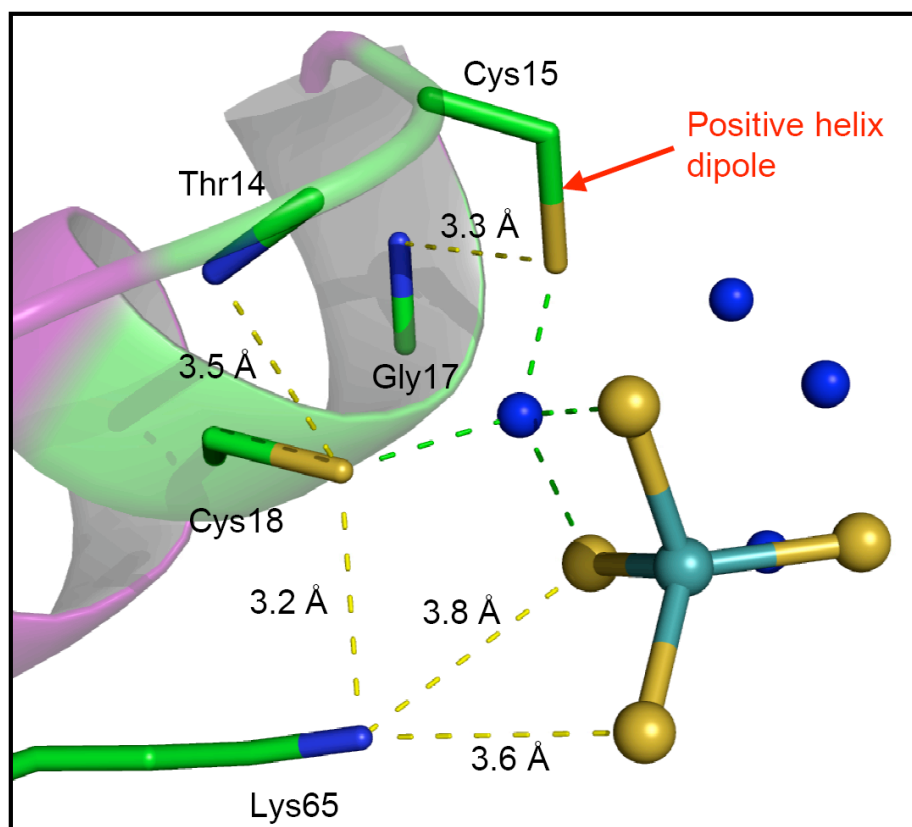
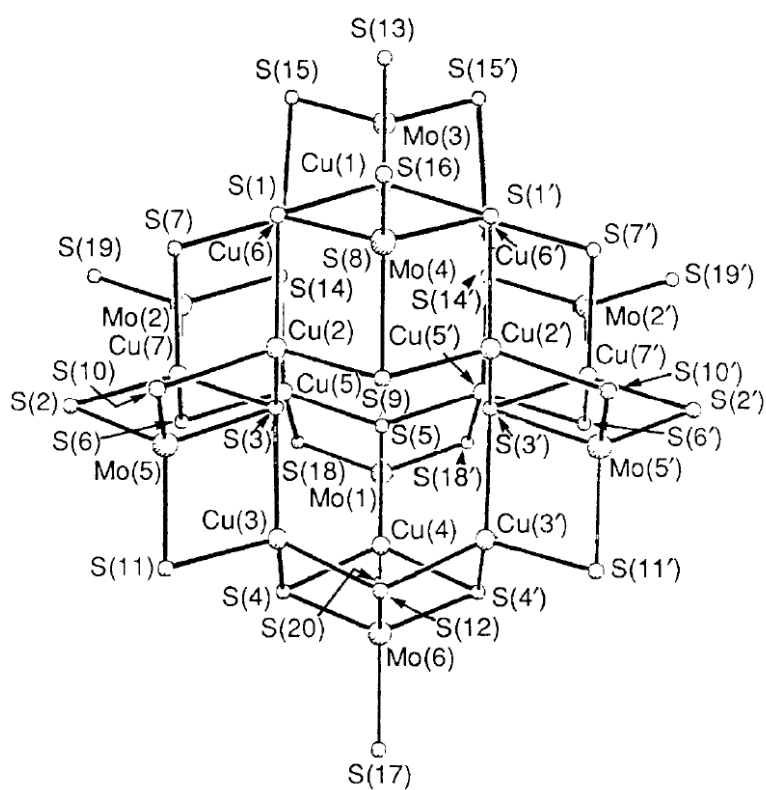


Figure 3.13 H-bond network (with Lys65, Thr14 and Gly17) and positive α helix 2 dipole, which help in the neutralization of the negatively charge $[\text{Cu}_4\text{MoS}_4]^{4-}$ cluster via interactions with sulfides of TM, and the thiolates of Cys 18 and Cys 15 (Cu atom = blue sphere, S atom = yellow sphere, Mo atom = cyan sphere, H-bond = yellow dashed line & Cu-S bond = green dashed line).

Several inorganic clusters (with P- and N-donor ligands) have been reported with a similar ‘nest-shaped’ $[\text{Cu}_3\text{MoS}_4]$ or $[\text{Cu}_3\text{MoS}_3\text{O}]$ cluster core centers.^{23,24} The closest molecular analogue of our protein-drug adduct was represented by the large $[\text{Bu}^n_4\text{N}]_4[\text{Cu}_{12}\text{Mo}_8\text{S}_{32}]$ complex with a $[\text{S}_6\text{Cu}_3\text{MoS}_4]$ metal cluster (Scheme 3.1), showing similar bond distances (Mo–Cu = 2.69 ~ 2.75 Å, Mo–S = 2.06~2.25 Å and Cu–S = 2.29~2.36 Å) to the ones found in $[\text{TM}][(\text{Cu})(\text{Cu-Atx1})_3]$.²⁵ Only one structurally-characterized $[\text{CuSMo}]$ complex has been described in the CO dehydrogenase, with a substantially different dinuclear $[\text{CuSMo}(=\text{O})\text{OH}]$ metal coordination core.²⁶

Scheme 3.1 Structure of the anion $[\text{Cu}_{12}\text{Mo}_8\text{S}_{32}]^{4-}$.²⁵



Here for the first time we successfully obtained the Cu form of Atx1 within the structure of the [TM][(Cu)(Cu-Atx1)₃] complex, where the highly exposed Cu^I (suggested by XANES)²⁷ is also bound by the two cysteines (Cys15 and Cys18) as seen in the Hg^{II}-Atx1 complex.¹⁹ The three primary Cu^I sites in the [TM][(Cu)(Cu-Atx1)₃] shows distorted tetrahedral coordination with bonds to two sulfurs from TM, and two cysteines from Atx1. The S-Cu-S bond angles range from 118 - 124°, while the Hg^{II} from the Hg^{II}-Atx1 shows a nearly linear coordination geometry with a S-Hg-S bond angle of 167°. Due to the fact that the S-Cu-S angle shows a value very close to 120°, we hypothesize that the Cu^I geometry is intermediate between trigonal and tetrahedral, which partially agrees with previous studies of Cu-Atx1 (without TM) by EXAFS²⁷ and NMR²⁸. Interesting, a recent computational simulation study of Cu-Atx1 proposed a nearly linear S-Cu-S bond with an angle of 166° in the absence of TM.²⁹

A superposition of the coordinates of Hg-Atx1 and the monomer B of [TM][(Cu)(Cu-Atx1)₃] (Figure 3.14) showed that the region around the metal binding loop are nearly identical, indicating that the binding of TM does not significantly affect the protein conformation. The average rms deviation for the main chain atoms is 0.6 Å, being of 0.56 Å for C_α positions, while Cys15 and Cys18 shift by 0.47 Å and 0.59 Å, respectively. They are only two regions with a large rms deviation: residues 40-41 (~ 1.4 Å) probably due to the interactions with monomers from adjacent trimers (red enclosures), and residues 27-28, 30-31 (~1 Å) (no obvious interactions contributed to the deviations) (green enclosures).

Finally, we can hypothesize that one of the possible pathways of the mechanism of action of TM (Cu-lowering therapy in Wilson's disease and cancer) can be the inhibition of the Atx1 metallochaperone by formation of the suggested [TM][(Cu)(Cu-Atx1)₃] complex, following a reaction shown in Scheme 3.2. In conclusion, this [TM][(Cu)(Cu-Atx1)₃] complex provides a

number of insights into the molecular mechanism of the therapeutic effects of TM, and may serve as a promising model to design more efficient and targeted TM-based drugs.

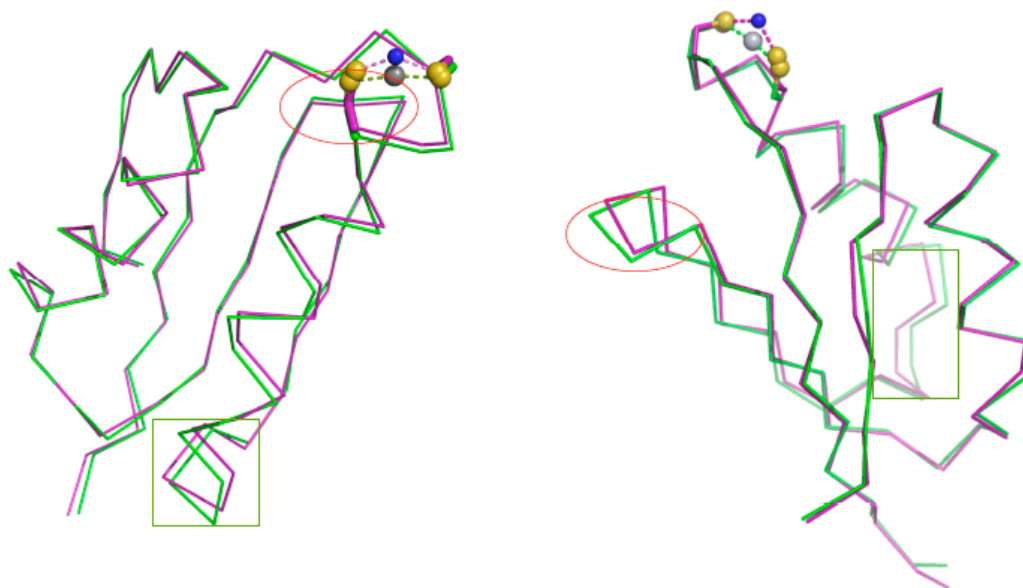
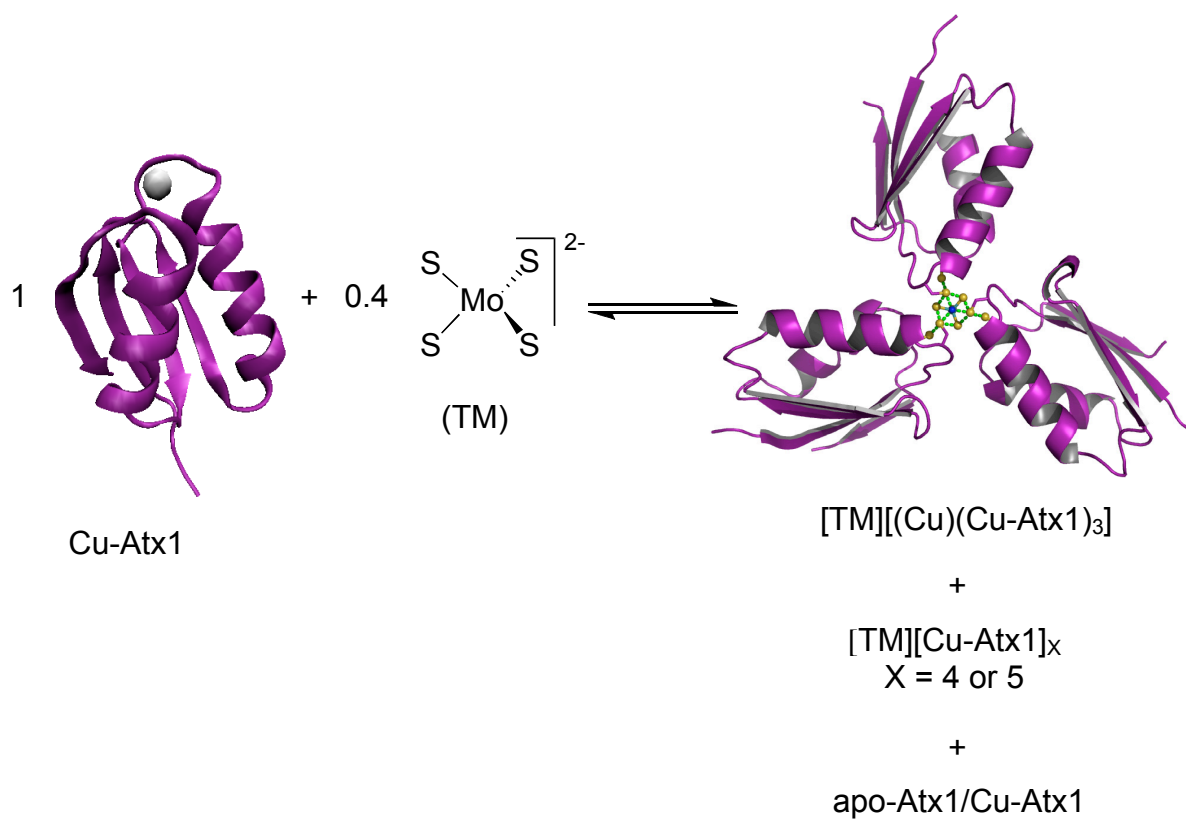


Figure 3.14 Superposition of Hg-Atx1 with the interaction of Cu-Atx1 monomer B from the [TM][Cu(Cu-Atx1)₃]. (Cu atom = blue sphere, S atom from Cys15 (Atx1) & Cys18 (Atx1) = yellow sphere, Hg atom = grey sphere, purple chain = Cu-Atx1, green chain = Hg-Atx1, residues 40-41 = red enclosures, residues 27-28, 30-21: green enclosures).

Scheme 3.2 Summary of TM reaction with Cu-Atx1.

Chapter 4

Solution Coordination Chemistry and Inhibition of the Bovine Superoxide

Dismutase (Cu, Zn-beSOD1) with TM

Abstract

Copper is involved in many intracellular trafficking pathways, which strength a proposed TM intracellular mechanism of action where the copper proteins will be potential targets of TM. In this Chapter we suggest that TM reacts quickly with the bovine Cu, Zn superoxide dismutase (SOD1). In contrast to the reaction with Cu-Atx1, we found that extended reaction of TM with SOD1 leads to the removal of one of the tightly bound coppers and the formation of a $[\text{CuTM}]_x$ polymeric complex, which was characterized by ultrafiltration, native gel electrophoresis/gel extraction, UV-Vis, gel filtration chromatography and XAS. Moreover, the ability of TM to inhibit SOD1 was confirmed by a native activity gel and UV-VIS spectroscopy assay with a maximal $\text{IC}_{50} = 2.51 \mu\text{M}$.

The reactivity and inhibitory capacity of TM against SOD1, not only validate this copper protein as a possible therapeutic target of this new copper chelation therapy, but also reveals that the interaction mode of TM with this protein is quite different from the one observed for Cu-Atx1. These results suggest that copper proteins may have variable pathways as part of the intracellular mechanism of action of this drug.

4.1 Introduction

Copper, zinc superoxide dismutase (SOD1) is a highly expressed homodimer protein of 32 kDa, which catalyzes a two-step dismutation of the toxic superoxide radical through the reduction and oxidation of the copper site, located at the bottom of a high positively-charged deep channel.^{1,2} Currently, SOD1 is considered as a promising target for the inhibition of angiogenesis. This is based on the observation that the overexpression of SOD1 stimulates the VEGF production, and increases the ability of endothelial cells to confront high levels of ROS during angiogenesis.^{3,4}

It was shown long ago that different small compounds can be used as O_2^- competitors for the binding of copper at the catalytic site of superoxide dismutase [cyanide (CN^-), hydroxyl ion (OH^-), azide (N_3^-), among others].^{5,6} Due to the high toxicity of these chemicals and their limited medical applications, alternative approaches have been studied. Between 1979 and 1999, Misra and Wambi Kiese, discovered that a heavy metal chelator drug initially used for treatment of chronic alcoholism, called Disulfiram [DSF, active form of DSF = diethyldithiocarbamate (DCC)] inhibits pure SOD1 and SOD1 isolated from canine basilar arteries by removing copper from its active site.^{7,8} In 2000, Haung proposed the use of a different kind of SOD1 inhibitor called 2-Methoxyoestradiol (2-ME), which induces apoptosis in human leukemia cells by causing damage to mitochondrial membranes.⁹ Two years later, Marikovsky demonstrated that DSF can induce apoptosis by inhibiting angiogenesis in endothelial cells from a transgenic mouse model with SOD1 overexpression.⁴

In 1984, Chidambaram was the first to propose that TM causes the intracellular inhibition of SOD1 in a cytoplasmatic extract of human red blood cells (RBC) with a IC_{50} of 5.0 μM . Other copper enzymes are also inhibited by TM, including ascorbate oxidase ($IC_{50} = 1.0 \mu M$),

cytochrome oxidase ($IC_{50} = 2.0 \mu\text{M}$), tyrosinase ($IC_{50} = 3.0 - 4.5 \mu\text{M}$), ceruloplasmin ($IC_{50} = 2.7 - 3.0 \mu\text{M}$)]¹⁰ Much more recently, Juarez suggested that choline tetrathiomolybdate (ATN-224[®]) inhibited pure beSOD1 ($IC_{50} = 0.33 \mu\text{M}$).¹¹ Intracellular SOD1 inhibition was also reported in human umbilical vein endothelial cells (HUVEC, $IC_{50} = 0.02 \mu\text{M}$), and multiple myeloma cells (MM1S, $IC_{50} = 0.04 \mu\text{M}$).¹¹ In Chapter 5, TM is shown to inhibit intracellular human SOD1 in cytoplasmic extracts of hepatocellular carcinoma cells (HEPG2, $IC_{50} = 0.31 \mu\text{M}$).¹²

Here we provide a detailed view of the in-vitro molecular characterization of the interaction between TM and beSOD1. These results confirm the initial TM inhibition of SOD1 and suggest the 50% removal of copper from the buried SOD1 active site by formation of a $[\text{CuTM}]_x$ polymeric complex. This leads to conclude that the structural differences of the copper binding sites in SOD1 and Atx1 exhibit different reactivities with TM, which represents two possible pathways of how this metallodrug react with copper proteins. These results support SOD1 as one of the most encouraging targets for the inhibition of angiogenesis.

4.2 Experimental Procedures

4.2.1 Synthesis and characterization of ammonium tetrathiomolybdate. As described by Mellor¹³ and Laurie¹⁴, ammonium tetrathiomolybdate was synthesized and characterized by ⁹⁵Mo NMR data (in D₂O): δ 2260 ppm (s), IR data (cm⁻¹): 3125 (sh), 2360 (w), 2336 (w), 1384 (m), 835 (w) and UV/Vis [H₂O, λ_{max} (nm), $\epsilon \times 10^{-3}$ (M⁻¹ cm⁻¹): 241 (23.3), 317 (16.1), 468 (11.1).

4.2.2 Preparation and purification of protein samples. Lyophilized beSOD1 (~99% Biuret) isolated from bovine erythrocytes was purchased from Sigma Aldrich (St. Louis, MO). Purity was confirmed by gel electrophoresis and electrospray mass spectrometry (ESI-MS of monomer): $m/z^{\text{obs}} = 15591.8$, $m/z^{\text{calc}} = 15600.0$.

4.2.3 Ultrafiltration. Ultrafiltration studies were performed using a centrifugal filter device (MICROCON) with a MW cut-off membrane of 3 kDa (Millipore, Bedford, MA). 250 μ L of a mixture of 0.5 mM Cu,Zn-beSOD1 plus TM (1:1) was loaded into the Microcon-3 at 4°C and placed in a Fisher Scientific Marathon 16 Km centrifuge at 10,000 rpm for 30 min. Unreacted TM was washed away using 3 ultrafiltration cycles of 50 mM NaPi, pH = 7.3. Cu and Mo concentrations in the final protein solution were determined by ICP-OES (Table 3.1). The protein concentration of Cu, Zn-beSOD1 was determined for the same sample by quantitative amino acid hydrolysis (Protein Chemistry Laboratory, Texas A & M University) and later by Bradford assay (Bio-Rad, with IgG calibration standard) and with a calculated extinction coefficient $\epsilon_{280} = 1490 \text{ M(monomer)}^{-1}\text{cm}^{-1}$ from the Edelhoch method.¹⁵ Comparison of protein concentrations revealed that both the Bradford assay and the absorption at 280 nm overestimated the concentration of the Cu, Zn-beSOD1 by 2.17 and 3.12 fold respectively. These correction factors were then used routinely for the analysis of Cu, Zn-beSOD1 protein concentration.

4.2.4 UV-visible spectroscopy. Absorption spectra (λ : 200 – 700 nm) were recorded at 25°C using a Cary 300 Bio UV-Visible spectrophotometer using quartz cuvettes (teflon stoppers) with a 1 cm path length and 1 ml cell volume. UV-visible spectra of 0.08 mM Cu,Zn-beSOD1, 0.08 mM Cu, Zn-beSOD1 plus TM (1:1), 0.08 mM TM, and 0.08 mM $\text{CuSO}_4 \cdot 5\text{H}_2\text{O}$ plus TM (1:1) were recorded after 30 min of reaction.

4.2.5 UV-Vis Titration spectroscopy. To a 38.4 μ M solution of TM (50 mM NaPi, pH = 7.3) were added 3.84 μ l aliquots of a 0.5 mM Cu, Zn-beSOD1 solution at 25°C. Upon each addition, the sample solution was stirred for 10 min with a magnetic stirring device and the UV-visible spectrum was subsequently measured and corrected for dilution.

4.2.6 Protein gel extraction. Cu, Zn-beSOD1 and Cu, Zn-beSOD1 plus TM (1:25) mixture ($[\text{SOD1}]_f = 0.55 \text{ mM} \sim 170 \text{ } \mu\text{gs}$, in 50 mM NaPi, pH = 7.3) were separated by native-PAGE in 4-15% gradient Tris-HCl ready gels (Bio-Rad, Hercules, CA). The samples were dissolved in Laemmli buffer (no DTT), boiled at 95°C and ran at a constant voltage of 150 V, without any further staining. Controls (one per sample) were stained using Coomassie blue to determine the proper band migration for the gel extraction procedure. Protein bands were cut from the gel, incubating each of them in 1 ml of an extraction buffer solution composed of 0.1 M NaPi pH 7.3, 2 mM EDTA, and 100 mM NaCl, allowing the protein to passively elute by diffusion for 48 h at 37°C with shaking at 180 rpm using a series 25 incubator shaker from New Brunswick Scientific (Edison, NJ). The protein gel extracts were then centrifuged (using a Marathon 16 km microcentrifuge from Fisher Scientific) to isolate the supernatant for further analysis. Finally, the Cu, Zn, Mo and protein concentrations of the supernatant were measured by ICP-OES and Bradford assay, and UV-Visible spectra were recorded using conditions described later.

4.2.7 Copper depletion studies. To measure copper depletion from this protein, 0.5 mM Cu, Zn-beSOD1 samples (1.5 ml, 50 mM NaPi, pH 7.3) were incubated with different concentrations of TM at 4°C for 30 min in aerobic conditions and separated by size exclusion chromatography using PD10 rapid gel filtration columns (matrix excludes solutes bigger than 6 kDa) (Bio-Rad, Hercules, CA). Cu, Zn, Mo and protein concentrations of the initial mixtures and of the collected eluates after PD-10 gel filtration were determined using ICP-OES and Bradford assay, respectively. Data were fitted using IGOR Pro Version 4.07 software (WaveMetrics, Inc., Lake Oswego, OR).

4.2.8 Electrophoresis: SDS-PAGE. For analysis using SDS-PAGE, Cu, Zn-beSOD1

and Cu, Zn-beSOD1 plus TM ($[SOD1]_f = 0.022$ mM) samples were separated on a 12% polyacrylamide Tris-HCl gel with 5.4% polyacrylamide stacking gel. Samples were incubated with different concentrations of TM anaerobically. Samples were dissolved in Laemmli buffer with or without DTT and boiled at 95°C for 2 min before loading. The gels were run at a constant voltage of 150V, and then separated proteins were stained by Coomassie blue.

4.2.9 Electrophoresis SOD1 activity assay. SOD1 activity was monitored with a nondenaturing gel electrophoresis. Cu, Zn-beSOD1 samples (250 ng in 50 mM NaPi, pH 7.3) were incubated with different concentrations of $[MoS_4]^{2-}$ and $[MoO_2S_2]^{2-}$ at 4 or 37°C for 1 or 48 h in aerobic conditions. Proteins were separated by in 4 - 15% gradient Tris-HCl ready gels (Bio-Rad, Hercules, CA) at a constant voltage of 150 V and stained by riboflavin, nitro-blue tetrazolium (NBT) and TEMED.¹⁶ After 15 min incubation in the dark and illumination, the gels become purple-blue except at the positions containing active SOD1. These SOD1 bands were subjected to densitometric tracings by using the Kodak DC-120 camera with a Kodak 1D 2.0.2 software (H. Godwin's Lab). Integrated density of pixel intensity was recorded, and transformed to %SOD1 activity by a 2-point calibration curve using 2 standards: pure SOD1 (internal achromatic zone, 100% SOD1 activity) and a background area (internal purple-blue zone, 0% SOD1 activity). This technique was also used to analyze the SOD1 activity of the eluate fractions during copper depletion studies.

4.2.10 UV-visible spectroscopy SOD1 activity assay. SOD1 activity was also assayed by measuring the inhibition of reduction of the water-soluble tetrazolium salt, WST-1: 2-(4-iodophenyl)-3-(4-nitrophenyl)-5-(2,4-disulfido-phenyl)-2H-tetrazolium monosodium salt, which produces a water-soluble diformazan dye (WST-1D, $\lambda_{max} = 450$ nm) on reduction with a superoxide anion (Dojindo Molecular Technologies Inc., Gaithersburg, MD) (Scheme 4.1).

Superoxide anion is generated by xanthine, O₂ and xanthine oxidase; and Cu, Zn-beSOD1 was used to generate a standard curve (Sigma Aldrich, St. Louis, MO) (Figure 4.1). The %SOD1 activity for the inhibition of Cu, Zn-beSOD1 with TM and the standard curve, was calculated using the manufacturer's instructions and the following equation,

$$\% \text{ SOD1 activity } (\sim \% \text{ inhibition WST-1 D}) = [(A_{B1} - A_{B3}) - (A_{\text{SAMPLE}} - A_{B2}) / (A_{B1} - A_{B3})] \times 100$$

where, A_{SAMPLE}: Abs of mixture of sample + WST-1 + xanthine + xanthine oxidase (XO), A_{B1}: Abs of mixture of WST-1 + xanthine + XO, A_{B2}: Abs of mixture of sample + WST-1, A_{B3}: Abs of mixture of WST-1. Data were fitted to a sigmoidal function and presented as mean ± SD (n = number of separate experiments) using IGOR Pro Version 4.07 software (WaveMetrics, Inc., Lake Oswego, OR). This technique was also used to calculate the %SOD1 activity of the eluate fractions during copper depletion studies.

4.2.11 Preparation of XAS samples. Duplicate samples were prepared for XAS analysis. The (Cu, Zn-beSOD1 + TM) sample was prepared using a mixture of approximately 890 µl of a 3.0 mM Cu, Zn-beSOD1 plus TM (1:1) (t_{rxn} = 30 min, aerobic conditions) (50 mM NaPi, pH = 7.3). The mixture solution was concentrated to approx. 100 µL using a centrifugal filter device with a MW cut-off membrane of 3 kDa (MICROCON). Unreacted TM was washed away using 3 ultrafiltration cycles (10, 000 rpm, 30 min) of the appropriate buffer. The [SOD1] = 3.4 mM, [Cu] = 2.8 mM and [Mo] = 2.3 mM ([Cu]:[Mo] = 1.2; [Cu]:[SOD1] = 0.8; [SOD1]:[Mo] = 1.5). Glycerol was added to a final concentration of 30%. Both samples were transferred to XAS cuvettes (Lucite body with Kapton windows), frozen in N₂(l) at – 20°C and stored at – 80°C until XAS measurements were made. The protein concentration was measured by the Bradford assay and Cu, Mo concentrations by ICP-OES.

Scheme 4.1 Principle of the WST-1 UV-Visible spectroscopy SOD1 activity assay.

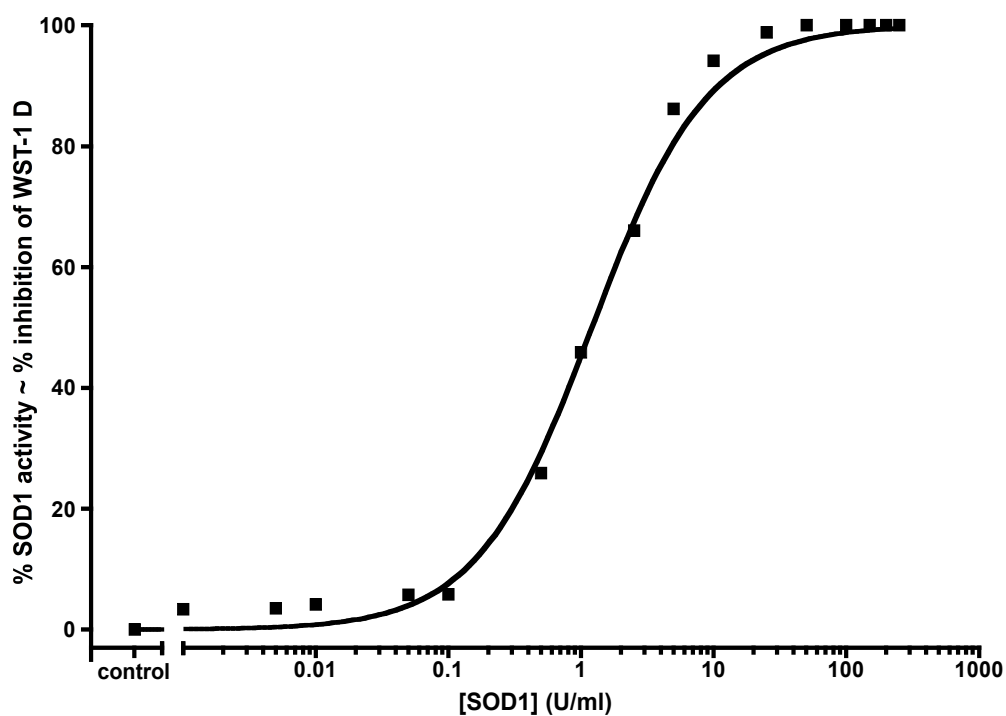
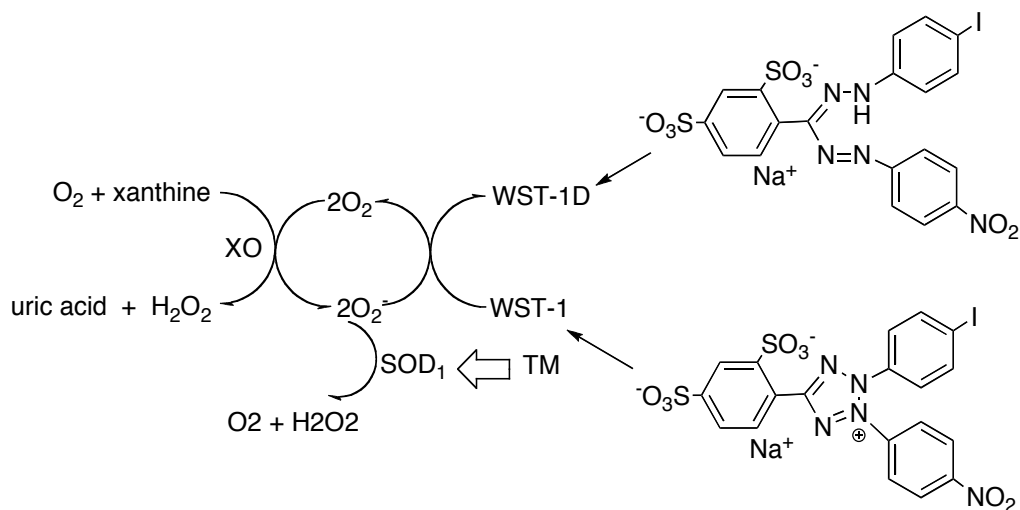


Figure 4.1 Cu, Zn-beSOD1 inhibition calibration curve using WST-1 UV-Visible spectroscopy SOD1 activity assay. One SOD1 unit is defined as a point where a sample gives 50% inhibition of the colorimetric reaction between the reactive dye (WST-1) and O_2^- (generated by the mixture of xanthine, XO and O_2).

4.2.12 X-ray absorption data collection and analysis. Frozen samples were sent to out collaborators. Data collection and analysis for this experiment was performed and analyzed by Dr. Rebekah Kelly and Prof. James Penner-Hahn. A brief account of their conclusions follows here. The Cu K-edge data were collected at SSRL on beamline 9-3 (3 GeV, ~ 90 mA), using a Si(220) double-crystal monochromator with a Rh-coated mirror upstream for harmonic rejection. Incident intensity was measured using an N_2 -filled ion chamber. Fluorescence data was collected using a 30-element Ge solid-state detector array. The sample temperature was held at 12 K in an Oxford liquid helium flow cryostat during the measurements. The total integrated count rate was held below 90 kHz to avoid saturating the detector, and the average windowed fluorescence count rate was ~ 7 -12 KHz per channel in the EXAFS region. Each scan had 10 eV increments prior to the edge (8780 - 8970 eV), 0.5 eV increments for the pre-edge and edge region (8970 - 9020 eV), 0.05 \AA^{-1} increments for two EXAFS regions (2.29 – 13.1 \AA^{-1}) with integration times of 1 s in the pre-edge and edge regions and 1-10 s (k^3 weighted) in the EXAFS for a total scan time of ~ 35 minutes. Energy calibration was done using a Cu(s) foil as an internal standard, with the first inflection point of the foil defined as 8980 eV. For all samples each detector channel was checked for glitches and all good channels (~ 20 -24) were averaged and were calculated using 3 scans for Cu,Zn-beSOD1. XANES data were normalized by fitting the data to the McMaster absorption coefficients below and above the edge using a single background polynomial and scale factor.^{17,18} The EXAFS background correction was performed by fitting a three-region quartic spline for all the copper samples. Fourier transforms were calculated using k^3 weighted data over a range of 1.13 – 13 \AA^{-1} for both the copper samples. The data were then converted to k -space using

$$k = \sqrt{\frac{2m_e(E - E_0)}{\hbar^2}} \quad \text{where } E_0 = 9000 \text{ eV.}$$

EXAFS data can be described by following equation, where $c(k)$ is the fractional modulation, in the absorption coefficient above the edge, N_s is the number of scatterers at

$$\chi(k) = \sum_s \frac{N_s S_s(k) A_s(k)}{k R_{as}^2} \exp(-2k^2 \sigma_{as}^2) \exp\left(\frac{-2R_{as}}{\lambda}\right) \sin(2k R_{as} + \phi_{as}(k))$$

a distance R_{as} , $A_s(k)$ is the backscattering amplitude, σ_{as}^2 is the root-mean-square variation in R_{as} , $\phi_{as}(k)$ is the phase shift experienced by the photoelectron wave in passing through the potentials of the absorbing, l is the mean free path of the photoelectron and backscattering atoms, and $S_s(k)$ is a scale factor specific to the absorber-scattering pair and the sum is taken over all scattering interactions.¹⁹ The program FEFF v7.02²⁰ was used to calculate amplitude and phase functions, $A_s(k)\exp(-2R_{as}/l)$ and $\phi_{as}(k)$ for a copper-sulfur interaction at 2.26 Å, a copper-molybdenum interaction at 2.70 Å and a copper-copper interaction at 5.40 Å. E_0 was initially set at 9000 eV and S_s , was fixed at 0.89.

Mo K-edge data was collected as described above with the following exceptions. The total integrated count rate was held below 90 kHz to avoid saturating the detector, and the average windowed fluorescence count rate was ~ 2-7 KHz per channel in the EXAFS region. Each scan had 10 eV increments prior to the edge (19788 - 19988 eV), 0.3 eV increments edge region (19989 - 20030 eV), 0.05 Å⁻¹ increments for two EXAFS regions (1.62 – 16.1 Å⁻¹) with integration times of 1 s in the pre-edge and edge regions and 1-20 s (k^3 weighted) in the EXAFS

region for a total scan time of ~ 26 minutes. Energy calibration was done using a Mo(s) foil as an internal standard, with the first inflection point of the foil defined as 20003 eV. For all samples each detector channel was checked for glitches and all good channels (25) were averaged and were calculated using 4 scans for Cu, Zn-beSOD1. XANES data were normalized by fitting the data to the McMaster absorption coefficients below and above the edge using a single background polynomial and scale factor^{17,18} The EXAFS background correction was performed by fitting a three-region quartic spline for all the cobalt samples. Fourier transforms were calculated using k^3 weighted data over a range of 1-15.5 \AA^{-1} for all the molybdenum samples. EXAFS fits were performed as described above with the following exceptions. The program FEFF v7.02²⁰ was used to calculate amplitude and phase functions, $A_s(k)\exp(-2R_{as}/l)$ and $f_{as}(k)$ for a molybdenum-sulfur interaction at 2.21 \AA , a molybdenum-copper interaction at 2.70 \AA . Multiple scattering interactions were calculated based on crystallographic parameters of a model in which Mo was ‘sandwiched’ by two Cu scatters ligated by sulfur between Mo and Cu.²¹ E_0 was initially set at 20020 eV and S_s , was fixed at 0.9.

4.3 Results

4.3.1 Ultrafiltration. Ultrafiltration studies of Cu, Zn-beSOD1 + TM (1:1) showed similar results as with the Cu-Atx1 (Chapter 2). The copper, molybdenum and protein were retained again in the supernatant fraction after centrifugation (Table 4.1), confirming the proposed interaction between TM and Cu, Zn-beSOD1, which will be later identify as the partial removal of copper and formation of a $[\text{CuTM}]_x$ polymeric complex.

Table 4.1. Mass balance of protein, Cu, and Mo during ultrafiltration experiments^a.

		Reaction Mixture mmoles ^a	Supernatant Fraction mmoles ^a	Eluate Fraction mmoles ^a
Cu,Zn- beSOD1 + TM	SOD1	1.25×10^{-4}	1.14×10^{-4}	----
	Cu	9.60×10^{-5}	9.12×10^{-5}	0.38×10^{-5}
	Mo	9.60×10^{-5}	7.68×10^{-5}	1.80×10^{-5}

^anumber of mmols (Cu, Mo and protein) calculated before and after ultrafiltration in supernatant and eluate fractions.

4.3.2 UV-Visible Spectroscopy. UV-visible spectra revealed that addition of TM to either Cu, Zn-beSOD1 or $\text{CuSO}_4 \cdot 5\text{H}_2\text{O}$ yields similar spectral features, suggesting the formation of a [Cu-TM] interaction, which will be later identified as a $[\text{CuTM}]_x$ polymer complex (Figure 4.2). When different proportions of Cu, Zn-beSOD1 and TM were mixed in buffered solutions during a titration monitored by UV-visible spectroscopy, the loss of the characteristic S—Mo ligand to metal charge transfer bands (LMCT) ($t_1 \rightarrow 4t_2$; $\lambda = 241 \text{ nm}$, $3t_2 \rightarrow 2e$; $\lambda = 317 \text{ nm}$, $t_1 \rightarrow 2e$; $\lambda = 467 \text{ nm}$) of TM was observed (Figure 4.3.A). Addition of TM lead to a broadening of the spectrum with the formation of two shoulders with λ_{max} around 350 and 512 nm, which are the result of the shifting of the S—Mo LMCT bands due to the new coordination with a copper center [Cu—S—Mo]. These changes are indicative of the previously suggested $[\text{CuTM}]_x$ polymeric complex. Titration of TM with $\text{Cu}^{(\text{II})}$ ($\text{CuSO}_4 \cdot 5\text{H}_2\text{O}$) salt showed similar results to those obtained for the SOD1 system (data not shown). Shifting of the UV-visible S—Mo LMCT bands due to coordination with Cu reveals that TM reacts with this copper protein (Cu, Zn-beSOD1) perhaps leading to the formation of a $[\text{CuTM}]_x$ polymeric complex.

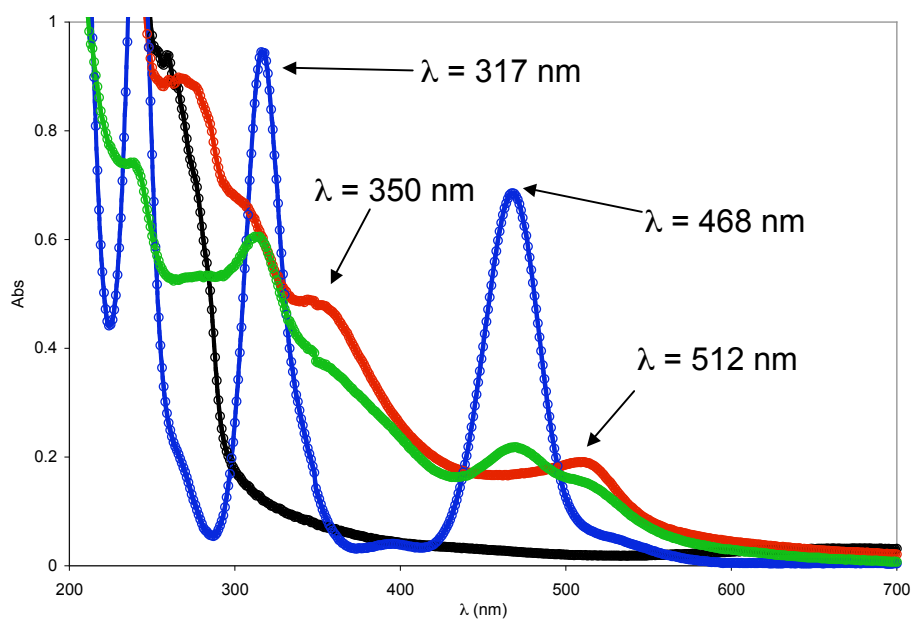


Figure 4.2. UV-visible absorbance of 0.08 mM Cu, Zn-beSOD1 (○), 0.08 mM Cu, Zn-beSOD1 + TM (1:1) (○), 0.08 mM TM (○), 0.08 mM CuSO₄•5H₂O + TM (1:1) (○), after reaction for 30 min (20 mM MES, pH = 6.0, 0.15 M NaCl, 25°C, aerobic conditions).

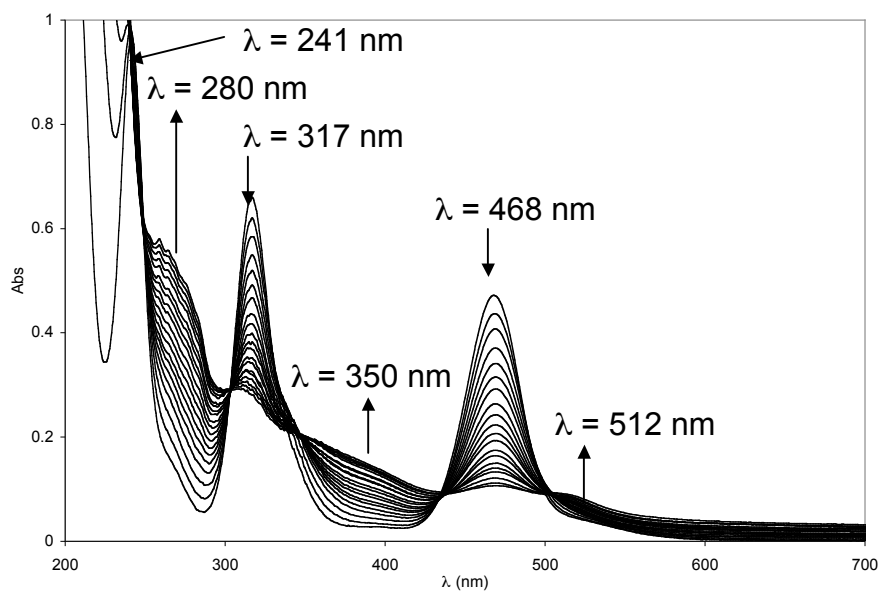


Figure 4.3 UV-visible absorbance of TM as a function of Cu, Zn-beSOD1 concentration. 38.4 μ M of TM was titrated with 0 – 2.0 equiv of 0.5 mM Cu, Zn-beSOD1 (50 mM NaPi, pH = 7.3, 25°C, aerobic conditions).

4.3.3 Protein gel extraction. Native gel extraction studies (Figure 4.4) resulted in the recovery of $\sim 10\%$ of the loaded SOD1 (extraction protocol is described in the experimental procedures section). The gel extract of pure SOD1 band (Figure 4.4.A) showed the characteristic UV-visible spectrum with a maximum at 280 nm (Tyr) while the Bradford assay and ICP-OES detected the presence of protein, Cu and Zn ([SOD1] = 37.8 μM , [Cu] = 15.2 μM , and [Zn] = 18.0 μM) (Figure 4.4.C and Table 4.2). The SOD1 plus TM (25X excess) mixture produces two bands: one characteristic of the protein, and one unknown at the bottom of the gel (Figure 4.4.B). The gel extract of the SOD1 band (mixture) showed again the characteristic UV-visible spectrum with a maximum at 280 nm and protein/metal concentrations of [SOD1] = 31.0 μM , [Cu] = 1.85 μM , [Zn] = 13.7 μM and [Mo] = 2.6 μM . The gel extract of the unknown band (brown colored) showed two S—Mo LMCT bands at λ_{max} of 350 and 512 nm, and protein/metal concentrations of [SOD1] = 2.9 μM , [Cu] = 70.2 μM , [Zn] = 1.18 μM and [Mo] = 126 μM (Figure 4.4.C and Table 4.2). These results suggested that the reaction of SOD1 and TM is producing two products, a SOD1 fraction with a very low concentration of copper that can be identified as a Cu, Zn₂-beSOD1 (dimer) and a second fraction with almost no zinc or protein, which can be identified as a [CuTM]_x polymeric complex, which was already suggested by ultrafiltration and UV-visible spectroscopy studies.

4.3.4 Copper Depletion. The protein products produced by the reaction of TM with Cu, Zn-beSOD1 could not be sufficiently characterized by analytical gel filtration, as no high molecular weight complexes were isolated. A copper depletion experiment showed that different amounts of TM ([TM]:[SOD1] = 0 – 5) are able to produce a partial removal of copper from Cu, Zn-beSOD1. TM is taken out approximately 50% of the original copper content in the protein. Additional depletion of copper from SOD1 was not observed when [TM]:[SOD1] > 5

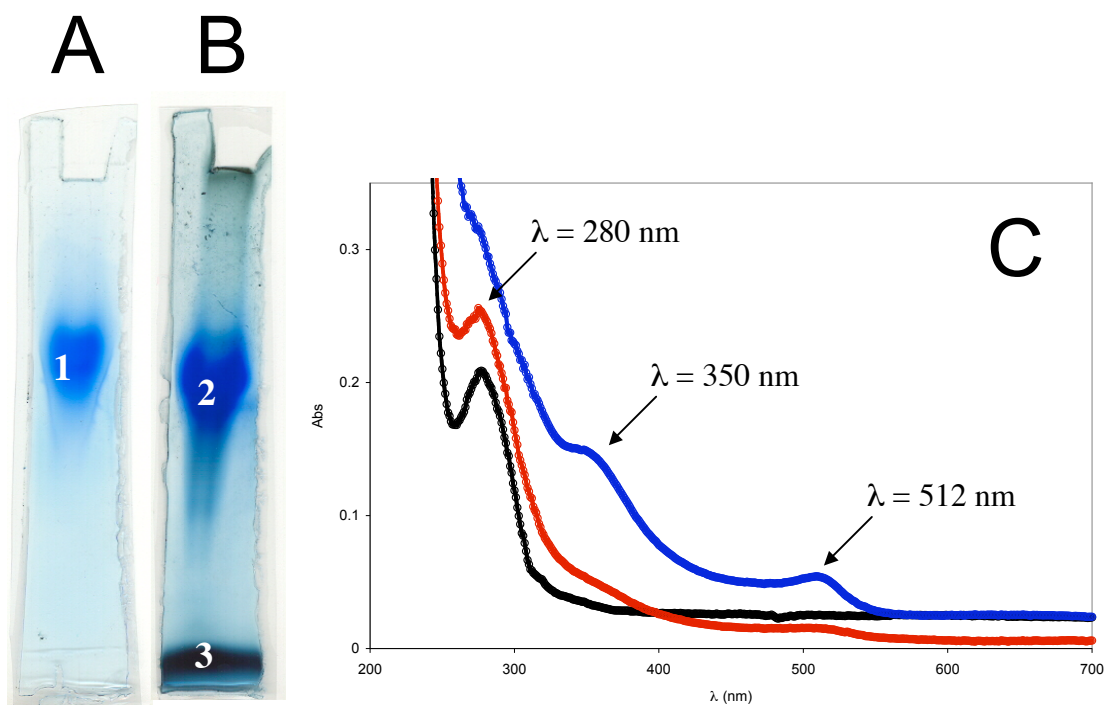


Figure 4.4 SOD1 gel extraction. A. 4-15% NATIVE-PAGE of 0.55 mM Cu, Zn-beSOD1 (1: SOD1 band); B. 4-15% NATIVE-PAGE of 0.55 mM Cu, Zn-beSOD1 + TM (1:25) (2: Cu, Zn₂-SOD1 (dimer) band and 3: [CuTM]_x band); C. UV-Visible spectra of gel extracts [1. Cu, Zn-SOD1 (○), 2. Cu,Zn₂-beSOD1 (dimer) (○), 3. [CuTM]_x (○)].

Table 4.2 Metal and protein concentration table of gel extracts (μM).

	[SOD1]	[Zn]	[Cu]	[Mo]
[SOD1]	37.8	18.0	15.2	----
[Cu, Zn ₂ -SOD1]	31.0	13.7	1.85	2.60
[CuTM] _x	2.9	1.18	70.2	126

were tested (data not shown). No significant Mo content was detected in any protein fractions. The Zn concentration remained constant even when significant amounts of TM were used, indicating that TM does not affect the Zn content of the SOD1 (Figure 4.5.1). Native gel electrophoresis followed by in-gel nitro blue tetrazolium (NBT)¹⁶ in conjunction with a UV-visible spectroscopy assay for SOD1 activity revealed that the activity of the TM treated SOD1 eluate-samples decreased when higher amounts of TM were used, going from 93.5 % ([TM]:[SOD1] = 1.0) to 25.1% ([TM]:[SOD1] = 25.0) (Figure 4.5.2). TM may inhibit SOD1 by removing copper (0.5 Cu of SOD1 per monomer or 1.0 Cu of dimeric SOD1) and sequestering it as a [CuTM]_x polymeric complex, whose existence will be suggested later by XAS spectroscopy (for inhibition studies see section 4.3.6 of this Chapter).

4.3.5 Electrophoresis: SDS-PAGE. According to the previous experiments, the reaction of TM with Cu, Zn-beSOD1 produced the formation of a [CuTM]_x polymeric complex and a hypothetical Cu, Zn₂-beSOD1 (dimer). SOD1 is a homodimer of 31.2 kDa with unusual non-covalent stability, resistant to dissociation by different agents as urea or guanidinium chloride with EDTA. It was already hypothesized that metal binding sites and the intramolecular disulfide are contributors to the stability of this dimer. Using SDS-PAGE we analyzed the effect of TM and copper removal on the homodimeric nature of Cu, Zn-beSOD1. Control experiments (SOD1 and SOD1 with DTT) suggested as previously observed²⁹, that DTT produces the dissociation of the Cu, Zn-beSOD1 homodimer (31.2 kDa) into monomeric units (15.6 kDa). SDS-PAGE of Cu, Zn-beSOD1 plus TM at different concentrations [TM]:[SOD1] = 0, 0.5, 1.0, 2.5, 5.0, 25 and 50 ($t_{\text{incub}} = 30$ min, anaerobic, without DTT) (Figure 4.6); and at different incubation times of 0, 2, 12 and 24 h ([TM]:[SOD1] = 2.5 and 5.0, anaerobic, without DTT) (data not shown);

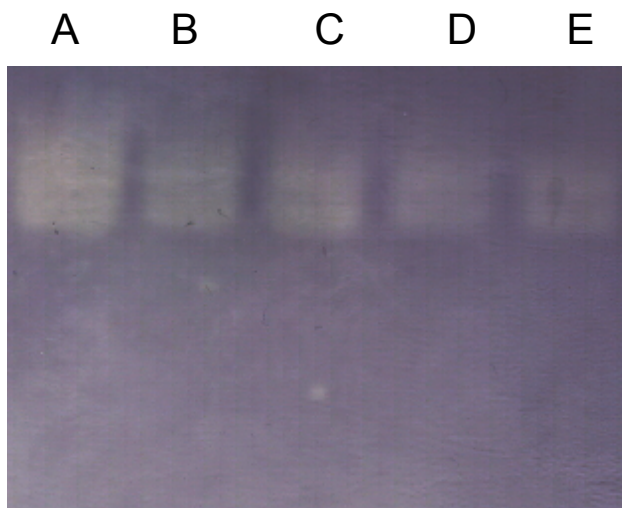
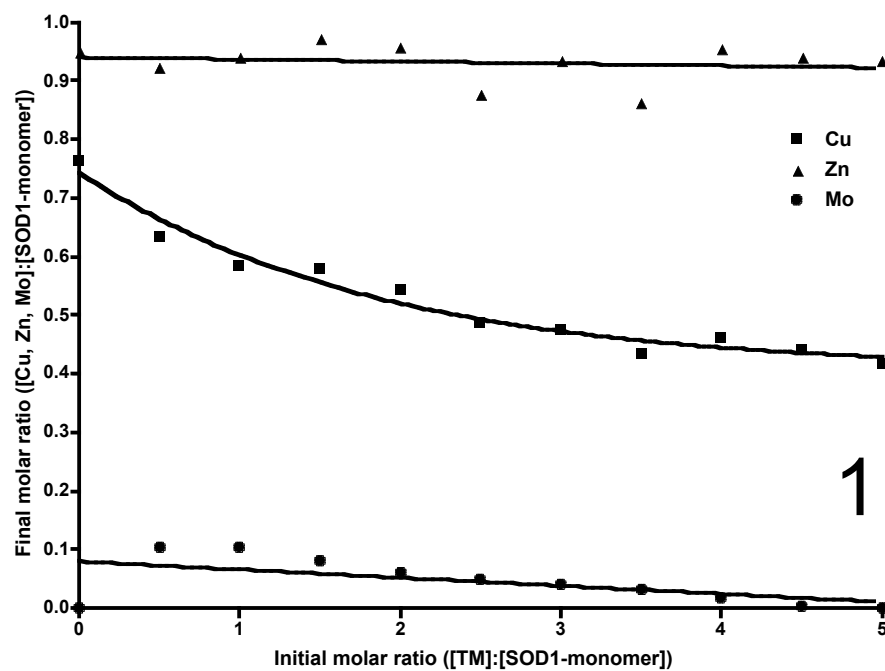


Figure 4.5 1. Changes in Mo, Zn and Cu concentration in 0.5 mM Cu, Zn-beSOD1 incubated with different amounts of TM after PD-10 gel filtration chromatography; 2. 4 - 15% NATIVE-PAGE SOD1 activity assay ([TM]:[SOD1]): A. 0, B. 1, C. 2.5, D. 5, E. 25 and UV-visible spectroscopy activity assay (% SOD1 activity): A. 100%, B. 93.5%, C. 70.4%, D. 62.2%, E. 25.1%.

showed a more clear progressive dissociation of the SOD1 dimer into SOD1 monomer with increasing TM concentration. These preliminary results suggested that the copper removal from Cu, Zn-beSOD1 due to its reaction with TM, may result in the dissociation of the homodimer SOD1 structure.

4.3.6 SOD1 Activity Assay: Electrophoresis and UV-Visible Spectroscopy. The inhibition of purified Cu, Zn-beSOD1 activity was initially suggested by in-gel nitro blue tetrazolium (NBT)¹⁶ activity assays. SOD1 activity was inhibited by TM in a concentration, time and temperature dependent way. Longer incubation times and higher reaction temperatures facilitate the inhibition of SOD1, with a complete inhibition using a 10-fold excess of TM for 48 h and 37° (Figure 4.7). Additionally, in Figure 4.8 we analyzed the SOD1 inhibition with TM in comparison with $[\text{MoO}_2\text{S}_2]^{2-}$ ($t_{\text{incub}} = 1 \text{ h}$) by activity gels and densitometric analysis. The % of SOD1 activity remaining after incubation is tabulated in Table 4.3. SOD1 inhibition is accentuated at higher temperatures with increasing amounts of TM and $[\text{MoO}_2\text{S}_2]^{2-}$, but TM is a much stronger inhibitor in comparison with $[\text{MoO}_2\text{S}_2]^{2-}$.

Table 4.3 % of SOD1 activity remaining after incubation with TM and $[\text{MoO}_2\text{S}_2]^{2-}$.

[TM]: [SOD1]	% SOD1 activity at 4°C	% SOD1 activity at 37°C	$[\text{MoO}_2\text{S}_2]$: [SOD1]	% SOD1 activity at 4°C	% SOD1 activity at 37°C
0	100	100	0	100	100
1.0	80	70	1.0	91	89
5.0	68	58	5.0	82	66
25.0	18	13	25.0	76	45
100.0	0	0	100.0	59	40

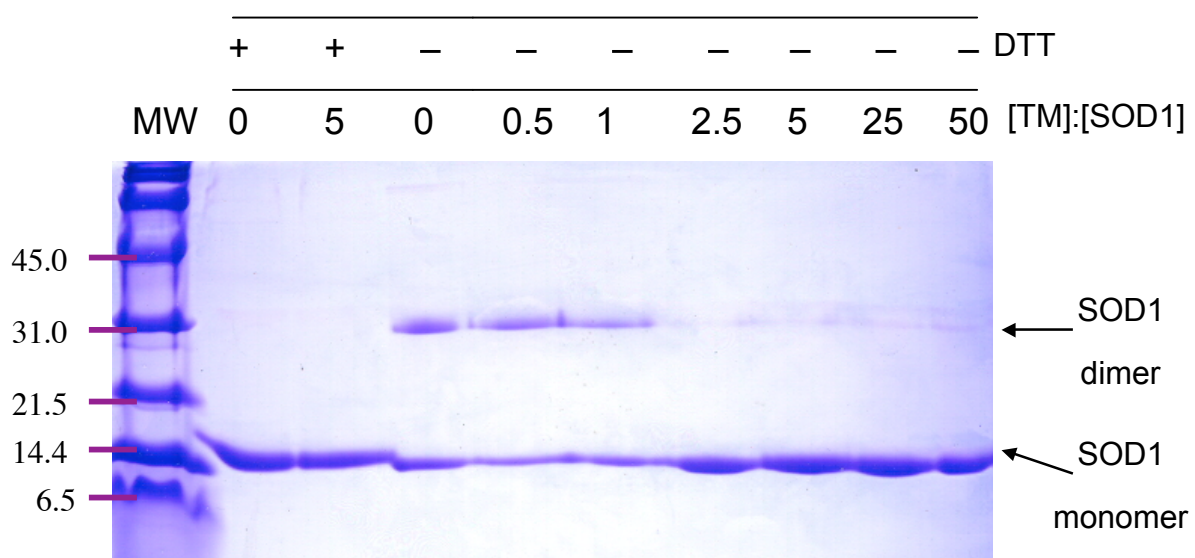


Figure 4.6 12% SDS-PAGE of Cu, Zn-beSOD1 (0.022 mM) with different amounts of TM ($t_{\text{incub}} = 30$ min, anaerobic).

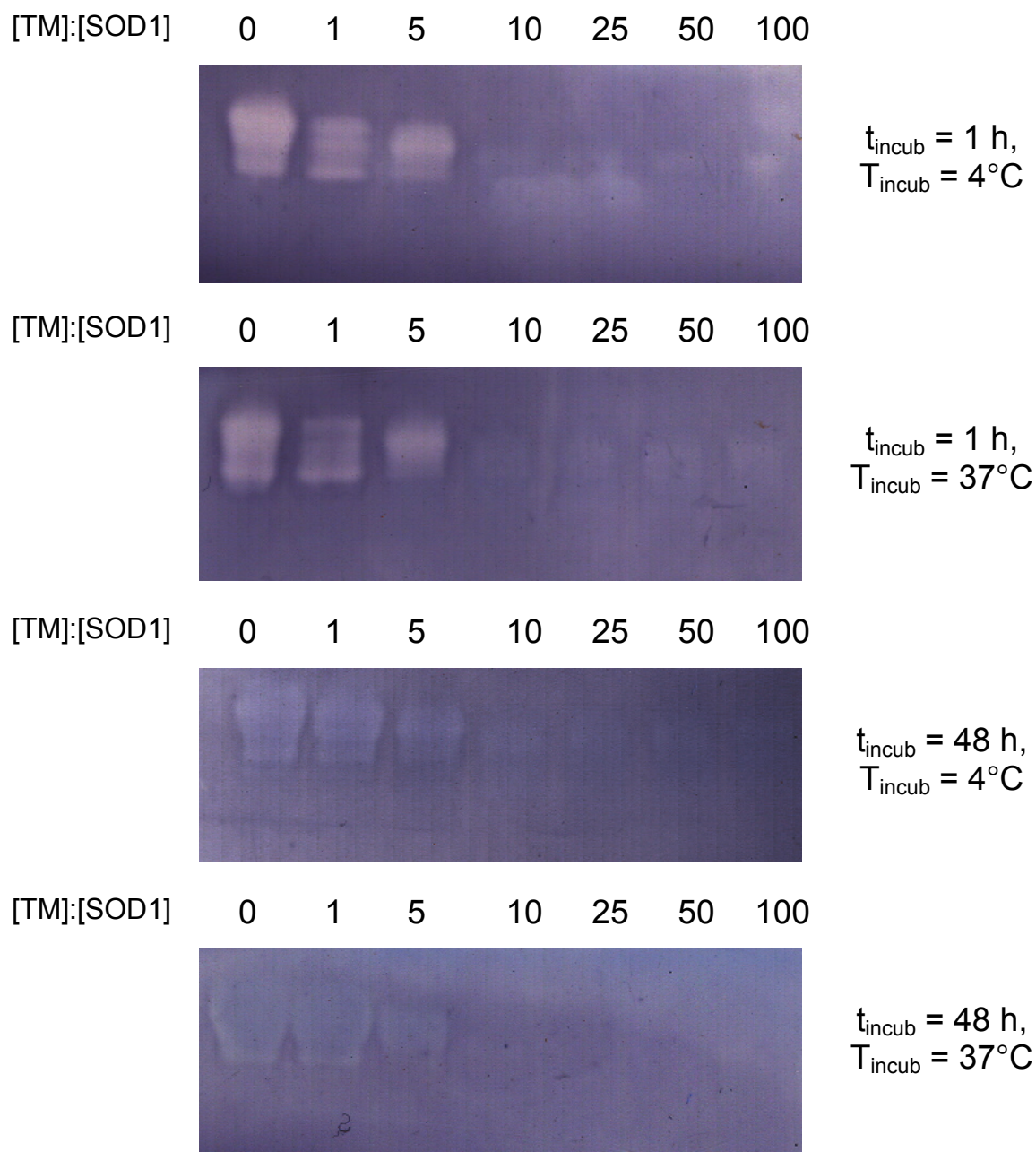


Figure 4.7 4 - 15% NATIVE-PAGE Cu, Zn-beSOD1 (250 ngs) activity assay as a function of TM treatment.

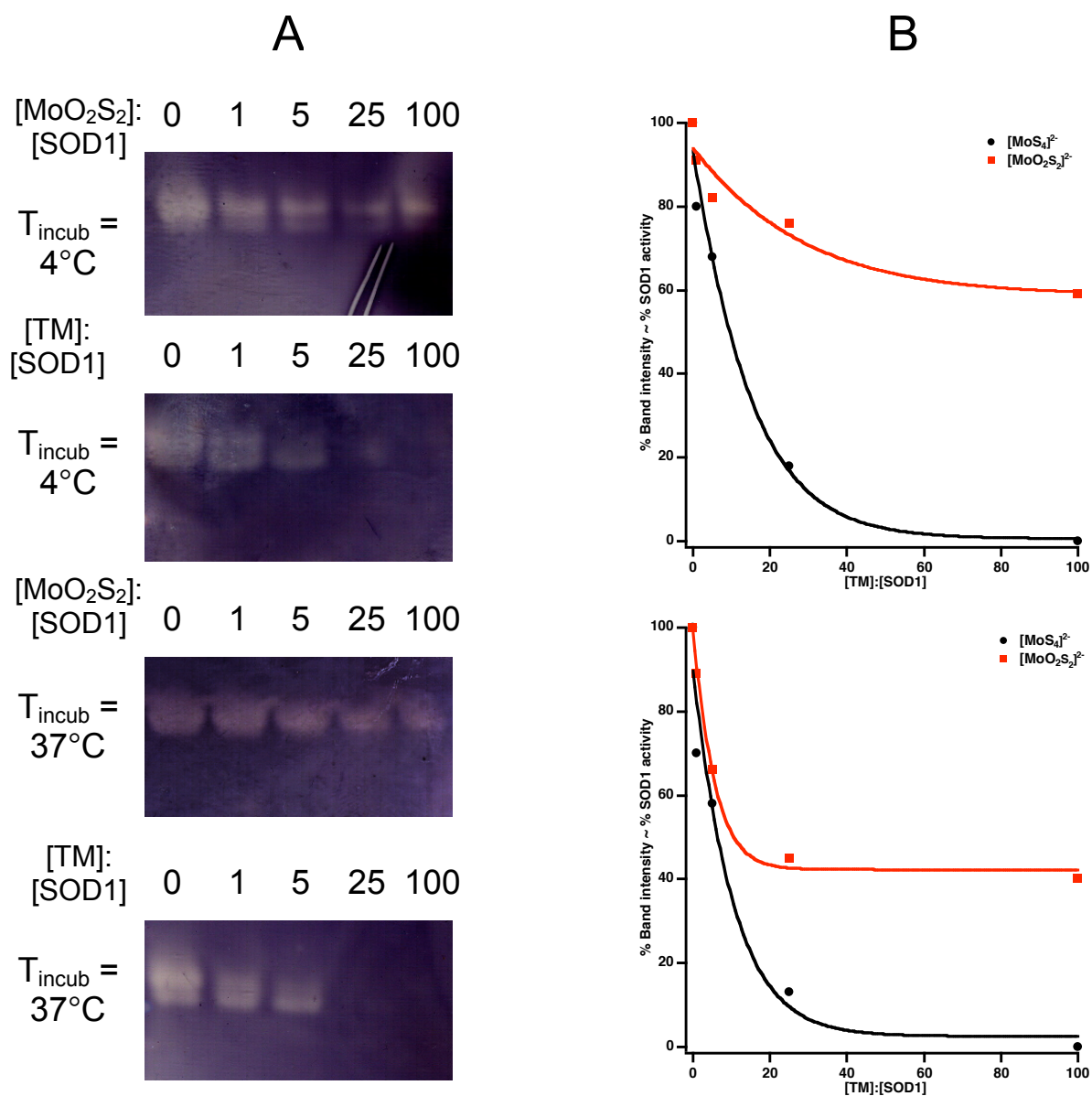


Figure 4.8 A. 4 - 15% NATIVE-PAGE Cu, Zn-beSOD1 (250 ngs) activity assay as a function of TM or MoO₂S₂ treatment ($t_{\text{incub}} = 1$ h), and B. Densitometric analysis (%SOD1 activity remaining after incubation with TM and [MoO₂S₂]²⁻) (see Table 4.3 for tabulated values).

A more accurate determination of the inhibition of Cu, Zn-beSOD1 activity (IC_{50}) by TM was elucidated by a UV-visible spectroscopy activity assay. TM was able to inhibit the SOD1 activity with an IC_{50} of $2.51 \pm 0.05 \mu\text{M}$ after 24 hours of incubation in a time- and dose-dependent manner (Figure 4.9), which is 8-fold higher in comparison with a previously reported value of $0.33 \mu\text{M}$ for the drug ATN-224[®] (using the same beSOD1), which is TM with a choline (rather than ammonium) counter ion.¹¹ The difference in IC_{50} values is mostly due to the uncorrected SOD1 protein concentrations used by Juarez et al.¹¹

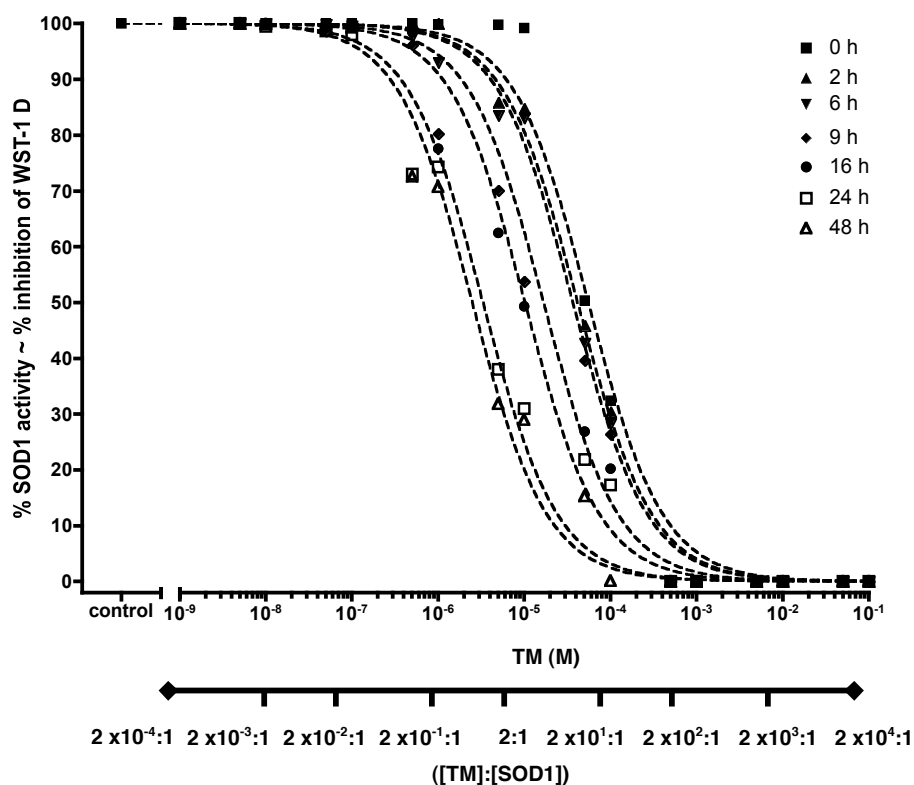


Figure 4.9 UV-visible spectroscopy Cu, Zn-beSOD1 activity assay (maximal $IC_{50} = 2.51 \pm 0.05 \mu\text{M}$, $n = 3$, $[\text{TM}]:[\text{SOD1}] = 0.4$, $t_{\text{incub}} > 24 \text{ h}$).

4.3.7 X-ray Absorption Spectroscopy. The coordination environment of the (Cu, Zn-beSOD1 + TM) sample was assessed by X-ray absorption spectroscopy by Dr. Rebekah Kelly (Penner-Hahn's Lab) to probe the structural features of the product of the interaction of TM with this copper protein. The Cu and Mo K near-edge structure (XANES) spectra of the (Cu, Zn-beSOD1 + TM) sample are described in detail in Figure 4.10.

The Cu K near-edge structure (XANES) of the (Cu, Zn-beSOD1 + TM) sample (Figure 4.10) suggests that copper is four coordinate (tetrahedral) and has a mixed oxidation state of 1^+ and 2^+ , as there is a slight shift to higher energy ($8984 \rightarrow 8986$ eV) of the $\text{Cu}^{1+} 1s \rightarrow 4p$ transition with a $\text{Cu}^{2+} 1s \rightarrow 3d$ transition at 8982 eV. The Mo K near-edge spectrum features a nearly identical spectrum in comparison with TM,²² and with the $[\text{TM}][\text{Cu-Atx1}]_3$ trimer complex.

The Cu K-edge extended X-ray absorption fine structure (EXAFS) of the (Cu, Zn-beSOD1 + TM) sample (Figure 4.11) showed 3 major peaks; a more prominent peak at $R + \alpha = 1.8 \text{ \AA}$ that can be modeled by 4 Cu—S at 2.29 \AA , plus a less intense peak at $R + \alpha = 2.4 \text{ \AA}$ that can be modeled by 2 Cu \cdots Mo at 2.71 \AA , and a third peak at $R + \alpha = 4.9 \text{ \AA}$ that can be tentatively identified as a nearly linear Cu \cdots Mo \cdots Cu multiple scattering interaction with a Cu \cdots Cu at 5.3 \AA ; while the Mo showed 3 major peaks also, a prominent peak at $R + \alpha = 1.8 \text{ \AA}$ that can be modeled by 4 Mo—S at 2.21 \AA , plus a less intense peak at $R + \alpha = 2.4 \text{ \AA}$ that can be modeled by 2 Mo \cdots Cu at 2.70 \AA , and a third peak at $R + \alpha = 5.0 \text{ \AA}$ that can be tentatively identified as a nearly linear Mo \cdots Cu \cdots Mo multiple scattering interaction with a Mo \cdots Mo at 5.4 \AA . The fit results of Cu and Mo K-edge EXAFS data for the (Cu, Zn-beSOD1 + TM) sample are shown in Table 4.4. The fit worsens when N is included in the fit, suggesting that copper may no longer be bound in the active site of the protein, which in addition to the observed multiple scattering interactions, confirm the previously suggested formation of an anionic inorganic $[\text{CuTM}]_x$ polymeric

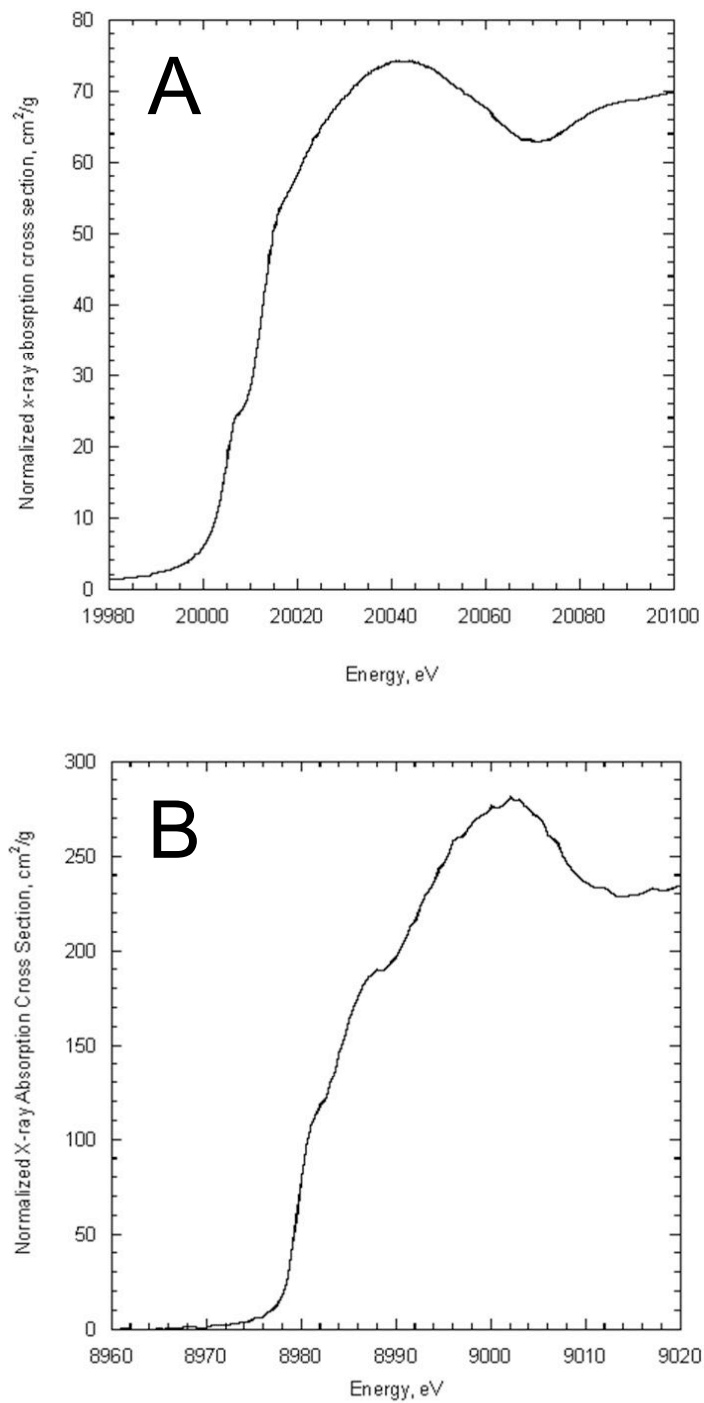


Figure 4.10 A. Cu-XANES of (Cu, Zn-beSOD1 + TM): Suggests a mixed a Cu^{1+/2+} oxidation state; B. Mo-XANES of (Cu, Zn-beSOD1 + TM): Similar features in comparison with TM and [TM][Cu-Atx1]₃ (Chapter 2).

cluster that seems to be associated with the surface of the protein.

Table 4.4 Results of the Cu and Mo EXAFS Curve Fitting for (Cu, Zn-beSOD1 + TM).

	CN ^a	R ^b	σ^{2c}	CN ^a	R ^b	σ^{2c}	F ^d
Cu ^{1+/2+}	4S	2.29	4.8	2Mo	2.71	3.2	0.430
				4Mo	3.93	3.2	
				3.4Mo	5.27	3.2	
Mo ⁶⁺	4S	2.21	5.2	2Cu	2.70	2.3	1.031
	4S	4.01	5.2	4Cu	3.62	2.3	
	4S	4.61	5.2	2Cu	5.41	2.3	

^aInteger coordination number. ^bBond length in Å. ^cDebye-Waller factor x 10³ in Å². ^dMean-square-deviation between data and fit.

4.4 Discussion and Conclusion

Ultrafiltration and UV-visible studies revealed an interaction between Cu, Zn-beSOD1 and TM but were not able to differentiate between a [TM][Cu, Zn-beSOD1] complex or a partial depletion of Cu from Cu, Zn-beSOD1 plus the formation of a [CuTM]_x. A combination of X-ray absorption spectroscopy (in collaboration with the Dr. James Penner-Hahn's group) and copper depletion with protein gel extraction studies revealed that the removal of copper from Cu, Zn-beSOD1 is the way in which this protein and TM interact in solution. This reaction explains the observed inhibition of SOD1 activity by TM.

UV-visible studies in conjunction with protein gel extraction studies, allowed the characterization of this [CuTM]_x polymeric complex (with a Cu¹⁺/Cu²⁺ mixture, suggested by

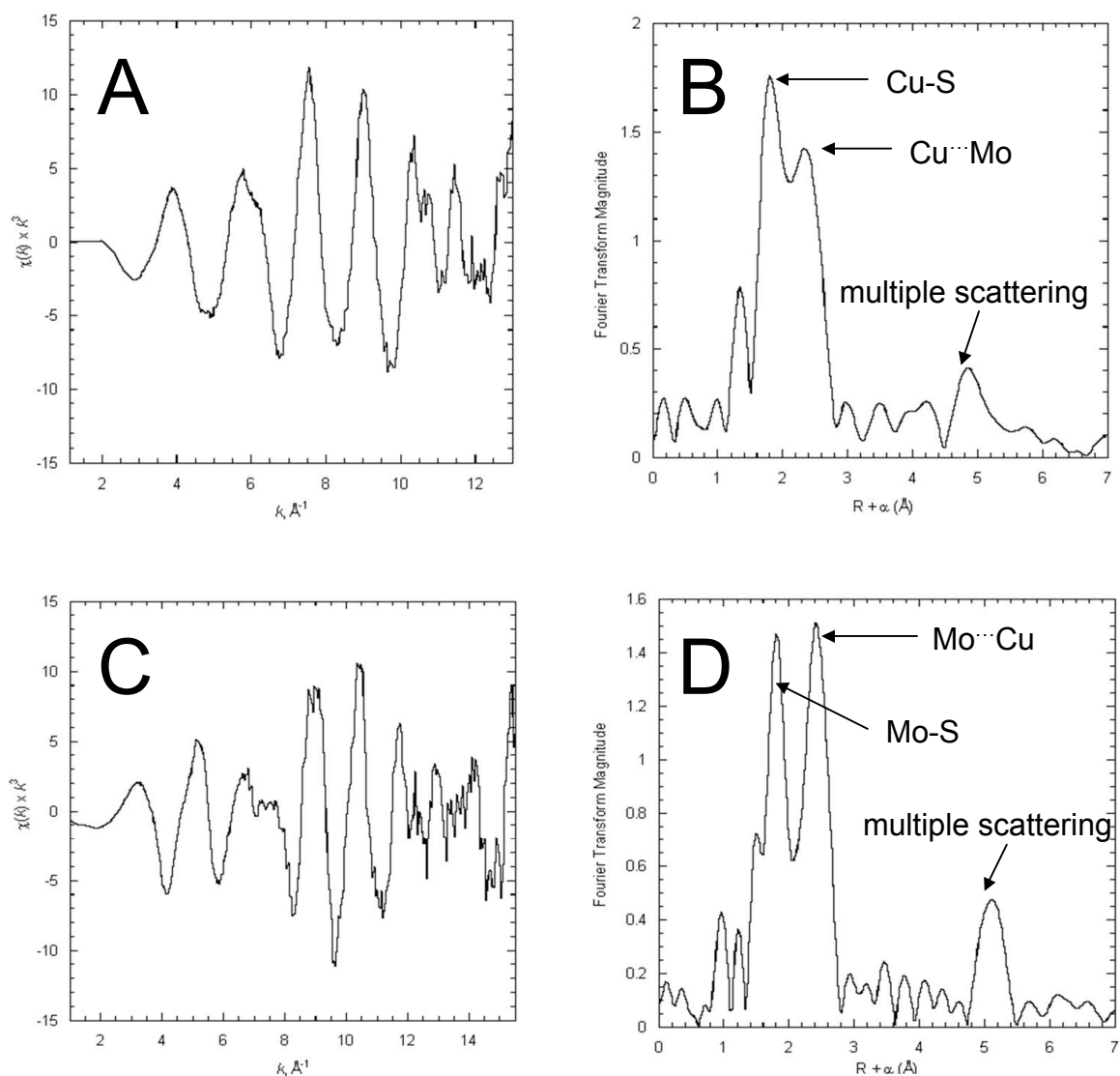


Figure 4.11 A. Cu EXAFS spectra and B. Cu K-edge Fourier transform of (Cu, Zn-SOD1 + TM): 4 Cu—S at 2.29 Å with $\sigma^2 = 0.0048$, 2 Cu—Mo at 2.71 Å with $\sigma^2 = 0.0032$ and a nearly linear Cu...Mo...Cu multiple scattering interaction with a Cu...Cu at 5.3 Å; C. Mo EXAFS spectra and D. Mo K-edge Fourier transform of (Cu, Zn-beSOD1 + TM): 4 Mo—S at 2.21 Å with $\sigma^2 = 0.0052$, 2 Mo—Cu at 2.70 Å with $\sigma^2 = 0.0023$ and a nearly linear Mo...Cu...Mo multiple scattering interaction with a Mo...Mo at 5.4 Å.

XANES). The two LMCT bands at 350 nm and 512 nm were attributed to the bathochromic shifting of the S–Mo LMCT bands as previously observed for the [TM][Cu(Cu-Atx1)₃] (Chapter 2). This shift is due mostly to the d–d transitions caused by an orbital overlap of a molybdenum with an open d-shell (d⁹) copper, which increases the electron density of the binding sulfurs of TM explaining the formation of the polymeric [CuTM]_x complex. This bathochromic shifting effect was also observed for small [L_xCuTM] complexes found in the literature, as in the [(CN)CuTM]²⁻, [(PhS)CuTM]²⁻, [(o-phen)CuTM], [(PPh₃)₃CuTM], etc.²³

As suggested by the copper depletion, TM inhibits Cu, Zn-beSOD1 by partially removing copper from the protein, even at higher concentration of TM ($5 < [\text{TM}]:[\text{SOD1}] < 25$). TM treatment of Cu, Zn-beSOD1 results in SOD1 with a copper occupancy of ~ 50% (0.5 Cu/SOD1 monomer or 1.0 Cu/SOD1 dimer). This phenomenon may be explained by the different nature of the copper centers in the Cu, Zn-beSOD1, observed in 2000 by Hough using protein X-ray crystallography. The copper center in the subunit A is shown to be highly variable being found in the oxidized state (penta-coordinate Cu²⁺) or in the reduced state (tri-coordinate Cu¹⁺), while this behavior was not observed for the copper center of subunit B which is highly stable, being only found in the oxidized state (penta-coordinate Cu²⁺).^{24,25} It seems that TM is able to remove only 1.0 Cu/SOD1 dimer, probably because this copper chelator is only capable of selectively removing the highly variable and unstable copper atom from subunit A, producing the inhibition of this enzyme (as discussed later) even without interacting with the other copper center.

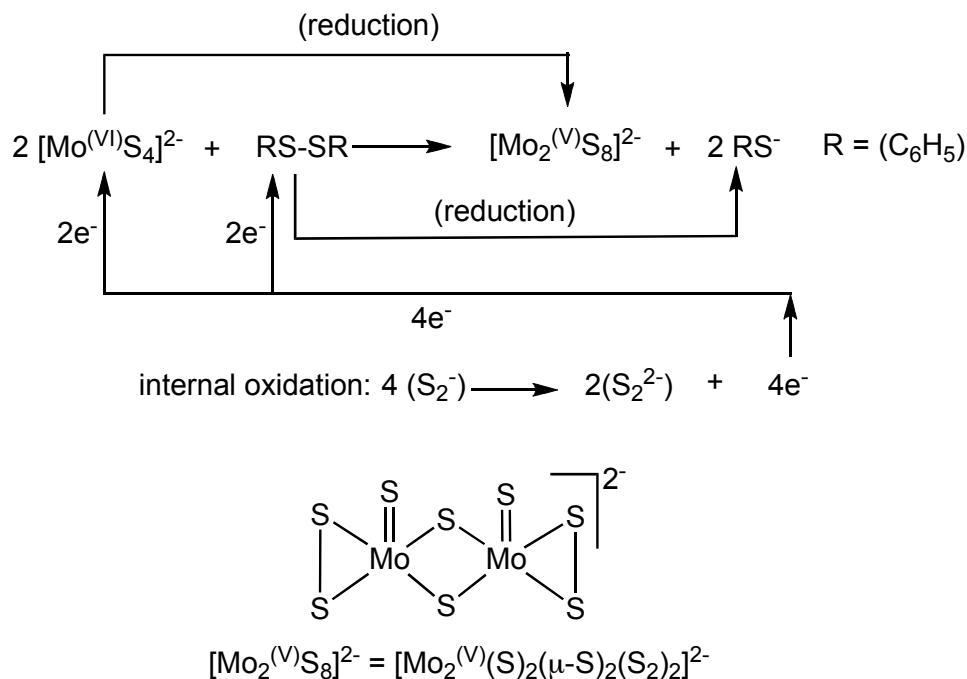
Even though the SOD1 dimer species possesses a high stability, which is resistant to different perturbing factors²⁶⁻²⁸, we proposed in this Chapter that the TM partial copper depletion of Cu, Zn-beSOD1 may cause the SOD1 homodimer dissociation into monomers at high concentrations of TM ($[\text{TM}]/[\text{SOD1}] \geq 2.5$, $[\text{TM}] \geq 0.055 \text{ mM}$). It is important to note that

further experiments are necessary to confirm this preliminary hypothesis.

The inhibition data suggested that we easily produced the inhibition of the SOD1 activity with TM at longer incubation times, higher concentrations of TM and higher reaction temperatures. We find that TM is a much stronger inhibitor than $[\text{MoO}_2\text{S}_2]^{2-}$, but the choline analogue of ammonium tetrathiomolybdate (ATN-224) (IC_{50} of $0.33 \mu\text{M}$)¹¹ is a slightly better inhibitor than TM (IC_{50} of $2.51 \mu\text{M}$) due maybe to a proposed higher stability in solution conferred by the choline cation. The difference in IC_{50} values can be also explained due to the uncorrected SOD1 protein concentrations used by Juarez et al.¹¹ Together with the copper depletion, SDS-PAGE and protein gel extraction studies, we can suggest that TM inhibits Cu, Zn-beSOD1 in vitro with a minimal amount of TM ($[\text{TM}]:[\text{SOD1}] = 0.4$) by a partial copper depletion ($\sim 1\text{Cu}/\text{SOD1}$ dimer), dissociation of the SOD1 homodimer, and formation of a $[\text{CuTM}]_x$ polymeric complex.

As part of the future studies of the research proposed in this Chapter, we suggest to test the hypothetical TM-induced reduction of the highly important Cu, Zn-SOD1 intramolecular disulfide bond²⁹ which may follow the internal electron transfer reaction model proposed by Stiefel in 1984 (Scheme 4.2).³⁰ Additional experiments with several qualitative thiol-reactive probes such as Ellman's (DTNB), iodoacetamide (IA), acetamido-4'-malei-midylstilbene-2,2'-disulfonic acid (AMS), etc, are required to confirm this hypothetical step in the inhibition of SOD1 by TM.

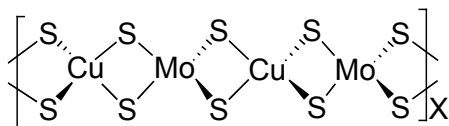
X-ray absorption spectroscopy allowed us to characterize the molecular coordination of this $[\text{CuTM}]_x$ polymer. The best fit of the Cu-EXAFS for the $[\text{Cu}, \text{Zn-beSOD1} + \text{TM}]$ sample excludes any N shell of scatterers, suggesting that the copper has been removed from the active site of the protein and has formed this inorganic $[\text{CuTM}]_x$ cluster or clusters that are in some way

Scheme 4.2 Stiefel's internal electron transfer reaction model.³⁰

associated with the protein after ultrafiltration. Attempts to include a shell of N scatterers resulted in either negative Debye-Waller factors or a combination of longer than reasonable bond lengths with unreasonably high Debye-Waller factors. The best fit suggests a CuS_4 at 2.29 Å and two $\text{Cu}\cdots\text{Mo}$ interactions at 2.71 Å, in a manner that would lead to Cu being 'sandwiched' by Mo. There is also a multiple scattering peak with a $\text{Cu}\cdots\text{Cu}$ at 5.3 Å. Fits using multiple scattering paths of a model system based on a linear arrangement of a copper coordinated by TM, indicates that the $[\text{CuTM}]_x$ inorganic cluster has a linear or nearly linear arrangement of atoms. The best fit of the Mo-EXAFS suggests a MoS_4 ($\text{Mo-S} = 2.21$ Å) with two $\text{Mo}\cdots\text{Cu}$ at 2.70 Å, which is consistent with the $\text{Cu}\cdots\text{Mo}$ distance suggested by Cu-EXAFS. There is also multiple scattering peak with a $\text{Mo}\cdots\text{Mo}$ at 5.4 Å, which barely differs with the one determined by Cu-EXAFS suggesting a very small amount of heterogeneity in the EXAFS data. So using

XAS, we were able to model this $[\text{CuTM}]_x$ complex as a linear chain in which there is at least two Cu and two Mo scatterers, where the Cu is ‘sandwiched’ between two Mo’s ($\text{Mo}\cdots\text{Cu}\cdots\text{Mo}$) and the Mo is ‘sandwiched’ between two Cu’s ($\text{Cu}\cdots\text{Mo}\cdots\text{Cu}$) (Scheme 4.3).

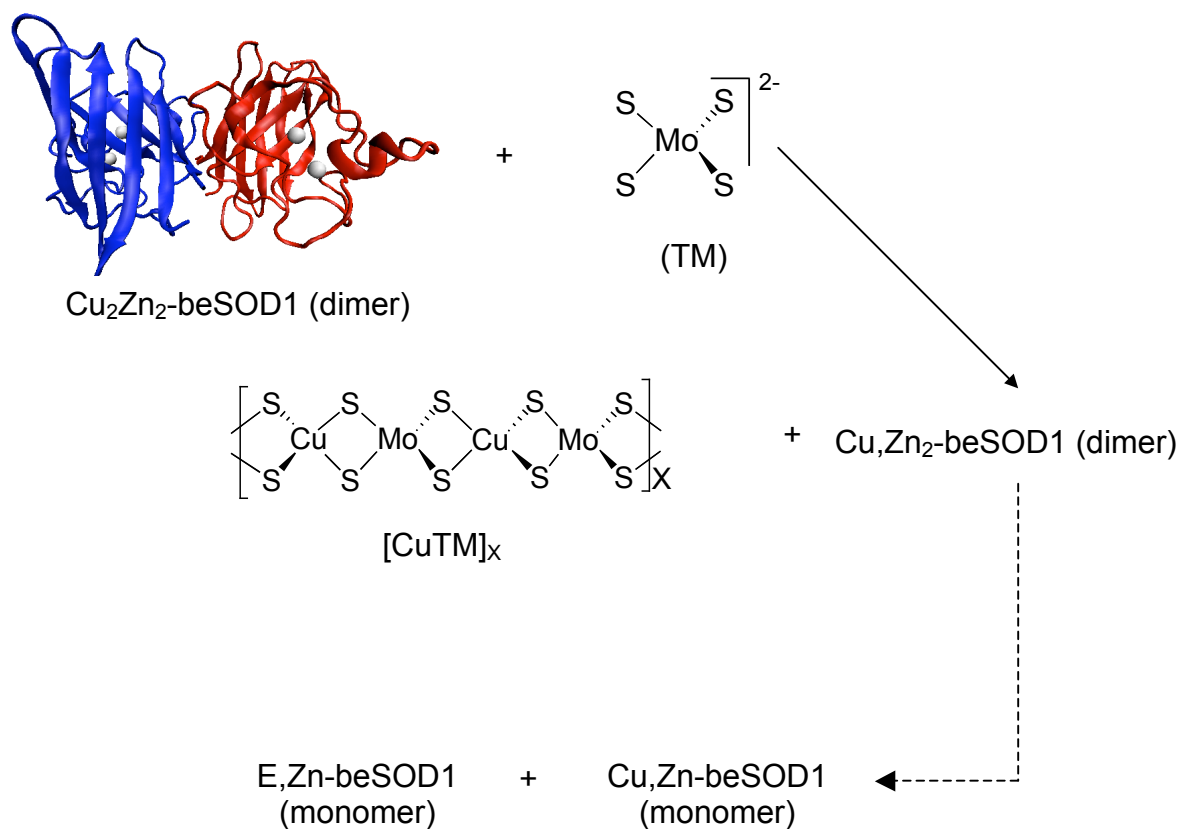
Scheme 4.3 Model for the polymeric $[\text{CuTM}]_x$ cluster.



The Cu–S, Mo–S, and Cu \cdots Mo distances for this $[\text{CuTM}]_x$ cluster are in agreement with crystallography distances found for $[(\text{CuL})_n\text{TM}]$ ($n = 1 - 6$) compounds.³¹⁻³⁹ For example, the $(\text{PPh}_4)_2(\text{Cu}_3\text{MoS}_4\text{Cl}_3)\cdot\text{CH}_3\text{CN}$ and the $(\text{NMe}_4)_5[\text{MoS}_4(\text{CuCl})_6\text{Cl}_3]$ show a Mo \cdots Cu = 2.62, 2.67 Å, Mo–S = 2.20, 2.26 Å, and Cu–S = 2.24, 2.30 Å, respectively.^{39,36} In comparison, the hitherto protein-bound sulfur bridged Mo₂Cu cluster of the orange protein (ORP) from *D. gigas* shows a weaker multiple scattering peak with a Mo \cdots Mo at 5.6 Å only in the Mo-EXAFS, suggesting a multiple Mo \cdots Cu \cdots Mo linear interaction without a Cu \cdots Mo \cdots Cu linear arrangement.⁴⁰

This chapter suggests that the inhibition of the Cu, Zn-beSOD1 activity with TM (previously proposed) is due to the copper removal (1 Cu per SOD1 homodimer) from the deeply buried active site of the protein with the formation of a $[\text{CuTM}]_x$ polymeric complex and the hypothetical dissociation of the SOD1 homodimer (Scheme 4.4). The different reactivity and behavior of this Cu-protein (SOD1) with TM (in comparison to Cu-Atx1), provides a starting point for understanding how TM may interact with intracellular and plasma-serum copper proteins, using a different mechanism of action.

Scheme 4.4 Diagram for inhibition mechanism of beSOD1 by TM.



Chapter 5

Cellular Uptake, Distribution and Cytotoxicity of TM in Human Hepatocellular Carcinoma Cells (HEPG2)

Abstract

An intracellular TM mechanism of action has been proposed on this thesis based in two copper protein targets: Cu-Atx1 and Cu, Zn-beSOD1, but a complete detailed study of the intracellular uptake of this metallo-drug is still missing.

The cellular uptake of TM by human hepatocellular cancer cells (HEPG2) in culture was explored by ICP-MS and X-ray fluorescence microscopy (XRF). We find that incubation of cancer cells with TM lead to significant uptake of the drug. Analysis of whole cells by XRF shows a high concentration of TM near the nucleus, while micro-XANES measurements at various cellular locations show a characteristic TM - Mo near-edge feature. Moreover, the ability of TM to inhibit cell proliferation and intracellular SOD1 activity was determined by a modified MTT and UV-VIS spectroscopy assay with a maximal IC₅₀ of 7.3 μ M and 0.309 μ M, respectively.

The TM cellular uptake, distribution and cytotoxicity in HEPG2 cells provide new insights to validate the already proposed intracellular mechanism of action for this metallodrug.

5.1 Introduction

For several years, different small inorganic complexes have been used as antivirals, antiacids, mineral supplements, antimicrobial and antiarthritic agents.¹⁻³ Metal-based drugs have also been used as anti-tumor agents for the treatment of cancer since B. Rosenberg discovered the *cis*-diamminedichloridoplatinum (II) compound ('cis-platin') more than forty years ago.^{4,5} Due to the success in clinical trials of some of these compounds, more and more metallodrugs are currently being tested in the search of more effective and less toxic drugs. Among them, TM is a promising anticancer agent that targets the Cu-dependence of angiogenesis. Currently, TM is undergoing 3 phase II clinical trials in esophageal carcinoma, prostate cancer and colorectal carcinoma.⁶⁻⁸

Although it appears that TM-induced copper deficiency is produced only by an extracellular mechanism,⁹ we can envision also an intracellular mechanism based on the previously described interactions of TM with two cytoplasmatic copper proteins (Cu-Atx1 and Cu, Zn-beSOD1), and on some cell uptake studies described in the literature.

In 1984, S. Gooneratne and H. Jones found detectable concentrations of copper, molybdenum and sulfur in apical lysosomes of kidney tubule cells from a TM-treated copper intoxicated sheep (subcellular fractionation with atomic absorption spectroscopy), which is considered the first example of an intracellular sequestration of TM.^{10,11} In the same year, Chidambaran, proposed for the first time the intracellular inhibition of SOD1, using a cytosolic extract of human red blood cells,¹² which provides further evidence for the intracellular uptake of this drug. Much more recently, Juarez in 2006 proposed the ATN-224[®] intracellular SOD1 inhibition, cytotoxicity, and cellular uptake using human umbilical vein endothelial cells.¹³

Here, we present more detailed studies of the cellular uptake of TM in human cancer

cells, using a combination of ICP-MS and X-ray fluorescence microscopy, and also measuring the effect of TM in cell proliferation and intracellular inhibition of SOD1. The results presented in this Chapter provide new insights to validate the hypothetical intracellular mechanism of action of TM, and identify SOD1 as one of its molecular targets.

The XRF data presented in this Chapter was acquired and analyzed in collaboration with Dr. Stefan Vogt and Dr. Barry Lai from the Advanced Photon Source at the Argonne National Laboratory.

5.2 Experimental Procedures

5.2.1 Synthesis and characterization of ammonium tetrathiomolybdate. As described by Mellor¹⁴ and Laurie¹⁵, TM was synthesized and characterized by ⁹⁵Mo NMR data (in D₂O): δ (in ppm) 2260, IR data (cm⁻¹): 3125 (sh), 2360 (w), 2336 (w), 1384 (m), 835 (w) and UV/Vis [H₂O, λ_{\max} (nm), $\epsilon \times 10^{-3}$ (M⁻¹ cm⁻¹)]: 241 (23.3), 317 (16.1), 468 (11.1).

5.2.2 Culture methods. Adherent Human Hepatocellular Carcinoma cells (ATCC, Manassas, VA) were cultured from frozen stocks, and were maintained in modified Eagle's Minimal Essential growth medium (EMEM) (with Earle's BSS, 2 mM L-glutamine, 1.0 mM sodium pyruvate, 0.1 mM nonessential amino acids and 1.5 g/L sodium bicarbonate) supplemented with 10% fetal bovine serum (FBS) (ATCC, Manassas, VA) and penicillin/streptomycin (P/S) (Invitrogen, Carlsbad, CA), and incubated at 37°C under an atmosphere of 95% air/5% CO₂. The cells were subcultured (PDL ~ 72 h) and all procedures were performed using sterile laminar flow cabinets. Optical images of HEPG2 cells were captured on a Nikon E600 Eclipse microscope equipped with a cooled CCD camera (Cool SNAP HQ) (Photometrics, Roper Scientific, Inc., Tucson, AZ).

5.2.3 Cytotoxicity Studies. TM was assayed for cytotoxicity against HEPG2 cells.

Cytotoxicity values were determined by a modified MTT [3-(4,5-dimethylthiazol-2-yl)-2,5-diphenyltetrazolium bromide] assay (ATCC, Manassas, VA), which measures changes in cell proliferation and conversely the reduction of cell viability, as indicated by the oxidation of MTT (yellow) to diformazan (purple, $\lambda_{\max} = 570$ nm) by action of the mitochondria's dehydrogenases (Scheme 5.1). An optimal HEPG2 cell count was determined prior to running the experiment using a haemocytometer ($[\text{HEPG2}] = 0.65 \times 10^6$ cell/ml) (Hausser Scientific, Horsham, PA) (Figure 5.1). The % cell viability for the inhibition of HEPG2 cell proliferation with TM (different concentrations: 10^{-7} – 10^{-3} M, different t_{incub} : 0–72 h) and for control experiments, was calculated using the manufacturer's instructions (plate 3×10^3 – 10^6 cells/well on a 96-well plate)¹⁶ and the following equation,

$$\% \text{ cell viability } (\sim \% \text{ reduction of MTT}) = (A_{\text{HEPG@-TM}} - A_{\text{BLANK}})$$

where, $A_{\text{HEPG@-TM}}$ (different concentrations, different t_{incub}): Abs of mixture of HEPG2 + TM + EMEM + MTT + detergent, and A_{BLANK} (different t_{incub}): Abs of mixture of EMEM + MTT + D; using a two-point calibration, where 100% of cell proliferation is represented by $A_{\text{HEPG2control}}$ (different t_{incub}): Abs of HEPG2 (different t_{incub}) – Abs blank (different t_{incub}), and the 0% of cell proliferation is represented by $A_{\text{HEPG2control}} (t_{\text{incub}} = 0 \text{ h})$: Abs of HEPG2 ($t_{\text{incub}} = 0 \text{ h}$) – Abs blank ($t_{\text{incub}} = 0 \text{ h}$). The results of the cytotoxicity experiments are represented by dose-response curves and IC_{50} values, which represent the concentration of TM at which the cell viability is 50% of the control viability. Additionally, two control experiments were performed to confirm the inhibition of cell proliferation by TM. The first control aimed to determine if longer HEPG2 incubation times (without TM) will cause a decreasing in cell proliferation, plotting a $A_{\text{HEPG2}} - A_{\text{blank}}$ curve [where, A_{HEPG2} (different t_{incub}): Abs of mixture of HEPG2 + EMEM + MTT + detergent, and

Scheme 5.1 Principle of the MTT cell cytotoxicity spectroscopy assay.

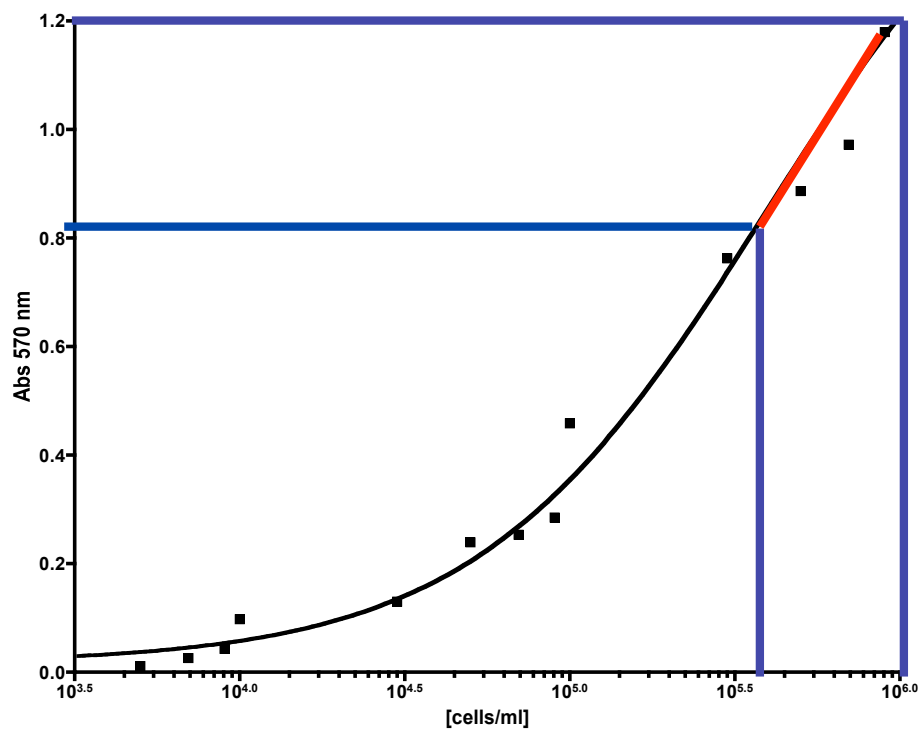
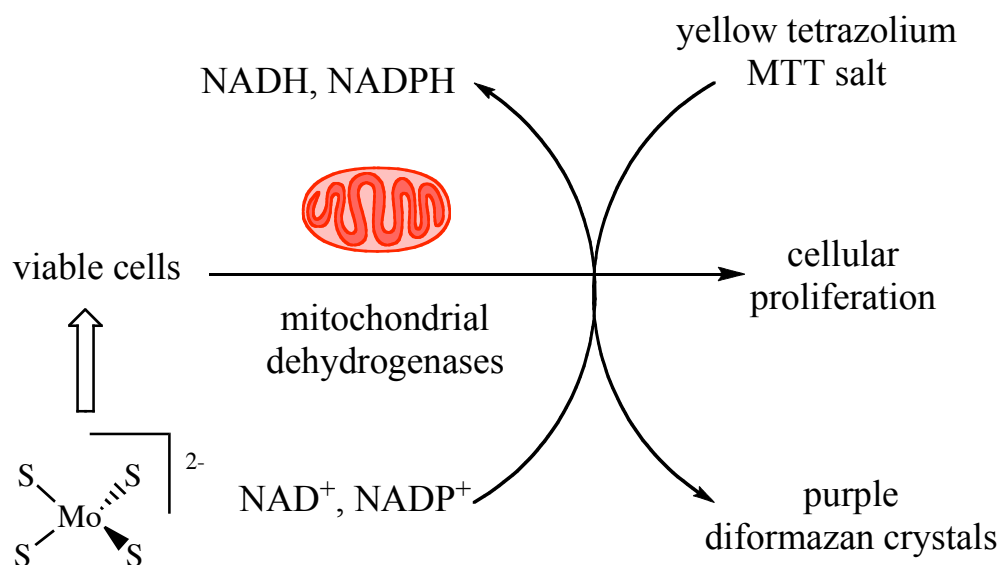


Figure 5.1 Graphical determination of optimal HEPG2 cell count (cell count should lie within the linear portion of the plot and yield an absorbance of 0.8 – 1.2).

A_{blank} (different t_{incub}): Abs of mixture of EMEM + MTT + detergent]. The second control aimed to determine the possible interference between the MTT and TM, plotting a $A_{\text{TM}} - A_{\text{blank}}$ curve [where, A_{TM} (different concentration, different t_{incub}): Abs of mixture of TM + EMEM + MTT + detergent, and A_{blank} (different t_{incub}): Abs of mixture of EMEM + MTT + detergent]. All cytotoxicity data were fitted to a sigmoidal function and presented as mean \pm SD (n = number of experiments) using IGOR Pro Version 4.07 software (WaveMetrics, Inc., Lake Oswego, OR).

5.2.4 Cell uptake studies (ICP-MS). HEPG2 cells were grown starting at a density of 0.65×10^6 cells/ml (haemocytometer) in modified growth medium (EMEM) and incubated at 37°C under an atmosphere of 95% air/5% CO_2 for 24 h. After handling recovery, the cell concentration was determined again, and the cells were treated with different concentrations of TM for 1 and 24 h (based in $t_{\text{incub}} = 24$ h and cytotoxicity, subtoxic concentration: 0–450 μM , IC_{50} concentration ~ 462 μM , and $> 50\%$ cell proliferation inhibition: 500–10000 μM). The cells were washed with 1X phosphate-buffered saline (PBS) (3 x 5 ml) to wash out the extra TM. Following this, the cells were harvested with 0.25% (w/v) Trypsin plus 0.53 mM EDTA solution and pelleted in acid-washed Teflon tubes (Nalgene, Rochester, NY). Pellets were dried overnight in an 80°C oven, dissolved in concentrated nitric acid for digestion (just enough to cover the cell pellet ~ 100 μl), and diluted with Mili-Q-water to get a final ICP-MS sample in 2% nitric acid ($V_f = 5$ ml), including 25 μl of 1 ppm ICP-MS internal standard (~ 5 ppb) (CPI International, Santa Rosa, CA). Tuning and calibration of the ICP-MS was performed with mixed elements standards (0, 0.5, 1, 10, 30, 70 and 100 ppb) (CPI International, Santa Rosa, CA).

The Mo content was measured by inductively coupled plasma mass spectrometry in ppb of Mo ($\mu\text{g/l}$) for each sample (5 ml) using a Thermo Fischer X Series II ICP-MS (Thermo Scientific, Minneapolis, MN). The total molybdenum cellular concentration (mM/cell) was

determined using the following equations:

$$[\text{Mo}] \text{ (mM/cell)} = [\text{N}_{\text{Mo}}] / [\# \text{ cells} \times \text{Vol} \text{ (ml/cell)} \times (1\text{L}/10^3\text{ml})]$$

$$[\text{N}_{\text{Mo}}] \text{ (mmol)} = [(\mu\text{g/L}) \times \text{Vol}_{\text{sample}} \text{ (0.005 L)}] / [Z_{\text{Mo}} \text{ (\mu g/\mu mol)} \times (10^3 \mu\text{mol}/\text{mmol})]$$

$$\# \text{ cells} = [\text{cells concentration by haemocytometer (cells/mL)} \times \text{Vol}_{\text{sample}} \text{ (5 mL)}]$$

$$\text{Vol} \text{ (cm}^3 \text{ or mL/cell)} = [4/3 \pi \{\text{dia (cm)}/2\}^3] \text{ (assuming spherical shape for HEPG2 cells)}$$

where, N_{Mo} = number of mmols of Mo (mmol), Z_{Mo} = atomic weight of Mo (95.94 $\mu\text{g}/\mu\text{mol}$), $\text{Vol}_{\text{sample}}$ = volume of ICP-MS sample (5 ml or 0.005 L), # cell = number of cells in ICP-MS sample, Vol = approx. volume of HEPG2 cell (2.42×10^{-9} ml/cell), dia = diameter of HEPG2 cell in cm using dimension of a grid of a haemocytometer (1.666×10^{-3} cm or 16.66 μm).

5.2.5 Preparation of whole cell samples for X-ray fluorescence analysis. HEPG2 cells were grown starting at a density of 1.6×10^6 cells/10 ml (by haemocytometer) in modified growth medium (EMEM) for 24 h using the conditions described before. The cells were harvested with 0.25% (w/v) Trypsin plus 0.53 mM EDTA solution, suspended in freshly modified EMEM (10 ml), and allowed to grow over silicon nitride windows (area, 2 x 2 mm; thickness, 1,000 nm) (Silson, Blisworth, UK), incubating them at 37°C under an atmosphere of 95% air/5% CO₂ for a further 48 h. Fresh modified EMEM was added to each dish (10 ml), followed by freshly prepared TM solution (dissolved in EMEM) to give an effective dish concentration of 1 mM. Control cells were treated in an identical manner, except that pure EMEM was added in place of the drug solution. The dishes were incubated at 37°C under an atmosphere of 95% air/5% CO₂ for 24 h. The TM treated HEPG2-silicon nitride windows were washed with 1X PBS (1 X 2 ml) and then 200 mM ammonium acetate (2 ml). Cells were fixed

by dipping the silicon-nitride window in liquid nitrogen followed by washing with acetone chilled to its freezing point. The window was allowed to dry at room temperature.

5.2.6 Preparation of thin-section cell samples for X-ray fluorescence analysis.

HEPG2 cells were grown starting at a density of 5.5×10^6 cells/10 ml (by haemocytometer) in modified growth medium for 24 h using the conditions described before. Cells were washed with 1X PBS (2 ml) and fresh modified EMEM (10 ml) was added to each dish, followed by freshly prepared TM solution (dissolved in EMEM) to give an effective concentration of 1 mM. The dishes were incubated at 37°C under an atmosphere of 95% air/5% CO₂ for a further 24 h. The growth medium was removed and each dish was washed thoroughly with 1X PBS. Cells were harvested with 0.25% (w/v) Trypsin plus 0.53 mM EDTA. The resulting suspension was centrifuged and washed with 1X PBS (3X, 1 ml) and 200 mM ammonium acetate (2 ml), and suspended in glutaraldehyde (1 ml, 2.5 %) for 1 h. After centrifugation, the pellet was dehydrated by incremental amounts of ethanol (2x50, 2x70, 3x95 and 4x100%; 1 ml, 10 min) and rotated for an extra 24 h in pure ethanol (0.5 ml) with Spurr's resin (0.5 ml) (Electron Microscopy Sciences, PA). Finally the cell pellet was treated with Spurr's resin for 24 h (1 ml, room temperature), and for 12 h (1 ml, 70°C) until polymerization occurred. The final polymer blocks were microtomed (Ultracut S, Leica, Germany) to produce thin sections of approximate 0.1 µM.

5.2.7 Collection of XRF data. The collection and analysis of the XRF data was done by Dr. Stefan Vogt and Dr. Barry Lai from the APS. Scanning of XRF microscopy was performed at beamline 2-ID-D and 2-ID-E of the Advanced Photon Source at the Argonne National Laboratory using an x-ray fluorescence microprobe described in Scheme 5.2.¹⁷ Individual cells were found over the silicon nitride windows with the help of an optical microscope at the APS.

Fluorescence-detected X-ray elemental distribution were collected at 295 K under a He atmosphere, using either 11.0 or 20.1 keV monochromatic X-ray incident beam, focused to a spot size of 0.20 x 0.20 μm^2 on the specimen. Fluorescence lines were collected using a high-purity Ge detector (Canberra Industries, CT), providing after analysis the spatial image of each element, where each data point represents the integration of a specified area around the K_{α} fluorescence elemental energy.

At 11.0 keV, XRF images were collected for P, S, Cl, K, Ca, Mn, Fe, and Cu, and at 20.1 keV images were collected for P, Cl, K, Ca, Mn, Fe, Cu, Zn and Mo. Data for control cells (without TM) were collected at 20.1 keV. The approximate location of the cells over the silicon nitride window was determined by comparison of the X-ray transmission image collected at the microprobe and the microscope image. Once a cell had been appropriately localized, high resolution scans were acquired with a 0.5 μm step size. For each elemental map, the metal concentration was expressed in $\mu\text{g}/\text{cm}^2$ scales. Signal was calibrated with NIST thin-film x-ray standards (1832 and 1833).

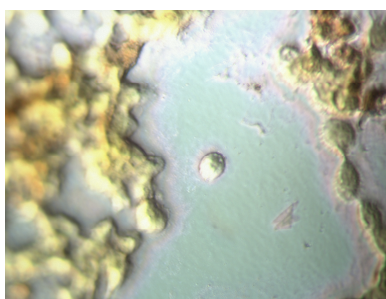
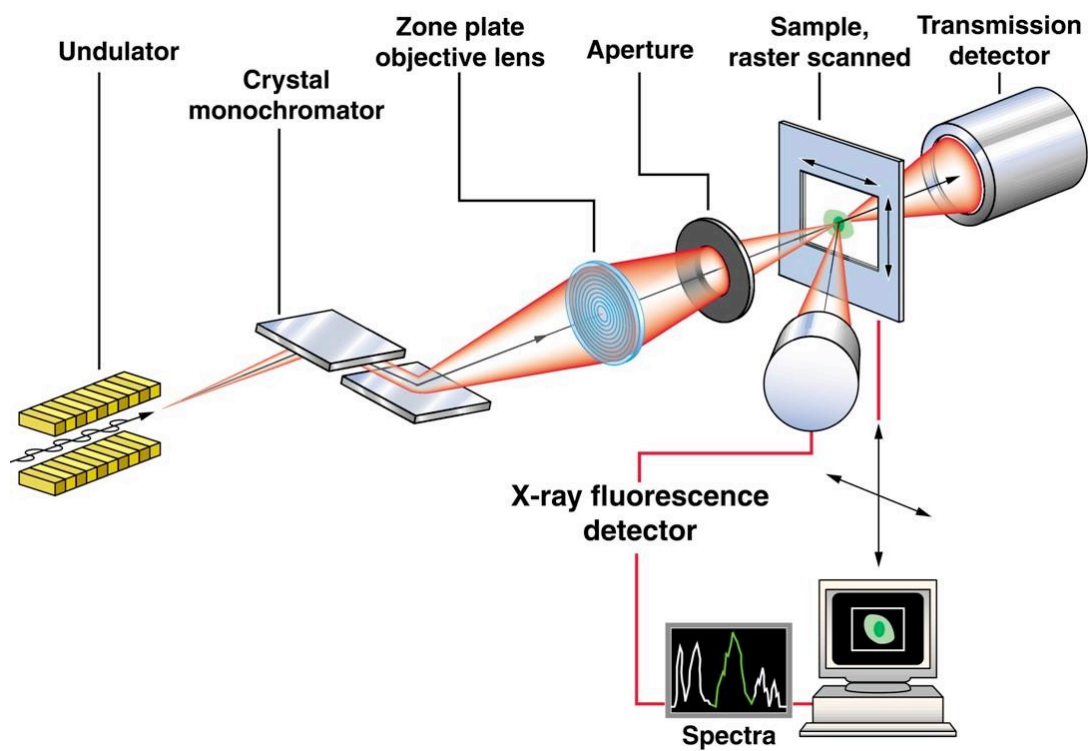
The total Mo cellular concentration (mM/cell) was also converted from $\mu\text{g}/\text{cm}^2$ to mmol/L for appropriate comparison to ICP-MS results, using the following equation:

$$[\text{Mo}] (\text{mM}/\text{cell}) = \frac{[\text{Total Mo} (\text{pc}/\text{cell}) \times (\text{mg}/10^9 \text{ pc}) \times (10^3 \text{ cm}^3/\text{L})]}{[Z_{\text{Mo}}(\text{mg}/\text{mmol}) \times \text{Vol} (\text{cm}^3/\text{cell})]}$$

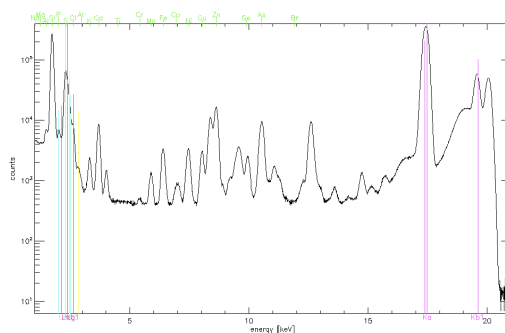
$$\text{Total Mo} (\text{pc}/\text{cell}) = [(\mu\text{g}/\text{cm}^2) \times \text{Area} (\text{cm}^2/\text{cell}) \times (10^6 \text{ pc}/\mu\text{g})]$$

where, Area = area of a particular HEPG2 cell (cm^2/cell) calculated by integration of cell image, Z_{Mo} = atomic weight of Mo (95.94 mg/mmol), and Vol = approximate volume of HEPG2 cell ($2.42 \times 10^{-9} \text{ cm}^3/\text{cell}$) calculated as explained before.

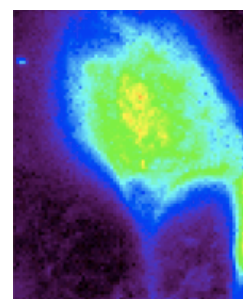
Scheme 5.2 Typical layout of a X-ray fluorescence microprobe.¹⁷



Cells air-dried
under light
microscope over Si-
nitride window



Elements
fluorescence
spectrum



XRF cell
elemental
map

5.2.8 Micro X-ray Absorption Near-Edge Structure (micro-XANES). Micro-XANES spectra were collected by initially finding different areas of interest within a single cell. Micro-XANES was run by scanning (from 19.98 to 20.1 keV) the energy of the incident X-ray across the Mo K-edge (~ 19.999 keV) at 5 – 6 different points per cell, where we want to analyze the Mo coordination environment.

5.2.9 Preparation of cytosolic extract from HEPG2 cells. HEPG2 cells were grown starting at a density of 10.0×10^6 cells/ml (by haemocytometer) using the conditions described before for 24 h. Cells were treated with different concentrations of TM (10^{-10} – 10^{-2} M) for 0 – 72 h. After incubation with TM, cells were harvest with a scraper (Falcon, Franklin Lakes, NJ) and centrifuged at 2,000 g for 10 min (4°C) using a Marathon 16 Km centrifuge (Fisher Scientific, Hampton, NH). The supernatant was discarded and the cell pellet was washed with cold 1X PBS. The centrifugation and washing step was repeated three times to wash out the growth medium. HEPG2 cells were broken by a combination protocol of freeze-thaw and sonication. First, the cells were treated three times in a cold bath (dry ice with ethanol, $\sim -20^\circ\text{C}$) for 20 min, and in incubated at 37°C for 10 min; with the subsequent sonication of the cell lysate using the Sonifier 450 (Branson, Danburn, CT) on an ice bath ($\sim 4^\circ\text{C}$) at 60 w for 15 min. The cell lysate suspension was centrifuged at 10,000 g for 15 min, recovering and transferring the supernatant to a tube pre-chilled on ice. The protein concentration of the cytosolic extract (supernatant) was determined using the Bradford assay. Serial dilutions of the cell extract were performed with cold 1X PBS to get a final protein concentration of 0.5 – 50 $\mu\text{g}/25 \mu\text{l}$. The cell lysate (250 μl) was treated with 800 μl of a mixture of ice-cold chloroform/ethanol [37.5/62.5 (v/v)] in order to inhibit the mitochondrial SOD2, according to manufacturer's protocol.

5.2.10 UV-visible spectroscopy SOD1 activity assay. Intracellular SOD1 activity in HEPG2's cytosolic extract was assayed by measuring the inhibition of reduction of the water-soluble tetrazolium salt, WST-1: 2-(4-iodophenyl)-3-(4-nitrophenyl)-5-(2,4-disulfido-phenyl)-2H-tetrazolium monosodium salt, which produces a water-soluble diformazan dye (WST-1D, $\lambda_{\text{max}} = 450 \text{ nm}$) on reduction with a superoxide anion (Dojindo Molecular Technologies Inc., Gaithersburg, MD). Superoxide anion is generated by xanthine, O_2 and xanthine oxidase; and Cu, Zn-beSOD1 was used to generate a standard curve (Sigma Aldrich, St. Louis, MO). The %SOD1 activity for the inhibition of intracellular SOD1 with TM, was calculated using the manufacturer's instructions (3X 25 μl of cell extract/well on a 96-well plate) and the following equation,

$$\% \text{ SOD1 activity } (\sim \% \text{ inhibition WST-1 D}) = [(A_{B1} - A_{B3}) - (A_{\text{SAMPLE}} - A_{B2}) / (A_{B1} - A_{B3})] \times 100$$

where, A_{SAMPLE} : Abs of mixture of sample + WST-1 + xanthine + xanthine oxidase (XO), A_{B1} : Abs of mixture of WST-1 + xanthine + XO, A_{B2} : Abs of mixture of sample + WST-1, A_{B3} : Abs of mixture of WST-1. All SOD1 inhibition data were fitted to a sigmoidal function and presented as mean \pm SD (n = number of separate experiments) using IGOR Pro Version 4.07 software (WaveMetrics, Inc., Lake Oswego, OR).

5.3 Results

5.3.1 Light Microscopy studies of TM-treated HEPG2 cells. Optical images of HEPG2 cells treated with different concentrations of TM were captured using a Nikon E600 Eclipse microscope (Figure 5.2). Cells were cultured under the conditions described before, incubating them with TM (0–5000 μM) for 1 h, any extra TM was washed out using consecutive washes with 1X phosphate-buffered saline (PBS). The microscope images showed that the cells are

becoming slightly red-colored as we increase the concentration of TM, which indicates that the TM is taken up by the HEPG2 cells or that the TM is simply trapped over the membrane of the cells.

5.3.2 Cytotoxicity studies of HEPG2 cells with TM. TM was assayed for cytotoxic activity against HEPG2 cells, an easy-to-handle standard human liver carcinoma cell line, which offers two key-points for this study. First, cells are coming from the liver, which is the central organ for copper metabolism, and second, the anticancer drug used for this study is a strong copper chelator agent (TM). Prior to measuring the cytotoxicity of TM against this cell line, two control experiments were performed. The first one suggested that longer incubation times (0–72 h) did not lead to a decrease in cell proliferation (without TM), which means that the assay can be performed for extended hours without any interference from cell death (Figure 5.3.A). A second control experiment showed that longer exposure times and high concentrations of TM (10^{-7} – 10^{-3} M) (without cells) lead only to a very small increment of the Abs at 570 nm (\sim [TM]: 10^{-4} – 10^{-3} M), which suggests that mostly there is no interaction or interference between the MTT reagent and TM (Figure 5.3.B). Finally, using the modified MTT cytotoxicity assay (as described before), we demonstrated that high concentrations and long exposure times to TM produce a reduction in HEPG2 cell proliferation, with an IC_{50} maximal value of 7.3 ± 0.09 μ M after 60 h of incubation at 37°C (Figure 5.4). This value is slightly higher than the previously IC_{50} reported for endothelial cells (HUVEC, 1.4 ± 0.3 μ M, $t_{incub} = 48$ h, ATN-224[®]), and much more similar to the one reported for a multiple myeloma cancer cell line (MM1S, 5.0 μ M, $t_{incub} = 96$ h, ATN-224[®]).¹³ Small differences in these values can be attributed to the particular physical characteristics found in different kinds of human cells.

5.3.3 HEPG2-TM Cell Uptake Studies. The total intracellular concentration of Mo

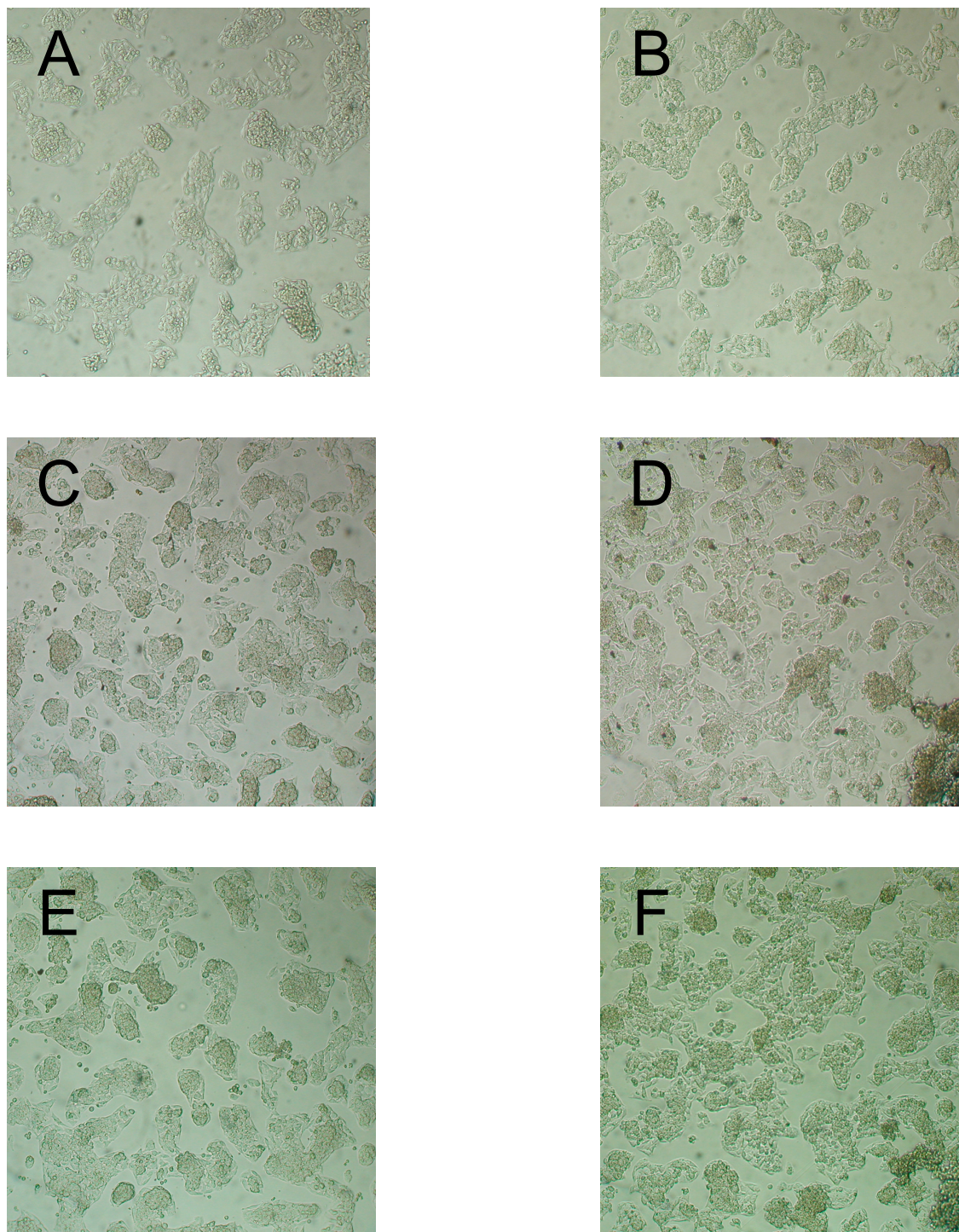


Figure 5.2 Light microscope images of HEPG2 cells (4.04×10^5 cell/ml) after 1h of incubation with different concentrations of TM (μM): A. 0, B. 1, C. 10, D. 100, E. 1000, F. 5000.

was calculated in ppb using ICP-MS and converted to millimolar as described in experimental procedures. TM was tested at 1 and 24 h exposure times to provide information on the rate of uptake of this drug (Figure 5.5.A, B). Also, different concentrations of TM were used on the basis of the cytotoxicity data (Section 5.3.2) to measure the potency of TM at intracellular level. For a 24 h treatment, the following concentrations of TM were used, 0–450 μM being sub-toxic concentrations, $\sim 462 \mu\text{M}$ being the approximate IC_{50} concentration, and 0.5–10 mM being concentrations that caused $> 50\%$ inhibition of cell proliferation. The results suggest that TM is accumulated in the cell. For example, when 1 mM TM is added to the cell culture, intracellular concentrations of TM/HEPG2 cell were much higher, showing values of 20.5 mM ($t_{\text{incub}} = 1\text{h}$) and ~ 21.0 mM ($t_{\text{incub}} = 24\text{h}$). These results suggested that TM may be able to enter HEPG2 cells and that the cellular uptake of TM is dose- and time-dependent. Cells treated for 1 h contain less Mo than cells treated for 24 h, specially when HEPG2 cells are treated with low TM concentrations (0.1–25.0 μM).

5.3.4 X-ray Fluorescence Microscopy (XRF) HEPG2 cells. 2-D elemental distribution maps of control and TM-treated HEPG2 cells were collected at 20.1 keV in order to detect the $\text{K}_{\alpha 1}$, $\text{K}_{\alpha 2}$ and $\text{K}_{\beta 1}$ emission lines of Mo. We avoided using lower energies (i.e. 11.0 keV), because we were not able to identify the molybdenum due to a fluorescence energy interference and overlap between the $\text{K}_{\alpha 1}$, $\text{K}_{\alpha 2}$ emission lines of Cl and $\text{L}_{\beta 2}$ of Mo, producing the formation of dark areas in the Mo map, which exactly matches the Cl distribution in its respective elemental map (Figure 5.6, Table 5.1).

Even though we performed these studies at two different energies (11.0 and 20.1 keV) we always obtained an inaccurate S map due to a fluorescence energy interference and overlap between the $\text{K}_{\alpha 1}$, $\text{K}_{\alpha 2}$ emission lines of S and $\text{L}_{\alpha 1}$, $\text{L}_{\alpha 2}$ of Mo; and the $\text{K}_{\beta 1}$ of S and $\text{L}_{\beta 2}$ of Mo.

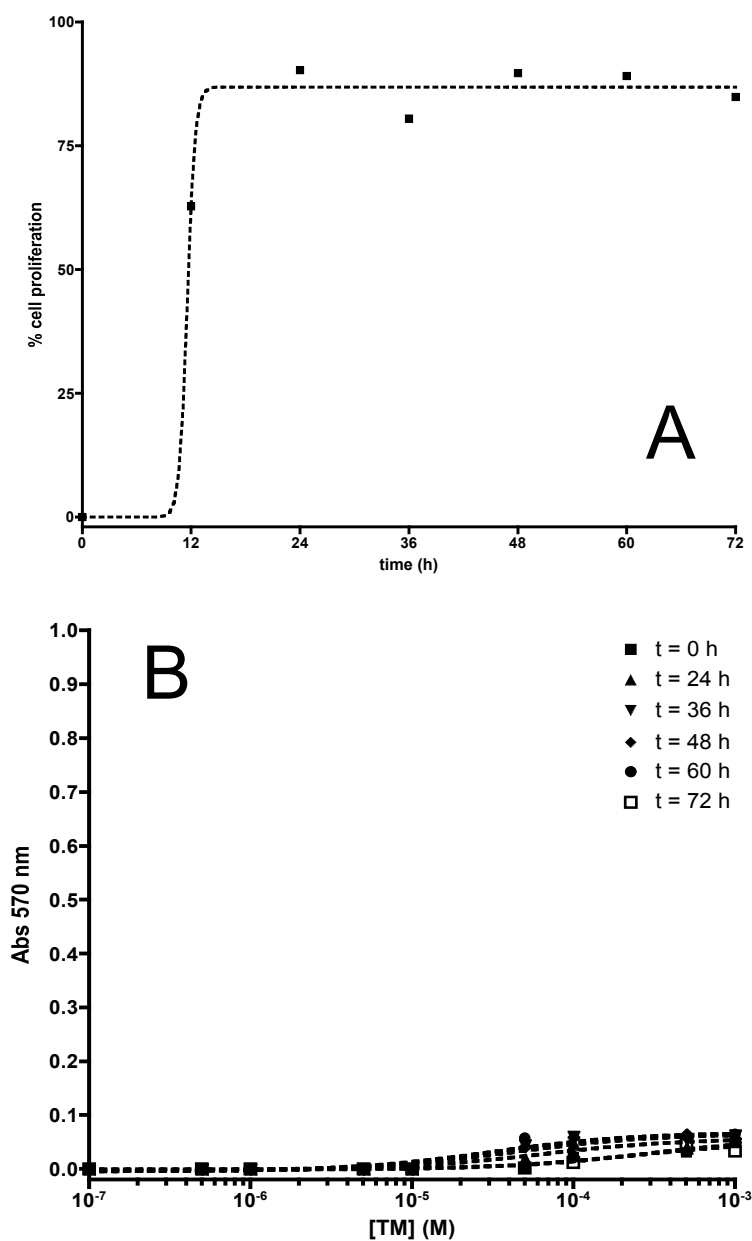


Figure 5.3 MTT cytotoxicity assay control experiment. A. HEPG2 cell proliferation vs. time: Longer exposures times does not lead to decrease cell proliferation (0 – 72 h); B. Interference TM–MTT in the absence of cells: Longer exposure times and higher TM concentration does not lead to an interaction between TM and MTT, only a slightly increment of the Abs₅₇₀ < 0.05 (~ diformazan) is observed between [TM]: 10⁻⁴ – 10⁻³ M.

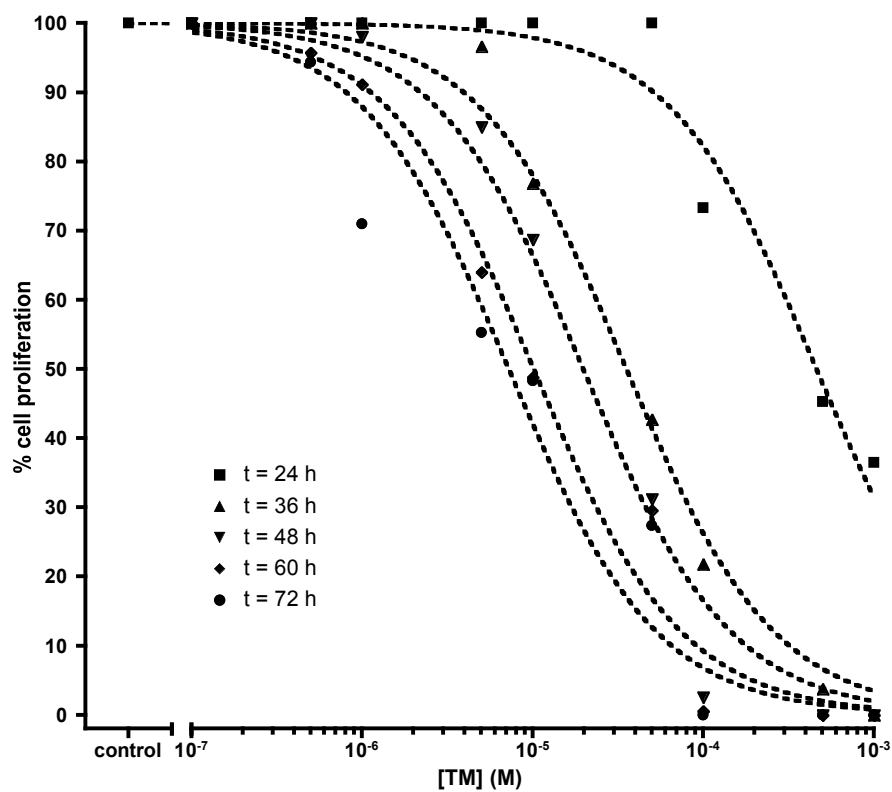


Figure 5.4 MTT cytotoxicity assay. TM inhibited HEPG2 cell proliferation with a maximal $IC_{50} = 7.3 \pm 0.09 \mu\text{M}$ ($n = 3$, $t_{\text{incub}} > 60 \text{ h}$).

Table 5.1. X-Ray Fluorescence Energies of S, Cl and Mo.

	$K_{\alpha 1}$	$K_{\alpha 2}$	$K_{\beta 1}$	$L_{\alpha 1}$	$L_{\alpha 2}$	$L_{\beta 1}$	$L_{\beta 2}$
S	2.30784	2.30664	2.46404				
Cl	2.62239	2.62078	2.81560				
Mo	17.47934	17.3743	19.6083	2.29316	2.28985	2.39481	2.51830

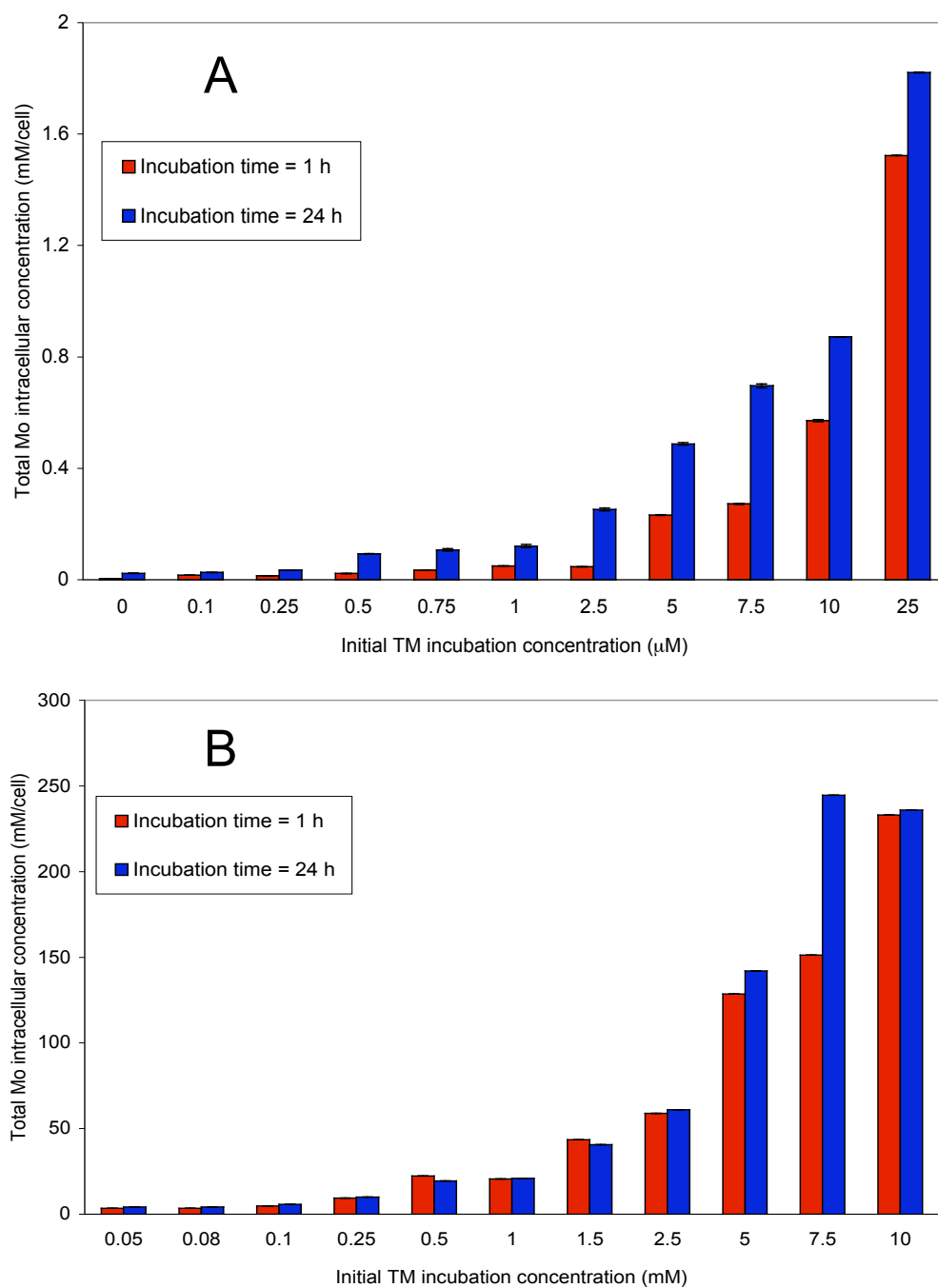


Figure 5.5 Comparison of the intracellular Mo concentrations in HEPG2 cells (mM/cell) determined by ICP-MS after 1 and 24 h of exposure to TM (A. 0–25 μ M; B. 0.05–10 mM). TM is taken up by HEPG2 cells in a dose- and time-dependent manner ($n = 3$).

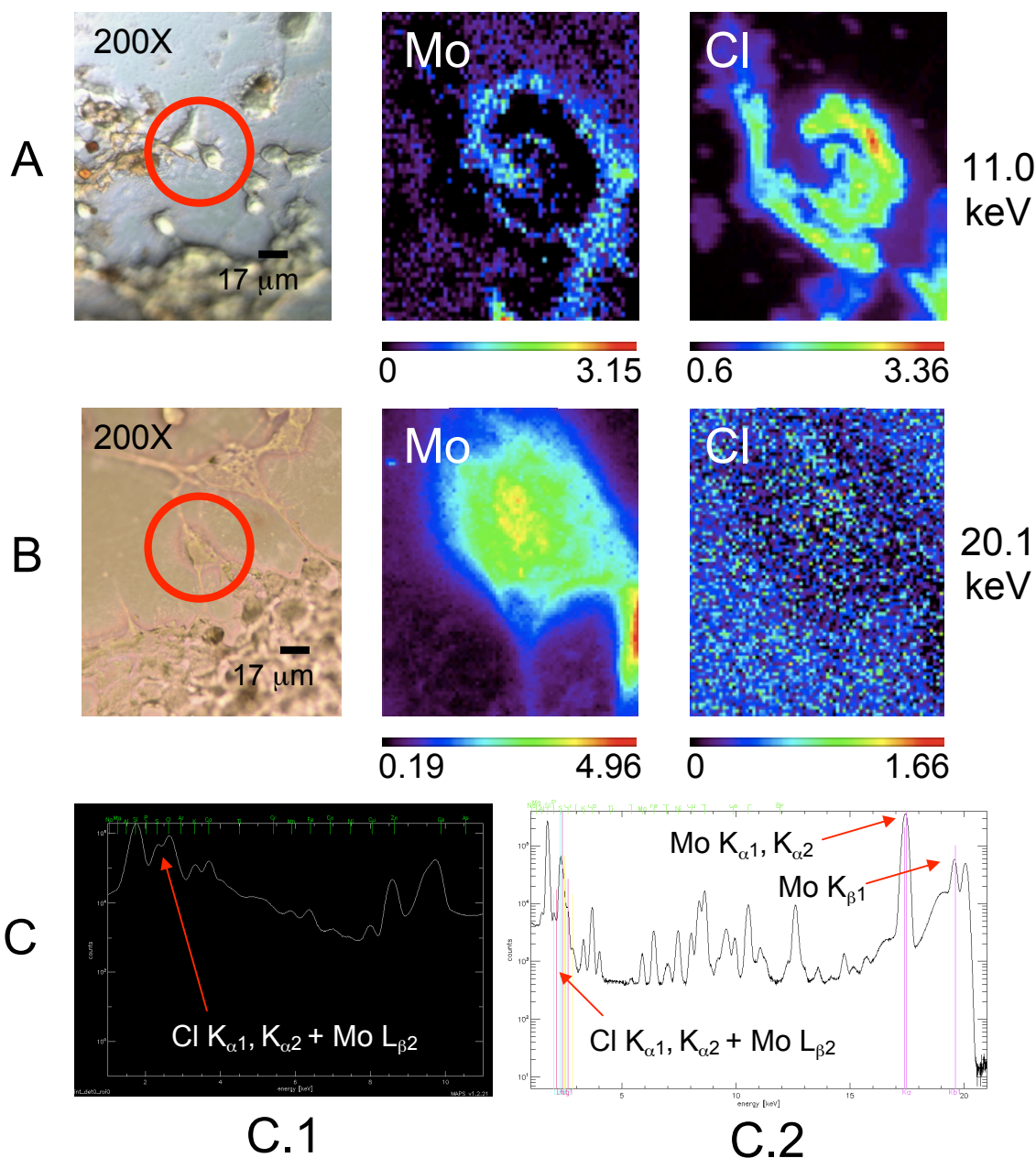


Figure 5.6 A. Light microscope image and XRF elemental distribution maps of Mo and Cl for a TM-treated HEPG2 whole cell (1 mM, 24 h), collected at 11.0 keV; B. Light microscope image and elemental distribution maps of Mo and Cl for a TM-treated HEPG2 whole cell (1 mM, 24 h), collected at 20.1 keV; C. Fluorescence spectrum integrated over TM-treated HEPG2 cell (1 mM, 24 h), collected at 11.0 (C.1) and 20.1 keV (C.2) (intensity scale in $\mu\text{g}/\text{cm}^2$).

5.3.5 XRF of control HEPG2 cells. Although the distribution maps for a single TM-untreated HEPG2 cell (average diameter $\sim 15 \mu\text{m}$) (Figure 5.7) were not clearly resolved mostly due to the high energy used (20.1 keV), cells were defined from the localization of only Zn, Cl and K, while Mo was not detected.

5.3.6 XRF of TM-treated HEPG2 cells. At 20.1 keV, elemental maps of TM-treated HEPG2 cells (average diameter $\sim 17 \mu\text{m}$) were clearly resolved and defined from localization of P, K, Ca and Zn (Figure 5.8, 5.9, 5.10). Areas of high concentration of P and Zn indicated the localization of the nucleus of the cell, representing the nuclear DNA and the Zn finger transcription factors. The Mo map showed an uneven cytoplasmatic dispersion of TM, being slightly higher near the area that represents the nucleus (colocalization P, Zn and Mo). These XRF data proposed two clear hypotheses: either TM is trapped in or on the membrane of these cells, or there is effective cellular uptake of TM. Additionally, the total Mo concentration for these TM-treated HEPG2 cells was calculated as explained before in experimental procedures, showing an average Mo concentration of 4.59 pc/cell (range: 3.29–5.35 pc/cell) or 19.8 mM/cell (range: 14.2–23.0 mM/cell) (pc = picograms) (Figure 5.11), results that agreed with data obtained by ICP-MS ($[\text{Mo}] = 21.0 \text{ mM/cell}$).

5.3.7 XRF of thin-section of TM-treated HEPG2 cells. To determine whether TM was taken to an intracellular level or was only trapped over membrane of the cell, we decided to analyze a 2D slice of a TM-treated HEPG2 cell by XRF at 20.1 keV (1 mM, 24 h). Only the elemental maps of Cl, K, Zn, Cu, Zr, and Mo are shown in Figure 5.12, because their signals significantly exceed the background produced by the Spurr's resin. There was a little higher concentration of Zn towards the tip of the cell, which may suggest the localization of the nucleus. The thin-section barely showed Mo inside of the cell, with very small detectable quantities

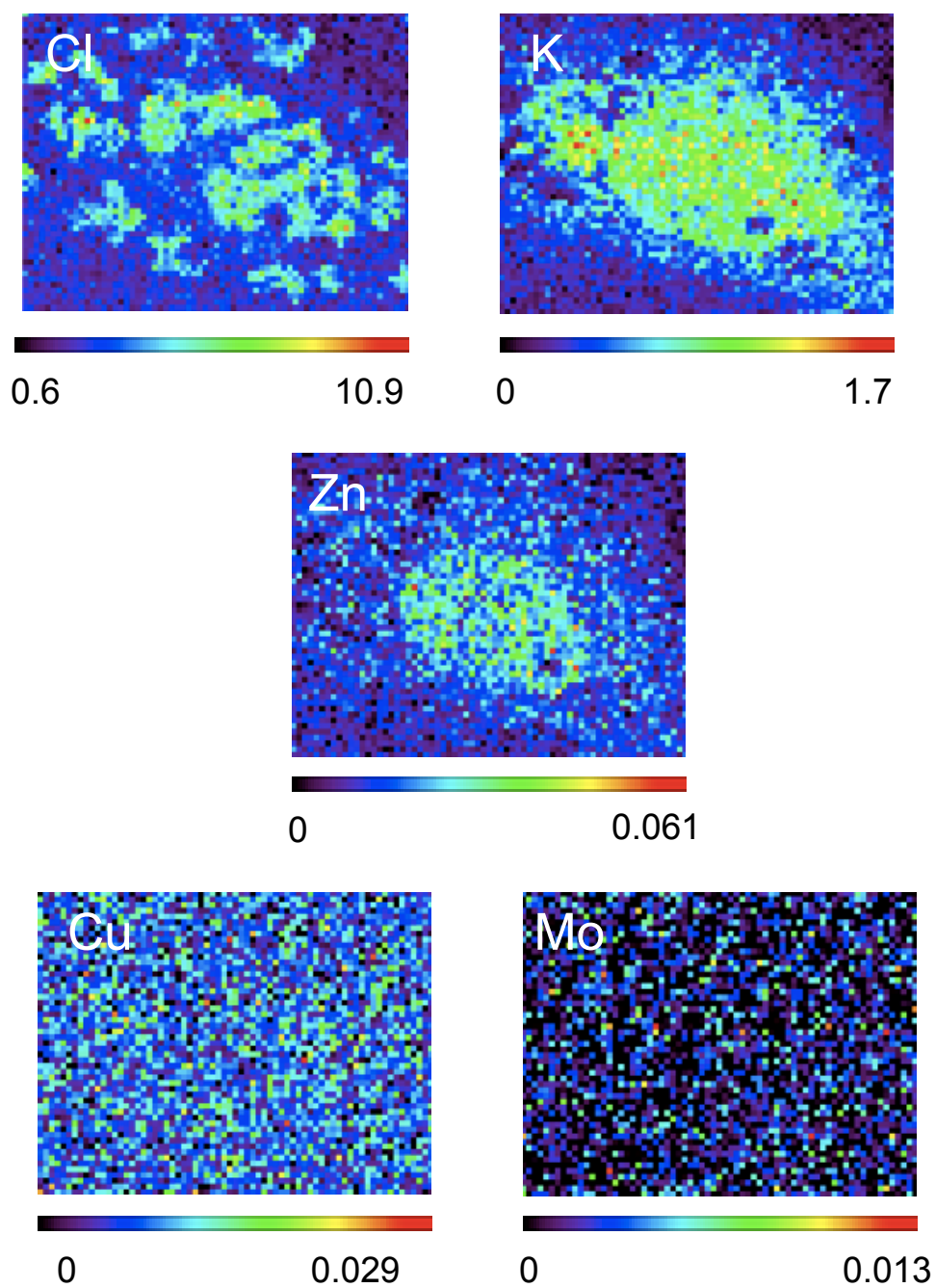


Figure 5.7 XRF elemental distribution maps of Cl, K, Zn, Cu and Mo for a TM-untreated HEPG2 whole cell, collected at 20.1 keV (intensity scale in $\mu\text{g}/\text{cm}^2$).

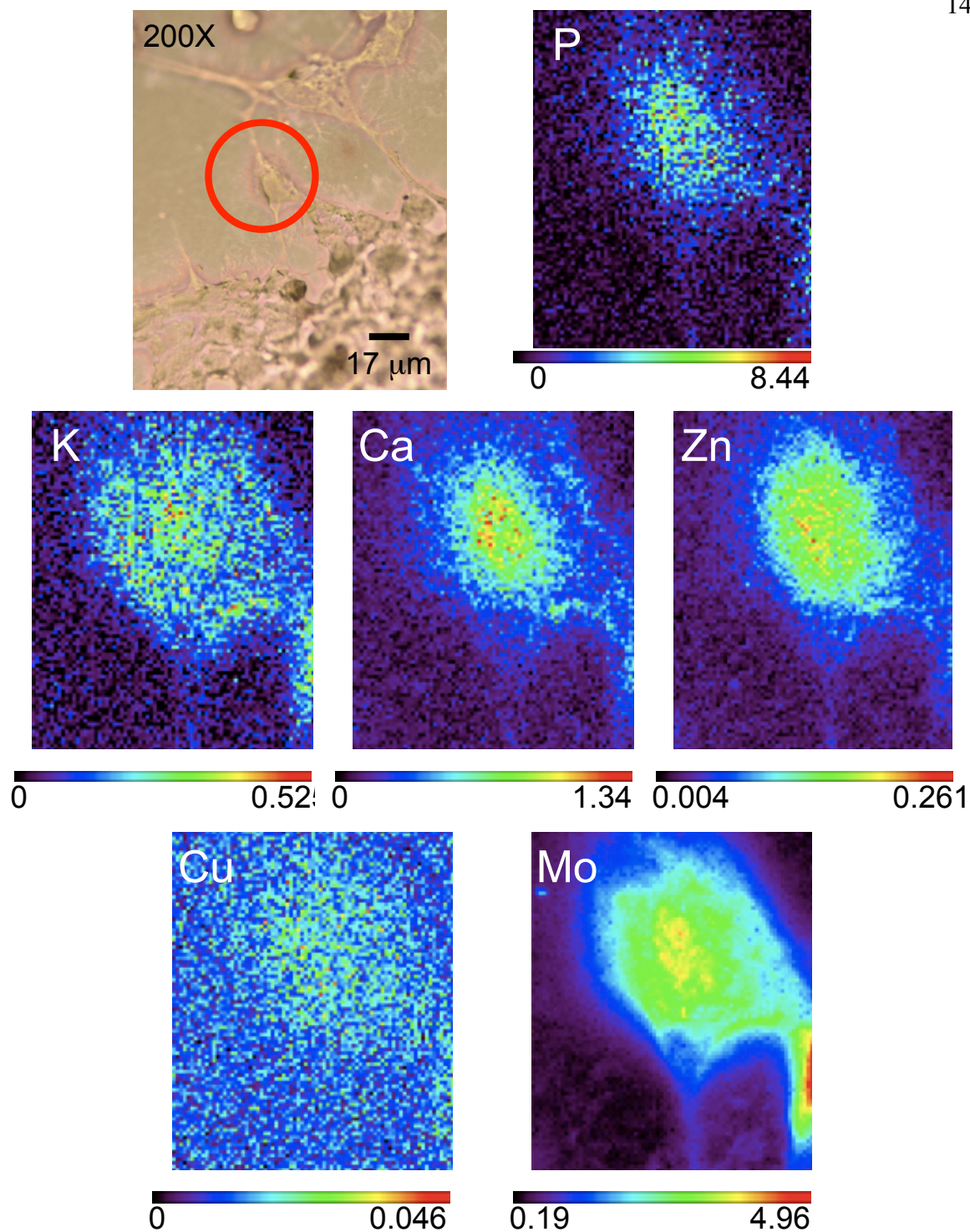


Figure 5.8 Light microscope image and XRF elemental distribution maps of P, K, Ca, Zn, Cu and Mo, for a TM-treated HEPG2 whole cell (1 mM, 24 h), collected at 20.1 keV (intensity scale in $\mu\text{g}/\text{cm}^2$).

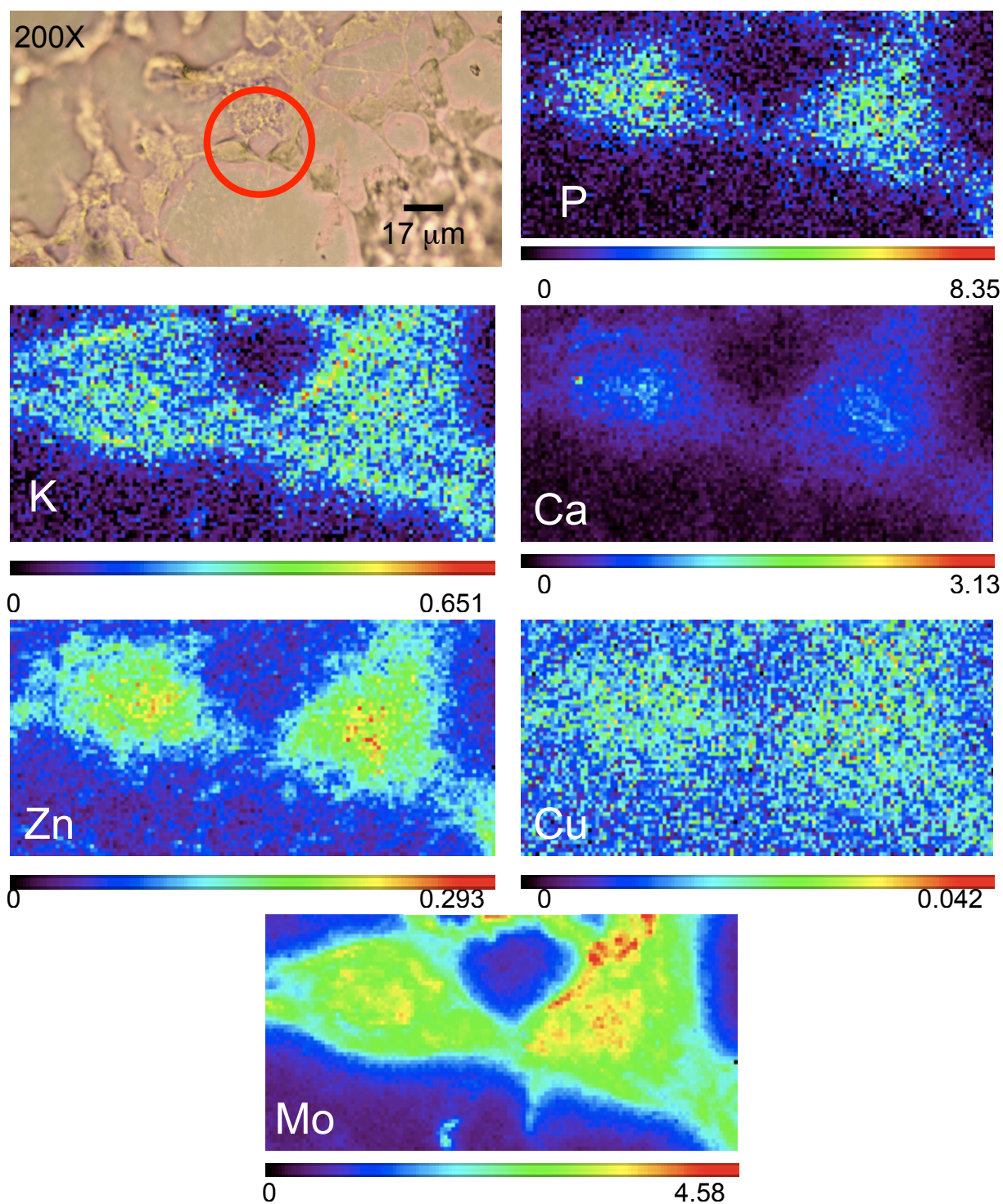


Figure 5.9 Light microscope image and XRF elemental distribution maps of P, K, Ca, Zn, Cu and Mo, for TM-treated HEPG2 whole cells (1 mM, 24 h), collected at 20.1 keV (intensity scale in $\mu\text{g}/\text{cm}^2$).

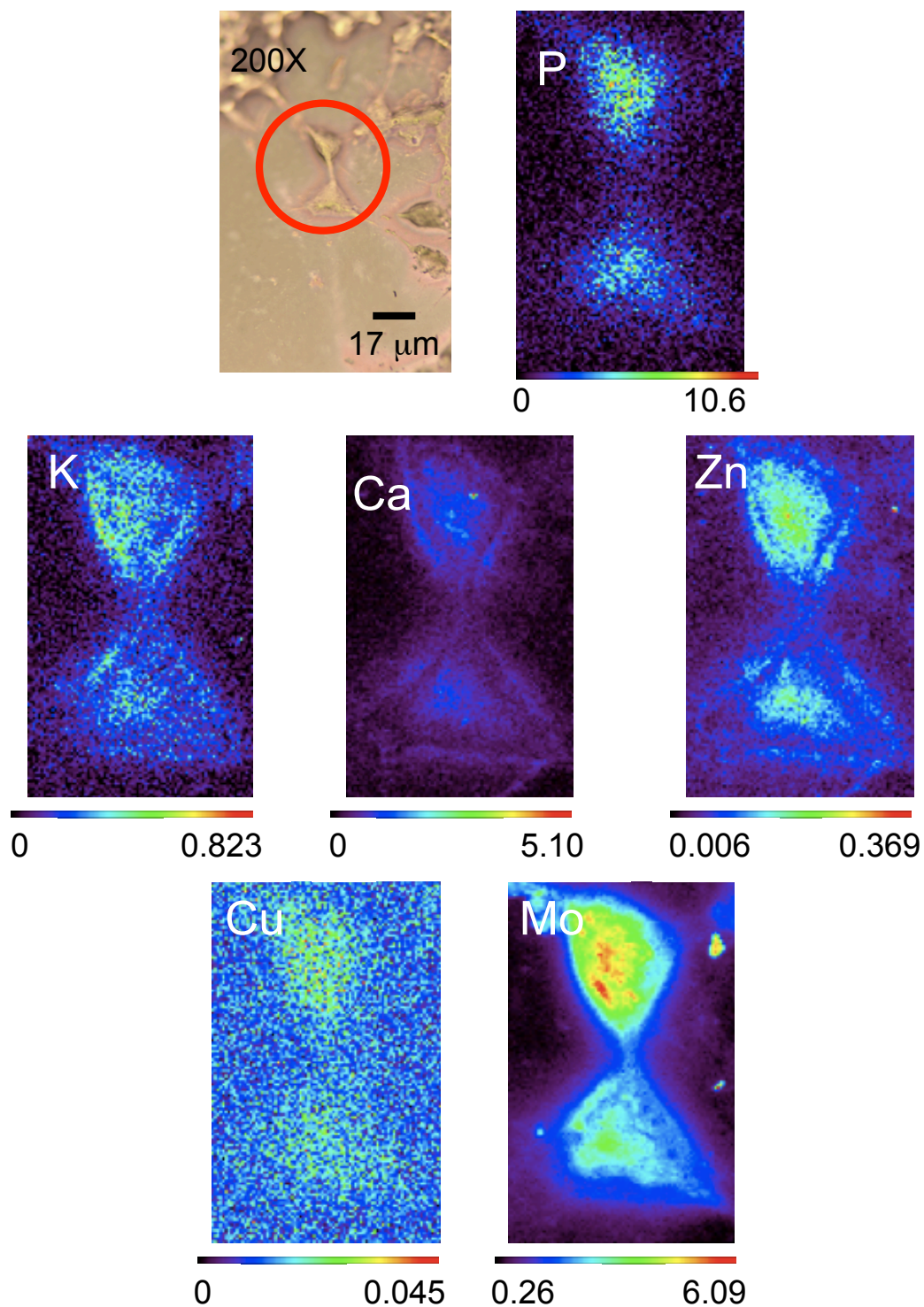


Figure 5.10 Light microscope image and XRF elemental distribution maps of P, K, Ca, Zn, Cu and Mo, for TM-treated HEPG2 whole cells (1 mM, 24 h), collected at 20.1 keV (intensity scale in $\mu\text{g}/\text{cm}^2$).

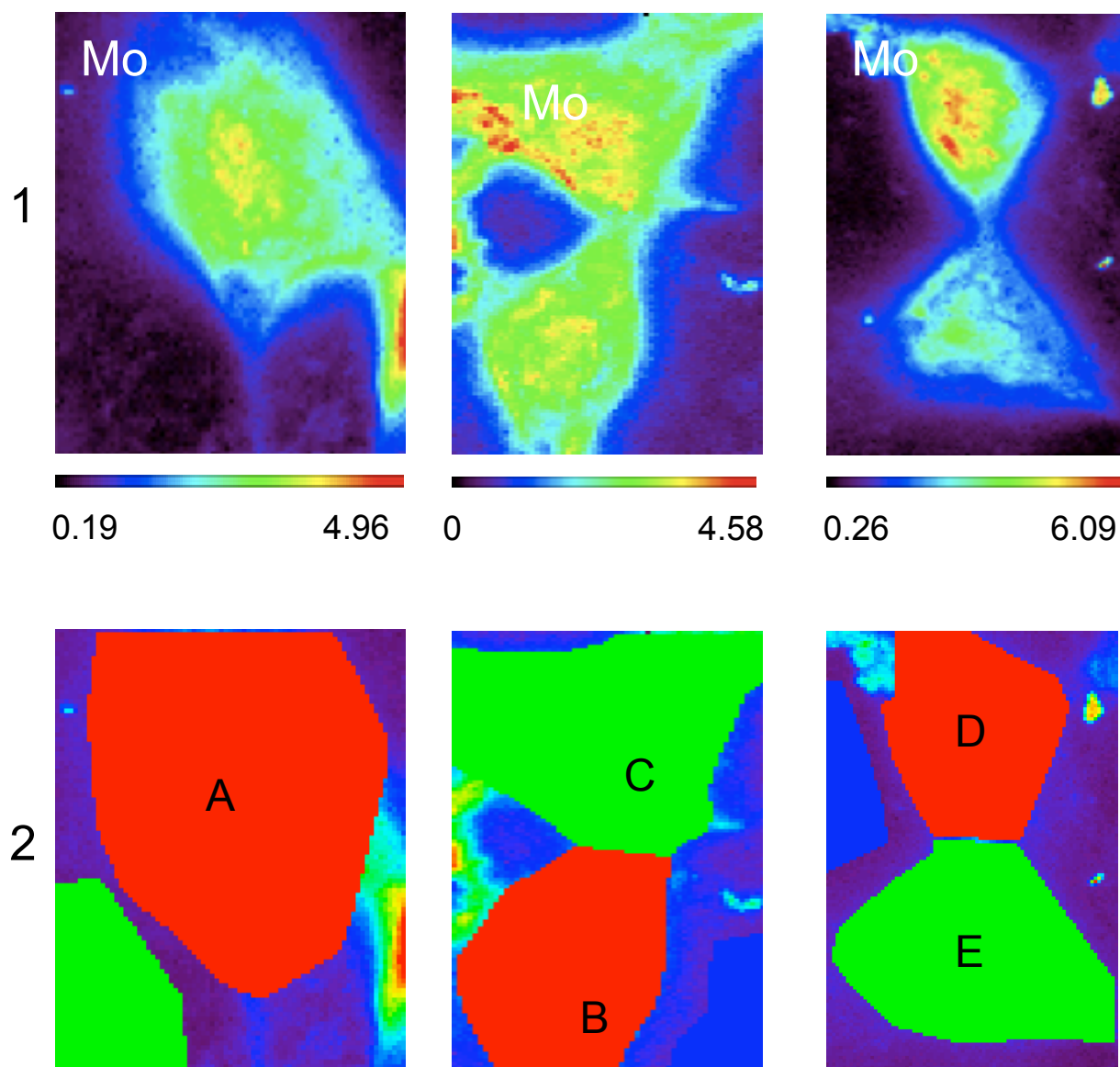


Figure 5.11 1. XRF elemental distribution maps of Mo for TM-treated HEPG2 whole cells (1 mM, 24 h), collected at 20.1 keV (intensity scale in $\mu\text{g}/\text{cm}^2$); 2. HEPG2 total intracellular Mo (\sim TM) concentration in mM/cell (pc/cell), A: 23.0 (5.35), B: 14.2 (3.29), C: 21.6 (5.02), D: 21.9 (5.08), E: 18.1 (4.20) (converted from pc/cell to mM/cell using formula described in experimental procedure).

([Mo]: 0–0.0191 $\mu\text{g}/\text{cm}^2$), maybe due to some contamination with Zr found on the sample ([Zr]: 0–0.334 $\mu\text{g}/\text{cm}^2$). The Zr $\text{K}\beta$ line at 17.67 keV overlapped considerably with the Mo $\text{K}\alpha$ line at 17.48 keV, which causes a very low Mo elemental map after fitting the fluorescence spectra (Figure 5.12).

5.3.8 Micro-XANES of TM-treated HEPG2 cells. Micro-XANES analysis of reference compounds showed the characteristic Mo pre-edge feature ($1s \rightarrow 4d$ transition) centered around 20,005 – 20,008 eV ([MoS_4] $^{2-}$ \sim 20,005 eV, [$\text{Mo}^{(\text{VI})}\text{S}_2\text{O}_2$] $^{2-}$ \sim 20,008 eV, [CuMoS_4] $_{\text{X}}$ \sim 20,007 eV) (Figure 5.13). Micro-XANES analysis of different TM-treated HEPG2 cells (1 mM, 24 h) showed a similar Mo pre-edge at all different tested regions [Figure 5.14 around 20,007.2 eV, Figure 5.15 around 20,007 eV, and Figure 5.16 around 20,007.8 eV], with the exception of the extracellular region E on Figure 5.16. Due that the Mo pre edge value for the TM-treated cells is more similar to the ones of [CuMoS_4] $_{\text{X}}$ and [$\text{Mo}^{(\text{VI})}\text{S}_2\text{O}_2$] $^{2-}$, we can suggest two different hypotheses: either the intracellular TM is coordinated to copper, or there is some kind of intracellular disruption by oxygenation of the TM.

5.3.9 TM inhibition of intracellular SOD1 activity in HEPG2 cells. Intracellular inhibition of SOD1 in HEPG2 cells was calculated using an UV-visible spectroscopy SOD1 activity assay, as described in experimental procedures. HEPG2 SOD1 cytoplasmatic inhibition was only time dependent during the first two hours, with a maximal IC_{50} value of 0.309 ± 0.03 μM after 24 of incubation (Figure 5.17). This IC_{50} value for cytoplasmatic inhibition of SOD1 is much lower than the IC_{50} for cell proliferation ($\text{IC}_{50} \sim 19.8$ μM , $t_{\text{incub}} > 24$ h), which means that we need higher concentrations of TM to produce any inhibition of the cell proliferation of this cancer cell line.

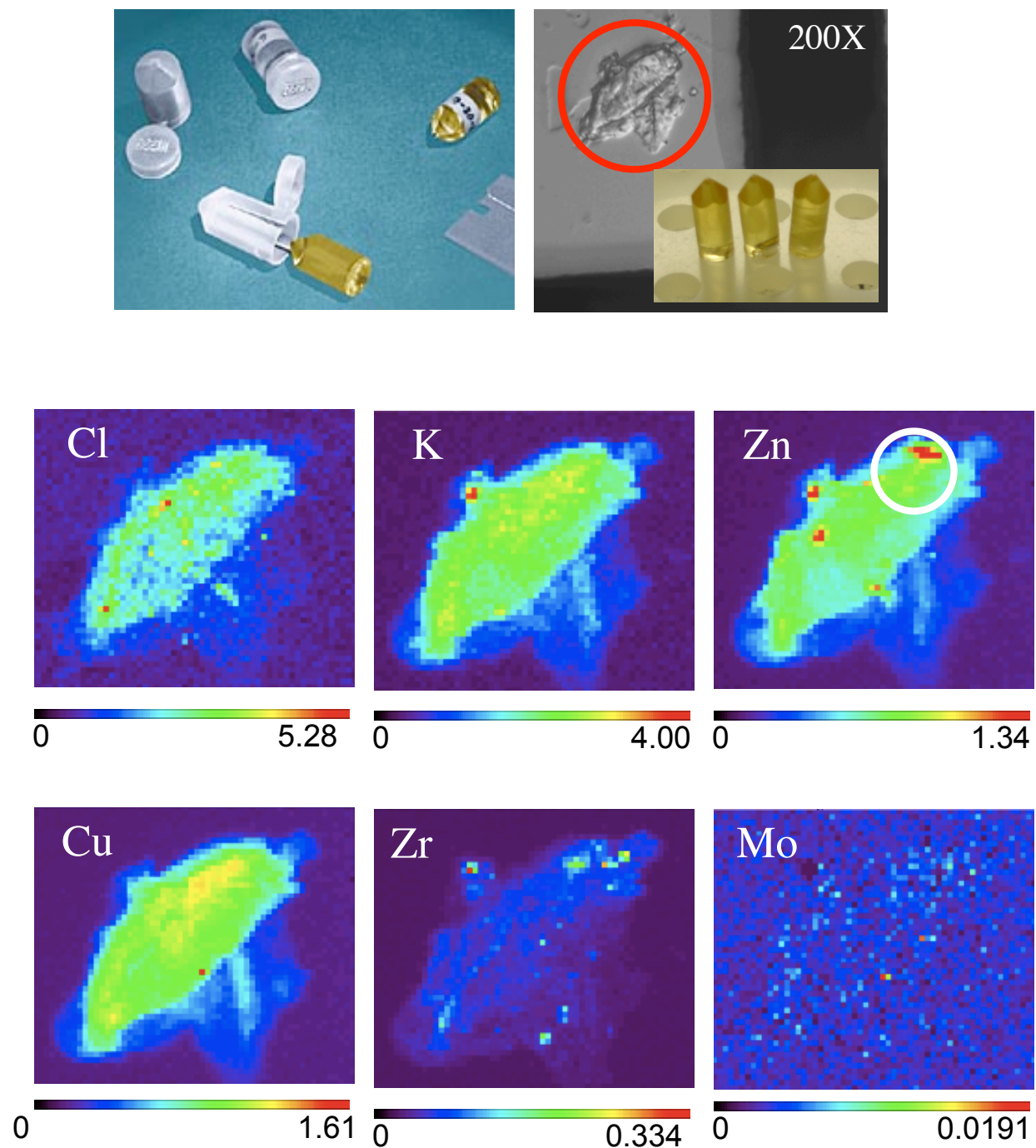


Figure 5.12 Light microscope image (inset: Spurr's resin blocks) and XRF elemental distribution maps of Cl, K, Zn, Cu and Mo, for a TM-treated thin-section ($0.1 \mu\text{M}$) HEPG2 cell (1 mM , 24 h), collected at 20.1 keV (intensity scale in $\mu\text{g}/\text{cm}^2$).

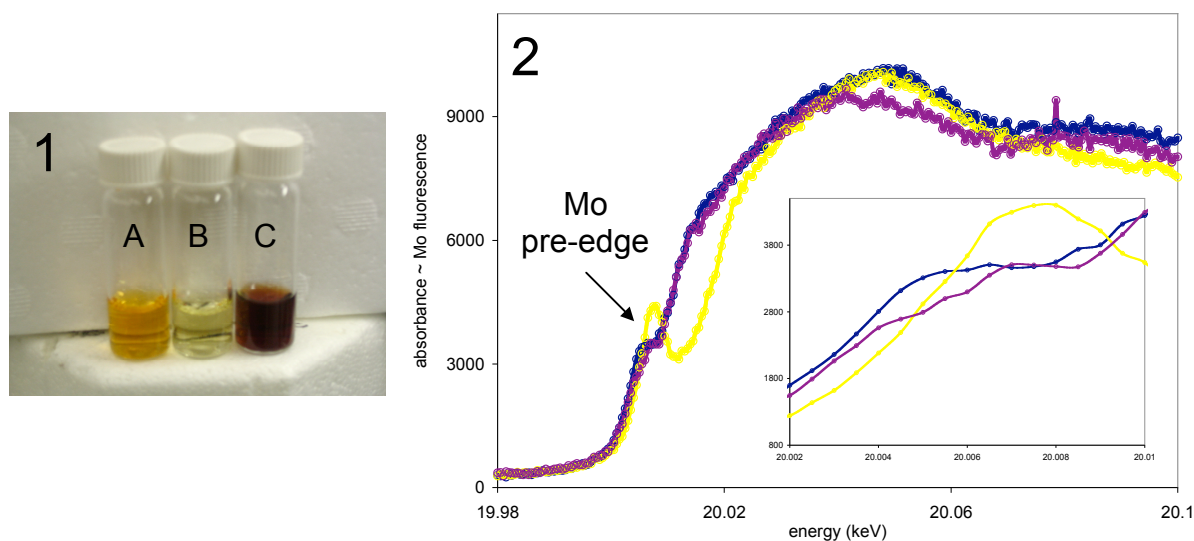


Figure 5.13 1. XANES reference compounds, 2. XANES reference spectra. $[\text{MoS}_4]$ (A, \circ), $[\text{MoS}_2\text{O}_2]$ (B, \circ), $[\text{CuMoS}_4]_x$ (C, \circ) (inset: closer view of K-edge XA bands).

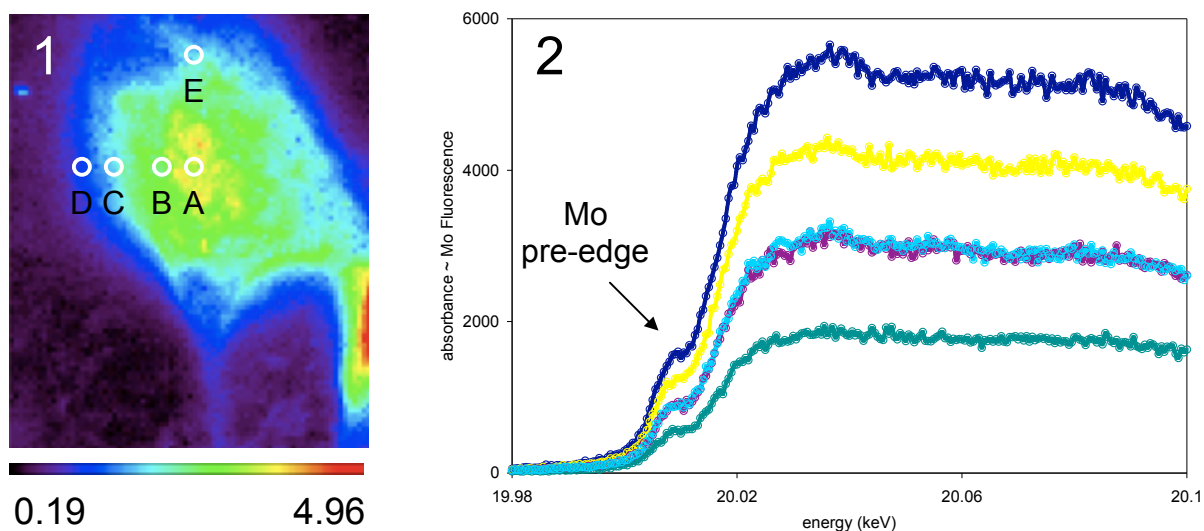


Figure 5.14 1. XRF elemental distribution map of Mo for a TM-treated HEPG2 whole cell (1 mM, 24 h), collected at 20.1 keV (intensity scale in $\mu\text{g}/\text{cm}^2$); 2. XANES spectra collected at different cell regions (white circles) (Mo pre-edge $\sim 20,007.2$ eV) [A (\circ), B (\circ), C (\circ), D (\circ), E (\circ)].

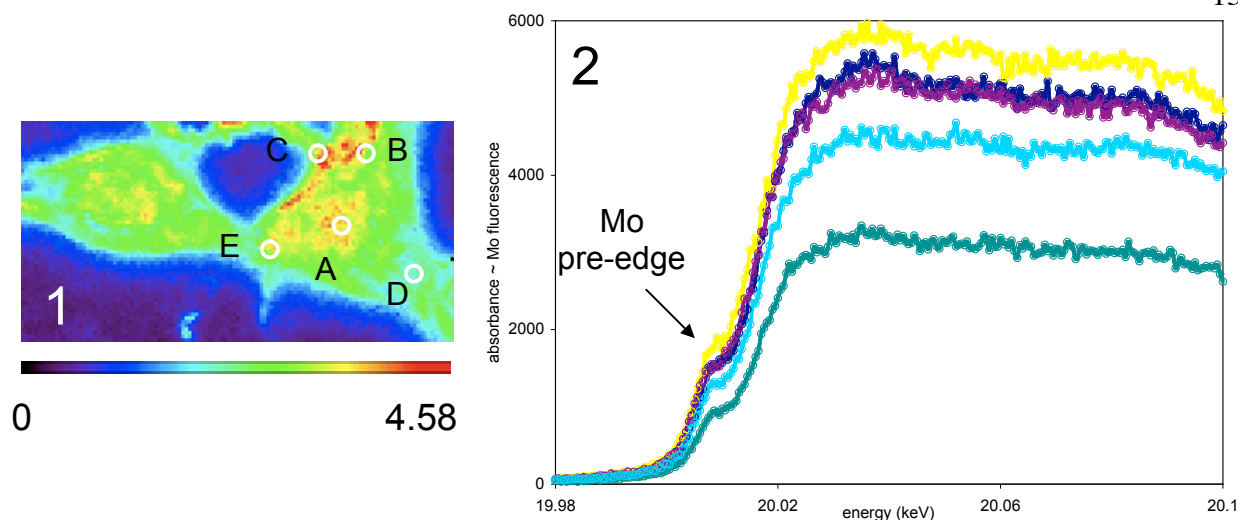


Figure 5.15 1. XRF elemental distribution map of Mo for TM-treated HEPG2 whole cells (1 mM, 24 h), collected at 20.1 keV (intensity scale in $\mu\text{g}/\text{cm}^2$); 2. XANES spectra acquired at different cell regions (white circles) (Mo pre-edge $\sim 20,007$ eV) [A (\circ), B (\circ), C (\circ), D (\circ), E (\circ)].

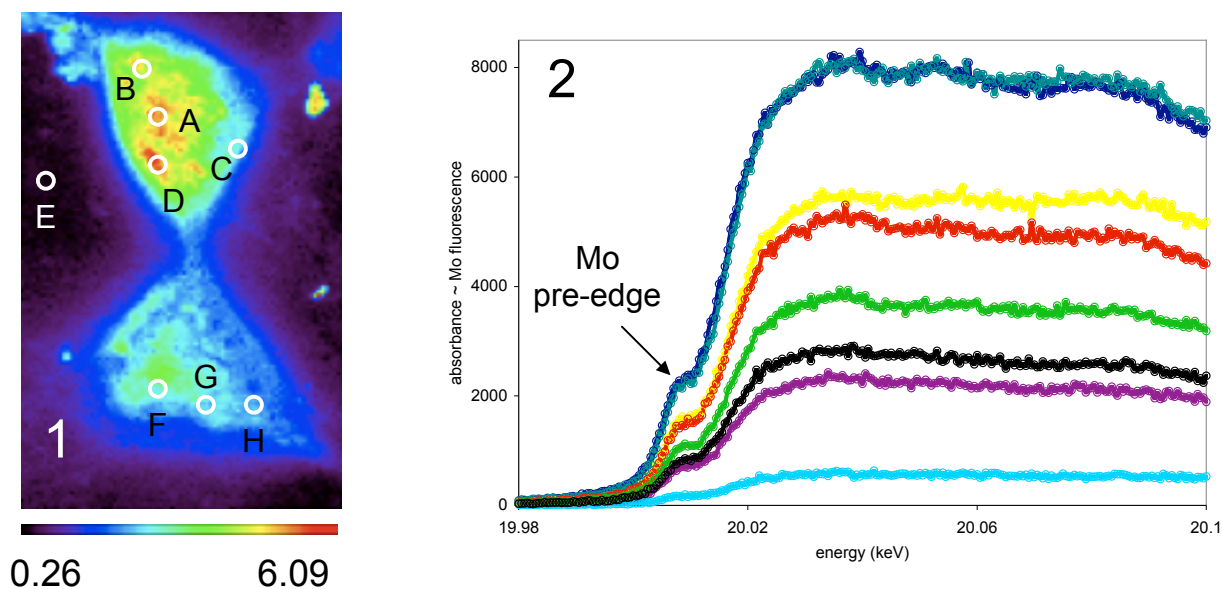


Figure 5.16 1. XRF elemental distribution map of Mo for TM-treated HEPG2 whole cells (1 mM, 24 h), collected at 20.1 keV (intensity scale in $\mu\text{g}/\text{cm}^2$); 2. XANES spectra acquired at different cell regions (white circles) (Mo pre-edge $\sim 20,007.8$ eV) [A (\circ), B (\circ), C (\circ), D (\circ), E (\circ), F (\circ), G (\circ), H (\circ)].

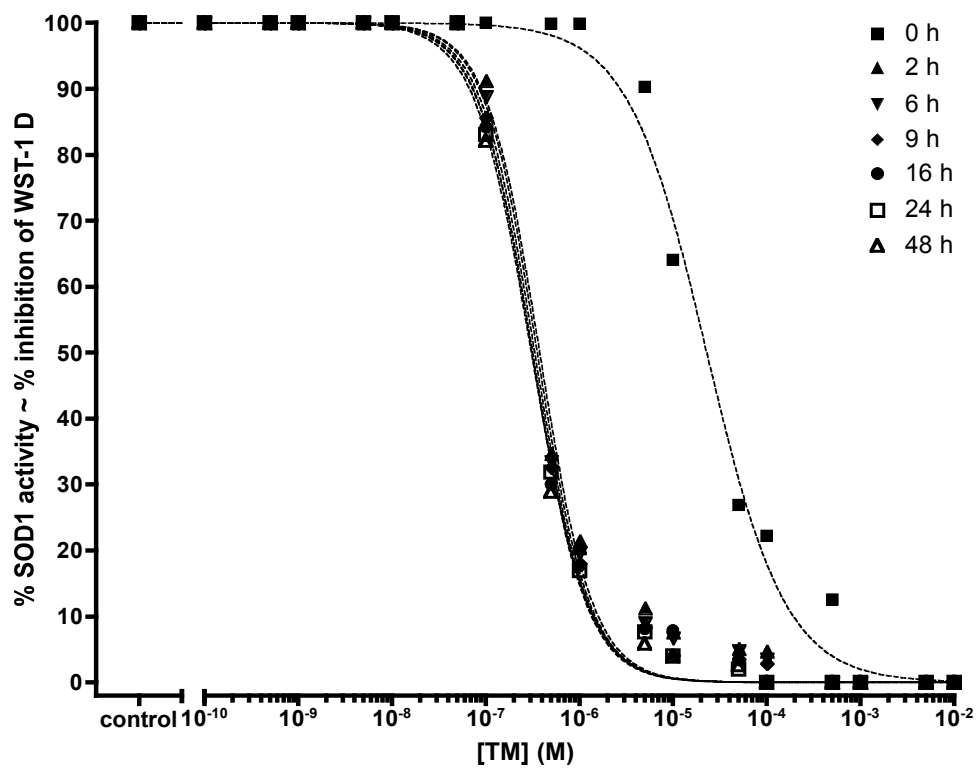


Figure 5.17 UV-visible spectroscopy HEPG2-SOD1 activity assay. TM inhibited intracellular-HEPG2 SOD1 activity with a maximal $IC_{50} = 0.309 \pm 0.03 \mu\text{M}$ ($n = 3$, $t_{\text{incub}} > 24 \text{ h}$).

5.4 Discussion and Conclusion

In this chapter, we utilized XRF microscopy and ICP-MS for detecting and analyzing the intracellular uptake, distribution and coordination environment of the TM drug in whole and thin-sectioned HEPG2 cells, in addition to cytotoxicity and SOD1 intracellular inhibition studies.

ICP-MS and XRF microscopy were performed in order to confirm that the sample preparation did not alter the Mo concentration and to evaluate if there is intracellular accumulation of the drug. Molybdenum ICP-MS measurements of TM-treated HEPG2 cells ($[TM]_i = 1.0 \text{ mM}$, $t_{\text{incub}} = 24 \text{ h}$) showed a total Mo intracellular concentration of 21.0 mM (~ 21 -fold higher), which matched the data from XRF, 19.8 mM (~ 20 -fold higher). It is important to highlight that these values are similar to the ones proposed for HUVEC cells treated with 20 μM ATN-224[®] ($t_{\text{incub}} = 16 \text{ h}$, $[Mo]_{\text{intracellular}} = 411 \text{ }\mu\text{M}$, ~ 21 -fold higher)¹¹, concluding that endothelial cells and cancer cells show a similar uptake of tetrathiomolybdate.

Other human cell types such as red blood cells (RBC) [$IC_{50} = 5.0 \text{ }\mu\text{M}$ (SOD1), TM],¹¹ umbilical vascular endothelial cells (HUVEC) [$IC_{50} = 0.02 \text{ }\mu\text{M}$ (SOD1), $t_{\text{incub}} = 16 \text{ h}$; $IC_{50} = 1.4 \pm 0.3 \text{ }\mu\text{M}$ (cell proliferation), $t_{\text{incub}} = 48 \text{ h}$, ATN-224[®]]¹³ and multiple myeloma cells (MM1S) [$IC_{50} = 0.04 \text{ }\mu\text{M}$ (SOD1); $IC_{50} = 5.0 \text{ }\mu\text{M}$ (cell proliferation), $t_{\text{incub}} = 96 \text{ h}$, ATN-224[®]]¹³ showed IC_{50} values for inhibition of intracellular SOD1 and proliferation (with TM or ATN-224), that are slightly different in comparison with the correspondent values for HEPG2 cells [$IC_{50} = 0.309 \pm 0.03 \text{ }\mu\text{M}$ (SOD1), $t_{\text{incub}} = 48 \text{ h}$; $IC_{50} = 7.3 \pm 0.09 \text{ }\mu\text{M}$ (cell proliferation), $t_{\text{incub}} = 72 \text{ h}$, TM). The small differences in inhibition of SOD1 and cell proliferation can be attributed to the particular characteristics of the composition of the cell membrane in different types of human cells.

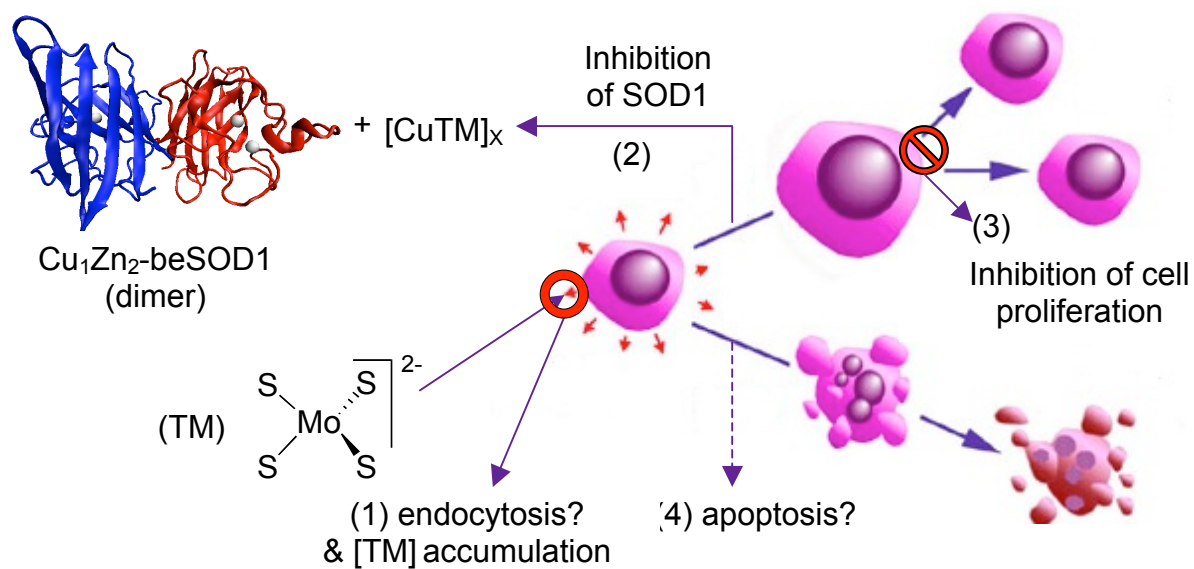
XRF microscopy studies of whole and thin-sectioned HEPG2 cells were performed to test the cellular uptake of TM, and to analyze the coordination environment of this drug. While XRF

analysis of whole cells suggested the intracellular uptake of the drug, the low-resolution Mo map of the thin-section sample showed a very low Mo concentration. A new thin-section cell sample should be analyzed by XRF avoiding any kind of Zr contamination to be able to finally confirm if there is an intracellular uptake of TM. Although no colocalization of Mo and Cu was observed in XRF elemental maps, the shifting of the Mo pre-edge feature detected by micro-XANES (20,005 \rightarrow 20,007.3 eV), may be understood as the hypothetical intracellular coordination of TM with copper.

Sub-cellular fractionation studies by ultracentrifugation of TM-treated cells are needed to confirm the apparent high TM nuclear concentration suggested by XRF microscopy, or to try to determine whether TM can be selectively trapped but any other organelles (i.e. lysosomes). It is important to mention that additional studies are necessary to determine if the transport of TM across the membrane of HEPG2 cells, is by a passive (simple diffusion, channel- or pore-mediated, membrane transporter-mediated) or active transport mechanism (endocytosis).

Moreover, additional cell studies of other well-studied cancer cell lines [e.g. breast (MCF-7), colon (HT-29), bone marrow (K-256), larynx (HEP-2), lung (NCI-H510A), etc] are still necessary to find out which cancer type is more susceptible to the action TM. Fluorescence microscopy studies of TM-treated cells should be performed to figure out the intracellular colocalization of Mo and Cu, using the preliminary luminescence studies of the [TM]([Cu)(Cu-Atx1)₃] complex (Chapter 2).

In conclusion, this chapter demonstrates the HEPG2 intracellular uptake of TM by an unknown mechanism, and the consequent inhibition of the SOD1 and cell proliferation (Scheme 5.3). These studies validate the proposed intracellular mechanism of action for TM.

Scheme 5.3 Intracellular uptake mechanism of TM by HEPG2 cells.

Chapter 6

TM inhibition of copper transfer activity of Atx1

Abstract

The stable and inert [TM][(Cu)(Cu-Atx1)₃] drug-protein adduct results of the interaction of TM with Cu-Atx1. This yeast metallochaperone transfers copper to an intracellular trafficking pathway via interaction with the domain A of the ATPase, Ccc2. We found that incubation of Cu-Atx1 with apo-Ccc2a (1:1) leads to the formation of the [Atx1-Cu-Ccc2a] heterodimer, while the reaction of [TM][(Cu)(Cu-Atx1)₃] with apo-Ccc2a (1:1) leads to the formation of two protein-protein complexes: [Atx1-Cu-Ccc2a] and a new [(TM)(Cu)(Atx1)(Ccc2a)]. The components of these complexes were characterized by native gel electrophoresis, ESI-MS, ICP-MS and LA-ICP-MS, which identified the proteins and the metals, respectively. We were able to detect the copper transfer between Cu-Atx1 and apo-Ccc2a. We also showed that TM binding to Atx1 prevents the copper transfer and thus inhibits the copper chaperon function of Atx1.

The proposed disruption of the intracellular copper metabolism provides insights into the possible intracellular mechanism of action of ammonium tetrathiomolybdate (TM), as a copper chelator drug for the antiangiogenic treatment of neovascularization diseases.

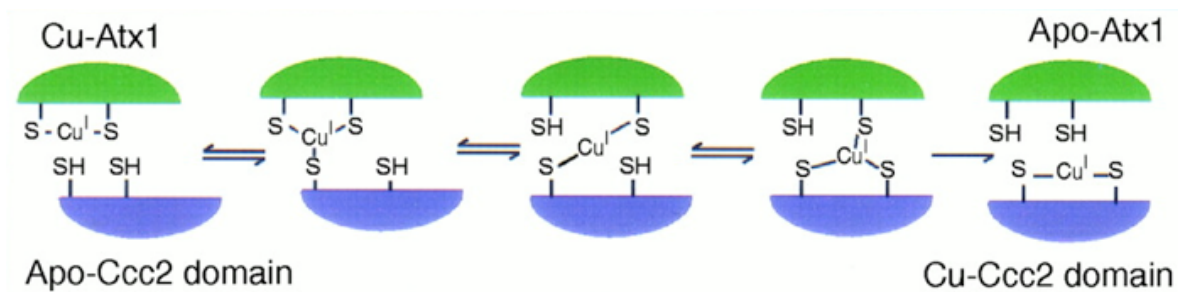
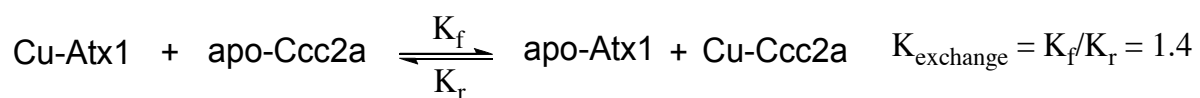
6.1 Introduction

Several human disorders are caused by the disruption of the physiological trafficking of copper.¹ Metallochaperones constitute a particular kind of protein that deliver metal ions, including copper, to proper cytoplasmic targets in the cell.² The yeast metallochaperone, Atx1, transfers copper to a trafficking pathway via interaction with the domain A of the ATPase, Ccc2.³ Positive lysine residues of Atx1 interact with a negatively charged region of Ccc2a. This electrostatic interaction between these two proteins facilitates the delivery of copper.⁴ The different copper-bridged intermediates between the active sites of these two enzymes are depicted in Scheme 6.1.^{3,4} By analogy, Atox1, the human copper metallochaperone interacts with two copper-transporting ATPases: Menke's and Wilson's disease proteins.⁵

Although an extracellular mechanism has been proposed for the copper deficiency caused by the action of ammonium tetrathiomolybdate (TM) during the treatment of Wilson's disease and cancer,⁶ in this last Chapter we will present the evidence that will lead us to introduce an additional step of the already hypothesized intracellular mechanism of action. Knowing that TM induced the inhibition of the *Enterococcus hirae* CopB copper-transporting ATPase ($IC_{50} = 34$ nM)⁷, here we demonstrate that the interaction of TM with Cu-Atx1 disrupts the cell's tightly controlled intracellular Cu trafficking pathway, preventing the translocation of copper to the domain A of the P-type ATPase Ccc2a and to the multicopper oxidase Fet3.

The work presented in this chapter was done in collaboration with Monica Canalizo (electrophoresis), Dr. Yang Wang (ESI-MS, UIC), and Rebeca Marvin (ICP-MS and LA-ICP-MS).

Scheme 6.1 Proposed path for the intracellular transfer of Cu^{I} from Atx1 to Ccc2a.^{3,4}



6.2 Experimental Procedure

6.2.1 Preparation and purification of protein samples. The wild-type Ccc2a, Cu-Cc2a, Se-Met-Atx1 and Cu-Se-Met-Atx1, and [TM][(Cu)(Se-Met-Cu-Atx1)₃] were expressed, prepared, purified and metallated, as previously described in Chapter 3.^{4,8,9}

6.2.2 UV-Vis Titration spectroscopy. To a 0.2 mM solution of [TM][(Cu)(Cu-Se-Met-Atx1)₃] (20 mM MES, pH 6.0, 0.15 M NaCl) were added 5.2 μ l aliquots of a 1.91 mM apo-Ccc2a solution at 25°C. Upon each addition, the sample solution was stirred for 10 min with a magnetic stirring device and the UV-visible spectrum was subsequently monitored. The UV-visible trace was corrected for dilution and analyzed by a molar ratio plot.

6.2.3 Native agarose gel electrophoresis. The 0.8% agarose gel (8 cm x 5.5 cm x 3 cm) was immersed in an electrophoresis box (Fisher Scientific) containing native gel buffer (25 mM Tris-Cl, pH 8.5, 19.2 mM glycine), placing the comb at the middle of the gel, and running it at 50 V for 2 h (room temperature). Each of the samples was prepared by mixing the protein (5 μ g of each protein) with loading buffer (20% glycerol, 0.2 % bromophenol blue, 0.12 M Tris base) in a 1:1 ratio ($V_l = 10 \mu$ l). Gel was stained in Coomassie blue for only 20 mins. After destaining, the gel was dried by sandwiching it between two pieces of cellophane for 48 h with compression (1–2 kg), using three sheets of filter paper on each side of the cellophane.¹⁰⁻¹² Samples include, apo-Se-Met-Atx1, Cu-Se-Met-Atx1, apo-Ccc2a, Cu-Ccc2a, [TM][(Cu)(Cu-Se-Met-Atx1)₃], Cu-Se-Met-Atx1 + apo-Ccc2a (1:1) ($t_{rxn} = 30$ min), and [TM][(Cu)(Cu-Se-Met-Atx1)₃] + apo-Ccc2a (1:1) ($t_{rxn} = 30$ min).

6.2.4 Isolation of proteins and components of protein-protein complexes by gel extraction. In order to extract the proteins and the components of the hypothetical protein–protein interactions, four identical samples of each protein or mixture (aprox. 5 μ g each

protein) were loaded on contiguous lanes using the same electrophoresis conditions previously described. Samples include, apo-Se-Met-Atx1, Cu-Se-Met-Atx1, apo-Ccc2a, Cu-Ccc2a, [TM][[(Cu)(Cu-Se-Met-Atx1)₃], Cu-Se-Met-Atx1 + apo-Ccc2a (1:1) ($t_{\text{rxn}} = 30$ min), and [TM][[(Cu)(Cu-Se-Met-Atx1)₃] + apo-Ccc2a (1:1) ($t_{\text{rxn}} = 30$ min). One of the four lanes was stained to identify the protein bands, and the unstained ones were cut out with a sharp glass. The isolated bands were transferred into an Ultrafree-DA unit (with gel nebulizer and filter device) (Millipore, Bedford, MA), and centrifuged at 5000 g for 10 min at 4°C. The gel particles were captured by the filter unit while the protein samples in the eluate were further concentrated by centrifugation at 14000 g, using a YM3 microcon ultrafiltration device (Millipore, Bedford, MA) until the volume of the samples were reduced to ~ 30 μl .¹³

6.2.5 Identification of proteins and components of protein-protein complexes by ESI-MS, ICP-MS and LA-ICP-MS. To identify the proteins present in each band observed in our native gel, we analyzed the concentrated protein samples after gel extraction by ESI-MS using a Finigan LTQ-FT LC/MS/MS ($m/z \pm 0.8$) (Thermo Scientific, Minneapolis, MN). The ESI-MS was previously calibrated with a Thermo Scientific calibration mixture (caffeic acid, peptide MRFA and ultramak). The 30 μl samples were injected in a Poroshell C3 0.2 x 75 mm reverse phase HPLC column (Agilent Technologies, Santa Clara, CA) and eluted using a mixture of 0.1% formic acid and 95% MQ H₂O and a gradient of 35-85% methanol. The molybdenum and copper concentrations (ppb) were measured by a Thermo Fischer X Series II ICP-MS (Thermo Scientific, Minneapolis, MN) and a UP 213 Nd:YAG LA (New Wave Research, Fremont, CA). For ICP-MS, samples were diluted with Mili-Q-water ($V_f = 3$ ml, 2% nitric acid), including 15 μl of 1 ppm ICP-MS internal standard (~ 5 ppb) (CPI International, Santa Rosa, CA) and subtracting the appropriate Mo and Cu control concentrations from a piece of the same

gel without any protein sample. Details for running ICP-MS experiments followed the conditions described in Chapter 5. Gel interrogation by laser ablation coupled with an ICP-MS (LA-ICP-MS)¹⁴⁻¹⁷ was conducted in collaboration with Rebecca Marvin. The gel was first dried for 48 h between two cellophane sheets to avoid cracks over the gel surface, and then mounted (with the cellophane) on a microscope slide. The 213 nm New Wave laser (1.2 mJ, 45 %) was set to initiate a single line scan starting at the top of each of the lanes of the gel with a scanning speed of $50 \mu\text{m s}^{-1}$, a pulse repetition frequency of 10 Hz and a 100 μm hole diameter. Pre-ablation of the full lane was performed at a reduced energy (20%) but using the same parameters as for the ablation. Tuning and calibration of the ICP-MS and quantification of estimates of Mo and Cu was performed with a SRM 612 glass standard (NIST, Gaithersburg, MD). Initially, a control gel (without any protein or metals) was analyzed as a blank for the experiment. Reported LA-ICP-MS scans (Cu & Mo) of native gel lanes represent the result of the second ablation.

6.3 Results

6.3.1 UV-Vis Titration spectroscopy. When different proportions of apo-Ccc2a and $[\text{TM}][(\text{Cu})(\text{Cu-Se-Met-Atx1})_3]$ were mixed in buffered solutions during a UV-visible titration, the immediately loss of the characteristic S—Mo ligand to metal charge transfer bands (LMCT) ($\lambda = 375 \text{ nm}$ and $\lambda = 532 \text{ nm}$, Chapter 2) of $[\text{TM}][(\text{Cu})(\text{Cu-Se-Met-Atx1})_3]$ was observed (Figure 6.1). Addition of apo-Ccc2a leads to the formation of two shoulders with λ_{max} at 332 and 495 nm, which are likely due to the shifting of the S—Mo LMCT bands due to the new interaction with the apo-Ccc2a forming a hypothetical $[(\text{TM})(\text{Cu})(\text{Atx1})(\text{Ccc2a})]$ or due to some kind of decomposition of the $[\text{TM}][(\text{Cu})(\text{Cu-Se-Met-Atx1})_3]$ into a mixture of apo-Atx1,

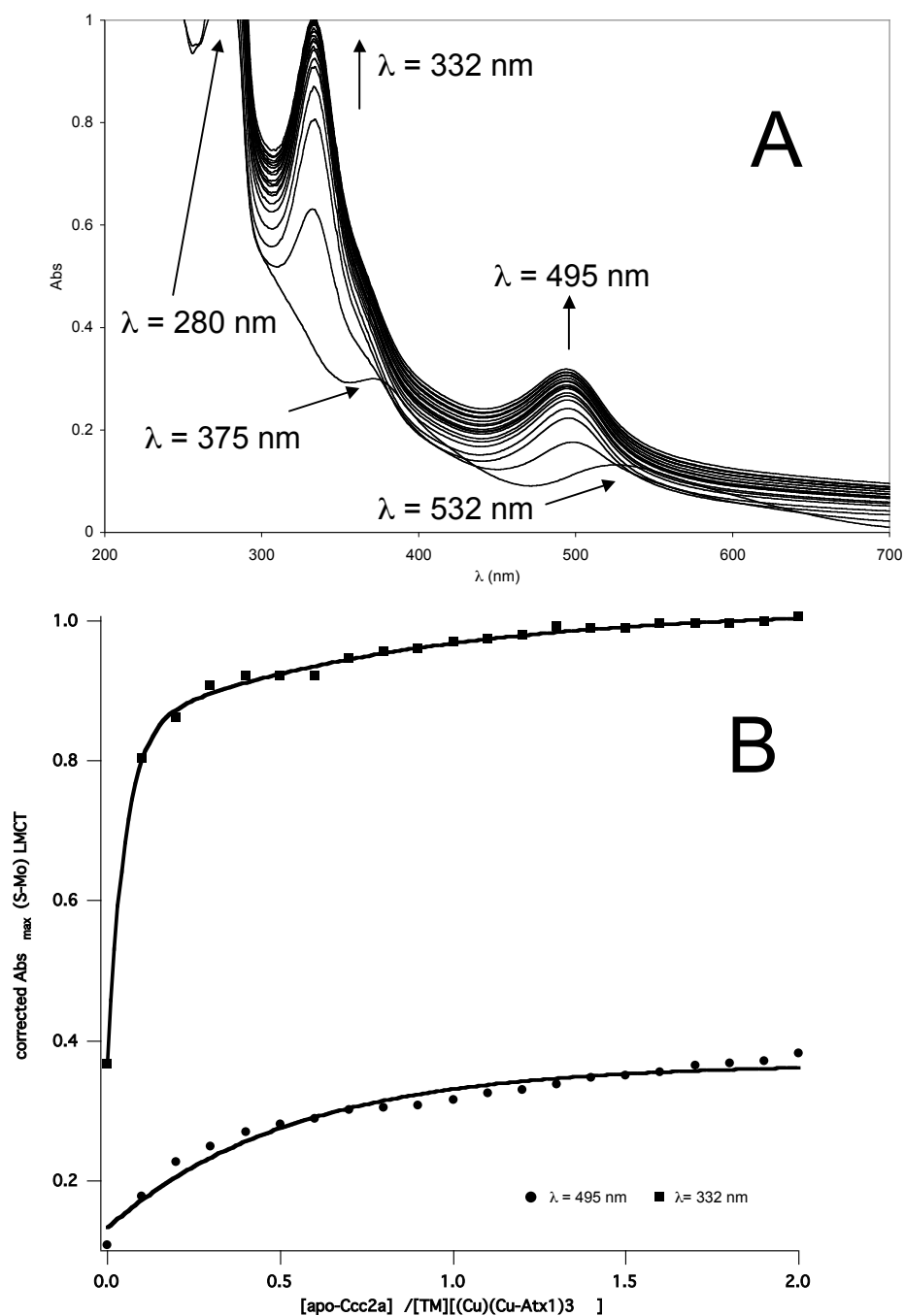
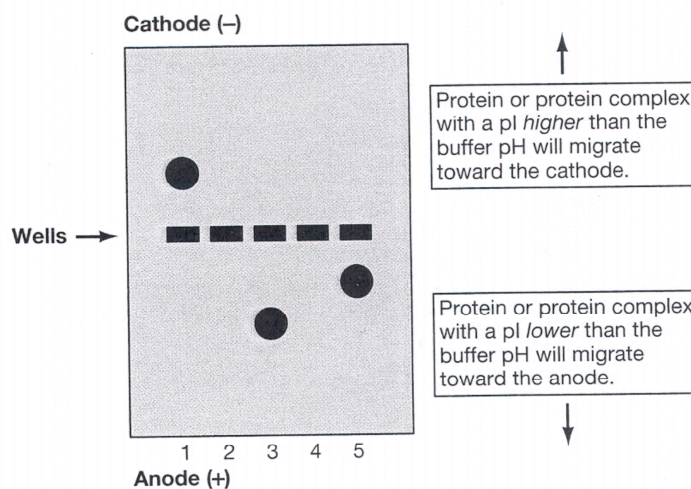


Figure 6.1 A. UV-visible absorbance of $[\text{TM}][(\text{Cu})(\text{Cu-Se-Met-Atx1})_3]$ as a function of added apo-Ccc2a. $[\text{TM}][(\text{Cu})(\text{Cu-Se-Met-Atx1})_3]$ (0.2 mM) was titrated with 0 – 2.0 equiv of 1.91 mM apo-Ccc2a (20 mM MES, pH = 6.0, 0.15 M NaCl, 25°C, aerobic conditions); B. Absorbance as a function of added apo-Ccc2a monitored at 332 and 495 nm (molar ratio plot).

Cu-Atx1, apo-Ccc2a, Cu-Ccc2a, TM and $[\text{CuTM}]_x$. The color change during the titration from purple to orange, and the current titration results suggested the formation of a new interaction of the $[\text{TM}][(\text{Cu})(\text{Cu-Se-Met-Atx1})_3]$ with the Ccc2a or that the Ccc2a is strong enough to disrupt the $[\text{TM}][(\text{Cu})(\text{Cu-Se-Met-Atx1})_3]$ complex.

6.3.2 Native agarose gel electrophoresis. The purpose of the native agarose gel electrophoresis experiment was to determine if the Ccc2a protein was causing the disruption of the $[\text{TM}][(\text{Cu})(\text{Cu-Se-Met-Atx1})_3]$ complex or was forming a new $[(\text{TM})(\text{Cu})(\text{Atx1})(\text{Ccc2a})]$ complex. Scheme 6.2 illustrates the migration of proteins with different pI and MW after running a native gel electrophoresis. The native agarose gel (Figure 6.2) showed some difference between apo-Atx1 (lane A) and Cu-Atx1 (lane B). The apo form clearly showed 2 bands (band # 1 & 2) which can be identified as the monomer and dimer respectively, while the Cu form showed only one (band # 3). Both proteins migrated to the cathode due to their basic character (positively charged, $pI = 8.64$). The apo-Ccc2a (lane D, band # 4) and Cu-Ccc2a (lane E, band # 5) migrated just slightly different to the anode due to their acidic character (negatively charged, $pI = 4.42$). The $[\text{TM}][(\text{Cu})(\text{Cu-Se-Met-Atx1})_3]$ (lane G, band # 6) migrated toward the cathode due that the Atx1 is constituent of this complex. The mixture of Cu-Se-Met-Atx1 + apo-Ccc2a (1:1) (lane H) showed two distinct bands that correspond to the Atx1 (band # 7) and Ccc2a (band # 9), with a very weak band that could represent the $[\text{Atx1-Cu-Ccc2a}]$ heterodimer interaction (band # 8). Finally, the mixture of $[\text{TM}][(\text{Cu})(\text{Cu-Se-Met-Atx1})_3]$ + apo-Ccc2a (1:1) (lane J), showed clearly the same bands as in lane H (Atx1: band # 10, Ccc2a: band # 13, and $[\text{Atx1-Cu-Ccc2a}]$: band # 11), but with the formation of a new band (band # 12), which likely represents the new $[(\text{TM})(\text{Cu})(\text{Atx1})(\text{Ccc2a})]$ protein-protein complex.



Scheme 6.2 Schematic representation of migration of negatively and positively charged proteins and a complex of the two (1: + charged protein, 2: blank, 3: - charged protein, 4: blank, and 5: complex of the two proteins).¹²

6.3.3 Identification of proteins and components of protein-protein complexes by ESI-MS. To determine the identity of all the protein bands observed in the native agarose gel (Figure 6.2) we analyzed each of the protein bands extracted from the gel (as described in experimental procedures) by ESI-MS, which identify the molecular weight of single proteins and of the individual components of the protein-protein complexes. SDS-PAGE was not useful in identifying these proteins because they are too close in MW [apo-Atx1: 8089.5 (red), apo-Ccc2a: 7882.9 (red)] to make a detectable difference by electrophoresis.

ESI-MS spectrum of protein band #1 (Figure 6.3) and #2 (Figure 6.4) showed clearly the apo-Se-Met-Atx1 [#1: $m/z^{\text{calc}} = 8136.4$ (red), $m/z^{\text{calc}} = 8134.4$ (oxid), $m/z^{\text{obs}} = 8134.2$ and #2: $m/z^{\text{obs}} = 8133.2$). In Figure 6.3, we also detected an apo-Se-Met-Atx1 plus one H_2O [$m/z^{\text{calc}} = 8136.4 + 18 = 8154.4$, $m/z^{\text{obs}} = 8150.5$], and an apo-Se-Met-Atx1 plus formic acid [$m/z^{\text{calc}} = 8136.4 + 42 = 8178.4$, $m/z^{\text{obs}} = 8179.0$]. It is important to note that an approximate characterization by ESI was applied to small relative abundance species, including protein

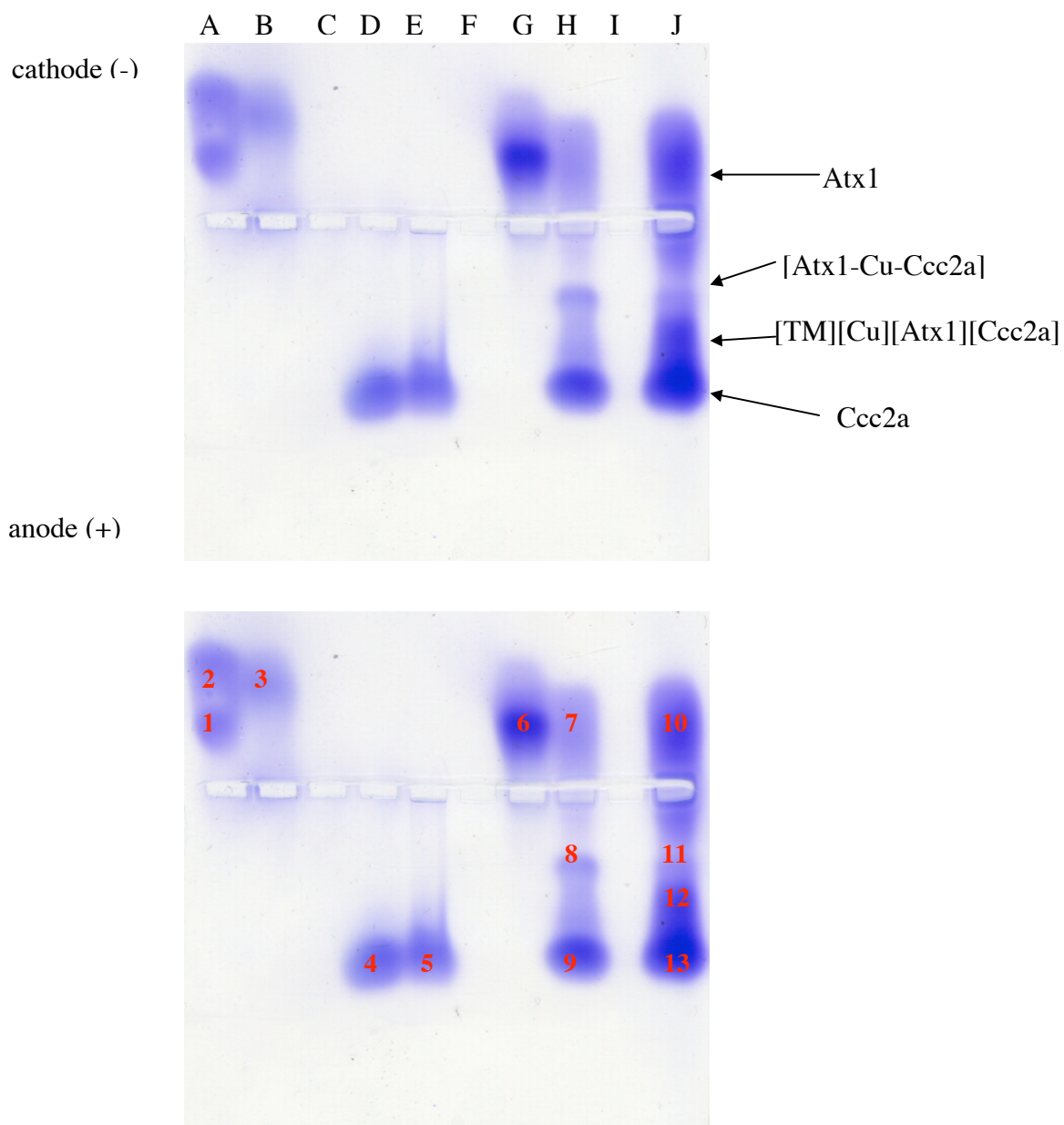


Figure 6.2 Native agarose gel electrophoresis with analysis of protein-protein complex formation. (A: apo-Se-Met-Atx1 (band #1 & 2), B: Cu-Se-Met-Atx1 (band # 3), C: blank, D: apo-Ccc2a (band # 4), E: Cu-Ccc2a (band # 5), F: blank, G: [TM][Cu](Se-Met-Cu-Atx1)₃ (band # 6), H: Cu-Se-Met-Atx1 + apo-Ccc2a (1:1) (band # 7, 8, & 9), I: blank, and J: [TM][Cu](Cu-Se-Met-Atx1)₃ + apo-Ccc2a (1:1) (band # 10, 11, 12 & 13).

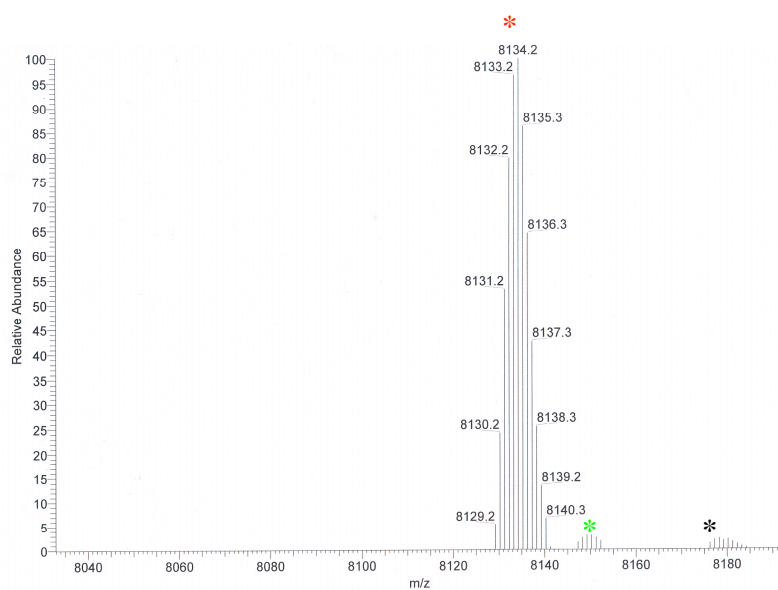


Figure 6.3 ESI-MS spectrum of protein band # 1 (*) [apo-Se-Met-Atx1: $m/z^{\text{calc}} = 8136.4$ (red), $m/z^{\text{calc}} = 8134.4$ (oxid), $m/z^{\text{obs}} = 8134.2$], (*) [apo-Se-Met-Atx1 + H₂O: $m/z^{\text{calc}} = 8154.4$, $m/z^{\text{obs}} = 8150.5$], (*) [apo-Se-Met-Atx1 + HCOOH: $m/z^{\text{calc}} = 8178.4$, $m/z^{\text{obs}} = 8179.0$].



Figure 6.4 ESI-MS spectrum of protein band # 2 (*) [apo-Se-Met-Atx1: $m/z^{\text{calc}} = 8136.4$ (red), $m/z^{\text{calc}} = 8134.4$ (oxid), $m/z^{\text{obs}} = 8133.2$].

adducts with H₂O, HCOOH, and MeOH. Protein band # 3 (Figure 6.5) showed the presence of apo-Se-Met-Atx1 with a low abundance of apo-Atx1 [apo-Se-Met-Atx1: $m/z^{\text{calc}} = 8136.4$ (red), $m/z^{\text{calc}} = 8134.4$ (oxid), $m/z^{\text{obs}} = 8134.3$, apo-Atx1: $m/z^{\text{calc}} = 8089.5$ (red), $m/z^{\text{calc}} = 8087.5$ (oxid), $m/z^{\text{obs}} = 8086.3$], and a barely detected mixture of Cu-Se-Met-Atx1 and Cu-Atx1 [Cu-Se-Met-Atx1: $m/z^{\text{calc}} = 8197.9$, $m/z^{\text{obs}} = 8196.2$, Cu-Atx1: $m/z^{\text{calc}} = 8151.0$, $m/z^{\text{obs}} = 8150.3$]. Protein-bound copper was lost due to competition with formic acid used to prepare the samples. In Figure 6.5, we also detected 2 low abundance species, which may correspond to apo-Se-Met-Atx1 plus methanol [$m/z^{\text{calc}} = 8136.4 + 32 = 8168.4$, $m/z^{\text{obs}} = 8169.0$], and Cu-Se-Met-Atx1 plus formic acid [$m/z^{\text{calc}} = 8197.9 + 46 = 8243.9$, $m/z^{\text{obs}} = 8248.9$].

Protein band # 4 (Figure 6.6) showed the clear presence of apo-Ccc2a [apo-Cc2a: $m/z^{\text{calc}} = 7882.9$ (red), $m/z^{\text{calc}} = 7880.9$ (oxid), $m/z^{\text{obs}} = 7891.7$]. The difference of approximately 9 mass units between the m/z^{calc} and m/z^{obs} is most likely due to a protonation caused by the mixture of solvents used to run the LTQ-FT ESI-MS experiment [apo-Ccc2a + 9H⁺: $m/z^{\text{calc}} = 7891.9$, $m/z^{\text{obs}} = 7891.7$]. In addition we detected two small relative abundance species, which can be assigned as the apo-Ccc2a with the oxidation of a N-terminal arginine to glutamic acid [$m/z^{\text{calc}} = 7891.9 - 27.1 = 7864.8$, $m/z^{\text{obs}} = 7863.7$],^{18,19} and a apo-Ccc2a plus one Na atom [$m/z^{\text{calc}} = 7891.9 + 23 = 7914.9$, $m/z^{\text{obs}} = 7913.7$].

In comparison, protein band # 5 (Figure 6.7) also showed the apo-Ccc2a [$m/z^{\text{obs}} = 7891.7$], in addition to a weak signal which can be attributed as the Cu loaded form of the Ccc2a that survives to the formic acid used to prepare the sample [Cu-Ccc2a: $m/z^{\text{calc}} = 7944.5$, $m/z^{\text{obs}} = 7948.7$]. In Figure 6.7, we can also detect three small relative abundance species, the apo-Ccc2a with a probable oxidation of a N-terminal arginine to glutamic acid [$m/z^{\text{calc}} = 7891.9 - 27.1 = 7864.8$, $m/z^{\text{obs}} = 7863.7$], an apo-Ccc2a plus one H₂O [$m/z^{\text{calc}} = 7891.9 + 18 = 7909.9$, m/z^{obs}

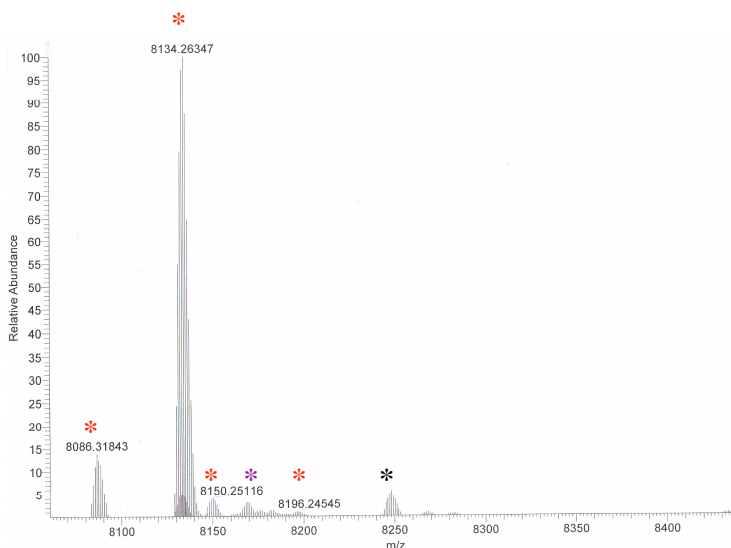


Figure 6.5 ESI-MS spectrum of protein band # 3 (*) [apo-Atx1: $m/z^{\text{calc}} = 8089.5$ (red), $m/z^{\text{calc}} = 8087.5$ (oxid), $m/z^{\text{obs}} = 8086.3$, apo-Se-Met-Atx1: $m/z^{\text{calc}} = 8136.4$ (red), $m/z^{\text{calc}} = 8134.4$ (oxid), $m/z^{\text{obs}} = 8134.3$, Cu-Atx1: $m/z^{\text{calc}} = 8151.0$, $m/z^{\text{obs}} = 8150.3$, Cu-Se-Met-Atx1: $m/z^{\text{calc}} = 8197.9$, $m/z^{\text{obs}} = 8196.2$], (*) [apo-Se-Met-Atx1 + MeOH: $m/z^{\text{calc}} = 8168.4$, $m/z^{\text{obs}} = 8169.0$], (*) [Cu-Se-Met-Atx1 + HCOOH: $m/z^{\text{calc}} = 8243.9$, $m/z^{\text{obs}} = 8248.9$].

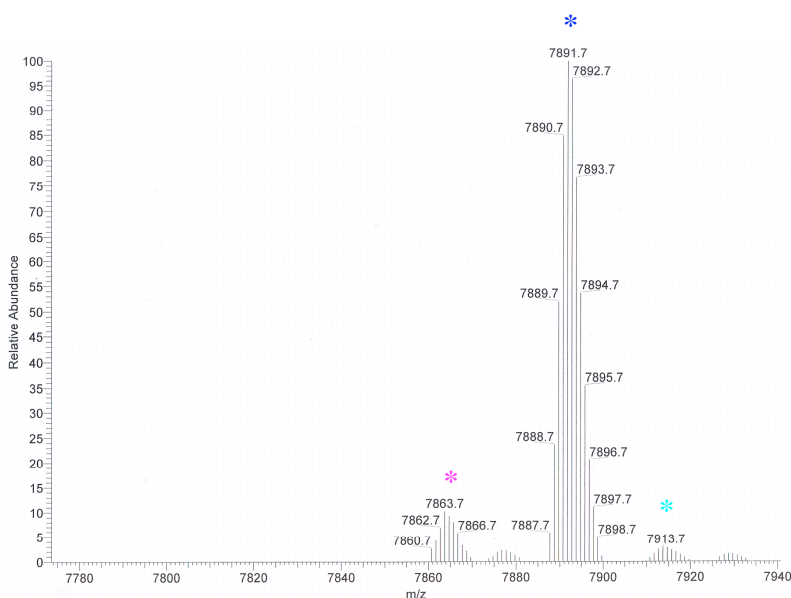


Figure 6.6 ESI-MS spectrum of protein band # 4 (*) [apo-Cc2a: $m/z^{\text{calc}} = 7882.9$ (red), $m/z^{\text{calc}} = 7880.9$ (oxid), $m/z^{\text{obs}} = 7891.7$], (*) [apo-Ccc2a with oxidation of arginine to glutamic acid: $m/z^{\text{calc}} = 7864.8$, $m/z^{\text{obs}} = 7863.7$], (*) [apo-Ccc2a + Na: $m/z^{\text{calc}} = 7914.9$, $m/z^{\text{obs}} = 7913.7$].

= 7908.7], and an apo-Ccc2a plus methanol [$m/z^{\text{calc}} = 7891.9 + 32 = 7923.9$, $m/z^{\text{obs}} = 7925.0$].

ESI-MS analysis of protein band # 6 (Figure 6.8) showed the apo-Se-Met-Atx1 [apo-Se-Met-Atx1: $m/z^{\text{obs}} = 8134.2$], with a small proportion of apo-Atx1, Cu-Se-Met-Atx1 and Cu-Atx1 [apo-Atx1: $m/z^{\text{calc}} = 8089.5$ (red), $m/z^{\text{calc}} = 8087.5$ (oxid), $m/z^{\text{obs}} = 8087.3$, Cu-Se-Met-Atx1: $m/z^{\text{calc}} = 8197.9$, $m/z^{\text{obs}} = 8197.2$, Cu-Atx1: $m/z^{\text{calc}} = 8151.0$, $m/z^{\text{obs}} = 8157.2$], which represent the Atx1 as a component in the [TM][(Cu)(Cu-Se-Met-Atx1)₃]. In Figure 6.8, we can also detect a small-relative abundance species, which is identified as Cu-Se-Met-Atx1 plus formic acid [$m/z^{\text{calc}} = 8197.9 + 46 = 8243.9$, $m/z^{\text{obs}} = 8248.0$].

For the Cu-Se-Met-Atx1 + apo-Ccc2a (1:1) mixture, we analyzed three bands # 7, 8 and 9. ESI-MS spectrum of protein band # 7 (Figure 6.9) showed clearly the apo-Se-Met-Atx1 [apo-Se-Met-Atx1: $m/z^{\text{obs}} = 8133.2$], with a small proportion of apo-atx1 [apo-Atx1: $m/z^{\text{obs}} = 8086.3$]; while protein band # 8 showed the apo-Ccc2a (RT: 11.38 min) (Figure 6.10) [apo-Cc2a: $m/z^{\text{obs}} = 7891.7$] and apo-Se-Met-Atx1 (RT: 12.48 min) (Figure 6.11) [apo-Se-Met-Atx1: $m/z^{\text{obs}} = 8134.2$] with a small abundance of apo-Atx1 [apo-Atx1: $m/z^{\text{obs}} = 8087.3$]. Finally, protein band # 9 (Figure 6.12) showed a mixture of apo-Ccc2a and Cu-Ccc2a with similar relative abundances [apo-Cc2a: $m/z^{\text{obs}} = 7891.7$, Cu-Ccc2a: $m/z^{\text{obs}} = 7948.7$], and an apo-Ccc2a plus one H₂O [$m/z^{\text{calc}} = 7891.9 + 18 = 7909.9$, $m/z^{\text{obs}} = 7908.7$].

For the [TM][(Cu)(Cu-Se-Met-Atx1)₃] + apo-Ccc2a (1:1) mixture, we analyzed bands # 10, 11, 12 and 13. ESI-MS of protein band # 10 (Figure 6.13) showed a mixture of apo-Se-Met-Atx1 and apo-Atx1 [apo-Se-Met-Atx1: $m/z^{\text{obs}} = 8133.2$, apo-Atx1: $m/z^{\text{obs}} = 8086.3$], with a very weak signal of Cu-Atx1 [Cu-Atx1: $m/z^{\text{obs}} = 8151.2$]; while protein band # 11 showed the apo-Ccc2a (RT: 10.08 min) (Figure 6.14) [apo-Cc2a: $m/z^{\text{obs}} = 7892.7$] with a small proportion of the Cu-Ccc2a [Cu-Ccc2a: $m/z^{\text{obs}} = 7947.7$], and a mixture of apo-Se-Met-Atx1 and apo-Atx1

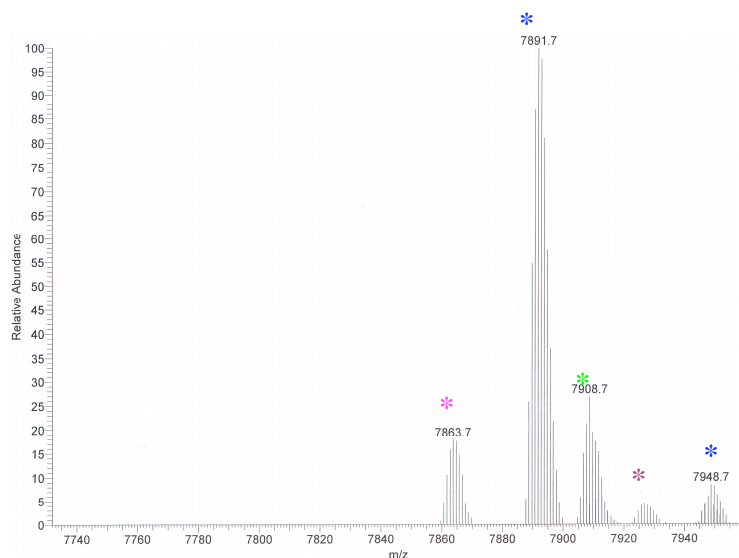


Figure 6.7 ESI-MS spectrum of protein band # 5 (*) [apo-Cc2a: $m/z^{\text{calc}} = 7882.9$ (red), $m/z^{\text{calc}} = 7880.9$ (oxid), $m/z^{\text{obs}} = 7891.7$, Cu-Ccc2a: $m/z^{\text{calc}} = 7944.5$, $m/z^{\text{obs}} = 7948.7$], (*) [apo-Ccc2a with oxidation of arginine to glutamic acid: $m/z^{\text{calc}} = 7864.8$, $m/z^{\text{obs}} = 7863.7$], (*) [apo-Ccc2a + H₂O: $m/z^{\text{calc}} = 7909.9$, $m/z^{\text{obs}} = 7908.7$], (*) apo-Ccc2a + MeOH: $m/z^{\text{calc}} = 7923.9$, $m/z^{\text{obs}} = 7925.0$].

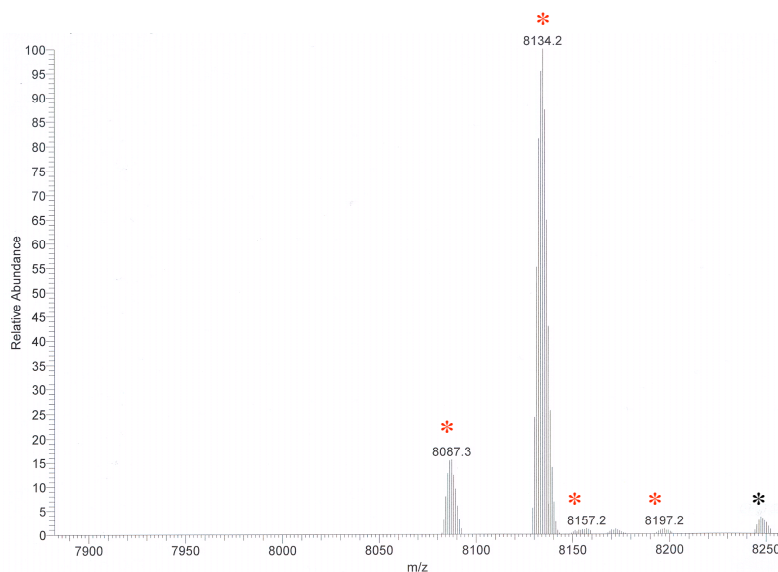


Figure 6.8 ESI-MS spectrum of protein band # 6 (*) [apo-Atx1: $m/z^{\text{calc}} = 8089.5$ (red), $m/z^{\text{calc}} = 8087.5$ (oxid), $m/z^{\text{obs}} = 8087.3$, apo-Se-Met-Atx1: $m/z^{\text{calc}} = 8136.4$ (red), $m/z^{\text{calc}} = 8134.4$ (oxid), $m/z^{\text{obs}} = 8134.2$, Cu-Atx1: $m/z^{\text{calc}} = 8151.0$, $m/z^{\text{obs}} = 8157.2$, Cu-Se-Met-Atx1: $m/z^{\text{calc}} = 8197.9$, $m/z^{\text{obs}} = 8197.2$], (*) [Cu-Se-Met-Atx1 + HCOOH: $m/z^{\text{calc}} = 8197.9 + 46 = 8243.9$, $m/z^{\text{obs}} = 8248.0$].

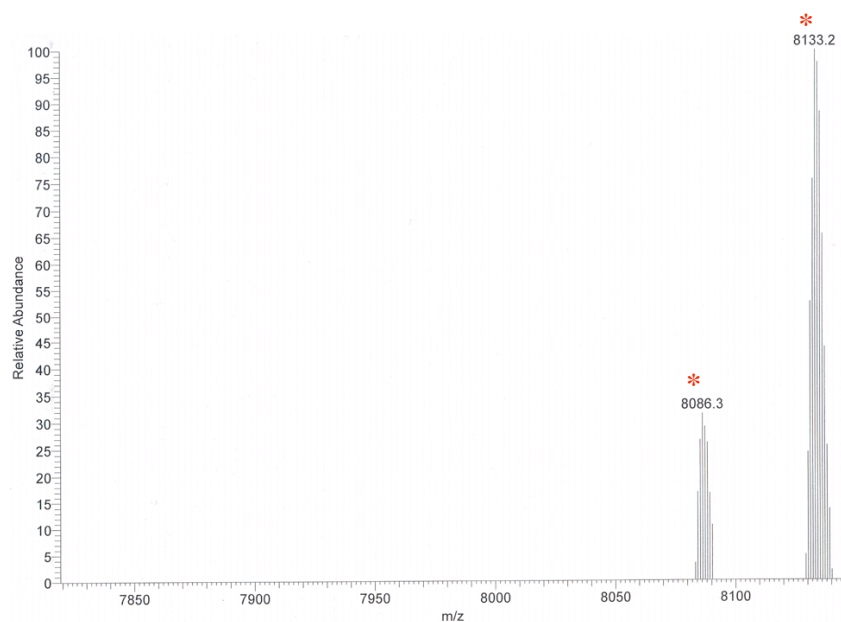


Figure 6.9 ESI-MS spectrum of protein band # 7 (*) [apo-Atx1: $m/z^{\text{calc}} = 8089.5$ (red), $m/z^{\text{calc}} = 8087.5$ (oxid) $m/z^{\text{obs}} = 8086.3$, apo-Se-Met-Atx1: $m/z^{\text{calc}} = 8136.4$ (red), $m/z^{\text{calc}} = 8134.4$ (oxid), $m/z^{\text{obs}} = 8133.2$].



Figure 6.10 ESI-MS spectrum of protein band # 8 (*) (RT: 11.38 min) [apo-Cc2a: $m/z^{\text{calc}} = 7882.9$ (red), $m/z^{\text{calc}} = 7880.9$ (oxid), $m/z^{\text{obs}} = 7891.7$].

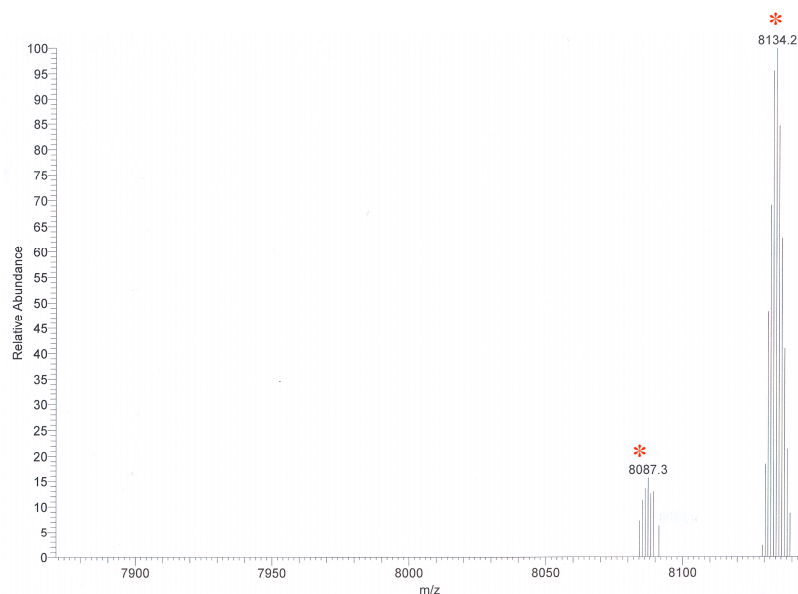


Figure 6.11 ESI-MS spectrum of protein band # 8 (*) (RT: 12.48 min) [apo-Atx1: $m/z^{\text{calc}} = 8089.5$ (red), $m/z^{\text{calc}} = 8087.5$ (oxid) $m/z^{\text{obs}} = 8087.3$, apo-Se-Met-Atx1: $m/z^{\text{calc}} = 8136.4$ (red), $m/z^{\text{calc}} = 8134.4$ (oxid), $m/z^{\text{obs}} = 8134.2$].

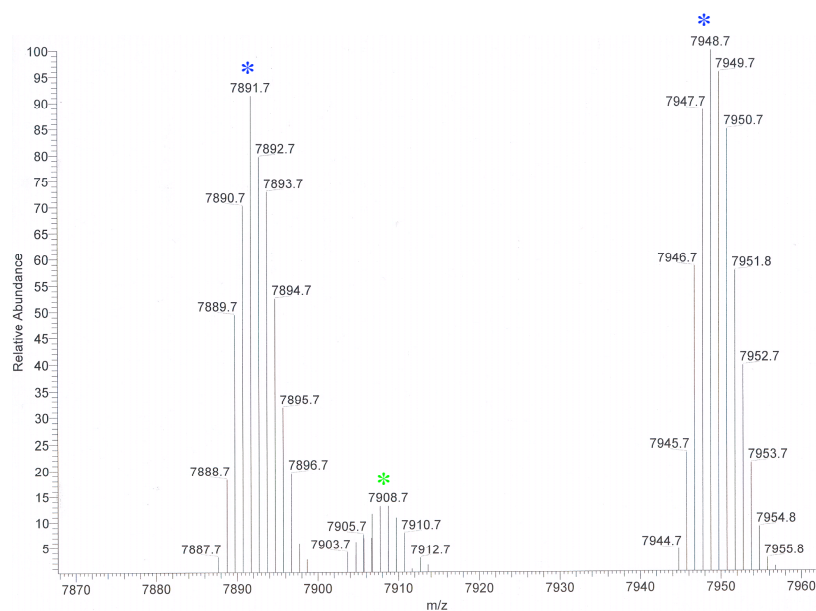


Figure 6.12 ESI-MS spectrum of protein band # 9 (*) [apo-Ccc2a: $m/z^{\text{calc}} = 7890.0$ (red), $m/z^{\text{calc}} = 7888.0$ (oxid), $m/z^{\text{obs}} = 7891.7$, Cu-Ccc2a: $m/z^{\text{calc}} = 7944.5$, $m/z^{\text{obs}} = 7948.7$], (*) [apo-Ccc2a + H_2O : $m/z^{\text{calc}} = 7909.9$, $m/z^{\text{obs}} = 7908.7$].

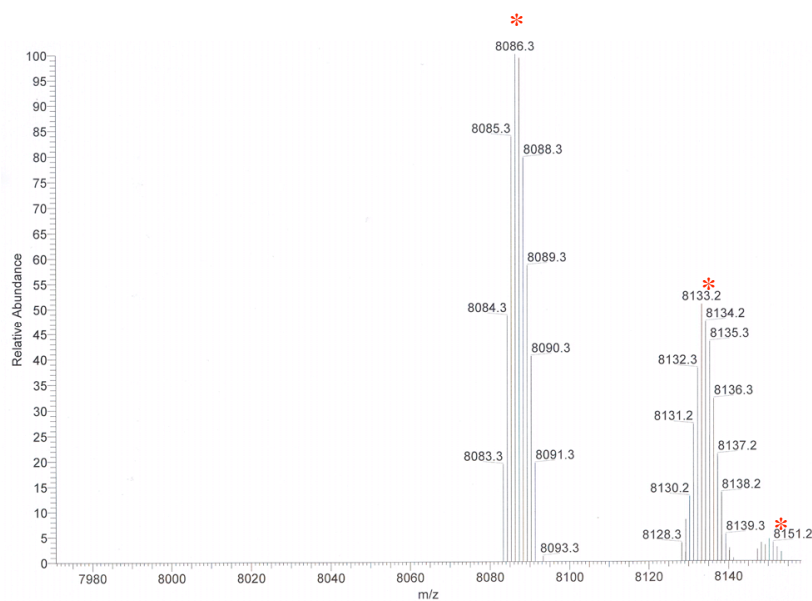


Figure 6.13 ESI-MS spectrum of protein band # 10 (*) [apo-Atx1: $m/z^{\text{calc}} = 8089.5$ (red), $m/z^{\text{calc}} = 8087.5$ (oxid) $m/z^{\text{obs}} = 8086.3$, apo-Se-Met-Atx1: $m/z^{\text{calc}} = 8136.4$ (red), $m/z^{\text{calc}} = 8134.4$ (oxid), $m/z^{\text{obs}} = 8133.2$, Cu-Atx1: $m/z^{\text{calc}} = 8151.0$, $m/z^{\text{obs}} = 8151.2$].

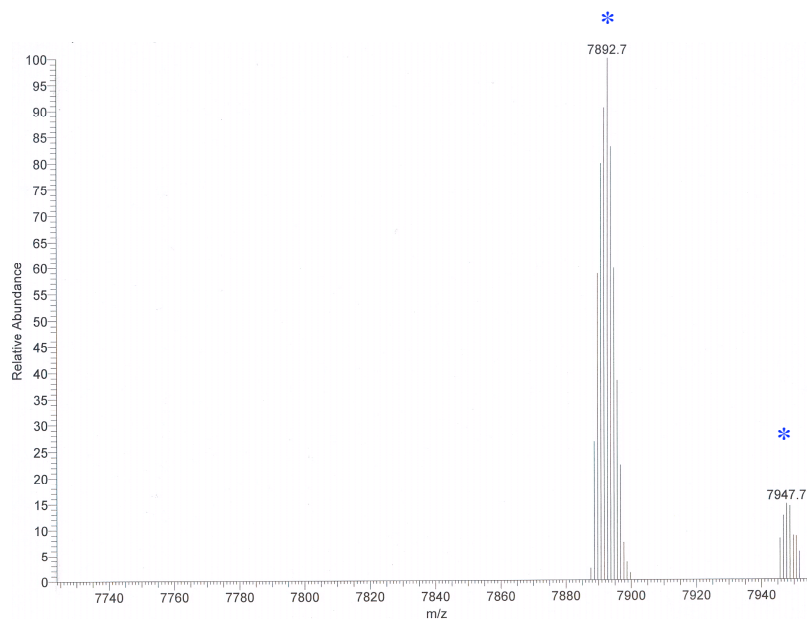


Figure 6.14 ESI-MS spectrum of protein band # 11 (*) (RT: 10.08 min) [apo-Cc2a: $m/z^{\text{calc}} = 7882.9$ (red), $m/z^{\text{calc}} = 7880.9$ (oxid), $m/z^{\text{obs}} = 7892.7$, Cu-Ccc2a: $m/z^{\text{calc}} = 7944.5$, $m/z^{\text{obs}} = 7947.7$].

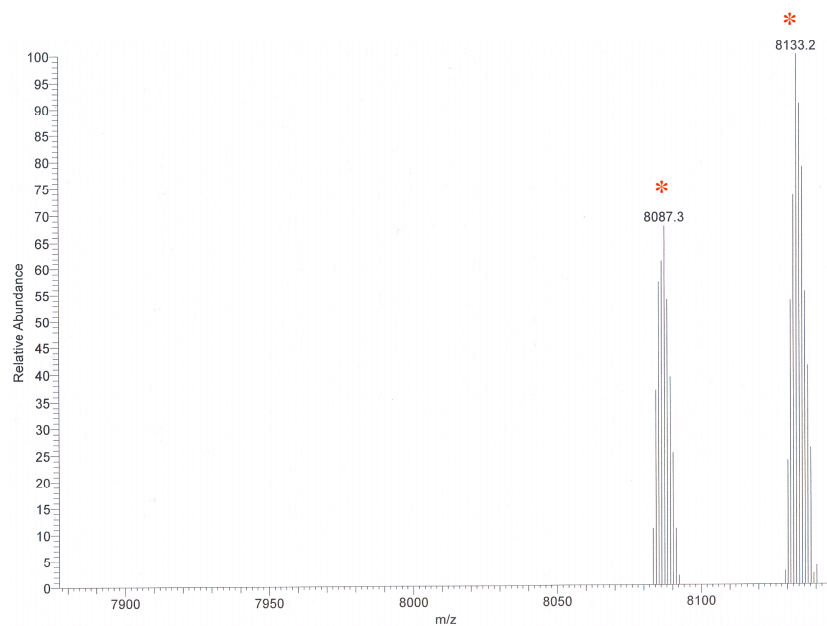


Figure 6.15 ESI-MS spectrum of protein band # 11 (*) (RT: 11.98 min) [apo-Atx1: $m/z^{\text{calc}} = 8089.5$ (red), $m/z^{\text{calc}} = 8087.5$ (oxid) $m/z^{\text{obs}} = 8087.3$, apo-Se-Met-Atx1: $m/z^{\text{calc}} = 8136.4$ (red), $m/z^{\text{calc}} = 8134.4$ (oxid), $m/z^{\text{obs}} = 8133.2$].

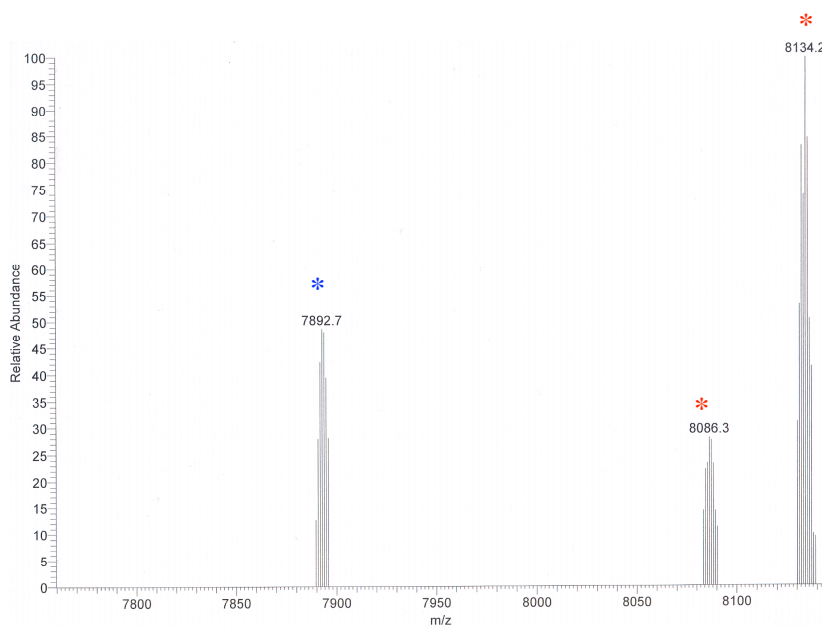


Figure 6.16 ESI-MS spectrum of protein band # 12: Atx1 (*) + Ccc2a (*) (RT: 12.01) [apo-Cc2a: $m/z^{\text{calc}} = 7882.9$ (red), $m/z^{\text{calc}} = 7880.9$ (oxid), $m/z^{\text{obs}} = 7892.7$; apo-Atx1: $m/z^{\text{calc}} = 8089.5$ (red), $m/z^{\text{calc}} = 8087.5$ (oxid), $m/z^{\text{obs}} = 8086.3$, apo-Se-Met-Atx1: $m/z^{\text{calc}} = 8136.4$ (red), $m/z^{\text{calc}} = 8134.4$ (oxid), $m/z^{\text{obs}} = 8134.2$].

(RT: 11.98 min) (Figure 6.15) [apo-Se-Met-Atx1: $m/z^{\text{obs}} = 8133.2$, apo-Atx1: $m/z^{\text{obs}} = 8087.3$]. ESI-MS of protein band # 12 (Figure 6.16) showed a mixture of apo-Ccc2a and apo-Se-Met-Atx1 with a small proportion of apo-Atx1 detected at the same retention time (RT: 12.01) [apo-Cc2a: $m/z^{\text{obs}} = 7892.7$; apo-Se-Met-Atx1: $m/z^{\text{obs}} = 8134.2$, apo-Atx1: $m/z^{\text{obs}} = 8086.3$]. Finally, the ESI-MS of protein band # 13 (Figure 6.17) showed the apo-Ccc2a [apo-Cc2a: $m/z^{\text{obs}} = 7891.7$], with a barely detectable signal of Cu-Ccc2a [Cu-Ccc2a: $m/z^{\text{obs}} = 7950.7$]. In Figure 6.17, we also detected four small relative abundance species, the apo-Ccc2a with the oxidation of a N-terminal arginine to glutamic acid [$m/z^{\text{calc}} = 7891.9 - 27.1 = 7864.8$, $m/z^{\text{obs}} = 7863.7$], an apo-Ccc2a plus one H₂O [$m/z^{\text{calc}} = 7891.9 + 18 = 7909.9$, $m/z^{\text{obs}} = 7908.0$], an apo-Ccc2a plus one Na atom [$m/z^{\text{calc}} = 7891.9 + 23 = 7914.9$, $m/z^{\text{obs}} = 7913.7$], and an apo-Ccc2a plus methanol [$m/z^{\text{calc}} = 7891.9 + 32 = 7923.9$, $m/z^{\text{obs}} = 7923.7$].

6.3.4 ICP-MS/LA-ICP-MS metal content determination in proteins and protein-protein complexes isolated from agarose gel. ICP-MS and LA-ICP-MS were performed in all samples extracted and contained at the previously observed native agarose gel (Figure 6.2) to confirm the stability, disruption or transfer of the copper among our species. The Cu and Mo content was detected and measured to identify the metal concentration of single proteins and of individual components of the protein-protein complex bands (Table 6.1).

ICP-MS and LA-ICP-MS of protein band # 1, 2 and 4 (Table 6.1 & Figure 6.18) showed the absence of any detectable Cu, confirming the apo states of both proteins: Se-Met-Atx1 (# 1, 2) and Ccc2a (# 4). Protein bands # 3 and 5 showed a Cu content confirming the metallated states: Cu-Se-Met-Atx1 (# 3) and Cu-Ccc2a (# 5), even though the percentage of sample recovery by ICP-MS was kind of low (22.2 and 16.9 %), and that the LA-ICP-MS of Cu-Se-Met-Atx1 barely detected Cu (Table 6.1 & Figure 6.18).

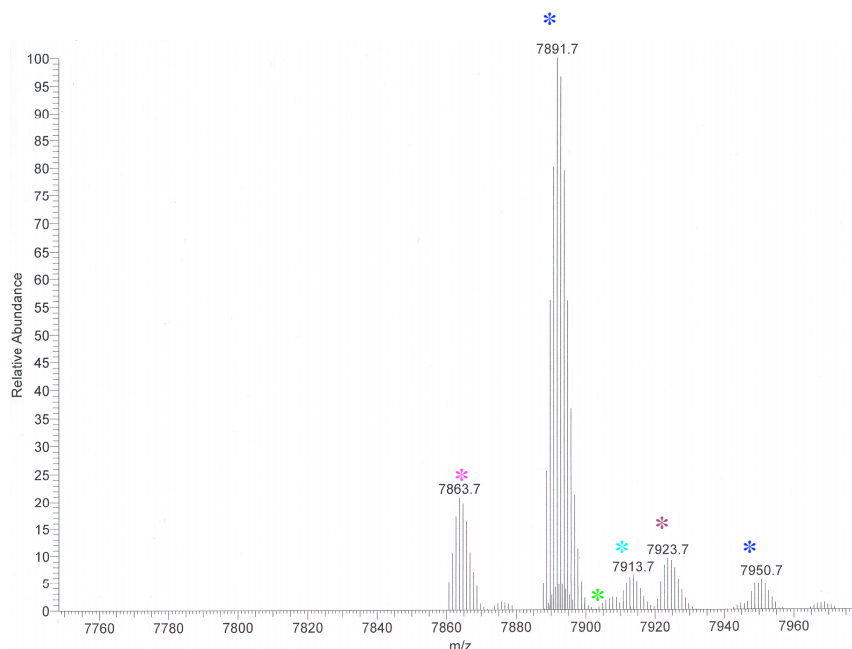


Figure 6.17 ESI-MS spectrum of protein band # 13 (*) [apo-Ccc2a: $m/z^{\text{calc}} = 7882.9$ (red), $m/z^{\text{calc}} = 7880.9$ (oxid), $m/z^{\text{obs}} = 7891.7$, Cu-Ccc2a: $m/z^{\text{calc}} = 7944.5$, $m/z^{\text{obs}} = 7950.7$], (*) [apo-Ccc2a with oxidation of arginine to glutamic acid: $m/z^{\text{calc}} = 7864.8$, $m/z^{\text{obs}} = 7863.7$], (*) [apo-Ccc2a + H_2O : $m/z^{\text{calc}} = 7909.9$, $m/z^{\text{obs}} = 7908.0$], (*) [apo-Ccc2a + Na: $m/z^{\text{calc}} = 7914.9$, $m/z^{\text{obs}} = 7913.7$], (*) apo-Ccc2a + MeOH: $m/z^{\text{calc}} = 7923.9$, $m/z^{\text{obs}} = 7923.7$].

ESI-MS and LA-ICP-MS of protein band # 6 (Table 6.1 & Figure 6.19) showed the presence of both metals with a very high % of recovery (ICP-MS: Cu = 63.4 & Mo = 64.9 %) and an approximate Cu/Mo of 3.6 ± 0.09 (ICP-MS) and 2.6 ± 0.01 (LA-ICP-MS), which are closed values to the one observed under initial conditions (Cu/Mo ~ 3.8), confirming the survival of the [TM][Cu(Cu-Se-Met-Atx1)₃] complex in the gel.

For the Cu-Se-Met-Atx1 + apo-Ccc2a (1:1) mixture, we analyzed three bands # 7, 8 and 9. For protein band # 7 (Table 6.1 & Figure 6.19), we did not detect any Cu, which suggests the presence of apo-Se-Met-Atx1 as one of the products of the reaction between Cu-Se-Met-Atx1 and apo-Ccc2a. In addition, protein band # 8 (Table 6.1 & Figure 6.19) showed a detectable

Table 6.1 Stoichiometry of Cu and Mo from protein gel extracts (μmol).

Band #	Protein (ESI-MS)	Initial			Final			% Rec.	
		N_{Cu}	N_{Mo}	Cu/Mo	N_{Cu}	N_{Mo}	Cu/Mo	Cu	Mo
1	Atx1	---	---	---	---	---	---	---	---
2	Atx1	---	---	---	---	---	---	---	---
3	Atx1	2.04×10^{-3}	---	---	4.53×10^{-4}	---	---	22.2	---
4	Ccc2a	---	---	---	---	---	---	---	---
5	Ccc2a	2.24×10^{-3}	---	---	3.78×10^{-4}	---	---	16.9	---
6	Atx1	2.57×10^{-3}	6.80×10^{-4}	3.8	1.63×10^{-3}	4.41×10^{-4}	3.6	63.4	64.9
7	Atx1				---	---	---		
8	Atx1/Ccc2a	2.04×10^{-3}	---	---	1.19×10^{-4}	---	---	13.5	---
9	Ccc2a				1.57×10^{-4}	---	---		
10	Atx1				---	---	---		
11	Atx1/Ccc2a	2.57×10^{-3}	6.80×10^{-4}	3.8	2.13×10^{-5}	---	---	35.4	41.2
12	Atx1/Ccc2a				8.89×10^{-4}	2.80×10^{-4}	3.1		
13	Ccc2a				---	---	---		

ICP-MS and LA-ICP-MS concentration of copper, which in combination with previous ESI-MS results suggests the formation of a [Atx1-Cu-Ccc2a] heterodimer, which structure was previously suggested by NMR studies.²⁰ Finally, protein band # 9 (Table 6.1 & Figure 6.19) showed a detectable concentration of Cu by ESI-MS and LA-ICP-MS, which in combination with ESI-MS results suggests the transferring of Cu from Cu-Se-Met-Atx1 to apo-Ccc2a and the consecutive formation of Cu-Ccc2a, consistent with the metallochaperone function of Atx1 in the absence of TM.

For the [TM][(Cu)(Cu-Se-Met-Atx1)₃] + apo-Ccc2a (1:1) mixture, we analyzed bands # 10, 11, 12 and 13. ICP-MS of protein band # 10 (Table 6.1 & Figure 6.19) revealed that Cu

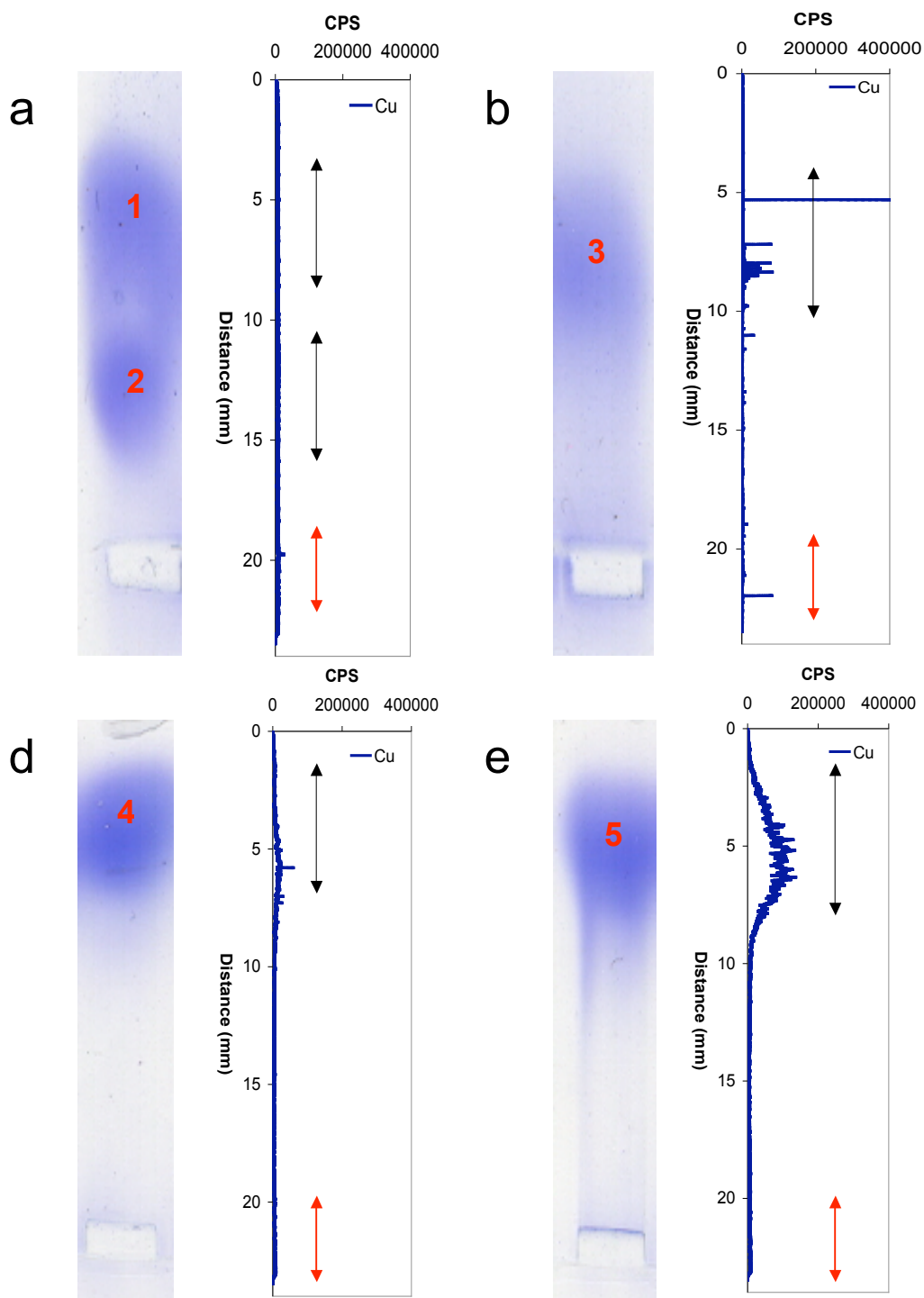


Figure 6.18. Control native gel lanes with corresponding LA-ICP-MS scans for Cu. a: apo-Se-Met-Atx1 (band # 1 & 2), b: Cu-Se-Met-Atx1 (band #3), d: apo-Ccc2a (band # 4), and e: Cu-Ccc2a (band # 5) (\leftrightarrow : protein band length, \leftrightarrow : protein loading well).

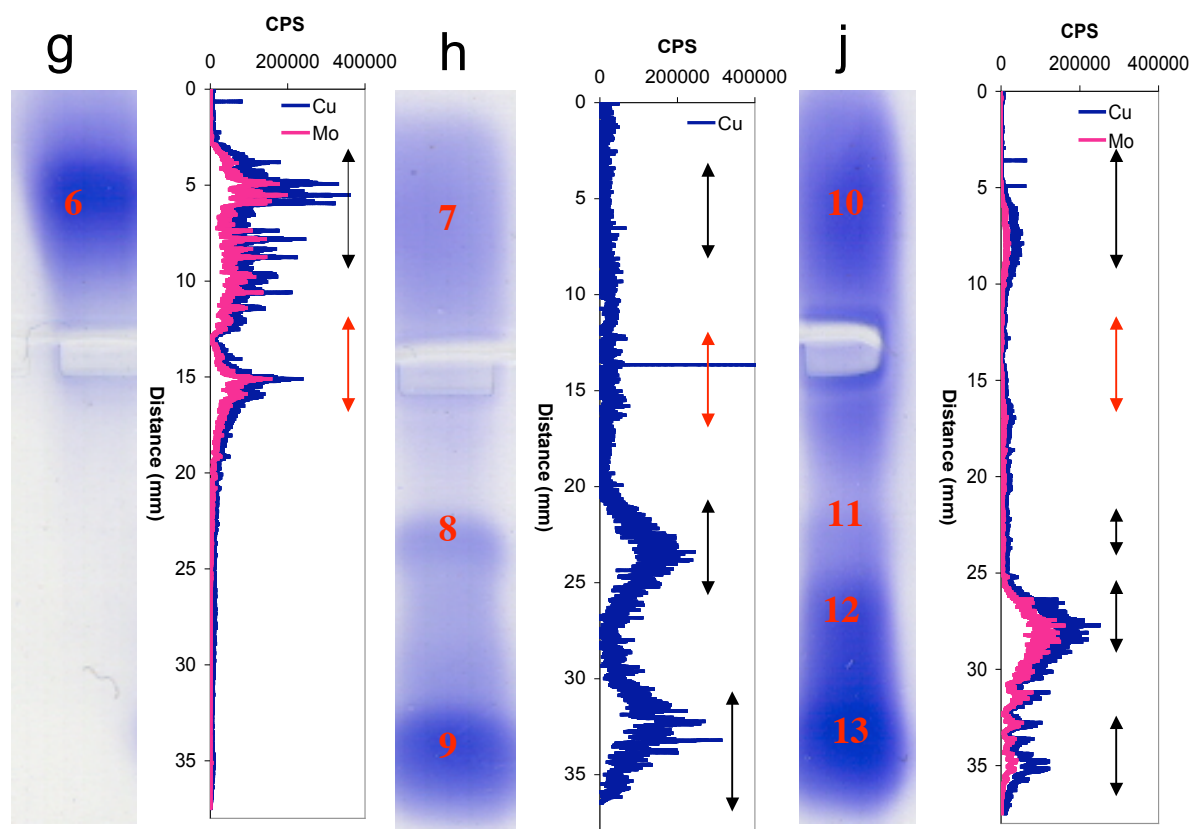


Figure 6.19. Native gel lanes with corresponding LA-ICP-MS scans for Cu & Mo. [g: [TM][(Cu)(Cu-Se-Met-Atx1)₃] (band 6), h: Cu-Se-Met-Atx1 + apo-Ccc2a (1:1) (band 7, 8 & 9), j: [TM][(Cu)(Cu-Se-Met-Atx1)₃] + apo-Ccc2a (1:1) (band 10, 11, 12 & 13) (↔: protein band length, ↔: protein loading well).

was barely detectable by ICP-MS and LA-ICP-MS, suggesting the formation of apo-Se-Met-Atx1 as one of the products of this reaction, while protein band # 11 showed a copper concentration (2.13×10^{-5} μmol) by ICP-MS (not detectable by LA-ICP-MS), suggesting the formation of a [Atx1-Cu-Ccc2a] heterodimer as in the previously described protein band # 8. Moreover, protein band # 12 (not observed in the mixture between Cu-Atx1 + apo-Ccc2a) showed Cu and Mo with a high % of sample recovery (ICP-MS: Cu = 35.4 & Mo = 41.2 %) and

an approximate Cu/Mo of 3.1 ± 0.08 (ICP-MS) and 2.2 ± 0.01 (LA-ICP-MS), which in combination with ESI-MS indicates the formation of a new protein-protein interaction: [(TM)(Cu)(Atx1)(Ccc2a)] (Table 6.1 & Figure 6.19). Finally, a very low Cu content was found in protein band # 13 (Figure 6.19) by LA-ICP-MS ($\sim 22.5\%$ of Cu loaded in lane J) (Cu was undetectable by ICP-MS, Table 6.1), which indicates significant disruption of the Cu trafficking pathway due to formation of apo-Ccc2a and the new [(TM)(Cu)(Atx1)(Ccc2a)] complex.

6.4 Discussion and Conclusion

Native gels allow the detection of both negative and positive proteins as well as protein-protein interactions in the same gel. Once a complex is formed, it can be extracted from the gel and routinely identify by SDS-PAGE, ESI-MS, ICP-MS and/or LA-ICP-MS. The mixture of these high sensitive techniques helped us to elucidate the disruption or inhibition of the copper trafficking pathway by the interaction of the [TM][(Cu)(Se-Met-Cu-Atx1)₃] with apo-Ccc2a, and the consecutive formation of a new protein-protein complex: ‘[(TM)(Cu)(Se-Met-Atx1)(Ccc2a)]’. In this last chapter we showed the initial attempts to understand how TM may disrupt the cell’s tightly controlled Cu trafficking pathway, explaining the implications of the formation of a [TM][(Cu)(Se-Met-Cu-Atx1)₃] complex proposed in Chapter 3.

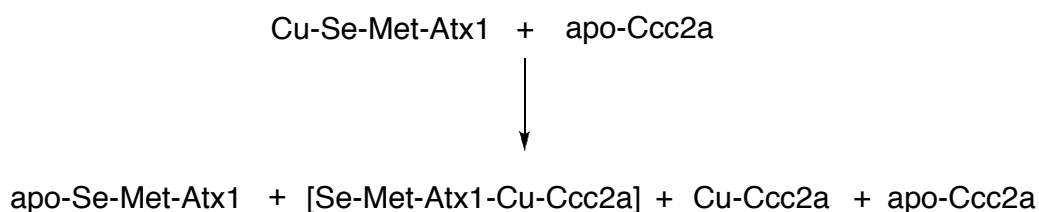
Initially, standard UV-visible spectroscopy titrations showed the shifting of the S—Mo LMCT bands (λ_{\max} : $375 \rightarrow 332$ nm, $532 \rightarrow 495$ nm), indicating the disappearance of the purple [TM][(Cu)(Cu-Se-Met-Atx1)₃], and the formation of a new complex, likely containing Ccc2a.

Native gel electrophoresis in combination with ESI-MS, ICP-MS and LA-ICP-MS confirmed a new unknown complex which forms as Ccc2a reacts with [TM][(Cu)(Cu-Se-Met-Atx1)₃]. ESI-MS allowed us to characterize very clearly the [TM][(Cu)(Cu-Se-Met-Atx1)₃] complex identifying the apo-Se-Met-Atx1 with a low abundance of the Cu loaded form, and high

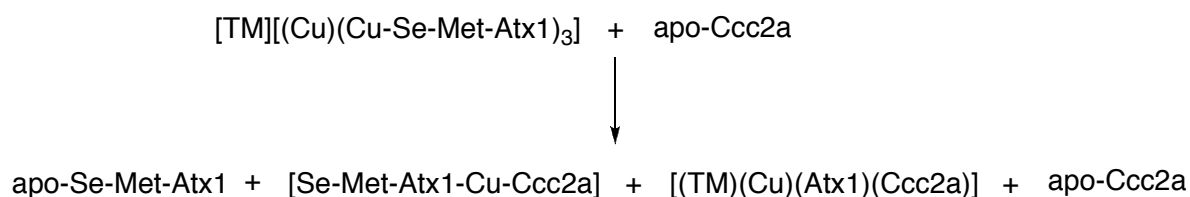
concentrations of both, Cu and Mo. Analysis by ICP-MS and LA-ICP-MS showed a Cu/Mo ratio very similar to the one reported by ICP-OES (Chapter 2 & 3). Some of the ESI-MS spectra of the Atx1 control proteins showed a low proportion of apo-Atx1 in addition to the apo-Se-Met-Atx1, due that the rate of incorporation of Se-Met in the apo-Atx1 is high (~ 90%) but not complete, as shown in Chapter 3.

ESI-MS of the 3 protein gel bands (# 7, 8 & 9) isolated from the reaction mixture of Cu-Se-Met-Atx1 + apo-Ccc2a (1:1), suggested the formation the 4 products: apo-Se-Met-Atx1, [Se-Met-Atx1-Cu-Ccc2a], apo-Ccc2a and Cu-Ccc2a (Scheme 6.3), while the ESI-MS of the 4 protein gel bands (# 10, 11, 12 & 13) isolated from the reaction of [TM][(Cu)(Cu-Se-Met-Atx1)₃] with apo-Ccc2a (1:1), suggested the formation of 4 products: apo-Se-Met-Atx1, [Se-Met-Atx1-Cu-Ccc2a], [(TM)(Cu)(Atx1)(Ccc2a)] and apo-Ccc2a (Scheme 6.4).

Scheme 6.3 Products of the reaction of Cu-Se-Met-Atx1 + apo-Ccc2a (1:1).



Scheme 6.4 Products of the reaction of [TM][(Cu)(Cu-Se-Met-Atx1)₃] + apo-Ccc2a (1:1).

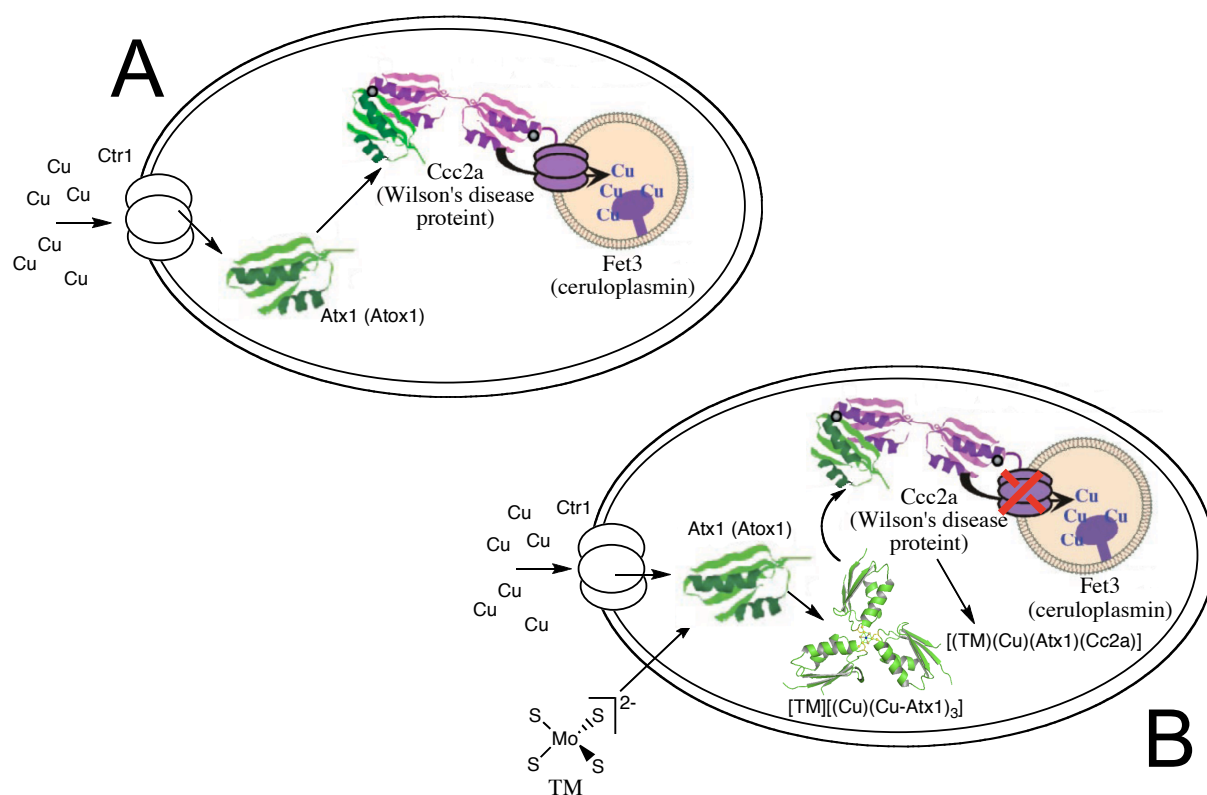


A mixture of apo-Se-Met-Atx1 with apo-Ccc2a was found at different HPLC retention times but at the same protein band for # 8 and # 11, indicating the formation of the [Se-Met-Atx1-Cu-Ccc2a] heterodimer, while protein band # 12 showed the same both proteins but at the same retention time by HPLC, indicating the formation of a heterodimer of different nature, which was characterized as the [(TM)(Cu)(Atx1)(Ccc2a)] complex, in combination with ICP-MS and LA-ICP-MS. Moreover, apo-Ccc2a with a very low relative abundance of Cu-Ccc2a was found in protein gel band # 13 by ESI-MS, while LA-ICP-MS found only a small amount of Cu (~ 22.5 % of Cu loaded in lane J), and ICP-MS on gel slice revealed none. According to ICP-MS we can conclude a total inhibition of the Cu transfer from Atx1 to Ccc2a, while LA-ICP-MS suggests only the partial inhibition of the Cu transfer between these two proteins.

Additional studies are necessary to identify the best way to isolate and characterize the new [(TM)(Cu)(Se-Met-Atx1)(Ccc2a)] complex. A combination of Cu and Mo XAS along with protein crystallization studies are essential to elucidate how the coordination environment of the metal core in the [TM][(Cu)(Cu-Se-Met-Atx1)₃] is affected after reaction with the apo-Ccc2a, and finally identify the molecular structure of this interaction.

TM appears to inhibit copper enzymes not only by direct removal of Cu (as in the case of the SOD1), but also by accruing Cu in an inactive TM-Atx1 complex. This work demonstrates an alternative inhibition pathway by disruption of the intracellular copper metabolism, affecting the translocation of copper to the P-type ATPase Ccc2 by formation of an unknown coordination [protein-protein-TM] complex: ‘[(TM)(Cu)(Atx1)(Ccc2a)]’. Additional studies are necessary to determine if this metabolically inert form of Atx1 is also decreasing the uptake and delivery of copper from the influx transporter yCtr1.

Finally, these studies reveal that this copper chaperone is one of the molecular targets of TM and that the therapy with this drug may disrupt the human intracellular copper trafficking mechanism inhibiting the Atox1 as a step in the mechanism of action of the drug. Moreover, TM will affect not only its copper chaperone role, but may also inhibit the newly proposed Atox1 role as a transcription factor affecting the copper-induced tumor angiogenesis in cancer.²¹



Scheme 6.5 A. Normal copper Atx1-chaperone pathway in yeast, B. TM affected copper Atx1-chaperone pathway in yeast.

REFERENCES

Chapter 1:

1. Berzelius, J. J. *Pogg. Ann. Phys. Chem.* 1826, 7, 261 – 268.
2. Ferguson, W. W.; Lewis, A. H.; Watson, S. J. *Nature (Lond.)* **1938**, 141, 553.
3. Mills, C. F.; Fell, B. F. *Nature* **1960**, 185, 20 – 22.
4. Gooneratne, S. R.; Howell, J. McC.; Gawthorne, J. M. *Br. J. Nutr.* **1981**, 46, 457 – 467.
5. Walshe, J. M. in *Orphan Diseases and Orphan Drugs* (eds. Scheinberg, I. H., Walshe, J. M.) 76 – 85 (Manchester Univ. Press, Manchester, UK, 1986).
6. Brewer, G. J.; Dick, R. D.; Grover, D. K.; LeClaire, V.; Tseng, M.; Wicha, M.; Pienta, K.; Redman, B. G.; Jahan, T.; Sondak, V. K.; Strawderman, M.; LeCarpentier, G.; Merajver, S. D. *Clin. Cancer Res.* **2000**, 6, 1 – 10.
7. Mills, C. F. *Philos. Trans. R. Soc. (Lond.), Ser. B.* **1979**, 288, 51 – 63.
8. Suttle, N. F. *Annu. Rev. Nutr.* **1991**, 11, 121 – 140.
9. Bennetts, H. W.; Chapman, F. E. *Aust. Vet. J.* **1937**, 13, 138 – 149.
10. Müller, A.; Diemann, E.; Jostes, R.; Bögge, H. *Angew. Chem. Int. Ed.* 1981, 20, 934 – 955.
11. Binnie, W. P.; Redman, M. J.; Mallio, W. J. *Inorg. Chem.* **1970**, 9, 1449 – 1452.
12. Ecclestone, T.; Harvey, I.; Laurie, S. H.; Symons, M. C. R.; Taiwo, F. A. *Inorg. Chem. Commun.* **1998**, 1, 460 – 462.
13. Laurie, S. H. *Eur. J. Inorg. Chem.* **2000**, 2443 – 2450.
14. Clegg, W. Garner, C. D.; Nicholson, J. R. *Acta Cryst.* **1983**, 39, 552 – 554.
15. Sécheresse, F.; Bénes, S.; Robert, F.; Jeannin, Y. *J. Chem. Soc. Dalton Trans.* **1991**, 2875 – 2881.
16. Todd, J. R.; Thompson, R. H. *Nature* **1961**, 191, 89 – 90.

- 17 Underwood, E. J. Trace Elements in Human and Animal Nutrition; Academic Press: New York, 1977.
18. Suttle, N. F.; *Proc. Nutr. Soc.* **1974**, *33*, 299–305.
19. Wilson, S. A. K. *Brain* **1912**, *34*, 295 – 508.
20. Sullivan, C. A.; Chopdar, A.; Shun-Shin, G. A. *Br. J. Opthal.* **2002**, *86*, 114–123.
21. Brewer, G. J. *J. Trac. Elemen. Exp. Med.* **2000**, *13*, 51–61.
22. Fatemi, N.; Sakar, B. *Environ Health Perspect.* 2002, *110*, 695 – 698.
23. Walshe, J. M. *Am. J. Med.* **1956**, *21*, 487 – 495.
24. Walshe, J. M. *Lancet* **1982**, *44*, 490 – 493.
25. Schouwink, G. De hepatocerebrale degeneratie, met een onderzoek naar zinkstroofwisseling. MD thesis, University of Amsterdam, Amsterdam, Netherlands, 1961.
26. Brewer, G. J.; Dick, R. D.; Johnson, V.; Wang, Y.; Yuzbasiyan-Gurkan, V.; Kluin, K.; Fink, J. K.; Aisen, A. *Arch. Neurol.* **1994**, *51*, 545 – 554.
27. Brewer, G. J.; Johnson, V.; Dick, R. D.; Kluin, K. J.; Fink, J. K.; Brunberg, J. A. *Arch. Neurol.* **1996**, *53*, 1017 – 1025.
28. Brewer, G. J.; Dick, R. D.; Yuzbasiyan-Gurkin, V.; Tankanow, R.; Young, A. B.; Kluin, K. *J. Arch. Neurol.* **1991**, *48*, 42 – 47.
29. Folkman, J. *N. Engl. J. Med.* **1971**, *285*, 1182 – 1186.
30. Folkman, J. *Cancer Res.* **1986**, *285*, 1182 – 1186.
31. Scappaticci, F. *J. Clin. Oncol.* **2002**, *20*, 3906 – 3927.
32. Fan, T.-P.; Yeh, J.-C.; Leung, K. W.; Yue, P. Y. K.; Wong, R. N. S. *Trends Pharmacol. Sci.* **2006**, *27*, 297 – 309.

33. Genentech Oncology's Page

<http://www.gene.com/gene/research/focusareas/oncology/angiogenesis.html> (accessed April 2008).

34. Ferrara, N.; Hillian, K. J.; Gerber, H. P.; Novotny, W. *Nat. Rev. Drug. Discov.* **2004**, *3*, 391 – 400.

35. Kim, K. J.; Li, B.; Winer, J.; Armanini, M.; Gillet, N.; Phillips, H. S.; Ferrara, N. *Nature* **1993**, *362*, 841 – 844.

36. Parke, A.; Bhattacharjee, P.; Palmer, R. M.; Lazarus, N. R. *Am. J. Pathol.* **1988**, *130*, 173 – 178.

37. Matsubara, T.; Saura, R.; Hirohata, K.; Ziff, M. *J. Clin. Invest.* **1989**, *83*, 158 – 167.

38. Brem, S.; Zagzag, D.; Tsanaclis, A.; Gatley, S.; Elkouby, M.; Brein, S. *Am. J. Path.* **1990**, *137*, 1121 – 1147.

39. Hu, G.-F. *J. Cell Biochem.* **1998**, *69*, 326 – 335.

40. Mandinov, L.; Mandinova, A.; Kyurkchiev, S.; Kyurkchiev, D.; Kehayov, I.; Kolev, V.; Soldi, R.; Bagala, C.; de Muinck, E. D.; Linder, V.; Post, M. J.; Simons, M.; Bellum, S.; Prudovsky, I.; Maciag, T. *Proc. Natl. Acad. Sci.* **2003**, *100*, 6700 – 6705.

41. Pan, Q.; Kleer, C.; van Golen, K.; Irani, J.; Bottema, K.; Bias, C.; De Carvalho, M.; Mesri, E.; Robins, D.; Dick, R. *Can Res.* **2002**, *62*, 4854–4859.

42. Finney, L.; Mandava, S.; Ursos, L.; Zhang, W.; Rodi, D.; Vogt, S.; Legnini, S.; Maser, J.; Ikpatt, F.; Olopade, O. I.; Glesne, D. *PNAS*, **2007**, *104*, 2247 – 2252.

43. Chakravarty, P. K.; Chowdhury, J. R. *J. Cancer Res. Clin. Oncol.* **1984**, *108*, 312–315.

44. Mc Ausland, B. R.; Relly, W. *Exp. Cell Res.* **1980**, *130*, 147 – 157.

45. Marniemi, J.; Järvisalo, J.; Toikka, T.; Rähä, I.; Ahotupa, M.; Sourander, L. *Int. J. Epid.*

1998, 27, 799-807.

46. Reunanen, A.; Knekt, P.; Marniemi, J.; Mäki, J. Maatela, J.; Aromaa, A. *Eur. J. Clin. Nutri.* **1996**, 50, 431 – 437.

47. Khan, M.; Miller, M.; Taylor, J.; Navkiranjit, K.; Dick, R.; van Golen, K.; Brewer, G.; Merajver, S. *Neoplasia* **2002**, 4, 1 – 7.

48. Redman, B. G.; Esper, P.; Pan, Q.; Dunn, R. L.; Hussain, H. K.; Chenevert, T.; Brewer, G. J.; Merajver, S. *Clin. Cancer Res.* **2003**, 9, 1666 – 1672.

49. Goodman, V. L.; Brewer, G. J.; Merajver, S. D. *Endocr. Rel. Cancer* **2004**, 11, 255 – 263.

50. ClinicalTrials.gov, Page. Active trials: Tetrathiomolybdate Available at <http://clinicaltrials.gov/ct2/show/NCT00176800?term=tetrathiomolybdate&rank=1>, (2001)

51. ClinicalTrials.gov, Page. Active trials: Tetrathiomolybdate Available at <http://clinicaltrials.gov/ct2/show/NCT00150995?term=tetrathiomolybdate&rank=3> , (2001)

52. ClinicalTrials.gov, Page. Active trials: Tetrathiomolybdate Available at <http://clinicaltrials.gov/ct2/show/NCT00176774?term=tetrathiomolybdate&rank=6>, (2001)

53. ClinicalTrials.gov, Page. Active trials: ATN-224 Available at <http://clinicaltrials.gov/ct2/show/NCT00383851?term=ATN-224&rank=1>, (2006).

54. ClinicalTrials.gov, Page. Active trials: ATN-224 Available at <http://clinicaltrials.gov/ct2/show/NCT00405574?term=ATN-224&rank=2>, (2006).

55. O'Halloran, T. V.; Culotta, V. C. *J. Biol. Chem.* **2000**, 275, 25057 – 25060.

56. Xiao, Z.; Loughlin, F.; George, G. N.; Howlett, G. J.; Wedd, A. G. *J. Am. Chem. Soc.* **2004**, 126, 3081-3090.

57. Arnesano, F.; Banci, L.; Bertini, I.; Huffman, D. L.; O'Halloran, T. V. *Biochemistry* **2001**, 40, 1528-1539.

58. Roe, J. A.; Selverstone Valentine, J. *Anal. Biochem.* **1990**, *186*, 31-40.
59. Tainer, J. A.; Getzoff, E. D.; Beem, K. M.; Richardson, J. S.; Richardson, D. C. *J. Mol. Biol.* **1982**, *160*, 181-217.
60. Tainer, J. A.; Getzoff, E. D.; Richardson, J. S.; Richardson, D. C. *Nature* **1983**, *306*, 284-287.
61. Getzoff, E. D.; Tainer, J. A.; Weiner, P. K.; Kollman, P. A.; Richardson, J. S.; Richardson, D. C. *Nature* **1983**, *306*, 287-290.

Chapter 2:

1. Solomon, E. I.; Szilagy, R. K.; DeBeer, G. S.; Basumallick, L. *Chem. Rev.* **2004**, *104*, 419–458.
2. Brewer, G. J. *Curr. Opin. Chem. Biol.* **2003**, *7*, 207–212.
3. Berzelius, J. J. *Ann. Phys. Chem.* **1826**, *7*, 262.
4. Laurie, S. H. *Eur. J. Inorg. Chem.* **2000**, 2443 – 2450.
5. Mellor, J. W. *A Comprehensive Treatise on Inorganic and Theoretical Chemistry, Sulphomolybdates and Oxysulphomolybdates*; Longman: London, 1922.
6. Laurie, S. H.; Pratt, D. E.; Yong, J. H. L. *Inorg. Chim. Acta.* **1984**, *93*, L57 – L59.
7. Müller, A.; Diemann, E.; Jostes, R.; Bögge, H. *Angew. Chem. Int. Ed.* 1981, *20*, 934 – 955.
8. Müller, A.; Diemann, E.; Neumann, F.; Menge, R. *Chem. Phys. Letters* **1972**, *16*, 521 – 525.
9. Minelli, M.; Young, C. G.; Enermark, J. H. *Inorg. Chem.* 1985, *24*, 111 – 1113.
10. Young, C. G.; Minelli, M.; Enermark, J. H.; Miessler, G.; Janietz, N.; Kauermann, H.; Wachter, J. *Polyhedron* **1986**, *5*, 407 – 413.
11. Minelli, M.; Enermark, J. H.; Brownlee, R. T. C.; O'Connor, M. J.; Wedd, A. G. *Coord. Chem. Rev.* **1985**, *68*, 169 – 278.

12. Clarke, N. J.; Laurie, S. H. *J. of Inorg. Biochem.* **1980**, *12*, 37 – 43.
13. Mason, J. *Irish Vet. J.* **1981**, *35*, 221 – 229.
14. Laurie, S. H.; Pratt, D. E. *Inorg. Chim Acta* **1986**, *123*, 193 – 196.
15. Brewer, G. J.; Dick, R. D.; Yuzbasiyan-Gurkan, V.; Tanakow, R.; Young, A. B.; Kluin, K. J. *Arch. Neurol.*, **1991**, *48*, 42 – 47.
16. Brewer, G. J.; Dick, R. D.; Johnson, V.; Wang, Y.; Yuzbasiyan-Gurkan, V.; Kluin, K. J.; Flink, J. K.; Aisen, A. *Arch. Neurol.*, **1994**, *51*, 545 – 554.
17. Brewer, G. J.; Johnson, V.; Dick, R. D.; Wang, Y.; Kluin, K. J.; Flink, J. K.; Brunberg, J. *Arch. Neurol.*, **1996**, *53*, 1017 – 1025.
18. Khan, M.; Miller, M.; Taylor, J.; Navkiranjit, K.; Dick, R. D.; Van Golen, K. L.; Brewer, G. J.; Merajver, S. D. *Neoplasia* **2002**, *4*, 164 – 170.
19. Van Golen, K. L.; Bao, L.; Brewer, G. J.; Pienta, K.; Kamradt, J.; Livant, D.; Merajver, S. D. *Neoplasia* **2002**, *4*, 373 – 379.
20. Brewer, G. J.; *EBM* **2001**, *226*, 665 – 673.
21. Juarez, J. C.; Betancourt, O.; Pirie-Shepherd, S. R.; Guan, X.; Price, M.; Shaw, D. E.; Mazar, A. P.; Donate, F. *Clin. Cancer Res.* **2006**, *12*, 4974 – 4982.
22. Lowndes, S. A.; Harris, A. L. *Oncology Res.* **2004**, *14*, 529 – 539.
23. Lowndes, S. A.; Harris, A. L. *J. Mammary Gland Biol. Neoplasia* **2005**, *10*, 299 – 310.
24. Pufahl, R. A.; Singer, C. P.; Peariso, K. L.; Lin, S.-J.; Schmidt, P. J.; Fahrni, C. J.; Cizewski Culotta, V.; Penner-Hahn, J. E.; O'Halloran, T. V. *Science* **1997**, *278*, 853-856.
25. Wernimont, A. K.; Huffman, D. L.; Lamb, A. L.; O'Halloran, T. V.; Rosenzweig, A. C. *Nat. Struct. Biol.* **2000**, *7*, 766 – 771.

26. McMaster, W. H.; Del Grande, N. K.; Mallet, J. H.; Hubbell, J. H.; Commerce, U.S.D.O., Ed. 1969.
27. Weng, T. C.; Waldo, G. S.; Penner-Hahn, J. E. *J. of Syn. Rad.* **2005**, *12*, 506 - 510.
28. Teo, B. K. EXAFS: Basic Principles and Data Analysis; Springer-Verlag: New York, 1985.
29. Zabinsky, S. I.; Rehr, J. J.; Ankudinov, A.; Albers, R. C.; Eller, M. J. *Phys. Rev. B* **1995**, *52*, 2995-3009.
30. Ford, P. C.; Vogler, A. *Acc. Chem. Res.* **1993**, *26*, 220 – 226.
31. Pountney, D. L.; Schauwecker, I.; Zarn, J.; Vasák, M. *Biochemistry* **1994**, *33*, 9699 – 9705.
32. Roschitzki, B.; Vasák, M. *J. Biol. Inorg. Chem.* **2002**, *7*, 611 – 616.
33. Kau, L.-S, Spira-Solomon, D. J.; Penner-Hahn, J. E.; Hodgson, K. O.; Solomon, E. I. *J. Am. Chem. Soc.* **1987**, *109*, 6433 – 6442.
34. George, G. N.; Kipke, C. A.; Prince, R. C.; Sunde, R. A.; Enemark, J. H.; Cramer, S. P. *Biochemistry* **1989**, *28*, 5075 – 5080.
35. Müller, A.; Diemann, E.; Jostes, R.; Bögge, H. *Angew. Chem. Int. Ed.* **1981**, *20*, 934 – 955.
36. Sarkar, S.; Mishra, S. B. S. *Coord. Chem. Rev.* **1984**, *59*, 239 – 264.
37. Bursakov, S. A.; Gavel, Gavel, O. Y.; Di Rocco, G.; Lampreia, J.; Calvete, J.; Pereira, A. S.; Moura, J. J. G.; Moura, I. *J. Inorg. Biochem.* **2004**, *98*, 833 – 840.
38. Quagraine, E. K.; Reid, R. S. *J. Inorg. Biochem.* **2001**, *85*, 53 – 60.
39. Coucouvanis, D.; Murphy, C. N.; Kanodia, S. K. *Inorg. Chem.* **1980**, *19*, 2993 – 2998.
40. George, G. N.; Pickering, I. J.; Yu, E. Y.; Prince, R. C.; Bursakov, S. A.; Gravel, O. Y.; Moura, I.; Moura, J. J. G. *JACS*, **2000**, *122*, 8321-8322.
41. George, G. N; Pickering, I. J.; Harris, H. H.; Gailer, J.; Klein, D.; Lichtmanegger, J.; Summer, K.-H. *JACS*, **2003**, *125*, 1704-1705.

Chapter 3:

1. Müller, A.; Diemann, E.; Jostes, R.; Bögge, H. *Angew. Chem. Int. Ed.* **1981**, *20*, 934 – 955.
2. Jones, H. B.; Gooneratne, S. R., Howell, J. *Res. in Vet. Sci.* **1984**, *37*, 273 – 282.
3. Brewer, G. J.; Dick, R. D.; Yuzbasiyan-Gurkan, V.; Tanakow, R.; Young, A. B.; Kluin, K. J. *Arch. Neurol.*, **1991**, *48*, 42 – 47.
4. Pan, Q.; Kleer, C. G.; Van Golen, K. L.; Irani, J.; Bottema, K. M.; Bias, C.; De Carvalho, M.; Mesri, E. A.; Robins, D. M.; Dick, R. D. *Cancer Res.* **2002**, *62*, 4854 – 4859.
5. Lowndes, S. A.; Harris, A. L. *Oncology Res.* **2004**, *14*, 529 – 539.
6. Lowndes, S. A.; Harris, A. L. *J. Mammary Gland Biol. Neoplasia* **2005**, *10*, 299 – 310.
7. Juarez, J. C.; Betancourt, O.; Pirie-Shepherd, S. R.; Guan, X.; Price, M.; Shaw, D. E.; Mazar, A. P.; Donate, F. *Clin. Cancer Res.* **2006**, *12*, 4974 – 4982.
8. Sarkar, S.; Mishra, S. B. S. *Coord. Chem. Rev.* **1984**, *59*, 239 – 264.
9. Chidambaram, M. V.; Barnes, G.; Frieden, E. *J. Inorg. Biochem.* **1984**, *22*, 231 – 239.
10. Bristow, S.; Garner, D.; Hagyard, S. K.; Morris, G. A. Nicholson, J. R.; Mills, C. F. *J. Chem. Soc. Chem. Commun.* **1985**, 479 – 481.
11. Quagraine, E. K.; Reid, R. S. *J. Inorg. Biochem.* **2001**, *85*, 53 – 60.
12. Suzuki, K.T.; Ogra, Y. *Res. Commun. Mol. Pathol. Pharmacol.* **1995**, *88*, 187 – 195.
13. Ogra, Y.; Suzuki, K. *Res. Commun. Mol. Pathol. Pharmacol.* **1995**, *88*, 196 – 204.
14. Pufahl, R. A.; Singer, C. P.; Peariso, K. L.; Lin, S. J.; Schmidt, P. J.; Fahrni, C. J.; Culotta, V. C.; Penner-Hahn, J. E.; O'Halloran, T. V. *Science* **1997**, *278*, 853 – 856.
15. Strub, M. P.; Hoh, F.; Sanchez J. F.; Strub, J. M.; Bock, A.; Aumelas, A.; Dumas, C. *Structure* **2003**, *11*, 1359–1367.

16. Guerrero, S. A.; Hecht, H.-J.; Hofmann, B.; Biebl, H.; Singh, M. *Appl. Microbiol. Biotechnol*, **2001**, *56*, 718 –723.
17. Otwinowski, Z.; Minor, W. *Methods Enzymol.* **1997**, *276*, 307 – 326.
18. Storoni, L. C.; McCoy, A. J.; Read, R. J. *Acta Crystallogr D Biol Crystallogr* **2004**, *60*, 432 – 438.
19. Rosenzweig, A. C.; Huffman, D. L.; Hou, M. Y.; Wernimont, A. K.; Pufahl, R. A.; O'Halloran, T. V. *Structure* **1999**, *7*, 605 – 617.
20. Hendrickson, W. A.; Horton, J. R.; LeMaster, D. M. *EMBO* **1990**, *9*, 1665–1672.
21. Mills, C. F. *Philos. Trans. R. Soc. (Lond.), Ser. B.* **1979**, *288*, 51.
22. George, G. N.; Pickering, I. J.; Harris, H. H.; Gailer, J.; Klein, D.; Lichtmanegger, J.; Summer, K. H. *J Am Chem Soc* **2003**, *125*, 1704 – 1705.
23. Chen, J.; Wei, Z.; Xu, Q.; Li, H.; Lang, J. *Chinese J. Struct. Chem.* **2004**, *23*, 464 – 469.
24. Zhang, C.; Song, Y.; Kuhn, F.; Xu, Y.; Xin, X.; Fun, H.; Herrmann, W. *Eur. J. Inorg. Chem.* **2002**, 56 – 64.
25. Li, J.; Xin, X.; Zhou, Z.; Yu, K. *Chem. Commun* **1991**, 249 – 250.
26. Dobbek, H.; Gremer, L.; Kiefersauer, R.; Huber, R.; Meyer, O. *Proc Natl Acad Sci.* **2002**, *99*, 15971 – 15976.
27. Pufahl, R. A.; Singer, C. P.; Peariso, K. L.; Lin, S. J.; Schmidt, P. J.; Fahrni, C. J.; Culotta, V. C.; Penner-Hahn, J. E.; O'Halloran, T. V. *Science* **1997**, *278*, 853 – 856.
28. Arnesano, F.; Banci, L.; Bertini, I.; Huffman, D. L.; O'Halloran, T. V. *Biochemistry*, **2001**, *40*, 1528 – 1539.
29. Dalosto, S. D. *J. Phys. Chem. B.* **2007**, *111*, 2932 – 2940.
30. Safei, R.; Blair, B. G.; Rasmussen, M. R.; Larson, B. J.; Howell, S. B. Unpublished data.

31. Hamza, I.; Prohaska, J.; Gitlin, J. D. *Proc. Natl. Acad. Sci.* **2003**, *100*, 1215 – 1220.

Chapter 4:

1. Mc Cord, J. M.; Fridovich, I. *J. Biol. Chem.* **1969**, *244*, 6049 – 6055.

2. Tainer, J. A.; Getzoff, E. D.; Richardson, J. S.; Richardson, D. C. *Nature* **1983**, *306*, 284 – 287.

3. Grzenkowicz-Wydra, J., *et al.*, *J. Mol. Cell Biochem.* 2004, *264*, 169 – 181.

4. Marikovsky, M., *et al.*, *Int. J. Cancer* **2002**, *97*, 34 – 41.

5. Rotilio, G.; Bray, R. C.; Fielden, E. M. *Biochim. Biophys. Acta* **1972**, *268*, 605–609.

6. Rigo, A.; Viglino, P.; G. Rotilio. *Biochem. Biophys. Acta* **1975**, *63*, 1013–1018.

7. Misra, H. P. *J. Biol. Chem.* **1979**, *254*, 11623–11628.

8. Wambi Kiese, C. O.; Katusic, Z. S. *Am. J. Physiol.* **1999**, *276*, 1043–1048.

9. Huang, P.; Feng, L.; Oldham, E. A.; Keating, M. J.; Plunkett, W. *Nature* **2000**, *407*, 390–395.

10. Chidambaram, M. V.; Barnes, G.; Frieden, E. *J. Inorg. Biochem.* **1984**, *22*, 231–239.

11. Juarez, J. C.; Betancourt, O.; Pirie-Shepherd, S. R.; Guan, X.; Price, M. L.; Shaw, D. E.; Mazar, A. P.; Doñate, F. *Clin. Cancer Res.* **2006**, *12*, 4974–4982.

12. Alvarez, H. M.; O'Halloran, T. V. Unpublished data.

13. Mellor, J. W. *A Comprehensive Treatise on Inorganic and Theoretical Chemistry, Sulphomolybdates and Oxysulphomolybdates*; Longman: London, 1922.

14. Laurie, S. H.; Pratt, D. E.; Yong, J. H. L. *Inorg. Chim. Acta.* **1984**, *93*, L57 – L59.

15. Lyons, T. J.; Nersissian, A.; Goto, J. J.; Zhu, H.; Gralla, E. B.; Valentine, J. S. *J. Biol. Inorg. Chem.* **1998**, *3*, 650 – 662.

16. Beauchamp, C.; Fridovich, I. *Anal. Biochem.* **1971**, *44*, 276–287.

17. McMaster, W. H.; Del Grande, N. K.; Mallet, J. H.; Hubbell, J. H.; Commerce, U.S.D.O., Ed. 1969.
18. Weng, T. C.; Waldo, G. S.; Penner-Hahn, J. E. *J. of Syn. Rad.* **2005**, *12*, 506 - 510.
19. Teo, B. K. EXAFS: Basic Principles and Data Analysis; Springer-Verlag: New York, 1985.
20. Zabinsky, S. I.; Rehr, J. J.; Ankudinov, A.; Albers, R. C.; Eller, M. J. *Phys. Rev. B* **1995**, *52*, 2995-3009.
21. Beheshti, A.; Clegg, W.; Sadr, M. H.; *Inorg. Chim. Acta* **2002**, *335*, 21.
22. George, G. N.; Kipke, C. A.; Prince, R. C.; Sunde, R. A.; Enemark, J. H.; Cramer, S. P. *Biochemistry* **1989**, *28*, 5075 – 5080.
23. Sarkar, S.; Mishra, S.B.S *Coord. Chem. Rev.* **1984**, *59*, 239 – 264.
24. Hough, M. A.; Samar-Hasnain, S. *J. Mol. Biol.* **1999**, *287*, 579–592.
25. Hough, M. A.; Strange, R. W.; Samar-Hasnain, S. *J. Mol. Biol.* **2000**, *304*, 231–241.
26. Forman, H. J.; Fridovich, I. *J. Biol. Chem.* **1973**, *248*, 2645–2649.
27. Inouye, K.; Osaki, A.; Tonomura, B. *J. Biochem.* **1994**, *115*, 507–515.
28. Doucette, P. A.; Whitson, L. J.; Cao, X.; Schirf, V.; Demeler, B.; Valentine, J. S.; Hansen, J. C; Hart, P. J. *J. Biol. Chem.* **2004**, *279*, 54558–54566.
29. Furukawa, Y.; Torres, A. S.; O’Halloran. T. V. *EMBO* **2004**, *23*, 2872–2881.
30. Pan, W. H.; Harmer, M. A.; Halbert, T. R.; Stiefel, E. I. *J. Am. Chem. Soc.* **1984**, *106*, 459–460.
31. Acott, S. R.; Garner, C. D.; Nicholson, J. R. *J. Chem. Soc. Dalton Trans.* **1983**, 713 – 719.
32. Müller, A.; Dartmann, M.; Römer, C.; Clegg, W.; Sheldrick, G. M. *Angew. Chem. Int. Ed.* **1981**, *20*, 1060 – 1061.
33. Clegg, W.; Garner, D.; Nicholson, J. R. *Acta Cryst.* **1983**, *C39*, 552 – 554.

34. Clegg, W.; Scattergood, C.; Garner, C. D. *Acta Cryst.* **1987**, C43, 786 – 787.
35. Sécheresse, F.; Béernes, S.; Robert, F.; Jeannin, Y. *J. Chem. Soc. Dalton Trans.* **1991**, 2875 – 2881.
36. Béernes, S.; Sécheresse, F.; Jeannin, Y. *Inorg. Chim. Acta* **1992**, 191, 11 – 13.
37. Binnie, W. P.; Redman, M. J.; Mallio, W. J. *Inorg. Chem.* **1970**, 9, 1449 – 1452.
38. Ecclestone, T.; Harvey, I.; Laurie, S. H. Symons, M. C. R.; Taiwo, F. A. *Inorg. Chem. Commun.* **1998**, 1, 460 – 462.
39. Potvin, C.; Manoli, J. M.; Salis, M.; Sécheresse, F. *Inorg. Chim. Acta* **1984**, 83, L19 – L21.
40. George, G. N.; Pickering, I. J.; Yu, E. Y.; Prince, R. C.; Bursakov, S. A.; Gravel, O. Y.; Moura, I.; Moura, J. J. G. *JACS*, **2000**, 122, 8321-8322.

Chapter 5:

1. Orvig, C.; Abrams, M. J. *Chem. Rev.* **1999**, 99, 2201–2203.
2. Sadler, P. J.; Guo, Z. *Pure & Appl. Chem.* **1998**, 70, 863–871.
3. Sadler, P. J. *Advances in Inorg. Chem.* **1991**, 36, 1–48.
4. Dyson, P. J.; Sava, G. *Dalton Trans.* **2006**, 1929–1933.
5. Lippard, S. J.; Berg, J. M. *Principles of Bioinorganic Chemistry*; University Science Books: California, 1994.
6. ClinicalTrials.gov, Page. Active trials: Tetrathiomolybdate Available at <http://clinicaltrials.gov/ct2/show/NCT00176800?term=tetrathiomolybdate&rank=1>, (2001)
7. ClinicalTrials.gov, Page. Active trials: Tetrathiomolybdate Available at <http://clinicaltrials.gov/ct2/show/NCT00150995?term=tetrathiomolybdate&rank=3>, (2001)
8. ClinicalTrials.gov, Page. Active trials: Tetrathiomolybdate Available at <http://clinicaltrials.gov/ct2/show/NCT00176774?term=tetrathiomolybdate&rank=6>, (2001)

9. Brewer, G. J.; Dick, R. D.; Yuzbasiyan-Gurkan, V.; Tanakow, R.; Young, A. B.; Kluin, K. *J. Arch. Neurol.*, **1991**, *48*, 42 – 47.
10. Gooneratne, S. R.; Howell, J. McC.; Gawthorne, J. M.; Kumaratilake, J. S. *J. Inorg. Biochem.* **1989**, *35*, 23–36.
11. Jones, H. B.; Gooneratne, S. R.; Howell, J. McC.; *Res. Vet. Sci.* **1984**, *37*, 273–282.
12. Chidambaram, M. V.; Barnes, G.; Frieden, E. *J. Inorg. Biochem.* **1984**, *22*, 231 – 239.
13. Juarez, J. C.; Betancourt, O.; Pirie-Shepherd, S. R.; Guan, X.; Price, M.; Shaw, D. E.; Mazar, A. P.; Donate, F. *Clin. Cancer Res.* **2006**, *12*, 4974 – 4982.
14. Mellor, J. W. *A Comprehensive Treatise on Inorganic and Theoretical Chemistry, Sulphomolybdates and Oxysulphomolybdates*; Longman: London, 1922.
15. Laurie, S. H.; Pratt, D. E.; Yong, J. H. L. *Inorg. Chim. Acta.* **1984**, *93*, L57 – L59.
16. Van de Loosdrecht, A. A.; Beelen, R.H.; Ossenkoppele, G. J.; Broekhoven, M. G. Langenhuijsen, M. M. *J. Immunol. Methods* **1994**, *174*, 311 – 320.
17. Stefan Vogt's Virtual Page. http://www.stefan.vogt.net/research_interests.html (accessed October 2007).

Chapter 6:

1. Andrews, N. C. *Curr Opin Chem Biol.* 2002, **6**, 181 – 186.
2. O'Halloran, T. V.; Culotta, V. C. *J. Biol. Chem.* **2000**, *275*, 25057 – 25060.
3. Pufahl, R. A.; Singer, C. P.; Peariso, K. L.; Lin, S.-J.; Schmidt, P. J.; Fahrni, C. J.; Cizewski Culotta, V.; Penner-Hahn, J. E.; O'Halloran, T. V. *Science* **1997**, *278*, 853-856.
4. Huffman, D. L.; O'Halloran, T. V. *J. Biol. Chem.* **2000**, *275*, 18611–18614.
5. Rosenzweig, A. C. *Acc. Chem. Res.* **2001**, *34*, 119–128.

6. Brewer, G. J.; Dick, R. D.; Yuzbasiyan-Gurkin, V.; Tankanow, R.; Young, A. B.; Kluin, K. *J. Arch. Neurol.* **1991**, *48*, 42–47.
7. Bissig, K.-D.; Voegelin, T. C.; Solioz, M. *FEBS Letters* **2001**, *507*, 367–370.
8. Alvarez, H. M.; Kelly, R.; Penner-Hahn, J.; O'Halloran, T. V. Unpublished data.
9. Alvarez, H. M.; Xue, Y.; Robinson, C.; Mondragón, A.; O'Halloran, T. V. Unpublished data.
10. Su, C.; Wang, F.; Ciolek, D.; Pan, Y.-C. E. *Anal. Biochem.* **1994**, *223*, 93 – 98.
11. Kim, R.; Yokota, H.; Kim, S.-H. *Anal. Biochem.* **2000**, *282*, 147–149.
12. Simpson, R. J. *Proteins and Proteomics, a laboratory manual*; Cold Spring Harbor Laboratory Press: Cold Spring Harbor, NY, 2003.
13. Krowczynska, A. M.; Donoghue, K.; Hughes, I. *BioTechniques* **1995**, *18*, 698 – 703.
14. Neilsen, J. L.; Abildtrup, A.; Christensen, J.; Watson, P.; Cox, A.; McLeod, C. W. *Spectrochim. Acta Part B.* **1998**, *53*, 339 – 345.
15. Binet, M. R. B.; Ma, R.; McLeod, C. W.; Poole, R. K. *Anal. Biochem.* **2003**, *318*, 30 – 38.
16. Ma, R.; McLeod, C. W.; Tomlinson, K.; Poole, R. *Electrophoresis* **2004**, *25*, 2469 – 2477.
17. Ballihaut, G.; Claverie, F.; Pécheyran, C.; Mounicou, S.; Grimaud, R.; Lobinski, R. *Anal. Chem.* **2007**, *79*, 6874 – 6880.
18. Amici A.; Levine, R. L.; Tsai, L.; Stadtman, E. R. *J. Biol. Chem.* **1989**, *264*, 3341 – 3346.
19. Requena J. R.; Chao C. C.; Levine R. L.; Stadtman E. R. *Proc. Natl. Acad. Sci.* **2001**, *98*, 69 – 74.
20. Banci, L.; Bertini, I.; Cantini, F.; Felli, I. C.; Gonnelli, L.; Hadjiliadis, N.; Pierattelli, R.; Rosato, A.; Voulgaris, P. *Nat. Chem. Biol.* **2006**, *2*, 367 – 368.
21. Itoh, S.; Kim, H. W.; Nakagawa, O.; Ozumi, K.; Lessner, S. M.; Aoki, H.; Akram, A.; McKinney, R. D.; Ushio-Fukai, M.; Fukai, T. *J. Biol. Chem.* **2008**, *283*, 9157 – 9167.

Hamsell M. Alvarez

e-mail: h-alvarez@northwestern.edu

Campus Address: 2145 Sheridan Road
Evanston, IL 60208 (847) 467 - 7280**Home Address:** 445 E. Ohio St. Apt # 3407
Chicago, IL 60611 (847) 212 - 4419**EDUCATION**

2008 **Northwestern University Evanston, Illinois** - *Ph.D. Candidate in Inorganic Biochemistry* under Dr. Thomas O'Halloran
 2002 **The University of North Carolina at Charlotte Charlotte, North Carolina** - *M.S. in Chemistry* (4.00/4.00 GPA) under Dr. Daniel Rabinovich
 2000 **Peruvian University Cayetano Heredia Lima, Peru** - *B.S. in Chemistry* (3.75/4.00 GPA) under Dr. Bertha Llanos

EXPERIENCE**Northwestern University Evanston, Illinois (2002 – 2008)**

Research Assistant – Determination of the Mechanism of Action of a New Anticancer and Antiangiogenic Drug, Ammonium Tetrathiomolybdate: Drug Intracellular Localization in Cancer Cells and Interaction with Copper Metalloproteins, with Dr. Thomas O'Halloran. Teaching Assistant – General Chemistry (Lab TA and Head TA). Laboratory Safety Officer (Biological and Chemical Safety).

The University of North Carolina at Charlotte Charlotte, North Carolina (2001 – 2002)

Research Assistant – Inorganic/Organic Synthesis and Structural Properties of Model Complexes for Nickel, Iron Hydrogenases. Teaching Assistant – General Chemistry (Lab TA)

Peruvian University Cayetano Heredia Lima, Peru (2000 – 2001)

Teaching Assistant – Pre-University General Chemistry

Royal Friesland Foods Peru Lima, Peru (1999 – 2000)

Research & Development/Quality Control assistant for Dairy Products

Peruvian University Cayetano Heredia Lima, Peru (1998 – 1999)

Research Assistant – Anticorrosive Agents for the Marine Industry under Dr. Bertha Llanos

PUBLICATIONS AND CONFERENCE PAPERS*** Publications**

“Inhibition of the Cu Transfer Activity of Atx1 by Ammonium Tetrathiomolybdate” Alvarez, H. M.; Xue, Y.; Robinson, C. D.; Canalizo-Hernández, M. A.; Mondragón, A.; O'Halloran, T. V. *Manuscript in preparation for Nature*, April 2008.

“Solution Coordination Chemistry of the interaction of intracellular Copper Proteins with the anticancer drug Ammonium Tetrathiomolybdate (TM)” Alvarez, H. M.; Kelly, R.; Penner-Hahn, J. E.; O'Halloran, T. *Manuscript in preparation for J. Amer. Chem. Soc.*, April 2008.

“Thalium Bis(mercaptoimidazolyl)borates” Alvarez, H. M.; Gillespie, P. A.; Gause, C. D.; Rheingold, A. L.; Golden, J. A.; Rabinovich, D. *Polyhedron* **2004**, *23*, 617 – 620

“Poly(mercaptoimidazolyl)borate Chemistry and the Predominance of K^3 -S,S,H over K^2 -S,S or K^3 -S,S,S Coordination Modes: Unexpected Formation of Square Pyramidal Ni(II) Complexes” Alvarez, H. M.; Tanski, J. M.; Rabinovich, D. *Polyhedron* **2004**, *23*, 395 – 403

“Homoleptic Group 12 Metal Bis(mercaptoimidazolyl)borate Complexes $M(Bm^R)_2$ ($M = Zn, Cd, Hg$)” Alvarez, H. M.; Tran, T.; Ritcher, M. A.; Alyounes, D. M.; Tanski, J. M.; Krawiec, M.; Rabinovich, D. *Inorg. Chem.* **2003**, *42*, 2149-2156

“Modelling Nickel Hydrogenases: Synthesis of Distorted Octahedral Complex with an Unprecedented $[NiS_4H_2]$ Core” Alvarez, H. M.; Krawiec, M.; Donovan-Merkert, B. T.; Rabinovich, D. *Inorg. Chem.* **2001**, *40*, 5736 – 5737

* **Conference papers and invited presentations**

“Insights on the Mechanism of Action of the Anticancer and Wilson’s Disease Drug: Ammonium Tetrathiomolybdate” Alvarez, H. M.; Kelly, R.; Penner-Hahn, J.; O’Halloran, T. V. Pontificia Universidad Catolica del Peru, May 2007. Lima, Peru.

“Insights on the Mechanism of Action of the Anticancer and Antiangiogenic Drug: Ammonium Tetrathiomolybdate (TM)” Alvarez, H. M.; Kelly, R.; Penner-Hahn, J.; O’Halloran, T. V. 233rd National ACS Meeting March 2007. Chicago, IL.

“Model Studies of the Tetrathiomolybdate (TM) and its Interactions with Copper Proteins: How does the Copper Antagonist Drug TM Interact with Copper Trafficking Proteins?” Alvarez, H. M.; Penner-Hahn, J.; O’Halloran, T. V. 12th International Conference on Biological Inorganic Chemistry August 2005. Ann Arbor, MI.

“Model Studies of the Tetrathiomolybdate and the Inhibition of Cu-Atx1 and Cu,Zn-SOD1” Alvarez, H.; Penner-Hahn, J.; O’Halloran, T. V. 4th International Meeting on Copper Homeostasis and its disorders; Molecular and Cellular Aspects. October 2004, Ischia, Italy.

“Interaction of Cu-Atx1 with Ammonium Tetrathiomolybdate” Alvarez, H. M.; O’Halloran, T. V. 9th Gordon Research Conference: Bioinorganic Chemistry. January 2004, Ventura, CA.

“Homoleptic Bis(mercaptoimidazolyl)borate Complexes” Alvarez, H. M.; Alyounes, D. M.; Rabinovich, D. 223rd National ACS Meeting April 2002. Orlando, FL.

“Thione Complexes of the First Row Transition Metals” Alvarez, H. M.; Alyounes, D. M.; Rabinovich, D. Southeastern Regional Meeting of the ACS September 2001. Savannah, GA.

HONORS, AWARDS, COURSES, FELLOWSHIPS AND SCHOLARSHIPS

2006 Outstanding Young Scientist - Lindau Meeting of Nobel Laureates in Chemistry, Lindau, Germany.

2005 Weinberg Outstanding Graduate Student Teaching Award, Northwestern University

2005 National School on Neutron and X-ray Scattering, Argonne National Laboratory, Argonne, IL

2005 Searle Center Teaching Assistant Fellow, Northwestern University

2005 Malkin and Rober H. Lurie Comprehensive Cancer Center Scholarship, Northwestern University

2002 Master’s Thesis Award in Physical Sciences, Conference of Southern Graduate Schools

2002 Graduate School Master’s Thesis Award for Excellence in Physical Sciences, UNC Charlotte

2002 Division of Inorganic Chemistry Student Travel Award – American Chemical Society (ACS)

2002 ACS Project SEED Scientist-Mentor for economically disadvantaged students

2001 North Carolina Chemical Club Scholarship

2001 Graduate Research Achievement Award, Department of Chemistry, UNC Charlotte

1995 - 1999 Undergraduate Honors Scholarship, Peruvian University Cayetano Heredia

LEADERSHIP AND PROFESSIONAL AFFILIATIONS

Public and Academic Secretary of the Northwestern Graduate Student Association for Latino Minorities

Phi Lambda Upsilon, Alpha Gamma Chapter, National Honorary Chemical Society

Division of Inorganic and Biological Chemistry, Student Member - American Chemical Society

ADDITIONAL SKILLS

* **Laboratory-Technical:** PCR, Protein Expression and Purification, SDS-PAGE, Protein Crystallization, Inorganic/Organic Synthesis, HPLC, FPLC, MALDI-TOF MS, ESI-MS, ICP-AES/MS, UV-Vis, FTIR, ¹H, ¹³C, Paramagnetic and Multinuclear NMR, Magnetic Susceptibility, Elemental Analysis, Cell Culture,

Microscopy, UV-Vis Light Scattering, X-ray Fluorescence Microscopy, X-ray Absorption Spectroscopy (XANES & EXAFS), Air Sensitive Techniques (glovebox), ChemDraw, MacPyMOL, IGOR Pro, VMD.

* **Foreign Language:** English and Spanish